Une opportunité pour les lasers visibles : les cristaux à base d'oxyde activés par des ions Tb3+ ou Dy3+

Hengjun Chen

▶ **To cite this version:**

HAL Id: tel-02860721

https://pastel.hal.science/tel-02860721

Submitted on 8 Jun 2020

THÈSE DE DOCTORAT

de l'Université de recherche Paris Sciences et Lettres
PSL Research University

Préparée à Chimie ParisTech

Une opportunité pour les lasers visibles: les cristaux à base d'oxyde activés par des ions Tb³⁺ ou Dy³⁺

Opportunity for visible laser: oxide-based crystals activated by Tb³⁺ or Dy³⁺ ions

Ecole doctorale n°397

Physique et chimie des matériaux

Spécialité **Chimie des matériaux**

COMPOSITION DU JURY :

M. WALLEZ Gilles
UPMC, Président du jury

M. DRUON Frédéric
Institut d'Optique, Rapporteur

M. BRAUD Alain
ENSICaen, Rapporteur

M. VEBER Philippe
Institut Lumière Matière, Examinateur

M. RYTZ Daniel
FEE GmbH, Examinateur

M. KRAENKEL Christian
Leibniz-Institut für Kristallzüchtung, Examinateur

M. AKA Gérard
Chimie ParisTech, Directeur de these

**Soutenue par Hengjun CHEN
le 25 octobre 2018**

Dirigée par **Gérard AKA**

RESUME

Les lasers émettant dans le domaine visible attirent depuis longtemps l'attention tant pour la recherche que pour les applications commerciales. Leurs utilités impliquent non seulement qu'ils peuvent être détectés à l'œil nu, mais aussi dans la région spectrale spécifique de la lumière visible, comprise entre 400 et 770 nm environ. Les laser visibles trouvent des applications dans divers domaines, notamment l'affichage, la défense, le stockage de données optiques, la spectroscopie, le diagnostic médical et la thérapie. Le développement des lasers visibles est également stimulé par les sciences et les technologies à la pointe du progrès. Tenant compte de la largeur de bande d'émission étroite, de la modulation et de la perte de transmission dans l'air, les lasers visibles ont été exploités pour les communications optiques sans fil, permettant un débit de transmission des données allant jusqu'à 100 Gb/s. Les lasers situés dans les plages spectrales bleues et vertes sont favorables à la cartographie laser bathymétrique, car ils sont capables de pénétrer dans l'eau avec une atténuation beaucoup moins grande que les lasers proches de l'infrarouge. Les nouveaux projecteurs laser offrent de bonnes perspectives sur le marché, car ils offrent une luminosité et une résolution bien meilleures que les projecteurs à lampe traditionnels. De plus, il existe une demande croissante en ce qui concerne la diversité de longueur d'onde d'émission cohérente pour des applications telles que la cytométrie en flux et la microscopie à super-résolution.

Les émissions de laser visibles peuvent être produites par différents types de résonateurs. Parmi ceux-ci, les lasers à l'état solide utilisant des cristaux activés par des lanthanides sont les plus mis en évidence. Ils se caractérisent par une qualité de faisceau élevée, une conception de résonateur compacte, une polyvalence de longueur d'onde de sortie et une capacité de fonctionnement dans plusieurs modes. Les ions Nd^{3+} et Yb^{3+} ont été largement étudiés pour générer des émissions laser dans le domaine spectral visible. Cependant, ces dispositifs nécessitent des conversions de fréquence de leurs émissions infrarouges fondamentales, ce qui réduit l'efficacité et complique le système laser. Ce désagrément peut être résolu en utilisant des ions actifs pouvant directement émettre des radiations visibles. Néanmoins, cette question n'a pas attiré beaucoup d'attention en raison du manque de sources de pompage efficaces au cours du siècle dernier.

Cette ébauche a été remplie par l'invention et le développement de diodes laser (LDs) à émission bleue. En 2004, A. Richter et al. ont décrit le premier laser à l'état solide pompé par LD émettant directement dans le domaine spectral visible, utilisant Pr^{3+} comme l'ion actif. Le laser a été pompé à 442 nm et exploité à 640 nm. Par la suite, de plus en plus d'ions lanthanides ont été exploités pour générer des émissions laser visibles selon le même schéma, profitant du développement rapide des sources de pompage laser à semi-conducteurs. Outre le Pr^{3+}, des opérations au laser visible utilisant comme ions actifs des ions Sm^{3+}, Eu^{3+}, Tb^{3+}, Dy^{3+}, Ho^{3+} ou Er^{3+} ont été démontrées au cours des dernières années.

Ces nouveaux lasers étendent considérablement les longueurs d'onde de sortie disponibles des lasers traditionnels convertis en fréquence. Néanmoins, les cristaux à base de fluorure étaient généralement utilisés comme milieu à gain dans ces démonstrations. Leur fabrication est difficile et coûteuse en raison de la nécessité d'une atmosphère de protection complexe telle que CF_4.

Un travail très utile consiste à réaliser de telles opérations laser visibles dans des matrices à base d'oxydes, qui ont de meilleures perspectives en termes d'industrialisation que les fluorures en raison des processus de croissance plus simples. Néanmoins, certains inconvénients des matériaux à base d'oxydes pourraient entraver considérablement l'émission laser dans le visible: la valeur élevée des énergies de phonon, la force du champ cristallin et la faible énergie de la bande interdite. Ces caractères peuvent entraîner une dépeuplement du niveau laser supérieur par le biais de processus de relaxation multiphonon ou de transfert d'énergie. Le principal défi consiste donc à sélectionner des matériaux hôtes appropriés et à fabriquer des matériaux monocristallins de taille et de qualité optique suffisantes.

Parmi les ions actifs mentionnés ci-dessus, nous nous sommes particulièrement intéressés aux ions Tb^{3+} et Dy^{3+} qui ont quelques avantages. Le Tb^{3+} peut être excité vers le niveau $^5D_4$ avec des sources OPSL ou LD. Les transitions d'émission vers les niveaux terminaux correspondant aux multiplets ^7F_J (J = 0 − 6) sont réparties sur toute la plage spectrale visible. La transition $^5D_4 \rightarrow ^7F_5$ autour de 545 nm est la plus prometteuse pour le fonctionnement laser car elle présente généralement le plus grand rapport de branchement et les meilleures sections efficaces d'émission. La transition $^5D_4 \rightarrow ^7F_4$ autour de 585 nm, qui peut fournir une émission laser jaune rare, attire également l'attention. De plus, le niveau émetteur $^5D_4$ est dépourvu d'effet de relaxation croisée. L'ion Dy^{3+} est également considéré comme un candidat pour des émissions laser jaunes. La transition d'émission jaune $^4F_{9/2} \rightarrow ^6H_{13/2}$ montre généralement le plus grand rapport de branchement, supérieur à 50% et une section efficace d'émission de l'ordre de 10^{-21} à 10^{-20} cm^2. La transition d'absorption $^6H_{15/2} \rightarrow ^4I_{15/2}$, correspondant à la longueur d'onde d'émission des diodes lasers InGaN courantes, présente la plus grande section efficace, de l'ordre de 10^{-21} cm^2, ce qui est prometteur pour le pompage. De plus, l'écart d'énergie, d'environ 7000 cm^{-1}, entre les niveaux $^4F_{9/2}$ et $^6F_{1/2}$ indique une relaxation inefficace de plusieurs phonons par rapport au niveau $^4F_{9/2}$.

Ce travail de thèse vise à développer de nouveaux monocristaux à base d'oxydes activés par des ions Tb^{3+} ou Dy^{3+} pour le développement de lasers visibles. Ces travaux sont motivés par les perspectives prometteuses et l'intérêt des recherches de plus en plus croissantes sur le développement non seulement des lasers solides dopés avec des ions lanthanides, Ln^{3+}, émettant directement dans la plage spectrale visible en général mais aussi des laser contenant des ions Tb^{3+}/Dy^{3+} en tant qu'ion actif en particulier. Ce sujet est également motivé par les rares études spectroscopiques de cristaux à base d'oxydes activés par des ions Tb^{3+}. Une étude systématique de cette classe de matériaux est utile pour comprendre les propriétés physiques et optiques de l'ion Tb^{3+}, qui revêtent une grande importance pour d'autres applications laser. Plusieurs matériaux activés par les ions Tb^{3+} ou Dy^{3+} ont été choisis pour cette étude, sur la base de plusieurs considérations afin d'éviter les effets néfastes : $Ba_3Tb(PO_4)_3$

(BTP), $Sr_3Tb(BO_3)_3$ (STB), $Li_6Tb(BO_3)_3$ (LTB), $TbCa_4O(BO_3)_3$ (TbCOB), $TbAl_3(BO_3)_3$ (TAB), $KTb(WO_4)_2$ (KTW), Dy:$CaYAlO_4$ (Dy:CYA), Dy:$YCa_4O(BO_3)_3$ (Dy:YCOB), et Dy:$Ca_2Al_2SiO_7$ (Dy:CAS).

Cette thèse comprend trois chapitres principaux. Le premier chapitre présente en détail le contexte de la recherche sur ce sujet. Les principes physiques fondamentaux qui sont essentiels pour comprendre les expériences et le mécanisme impliqué dans ce travail sont décrits. Tout d'abord, une introduction aux principes physiques fondamentaux centrés sur les ions lanthanides trivalents sera présentée. Cette connaissance est essentielle pour comprendre les phénomènes physiques et les mécanismes impliqués dans ce travail. La présentation des concepts théoriques concerne la structure énergétique des configurations $4f^N$, y compris l'effet du champ cristallin, et les intensités des transitions $4f \rightarrow 4f$ dans le cadre de la théorie de Judd-Ofelt. Nous discuterons également des processus non radiatifs pouvant influer de manière significative sur la propriété de luminescence réelle des ions Ln^{3+}. La deuxième sous-section se concentrera sur le développement des lasers visibles à émission directe. On notera comme point de départ un aperçu rétrospectif des premiers lasers visibles à émission directe basés sur les ions Ln^{3+} comme ions actifs. Par la suite, l'accent sera mis sur les sources pompage laser diodes élaborés ces dernières années. Un état de la technique des nouveaux lasers visibles utilisant Pr^{3+}, Sm^{3+}, Eu^{3+}, Tb^{3+} et Dy^{3+} en tant qu'ion actif sera présenté. Dans la troisième sous-section, nous analysons les problèmes potentiels liés au traitement laser de Tb^{3+} ou de Dy^{3+} dans des matériaux à base d'oxydes et discutons des critères de choix d'un matériau hôte approprié.

La relation structure-propriété est l'un des problèmes les plus importants de la science des matériaux. Une étude préalable de la structure du matériau monocristallin au niveau atomique peut non seulement fournir des informations relatives à la procédure de fabrication, mais aussi prévoir ses propriétés physiques. En relation étroite avec les propriétés spectroscopiques, les environnements de coordination des ions Tb^{3+} ou Dy^{3+} dans les cristaux seront discutés en détail.

La qualité du cristal est directement liée à la pureté du matériau de départ et à la configuration pour la croissance. Dans ce travail, nous avons utilisé des matériaux poly-cristallins de même composition que les monocristaux désignés comme matériaux de départ. Les poly-cristaux ont été préparés par des processus de réactions à l'état solide à haute température. Les matières premières ou les phases parasites incomplètement réagies formées au cours des réactions à l'état solide pourraient former des inclusions dans le cristal et modifier ses propriétés optiques. Les méthodes de préparation et l'analyse par diffraction des rayons X des produits poly-cristallins seront présentées dans cette section. Le processus de croissance cristalline est souvent influencé par les propriétés physiques du matériau, telles que le comportement de fusion congruente, la viscosité et la volatilité de la masse fondue et les propriétés thermiques du cristal. Par exemple, une viscosité élevée de la masse fondue est susceptible de former des inclusions dans le cristal et un cristal présentant une grande anisotropie de la dilatation thermique à tendance à se fissurer pendant la croissance. Pour contourner ces inconvénients, les conditions de fabrication du monocristal, y compris l'atmosphère, la configuration du four, l'orientation du germe, les paramètres du programme de croissance doivent être adaptés.

Le chapitre 2 décrit principalement la structure cristalline et la procédure de synthèse de tous les matériaux sélectionnés. Chaque matériau occupe une sous-section et chaque sous-section comprend une discussion comprenant les points suivants:

1- la structure cristalline et l'environnement de coordination des ions actifs;

2- les méthodes de préparation des matériaux poly-cristallins de départ s, qui ont un impact sur la qualité des monocristaux à élaborer;

3- le processus de croissance monocristalline;

4- la qualité optique des cristaux à l'aide de microscopes.

La technique conventionnelle de Czochralski a été appliquée pour faire croître les cristaux à base de Tb^{3+} et dopés au Dy^{3+} sélectionnés. Les concentrations en ions Dy^{3+}, qui ont un impact sur le taux de relaxation croisée, ont été définies comme étant d'environ $4,5\times10^{20}$ cm^{-3} en se référant aux cristaux de gain laser dopés au Dy^{3+} reportés dans la littérature. Les matériaux de départ poly-cristallins ont été synthétisés par réaction à l'état solide à haute température. Leurs puretés ont été examinées par diffraction des rayons X sur poudre et ont permis de satisfaire les croissances cristallines ultérieures. Les problèmes rencontrés au cours de la fabrication du cristal sont analysés, suivis d'une optimisation supplémentaire des conditions de croissance.

La formation de centres colorés a été observée lors de la croissance de cristaux à base de terbium sous air. Les bandes d'absorption supplémentaires dans le visible peuvent dissiper l'énergie d'excitation, atténuer l'émission luminescente et provoquer des effets thermiques néfastes. Par conséquent, pour les applications de laser visible ou de luminescence utilisant des matériaux activés par Tb^{3+}, l'absence de centres colorés est nécessaire. La deuxième section de chapitre 2 traite des centres colorés observés dans les cristaux à base de Tb^{3+} fabriqué sous air. L'origine des centres colorés est analysée par la technique spectroscopique de résonance paramagnétique électronique.

Les propriétés thermiques d'un matériau à gain laser sont très importantes, en particulier la conductivité thermique et la dilatation thermique. Le chauffage du milieu de gain pendant le fonctionnement du laser peut être problématique. Le gain de matériau avec une faible conductivité thermique conduit à un fort gradient thermique radial perpendiculaire à la direction d'émission laser, ce qui entraîne en outre des effets néfastes de cristallisation thermique, voire de fissuration. Une conductivité thermique élevée est particulièrement favorable aux lasers de forte puissance. D'autre part, le paramètre de résistance au choc thermique est inversement proportionnel au deuxième coefficient de dilatation thermique. Ainsi, une trop grande dilatation thermique des matériaux à gain le rend vulnérable aux chocs thermiques. La troisième partie de chapitre 2 présente la caractérisation des propriétés thermiques, y compris les coefficients de conductivité thermique et de dilatation thermique le long des axes cristallographiques.

Les propriétés optiques des cristaux sont caractérisées et discutées au chapitre 3. Tous les cristaux ont été orientés dans les directions optiques principales. Pour les cristaux biaxiaux de LTB, TbCOB, Dy: YCOB et KTW, la relation entre les axes crystallophysiques et cristallographiquse a été identifiée. Les indices de réfraction dépendant de la longueur d'onde du BTP, du STB et du LTB ont été mesurés pour

la première fois à l'aide de la méthode standard du minimum de déviation. L'ensemble des données a permis de déterminer des équations de dispersion de Sellmeier.

Les études spectroscopiques comprennent principalement les spectres d'absorption et d'émission, la décroissance de la fluorescence et l'ASE. Ces données ont été utilisées pour calculer des paramètres importants tels que les sections efficaces de transition, le taux de branchement, la durée de vie de la fluorescence et la force de l'oscillateur expérimental. La transition $^7F_6 \rightarrow {}^5D_4$ autour de 485 nm de Tb^{3+} et la transition $^6H_{15/2} \rightarrow {}^4I_{15/2}$ autour de 450 nm de Dy^{3+} sont particulièrement intéressantes car elles correspondent aux longueurs d'onde d'émission des diodes laser servant comme source de pompage optique. Ces transitions ont des sections efficace d'absorption relativement faible de 10^{-22} cm à 10^{-21} cm^2. Cependant, tous les cristaux activés par des ions Tb^{3+} ainsi que par des ions Dy^{3+} ont des sections efficaces d'absorption comparables, voire supérieures, aux matériaux à gain reportés correspondants. En ce qui concerne les transitions d'émission, la transition verte $^5D_4 \rightarrow {}^7F_5$ de Tb^{3+} et la transition jaune $^4F_{9/2} \rightarrow {}^6H_{13/2}$ de Dy^{3+} présentent des rapport de branchement de fluorescence supérieurs à 50% dans ces matrices. Sauf pour le BTP et le STB qui ont des sections efficaces de transition relativement faibles en raison de l'élargissement spectral significatif, les cristaux activés par des ions Tb^{3+} de LTB, TAB et TbCOB ainsi que les cristaux activés par des ions Dy^{3+} présentent des sections efficaces d'émission comparables avec d'autre matériaux à gain. En outre, les cristaux de TbCOB et de TAB sont particulièrement prometteurs pour l'affichage laser de la transition jaune $^5D_4 \rightarrow {}^7F_4$, car ils donnent une section efficace d'émission relativement grande à 593 nm et 584 nm, respectivement. De plus, le cristal Dy: YCOB peut fournir une section efficace d'émission exceptionnellement élevée à 760 nm, ce qui est intéressant pour le fonctionnement du laser dans le domaine spectral du rouge profond.

De plus, un comportement anisotrope des transitions magnétiques d'absorption et d'émission dipolaires a été observé dans les cristaux activés à la fois par Tb^{3+} et Dy^{3+}. Ce phénomène est dû à la contribution relativement importante de l'interaction dipôle magnétique pour plusieurs transitions de Tb^{3+} ou Dy^{3+}, confirmée par des calculs théoriques et des mesures expérimentales. Les mesures spectrales polarisées de routine qui ne prennent en compte que l'anisotropie des transitions dipolaires électriques génèrent des données spectroscopiques inexactes. De plus, les transitions dipolaires magnétiques de $^5D_4 \rightarrow {}^7F_5$ et $^6H_{15/2} \rightarrow {}^4I_{15/2}$ présentent une anisotropie significative. Le premier est utilisé pour le fonctionnement au laser vert de Tb^{3+} et le dernier est la transition de pompe la plus prometteuse pour les milieux activés par Dy^{3+}.

Les courbes de décroissance de la fluorescence ont été enregistrées pour étudier la dynamique de la fluorescence des niveaux laser supérieurs. Les courbes de temps de vie des composés activés par Tb^{3+} à partir du niveau $^5D_4$ montrent un comportement exponentiel unique, ce qui indique l'absence de processus de transfert d'énergie inter-ionique. Les durées de vie de fluorescence ont été calculées pour être aussi longues que 2 ~ 3 ms. Ainsi, les matériaux à base de Tb^{3+} sont favorables au stockage de l'énergie de la pompe. Par ailleurs, les profils de vie des monocristaux dopés au Dy^{3+} ne sont pas exponentiels, tandis que ceux des poly-cristaux à faible concentration d'ions Dy^{3+} sont presque exponentiels. Ceci est dû aux processus de relaxation croisée.

Une analyse Judd-Ofelt a été réalisée pour approfondir les transitions $4f \rightarrow 4f$. Les paramètres d'interaction électrostatique et spin-orbite, qui varient en fonction du réseau hôte, ont été ajustés pour permettre des calculs Judd-Ofelt plus précis. Les trois paramètres d'intensité Judd-Ofelt ont été calculés. Les forces et les taux de branchement résultants de l'oscillateur sont globalement en bon accord avec les données expérimentales. Les durées de vie radiatives ont été utilisées pour calculer les efficacités quantiques. Ceux des composés à base de Tb^{3+} se sont avérés être proches de l'unité (à l'exception de celle du KTW d'environ 50%), ce qui suggère des processus de désactivation négligeables, tels que la relaxation multiphonon et la relaxation croisée. Parmi les cristaux dopés au Dy^{3+}, Dy:CYA présente l'efficacité quantique la plus élevée de 54%.

Un comportement de gain négatif à 543 nm a été observé pour les cristaux de BTP, STB, LTB, TbCOB et KTW à base de Tb^{3+}. Cela indique que les processus d'absorption dans l'état excité (ESA) dépassent les émissions stimulées à cette longueur d'onde. L'ESA est particulièrement important pour KTW, ce qui est attendu en raison de la forte bande de transfert de charge d'inter valence à la position énergétique où l'ESA a lieu.

Enfin, des expériences au laser ont été menées avec plusieurs source de pompage LD ou OPSL. La diode laser Nichia LD (200 mW) émettant à 486 nm n'a pas permis de générer une oscillation laser, même en utilisant un cristal à 15% de Tb: YLF comme milieu de gain. Ceci est probablement dû à la faible puissance absorbée (75 mW) et à l'absence d'un coupleur de sortie approprié. Des essais supplémentaires sur les cristaux de BTP, STB, LTB et TbCOB à base de Tb^{3+} ont été réalisés avec une source de pompage OPSL d'une puissance de sortie jusqu'à 4 W et d'une excellente qualité de faisceau. Bien que cette pompe permette de générer des émissions laser avec des cristaux fluorures, aucun des cristaux à base d'oxydes n'a été en mesure de produire une émission laser verte. Ceci corrobore en quelque sorte les résultats négatifs des mesures de gain réalisées à 543 nm. En ce qui concerne les cristaux activés par les ions Dy^{3+}, les problèmes principaux sont la qualité médiocre de la source de pompage LD délivrée par fibre (testée avec des cristaux à gain activés par Pr^{3+}) comparativement à celle d'un module unique de diode laser, et la disparité de longueur d'onde d'absorption maximale du milieu (442 nm contre 453 nm).

CONTENTS

GENERAL INTRODUCTION

Lasers are known for their coherency, good monochromaticity, and high energy density. In light of these fascinating characters, lasers have been applied to a diversity of domains, from military industries to commercial products, and their research works are being constantly pushed forward. Lasers emitting in the visible spectral region are especially of interest. They can be seen by human eye thus the development has been flourished by the related applications, e.g. pointing, entertainment, and display [1–3]. Furthermore, several application areas require laser emissions in the specific spectral range from 400 to 770 nm, such as medical diagnosis, surgery, optical spectroscopy, bathymetric imaging, and laser guide stars [4–7].

Visible laser emissions can be produced by different types of resonators. Among them, solid-state lasers using lanthanide-activated crystals as gain media are the most highlighted. They feature high beam quality, compact resonator design, versatility of output wavelength, and capability of operating in several modes. Nd^{3+} and Yb^{3+} ions have been extensively studied to generate laser outputs in the visible spectral range. However, these devices require frequency conversions of their original infrared emissions, which reduce the efficiency and complicate the laser system. This inconvenience can be solved by employing active ions that can directly emit visible radiations. Nevertheless, this issue did not attract much attention due to the lack of efficient pump sources in the last century.

This blank was filled by the invention and development of blue-emitting laser diodes [8]. In 2004, the first LD-pumped solid-state laser emitting directly in the visible spectral range was reported by A. Richter et al., using Pr^{3+} as active ion [9]. The laser was pumped at 442 nm and operated at 640 nm. Afterwards, more and more lanthanide ions have been exploited to generate visible laser emissions in this scheme, benefiting from the rapid development of semiconductor laser pumps. Besides Pr^{3+}, visible laser operations using Sm^{3+}, Eu^{3+}, Tb^{3+}, Dy^{3+}, Ho^{3+}, or Er^{3+} as active ion have been demonstrated in recent years [10–15]. These novel lasers greatly expand the available output wavelengths of the traditional frequency converted lasers. Nevertheless, fluoride-based crystals were usually used as gain media in these demonstrations. They are difficult and expensive to be fabricated owing to the requirement of complicated protecting atmosphere such as CF_4.

A very practical subject is to realize such visible laser operations in oxide-based matrices, which have better prospect in terms of industrialization than the fluorides due to the simpler growth processes. Nevertheless, some disadvantages of the oxides could greatly impede lasing in the visible, e.g. the large phonon energy, strong crystal field strength, and small band gap energy. These characters can result in depopulation of the upper laser level through multiphonon relaxation or energy transfer processes. The main challenge is to select suitable host materials and to fabricate single crystalline materials with sufficient size as well as optical quality.

This PhD work aims at developing novel Tb^{3+}- as well as Dy^{3+}-activated oxide-based single crystals for visible lasers. This is motivated by the promising prospects and ascending research interests of the Ln^{3+}-based solid-state lasers emitting directly in the visible spectral range as well as the interesting characters of Tb^{3+}/Dy^{3+} as active ion. First, Tb^{3+} can provide high-efficiency green laser emissions due to the lack of detrimental energy transfer processes from the $^5D_4$ upper laser level. The optical-to-optical efficiency of a Tb:LiLuF$_4$ green-emitting laser reaches 44% [12], which is comparable to the well-developed green Nd^{3+}-lasers operated in a frequency conversion scheme [16]. Second, Tb^{3+} and Dy^{3+} are the only two Ln^{3+} ions that can produce direct laser emissions in the yellow spectral region, which derive from the $^5D_4 \rightarrow ^7F_5$ transition for the former and the $^4F_{9/2} \rightarrow ^6H_{13/2}$ transition for the latter. Moreover, both Tb^{3+} and Dy^{3+} show broad energy gaps between the upper and lower laser levels. Thus, they can be hosted by oxide-based matrices, which usually exhibit large phonon energies, without suffering efficient multi-phonon relaxation processes.

This subject is also motivated by the scarce spectroscopic studies of Tb^{3+}-activated oxide-based crystals. A systematic investigation on this class of material is helpful in understanding the physical and optical properties of Tb^{3+}, which are of great importance for further laser applications.

This thesis comprises three main chapters. The first chapter introduces in detail the research background of this subject. Fundamental physical principles that are essential to understand the experiments and mechanism involved in this work are described. A state of the art regarding Ln^{3+}-based direct visible lasers is presented. Potential problems are analyzed for lasing Tb^{3+} or Dy^{3+} in oxide-based materials. Finally, based on the above discussions, several compounds are chosen for this study.

The second chapter focuses on the synthesis procedures of the selected materials of $Ba_3Tb(PO_4)_3$, $Sr_3Tb(BO_3)_3$, $Li_6Tb(BO_3)_3$, $TbCa_4O(BO_3)_3$, $Dy:CaYAlO_4$, and $Dy:YCa_4O(BO_3)_3$. The structural properties of these materials are described. Efforts made to optimize the conditions and solve the problems during the synthesis procedures are stated. This chapter also deals with characterization of the thermal properties of the as-grown crystals, including thermal conductivity, specific heat capacity, and thermal expansion.

The last chapter presents the results of the optical spectroscopic characterization. Besides the above-mentioned compounds, crystals of $TbAl_3(BO_3)_3$, $KTb(WO_4)_2$, and $Dy:Ca_2Al_2SiO_7$, which are not fabricated in this work, are also available for the measurements. Refractive index measurements are conducted for those without reported data. The spectroscopic characterization is then focused on the potential pump and lasing transitions in the visible spectral region. Transition cross-sections are calculated and the fluorescence dynamics of the upper laser levels are studied. Calculations in the framework of classical Judd-Ofelt theory are performed. Lastly, gain/excited-state absorption measurements and laser experiments are carried out.

References

[1] Chao C. Huang, Structure of laser pointer, US5343376A, 1993. https://patents.google.com/patent/US5343376A/en.

[2] Christopher Meredith, Laser light sword, US20010024973A1, 1999. https://patents.google.com/patent/US20010024973A1/en.

[3] Brian E. Kruschwitz, Andrew F. Kurtz, Laser projection display system, US6594090B2, 2001. https://patents.google.com/patent/US6594090B2/en.

[4] W. DEMTRODER, LASER SPECTROSCOPY: basic concepts and instrumentation., SPRINGER, CHAM, 2003.

[5] H. Jelínková, ed., Lasers for medical applications: diagnostics, therapy, and surgery, WP/Woodhead Publishing, Oxford ; Philadelphia, 2013.

[6] K.D. Moore, J.S. Jaffe, B.L. Ochoa, Development of a New Underwater Bathymetric Laser Imaging System: L-Bath, J. Atmospheric Ocean. Technol. 17 (2000) 1106–1117. doi:10.1175/1520-0426(2000)017<1106:DOANUB>2.0.CO;2.

[7] L.A. Thompson, C.S. Gardner, Experiments on laser guide stars at Mauna Kea Observatory for adaptive imaging in astronomy, Nature. 328 (1987) 229–231. doi:10.1038/328229a0.

[8] S. Nakamura, S.J. Pearton, G. Fasol, The blue laser diode: the complete story, 2nd updated and extended ed, Springer, Berlin ; New York, 2000.

[9] A. Richter, E. Heumann, E. Osiac, G. Huber, W. Seelert, A. Diening, Diode pumping of a continuous-wave Pr^{3+}-doped $LiYF_4$ laser, Opt. Lett. 29 (2004) 2638. doi:10.1364/OL.29.002638.

[10] D.-T. Marzahl, P.W. Metz, C. Kränkel, G. Huber, Spectroscopy and laser operation of Sm^{3+}-doped lithium lutetium tetrafluoride ($LiLuF_4$) and strontium hexaaluminate ($SrAl_{12}O_{19}$), Opt. Express. 23 (2015) 21118. doi:10.1364/OE.23.021118.

[11] V.I. Dashkevich, S.N. Bagayev, V.A. Orlovich, A.A. Bui, P.A. Loiko, K.V. Yumashev, A.S. Yasukevich, N.V. Kuleshov, S.M. Vatnik, A.A. Pavlyuk, Red $Eu,Yb:KY(WO_4)_2$ laser at ~702 nm, Laser Phys. Lett. 12 (2015) 085001. doi:10.1088/1612-2011/12/8/085001.

[12] P.W. Metz, D.-T. Marzahl, A. Majid, C. Kränkel, G. Huber, Efficient continuous wave laser operation of Tb^{3+}-doped fluoride crystals in the green and yellow spectral regions: Efficient continuous wave laser operation…, Laser Photonics Rev. 10 (2016) 335–344. doi:10.1002/lpor.201500274.

[13] S.R. Bowman, S. O'Connor, N.J. Condon, Diode pumped yellow dysprosium lasers, Opt. Express. 20 (2012) 12906. doi:10.1364/OE.20.012906.

[14] I. G. Podkolzina, A. M. Tkachuk, V. A. Fedorov, and P. P. Feofilov, Multifrequency generation of stimulated emission of Ho^{3+} ion in LiYF4 crystals, Opt Spectrosc. 40 (1976) 111.

[15] F. Moglia, S. Müller, F. Reichert, P.W. Metz, T. Calmano, C. Kränkel, E. Heumann, G. Huber, Efficient upconversion-pumped continuous wave $Er^{3+}:LiLuF_4$ lasers, Opt. Mater. 42 (2015) 167–173. doi:10.1016/j.optmat.2015.01.004.

[16] Y.Q. Zheng, H.Y. Zhu, L.X. Huang, H.B. Chen, Y.M. Duan, R.B. Su, C.H. Huang, Y. Wei, J. Zhuang, G. Zhang, Efficient 532 nm laser using high gray-tracking resistance KTP crystal, Laser Phys. 20 (2010) 756–760. doi:10.1134/S1054660X10070406.

CHAPTER 1   INTRODUCTION AND FUNDAMENTALS

This chapter firstly introduces the research background of visible lasers, leading to the motivation of this PhD thesis. The second section describes the fundamental knowledge that is essential for the following state-of-the-art discussion and for the experiments performed in the next two chapters. The fundamental principles mainly concentrate on the general physical properties and light-matter interaction of lanthanide ions in crystal environments. The third section briefly introduces the history of Ln^{3+}-based lasers emitting directly in the visible spectral range. Then the state of the art of Ln^{3+}-based direct visible lasers is presented. This part compiles the spectroscopic properties and laser performances of several Ln^{3+} ions. This leads to the subsequent discussion on the host materials for laser operation of Tb^{3+} and Dy^{3+} to carry forward the positive results and to circumvent the negative results stated in the literature. Criteria of host materials for lasing Tb^{3+} or Dy^{3+} are established. Finally, based on these criteria, several Tb^{3+}- as well as Dy^{3+}-activated oxide-based matrices are selected for the following study.

1.1   Research background

Lasers emitting visible light have attracted longstanding attention for both research and market applications. Their utilities root in not only the character that they can be detected by human naked eye but also the specific spectral region of visible light, ranging approximately from 400 to 770 nm [1]. Mature applications can be found in various fields including entertainment, military, optical data storage, spectroscopy, medical diagnosis, and therapy [2–5]. The development of visible lasers is also boosted by the sciences and technologies on the cutting edge. Accounting for the narrow emission bandwidth, facility for modulation, and low transmission loss in the air, visible lasers have been exploited for optical wireless communication, which allows data transmission rate up to 100 Gb/s [6,7]. Lasers in the blue and green spectral range are favorable for bathymetric laser mapping since they are able to penetrate water with much less attenuation than the near-infrared lasers (Figure 1.1) [8]. Novel laser projectors foresee good market prospect, as they provide much better brightness and higher resolution than the traditional lamp projectors [9]. Furthermore, there is an ascending demand regarding the diversity of coherent emission wavelength for applications such as flow cytometry and super-resolution microscopy [10,11].
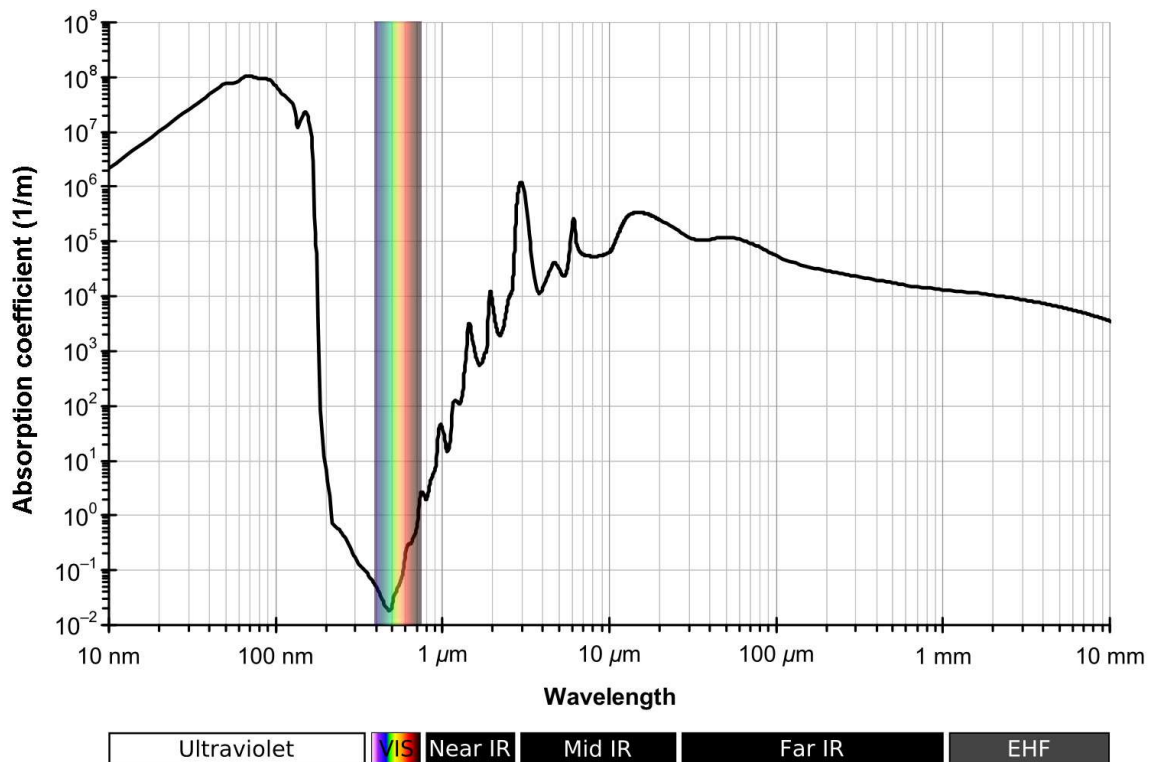
Figure 1.1   Absorption spectrum of liquid water, edited from [12].

Numerous efforts have been made to achieve laser emissions in the visible spectral region, the onset of which is the first demonstration of laser oscillation at 694 nm using ruby as gain medium in 1960 [13]. Visible lasers can be simply classified into three categories in terms of the phase of gain material, viz. gas, liquid, and solid. The well-known red-emitting He-Ne gas laser invented in 1962 are still

commonly used nowadays. However, in addition to the inconvenience from a long cavity, neutral gas laser devices suffer very limited output power and efficiency. Rare-gas (Ar, Kr) ion lasers can provide watt-level output through the visible spectrum, whereas the efficiency is still low. Additional water-cooling system is also required. Liquid dye lasers are available for output wavelength tuning from the UV to near-infrared with passable energy conversion efficiency, benefiting from the broad gain bandwidth and a variety of selections of laser dyes. However, the problems of chemical degradation of the organic dyes, limited output power, and toxicity of the dye components impede their further applications outside of academic usage.

Over the past few decades, research progresses were substantially made on solid-state laser devices which allow for more compact design, higher wall-plug efficiency, easier handling, and more versatile modes of operation in contrast with the aforementioned gas and liquid laser equipment. These advantages mainly come from the better energy-storage capability in solid-state gain materials. Laser diodes (LDs), although not included in the solid-state laser category generally, still possess most convenience of solid-state lasers. A couple of output wavelengths are available, varying from the type of p-n junctions. The electrically pumped LDs have a poor beam quality, to be more specific, the inhomogeneity of the spatial energy distribution, large emission bandwidth, instability of the output wavelength, fetters their applications to some fields. Nevertheless, LDs are very suitable for pumping solid-state lasers considering their typically high electrical-to-optical power efficiency and much weak thermal effects than the conventional lamp pumping. This class is known as diode-pumped solid-state lasers (DPSSLs). They feature high beam quality as well as the capability to different operating mode and thus are able to fill the blank of common LDs.

DPSSLs using rare-earth-doped single crystalline materials as gain medium such as Nd^{3+}:YAG and Nd^{3+}:YVO$_4$ have been well established and industrialized. The Nd^{3+}-doped gain media are generally pumped by an 808 nm LD and generate laser outputs in the near infrared. Therefore, a frequency conversion is necessary to obtain coherent visible emissions. The well-known Nd^{3+}-based green laser operated at 532 nm is realized by second harmonic generation (SHG) of the 1064 nm main emission through either a nonlinear crystal or a self-frequency doubling host material. Although the latter lessen the complexity of the system in the former approach, energy loss during the frequency conversion process is still inevitable. Visible laser operations at other wavelengths require frequency doubling of less intense emission lines or more intricate nonlinear processes such as sum-frequency generation, whereas these operation schemes result in more complex cavity designs and lower efficiencies. In a word, requirement of frequency conversion and difficulty in providing versatile output wavelengths are inherent drawbacks of the current visibly emitting DPSSLs systems.
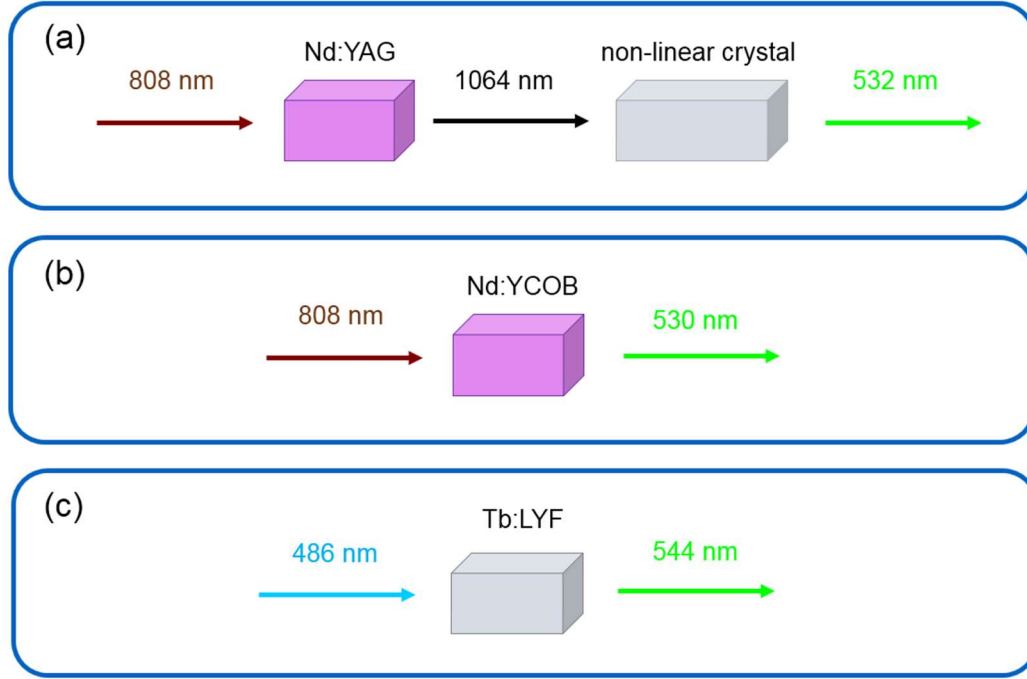
Figure 1.2   **Schemes of visible solid-state lasers: (a) frequency conversion using non-linear crystals; (b) self-frequency doubling; (c) direct emission.**

To get rid of these inconveniences, one strategy is to pump the active ions to higher energy levels (UV or blue spectral region) and thus visible laser emissions can be obtained directly without involving frequency conversion. Figure 1.2 compares the general approaches to yield visible coherent emission in the framework of DPSSL (for conciseness, "direct visible lasers" refers to "lasers directly emitting in the visible spectral range" hereafter). The direct emission approach has early been approved to be feasible since early ages (will be discussed in section 1.3). Those using trivalent lanthanide active ions varying from Pr^{3+} to Tm^{3+} are well documented. In spite of these successful attempts in the past, such direct visible lasers did not draw too much attention owing to the low efficiency provided by the primitive pump sources and/or inconvenient operation under cryogenic conditions.

Until this decade, the development of commercially available and high-efficiency blue semiconductor laser pump sources, viz. GaN/InGaN-based LDs and frequency-doubled optically pumped semiconductor lasers (OPSLs), has rekindled the research interest on this issue. Semiconductor-pumped visible lasers based on Pr^{3+}, Sm^{3+}, Tb^{3+}, Dy^{3+}, and Ho^{3+} were discovered. Some were able to yield watt-level continuous-wave outputs and slope efficiencies more than 50%. In addition, it is worth pointing out that laser outputs in the yellow and orange spectral region cannot be produced by conventional laser devices, whereas they are accessible by Tb^{3+}-, Dy^{3+}-, Pr^{3+}-, and Sm^{3+}-based lasers. It can be further expected that the ongoing development regarding the output power and the available wavelength of semiconductor pumps provide even more opportunities to the subject of discovering new laser channels and active ions.

A shadow of the prospering subject of direct visible laser is the narrow scope of gain material. Most of the abovementioned laser demonstrations were conducted using fluoride-based host materials, benefiting from their mild crystal field strengths and small phonon energies. Oxide-based crystals, on the other hand, are easier to be fabricated and thus more promising for industrialization. The challenge is to find suitable materials that can keep the intrinsic advantages as an oxide compound while exhibiting comparable spectroscopic properties to the fluorides which are successful.

1.2 Fundamentals

In this part, an introduction to the fundamental physical principles focused on trivalent lanthanide ions will be presented. This knowledge is essential to understand the physical phenomena and mechanism involved in this work. The presentation on the theoretical background concerns the energetic structure of the $4f^N$ configurations, including effect of the crystal field, and the transition intensities of $4f \rightarrow 4f$ transitions in the framework of the Judd-Ofelt theory. In addition, non-radiative processes that can significantly influence the actual luminescence property of Ln³⁺ ions will be discussed as well. Basic principles and parameters regarding the light-matter interaction can be found in Appendix A.

The second subsection will concentrate on the development of the direct visible lasers. As a starting point, a concise retrospect of the early-reported Ln³⁺-based direct visible lasers will be noted. Afterwards, more emphasis will be laid on diode-pumped lasers elaborated in recent years. A state-of-the-art of novel visible lasers utilizing Pr³⁺, Sm³⁺, Eu³⁺, Tb³⁺, and Dy³⁺ as active ion will be given.

1.2.1 Basic of lanthanides

The term "lanthanides" refers to a set of elements from lanthanum ($Z = 57$) to lutetium ($Z = 71$). In addition to scandium and yttrium, which often coexist with the lanthanides in natural ores and show similar chemical properties, these 17 elements are called rare-earth elements. The electronic configuration of lanthanides can be described as $[\text{Xe}]4f^N5d6s^2$ for La, Ce, Gd, and Lu, and $[\text{Xe}]4f^{N+1}6s^2$ for the others.

The lanthanides tend to form +3 oxidation state in compounds with the electronic configuration $[\text{Xe}]4f^N$. Due to the stability of an empty, half-filled, or full $4f$ orbital, some exhibit relatively stable divalent or tetravalent forms, such as Ce⁴⁺ ($[\text{Xe}]4f^0$), Eu²⁺ as well Tb⁴⁺ ($[\text{Xe}]4f^7$), and Yb²⁺ ($[\text{Xe}]4f^{14}$). In their trivalent oxidation states, the $4f$ electrons are shielded by the external fully occupied $5s^2$ and $5p^6$ shells. As a result, the $4f$ energy levels are not strongly affected by the external chemical environment. This is the origin of the unique physical properties of Ln³⁺.

1.2.2 Energetic structure of $[\text{Xe}]4f^N$ electron configuration

In the free-ion approximation, the Hamiltonian without an external potential can be written as:

$$\hat{H}_{free\text{-}ion} = \hat{H}_0 + \hat{H}_e + \hat{H}_{so} \tag{1.1}$$

in which $\hat{H}_0$, $\hat{H}_e$, and $\hat{H}_{so}$ represent the sum of kinetic and potential energy of electrons, the coulomb interaction between electrons, and the spin-orbit interaction. A common approach to deal with these multi-electron Hamiltonian is to introduce the central-field approximation. In this scheme, it is assumed that the electric field exerted to an electron by the other electrons can be treated as an averaged spherical field, and that each electron moves independently in this field as well as the field of the nucleus. Thus, the multi-electron electrostatic interaction can be substituted with an effective

spherical potential $U(r_i)$, leading to a great simplification for the following modeling. The three Hamiltonians are described by the following equations:

$$\widehat{H}_0 = \sum_{i=1}^{N} \left(-\frac{\hbar^2}{2m_e}\nabla_i^2 + U(r_i)\right) \tag{1.2}$$

in which

$$\sum_{i=1}^{N} U(r_i) = -\sum_{i=1}^{N}\frac{Ze^2}{4\pi\epsilon_0 r_i} + \langle \sum_{i,j\,(i<j)}^{N}\frac{e^2}{4\pi\epsilon_0 r_{ij}}\rangle \tag{1.3}$$

The Hamiltonian for the electrostatic and spin-orbit interaction are accordingly given by:

$$\widehat{H}_e = \sum_{i,j\,(i<j)}^{N}\frac{e^2}{4\pi\epsilon_0 r_{ij}} - \langle \sum_{i,j\,(i<j)}^{N}\frac{e^2}{4\pi\epsilon_0 r_{ij}}\rangle \tag{1.4}$$

$$\widehat{H}_{so} = \sum_{i=1}^{N}\frac{1}{2m_e^2 c^2 r_i}\frac{dU(r_i)}{dr_i}(\boldsymbol{l}_i \cdot \boldsymbol{s}_i) \tag{1.5}$$

where m_e, e and N are the charge, mass and number of electrons in the $4f$ shell, respectively; Z is the nuclear charge; ϵ_0 is the vacuum permittivity; r_i is the radial coordinate of the i-th electron; r_{ij} is the distance between the i-th and the j-th electrons; $\xi(r_i)$ is the function of spin-orbit coupling; $\boldsymbol{l}_i$ and $\boldsymbol{s}_i$ are the angular and spin momentum of the i-th electron.

The second term in equation 1.3 stands for the average of the electrostatic potential from the electron-electron repulsion, which is only related to the radial coordinate of the electron. The electrostatic and spin-orbit terms are considered to make minor contributions and can be added to the system as small perturbations. The solution to the free-ion Hamiltonian is described by energy levels labeled with an SLJ symbol ${}^{2S+1}L_J$, where S, L, and J are the spin, orbit, and total angular momentum, respectively. In brief, the electrostatic interaction produces different ${}^{2S+1}L$ terms and the coupling between spin and orbital angular momentum splits these terms.

1.2.2 Crystal field effect

When a lanthanide ion is introduced to a crystal field, it is subject to the electric fields of the ligands. The surrounding ions can be treated as point charges with a total effective charge of $-Z_k e$. Assuming that $\boldsymbol{r}_i$ and $\boldsymbol{R}_k$ are the coordinate vectors of the i-th electron of the central lanthanide ion and the k-th ligand, the Hamiltonian of the crystal field is:

$$\widehat{H}_{cr} = \sum_i \sum_k \frac{Z_k e^2}{4\pi\epsilon_0 |\boldsymbol{r}_i - \boldsymbol{R}_k|} \tag{1.6}$$

For the well shielded $4f$ electrons, this term can be added to the total Hamiltonian as a perturbation. As a matter of fact, variation of the energetic position of the $4f^N$ configuration is typically within several 100 cm^{-1}. The external crystal field leads to further splitting of $^{2S+1}L_J$ manifolds into at most $2J+1$ stark levels, while the degree of splitting depends on the point symmetry.

With regard to the $5d$ electron in the $4f^{N-1}5d^1$ configuration, which is located in a more external orbital, the crystal field effect becomes more predominant. As a result, the energetic position of the $4f^{N-1}5d^1$ configuration is host-dependent and can shift by several 10000 cm^{-1} from that of a free ion. Figure 1.3 schematically shows the overlap of the $4f^N$ and $4f^{N-1}5d^1$ states. The lowest $4f^{N-1}5d^1$ levels of most Ln^{3+} free ions are in the far-UV region, whereas a strong crystal field may depress them to the near-UV or even visible spectral range. This can greatly affect the spectroscopic properties of the Ln^{3+} in the lattice, since the parity-allowed inter-configurational $4f^N \rightarrow 4f^N 5d^1$ transitions are much stronger and exhibit broader spectral lineshape than the parity-forbidden intra-configurational $4f \rightarrow 4f$ transitions.
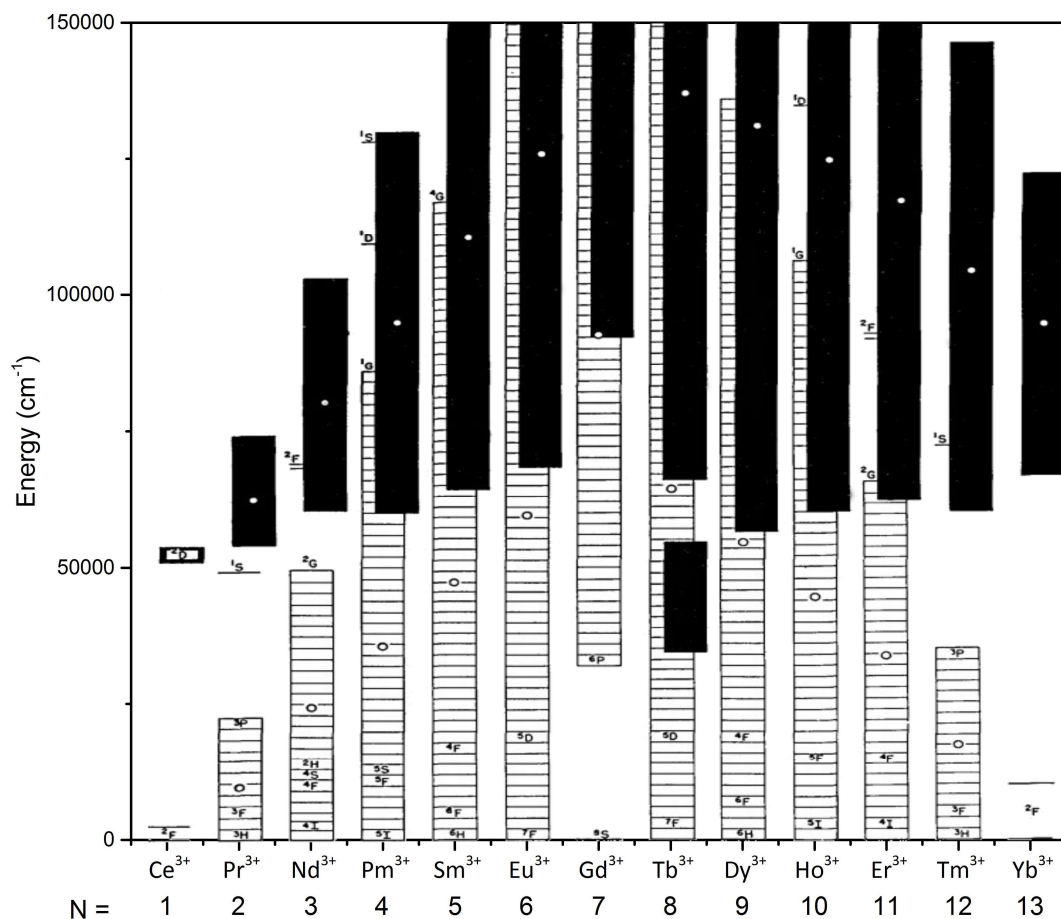
Figure 1.3 **Energetic position of the $4f^N$ (white block) and $4f^{N-1}5d^1$ (black block) configuration of Ln^{3+} free ions (After [14]).**

P. Dorenbos developed a semi-empirical method to predict the energy of the lowest $4f^{N-1}5d^1$ states [15,16]. It is found that when Ln^{3+} free ions are introduced to the same coordination environment, their $4f^{N-1}5d^1$ states, in disregard of their atomic number, exhibit almost the same values of red-shift. This energy difference in compound A compared to free ion is defined as the crystal-field depression $D(A)$:

$$E^{5d}(Ln, A) = E^{5d}(Ln, free\ ion) - D(A) \qquad (1.7)$$

Since $D(A)$ does not vary with the species of lanthanide ions, the crystal-field depression of one matrix can be extrapolated from the spectroscopy of an arbitrary trivalent lanthanide ion doped in this compound. Then the value of $D(A)$ can be used to calculate the energetic position of a $4f^{N-1}5d^1$ state for other Ln^{3+} species in compound A. The accuracy of this method is typically within 600 cm^{-1}. It will be discussed in Section 1.3 about the usage of this method to evaluate potentially suitable host materials.

1.2.3 Intensity of $4f \rightarrow 4f$ transition and Judd-Ofelt theory

The fascinating spectroscopic properties of the trivalent lanthanide ions mainly stem from their $4f \rightarrow 4f$ transitions that provide a substantial amount of optical frequencies. The issue of optical transition intensity can principally come down to the interaction between electron(s) and electromagnetic waves. Based on the static, free-ion, and single configuration approximations, B. R. Judd and O. S. Ofelt published their research on predicting the intensities of $4f \rightarrow 4f$ transitions independently in 1962 through the intermediate coupling scheme [17,18]. Up till now, spectroscopic studies of the $4f \rightarrow 4f$ transitions still rely on the Judd-Ofelt theory.

An atom can be considered as an oscillating dipole when it couples and decouples with light. The dominant electronic coupling to the electric and magnetic part of light are electric dipole (ED) and magnetic dipole (MD) interactions, respectively. The electric dipole moment operator is given by:

$$\boldsymbol{P} = -e \sum_i \boldsymbol{r}_i = -e\boldsymbol{D} \qquad (1.8)$$

where the sum runs over all the electrons and $-e\boldsymbol{D}$ is a first-rank tensor with components $-e\boldsymbol{D}_q$, and $q = 0,\ \pm 1$, depending on the polarization of the incident light. A dimensionless oscillator strength is generally used to quantify the intensity of an optical transition. It is assumed that during the transition the atom can be treated an electric dipole oscillating at some frequency. The oscillator strength between two $4f$ states $|4f^N SLJ\rangle$ and $|4f^N S'L'J'\rangle$ deriving from an electric dipole component is given by the following equation [17]:

$$f_{ED} = \frac{8\pi^2 m_e \upsilon}{h} \frac{\chi_{ED}^{abs}}{n} \left| \langle 4f^N SLJ | \boldsymbol{D}_q | 4f^N S'L'J' \rangle \right|^2 \qquad (1.9)$$

where m_e is the electron mass, υ is the mean transition frequency, n is the refractive index, h is the Planck constant, and χ_{ED} is the local-field correction given by $\chi_{ED}^{abs} = (n^2 + 2)^2/9$ in the virtual-cavity model based on the Lorentz local field [19]. The matrix elements are integrals of the dipole operator

between the initial and terminal wavefunctions of the transition. Nevertheless, $|4f^N SLJ\rangle$ and $|4f^N S'L'J'\rangle$ both have the odd parity. The matrix element $\langle 4f^N SLJ|D_q|4f^N S'L'J'\rangle$ should be equal to 0 according to the Laporte rule, whereas spectral lines of electric dipole $4f \rightarrow 4f$ transitions are well observed in solids or solutions. This can be explained by the admixture of states with opposite parity into the pure $4f$ wavefunctions. In a solid matrix, such admixtures can be mediated by odd-parity crystal-field components and lattice vibrations. A new wavefunction is obtained by admixing the even-parity states $|n'l'[S''L'']J''M''\rangle$ (denoted by $|\psi''\rangle$) into the original pure $4f$ wavefunction:

$$|4l^N[SL]JM\rangle = |4f^N[SL]JM\rangle + \sum_{\psi''} \frac{\langle\langle 4f^N SLJM|V_{cr}^u|\psi''\rangle|\psi''\rangle}{E(4f^N SLJM) - E(\psi'')} \tag{1.10}$$

where V_{cr}^u is the odd-parity crystal field interaction operator and the denominator in the sum is the energy difference between the $4f^N$ and the higher energy states (e.g. $4f^{N-1}5d^1$ and $4f^{N-1}6s^1$). The bracket indicates that S and L are no longer good quantum numbers. By substituting the admixed wavefunctions for the pure $4f$ wavefunctions, the electric dipole oscillator strength becomes:

$$\langle 4l^N[SL]J|D_q|4l^N[S'L']J'\rangle =$$

$$\sum_{\psi''}\left\{\frac{\langle 4f^N SLJM|V_{cr}^u|\psi''\rangle\langle 4f^N SLJM|D_q|\psi''\rangle}{E(4f^N SLJM) - E(\psi'')} + \frac{\langle 4f^N S'L'J'M'|V_{cr}^u|\psi''\rangle\langle 4f^N S'L'J'M'|D_q|\psi''\rangle}{E(4f^N S'L'J'M') - E(\psi'')}\right\} \tag{1.11}$$

To solve this equation, two approximations are proposed. First, the energy difference between the higher energy states and the two $4f^N$ states are considered to be approximately identical: $E(4f^N[SL]JM) - E(\psi'') = E(4f^N[S'L']J'M') - E(\psi'')$. However, this is a rough approximation due to the fact that the energy states closer to the $4f^N$ states make a greater contribution to the admixed wavefunctions. Second, it is assumed that the higher energy states are equally populated. Since the higher energy states are situated in more external orbitals, they are impacted by the crystal field and hence have much larger splitting. This is a rather rough assumption as well. Nonetheless, by applying these approximations it is able to greatly simplify the complicated matrix elements. Consequently, the ED oscillator strength becomes:

$$f_{ED}^{abs} = \frac{8\pi^2 m_e}{3h} \frac{\nu}{(2J+1)} \frac{\chi_{ED}^{abs}}{n} \sum_{\lambda=2,4,6} \Omega_\lambda \left|\langle l^N SLJ \| U^{(\lambda)} \| l^N S'L'J'\rangle\right|^2 \tag{1.12}$$

where Ω_λ ($\lambda = 2,4,6$) are the three Judd-Ofelt intensity parameters and $\langle l^N SLJ \| U^{(\lambda)} \| l^N S'L'J'\rangle$ is the reduced matrix element. It can be seen from the equation that the matrix element is diminished to only three terms and the polarization-dependent operator vanishes. With the Ω_λ parameters and the reduced matrix elements calculated from the wavefunctions, one is able to obtain the electric dipole oscillator strength of an arbitrary $4f \rightarrow 4f$ transition (for emission transitions, the local-field correction is replaced by $\chi_{ED}^{em} = n^3 \chi_{ED}^{abs}$). In the framework of the Judd-Ofelt theory, the selection rules for electric dipole transitions are [20]:

$$\Delta S = 0; \ |\Delta L| \leq 6; \ |\Delta J| \leq 6 \ (0 \nleftrightarrow 0); \ if \ J \ or \ J' = 0, |\Delta J| = 2, 4, 6 \tag{1.13}$$

In the experiments, however, people are able to observe transitions which do not follow the above selection rules, such as the $^6H_{15/2}\rightarrow{}^6F_{1/2}$ transition in Dy^{3+} with $\Delta L = 7$, and the $^5D_0\rightarrow{}^5F_0$ transition in Eu^{3+} giving $J = 0 = J'$. This is because the electronic orbitals are partially overlap with those of the other atoms in the matrix. The energy states become rather complex as linear combinations of the pure and the other quantum states. For example, the selection rule on the J quantum number is broken by the J-mixing effect deriving from the even-parity crystal-field perturbation [21]. Nevertheless, these transitions usually show more than an order of magnitude smaller transition probability than those obeying the selection rules.

With regard to the magnetic dipole transitions, they draw less attention owing to the much weaker intensity than the electric dipole transitions. This can be simply assigned to the fact that the force exerted by the electric field of light to an electron is a factor of c/v larger than the force exerted by the magnetic counterpart (assume that such interaction is in the form of Lorentz force), where v is the velocity of the electron [22]. In spite of this general rule, some relatively strong magnetic dipole transitions are found theoretically and experimentally in lanthanide ions [23–26]. The magnetic dipole moment operator is given by:

$$\boldsymbol{M} = -\frac{e\hbar}{2m_e c}\sum_i (\boldsymbol{l_i} + 2\boldsymbol{s_i}) \tag{1.14}$$

Via a similar intermediate coupling scheme, the reduced matrix element $\langle l^N SLJ||\boldsymbol{L} + g\boldsymbol{S}||l^N S'L'J'\rangle$ of the $\boldsymbol{L} + g\boldsymbol{S}$ tensor operator can be calculated and the MD oscillator strength is given by [27]:

$$f_{MD}^{abs} = \frac{hv}{6m_e c^2}\frac{n}{(2J+1)}|\langle l^N SLJ||\boldsymbol{L} + g\boldsymbol{S}||l^N S'L'J'\rangle|^2 \tag{1.15}$$

MD transitions obey the selection rule $|\Delta J| \leq 1\ (0 \nleftrightarrow 0)$ [28]. With the electric dipole as well as the magnetic dipole oscillator strengths of a radiative $4f \rightarrow 4f$ transition, several important spectroscopic parameters can be calculated accordingly, including the spontaneous radiative decay rate $A_{SLJ\rightarrow S'L'J'}$, the radiative lifetime of the excited state τ_{SLJ}^{rad}, and the branching ratio $\beta_{SLJ\rightarrow S'L'J'}$:

$$A_{SLJ\rightarrow S'L'J'}^{ED} = \frac{2\pi e^2 v^2}{m_e \varepsilon_0 c^3}f_{ED}^{em}\ ;\ A_{SLJ\rightarrow S'L'J'}^{MD} = \frac{2\pi e^2 v^2}{m_e \varepsilon_0 c^3}f_{MD}^{em} \tag{1.16}$$

$$\tau_{SLJ}^{rad} = \frac{1}{\sum_{S'L'J'}(A_{SLJ\rightarrow S'L'J'}^{ED} + A_{SLJ\rightarrow S'L'J'}^{MD})} \tag{1.17}$$

$$\beta = \frac{A_{SLJ\rightarrow S'L'J'}^{ED} + A_{SLJ\rightarrow S'L'J'}^{MD}}{\sum_{S'L'J'}(A_{SLJ\rightarrow S'L'J'}^{ED} + A_{SLJ\rightarrow S'L'J'}^{MD})} \tag{1.18}$$

1.2.4 Non-radiative processes

The equation 1.18 above describes the intrinsic radiative lifetime of an excited $4f$ state. The experimental fluorescence lifetime, however, is often noticeably shorter than this value. Besides the radiative process from the excited state to the energy lower states, the excited electron can be

depopulated through a couple of non-radiative processes. They can mainly be attributed to phonon-assisted relaxation and inter-ionic resonance energy transfers. The strengths of these non-radiative processes can also be quantified as transition rate. Hence the total transition rate is a linear combination of the radiative and all the non-radiative processes, which is the reciprocal of experimental fluorescence lifetime:

$$A_{total} = A_{rad} + W_{ph} + W_{ET} = \tau_f^{-1} \tag{1.19}$$

For applications related to the luminescence property, non-radiative transitions can dissipate the stored energy on the excited state and reduce the energy conversion efficiency. It is of great importance to circumvent these processes while developing a gain material. This section focuses on their basic theory and rules in solids.
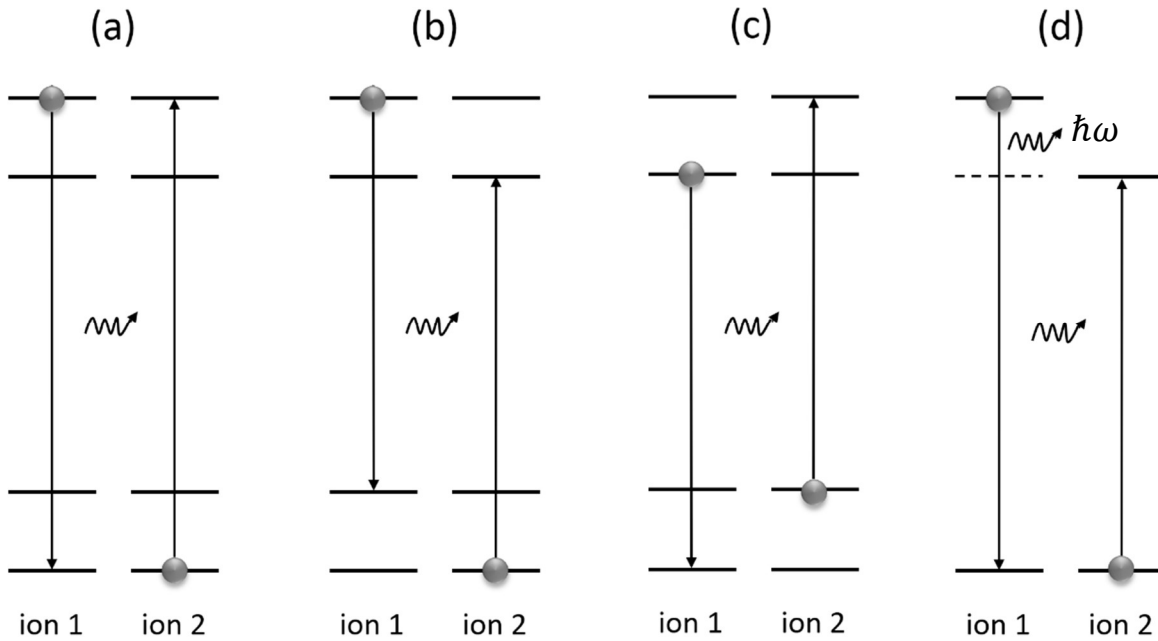
Figure 1.4   **Graphical representations of energy transfer processes: (a) energy migration; (b) cross-relaxation; (c) energy transfer upconversion; (d) phonon-assisted energy transfer.**

1.2.4.1 Resonance energy transfers

Resonance energy transfers take place between two ions, which could be the same or different species. As is shown schematically in Figure 1.4, the stored energy of ion **1** is totally or partially transfer to ion **2**. The mechanism can be described by dipole-dipole interactions between the two ions based on Dexter's theory [29]. By employing the approaches in the Judd-Ofelt theory, T. Kushida developed a method to estimate the probability of resonance energy transfer between two $4f$ states of Ln^{3+} [30]. Assume that during an energy transfer, the initial and terminal energy levels of i and j in ion **1**, and those of l and k in ion **2** participate in this process, the transition rate based on electric dipole-dipole interaction was found to be:

$$A_{DA}^{dd} = \frac{1}{(2J_i + 1)(2J_l + 1)} \left(\frac{2}{3}\right) \left(\frac{2\pi}{\hbar}\right) \left(\frac{e^2}{R_{DA}^3}\right)^2 \chi_{dd} \left[\sum_\lambda \Omega_\lambda^D \left\langle J_i \|U^{(\lambda)}\| J_j \right\rangle^2\right] \left[\sum_\lambda \Omega_\lambda^A \left\langle J_l \|U^{(\lambda)}\| J_k \right\rangle^2\right] S \quad (1.20)$$

Where R_{DA} is the distance between ion **1** and ion **2** (also known as donor and acceptor), χ_{dd} is the local field correction for dipole-dipole interaction, and S is the overlap integral regarding the convolution of the line shapes. Obviously, the energy transfer rate is positively correlated with the intensity of the transitions of $i \rightarrow j$ and $l \rightarrow k$, and with the spectral overlap of these two transitions. Furthermore, A_{DA}^{dd} is inversely proportional to the sixth power of the ionic distance. As a result, such interaction can only become prominent with a high concentration of active ion, which leads to shorter statistic distances between the donor and acceptor units. It is also worth noting that the resonance energy transfer is host-dependent. Because the splitting of stark levels strongly depends on the crystal field in the matrix and directly determines the S term, a host material with relatively small crystal field strength can to some extend suppress the energy transfer processes.

Figure 1.4 (a) depicts the energy migration process. It refers to resonance energy transfer among neighboring active ions of the same species. The final state of ion **2** is the same as the initial state of ion **1**. This process does not directly diminish the population on the excited state. Nevertheless, the excited electron can travel for a long distance and terminate at a quenching center, such as an impurity ion or lattice defect.

In contrast, the cross-relaxation process leads to a different final state of ion **2** which is energy lower than the initial state of ion **1** (Figure 1.4 (b)). Unlike energy migration, cross-relaxation is almost irreversible and causes significant quenching of the initial excited state. The complicated $4f$ states of Ln^{3+} provide a great many of cross-relaxation channels. Attention must be paid on the doping concentration of the Ln^{3+} ion if its energetic structure allows this process.

Additionally, if both ions are initially in an excited state, as depicted in Figure 1.4 (c), such process is usually classified as energy transfer upconversion. It is, however, much less common than the previous two cases since a large population on the excited levels is required.

1.2.4.2 Phonon-assisted relaxations

De-excitation of electron can take place via coupling to the vibration modes of the matrix. The vibration modes in crystal lattice are quantized as phonons possessing energy $E_{ph} = \hbar\omega$, where ω is the frequency of the harmonic oscillators. Moreover, the relaxation of the excited state can be synergetically fulfilled by more than one phonon. This is known as multi-phonon relaxation. For laser gain materials, this non-radiative process not only depletes the population on the upper laser level but also results in unwanted thermal effects. However, it is helpful to transfer the population from the lower laser level to the ground state. This is important because the accumulation of population on the lower laser level can lead to detrimental reabsorption of the stimulated emission.

To characterize the rate of a multi-phonon transition, two assumptions can be made. First, it is assumed that the relaxation process terminates on the first lower energy level below the excited state.

Second, it is assumed that only phonons with the same frequency are involved during this process, and that the highest-frequency phonons make the dominant contribution. Based on these assumptions, the temperature-dependent multi-phonon transition rate is given as [31]:

$$W_{ph}(T) = W_{ph}(0) \cdot [n(\omega) + 1]^p \tag{1.21}$$

where $W_{ph}(0)$ is the transition rate at 0 K, $n(\omega) = (e^{\hbar\omega/kT} - 1)^{-1}$ is the usual Boson thermal occupation number, and p is the number of phonon involved. It can be seen from this equation that the transition rate decreases exponentially with increasing number of necessary phonons. In case of a $4f$ excitation state of a lanthanide ion, it is commonly considered that the multi-phonon relaxation becomes negligible when more than 6 phonons are required.

Phonon-assisted relaxation can also take place together with inter-ionic energy transfer. As depicted in Figure 1.4 (d), the energy gap between the two states of ion **1** does not match well with that of ion **2**. However, if this energy difference is close to a phonon energy in the lattice, the energy coupling can be fulfilled with the assistance of phonon emission.

1.3 State of the art: Ln^{3+}-based direct visible lasers

A laser emission is realized by oscillation of stimulated emission with net gain in a resonator. With a bunch of superiority, lanthanide ions have been extensively employed as active ion to generate stimulated emissions. Their $4f \rightarrow 4f$ transitions are weakly allowed. This produces a relatively long lifetime on the upper laser level and thus benefits the population accumulation. Properties of these transitions are slightly host-dependent. Variation of the host material can lead to gain devices with different functions. In addition, the sophisticated $4f$ energy levels produce abundant optical transitions for pumping and lasing. Many of them are located in the visible spectral region, as is illustrated in Figure 1.5.
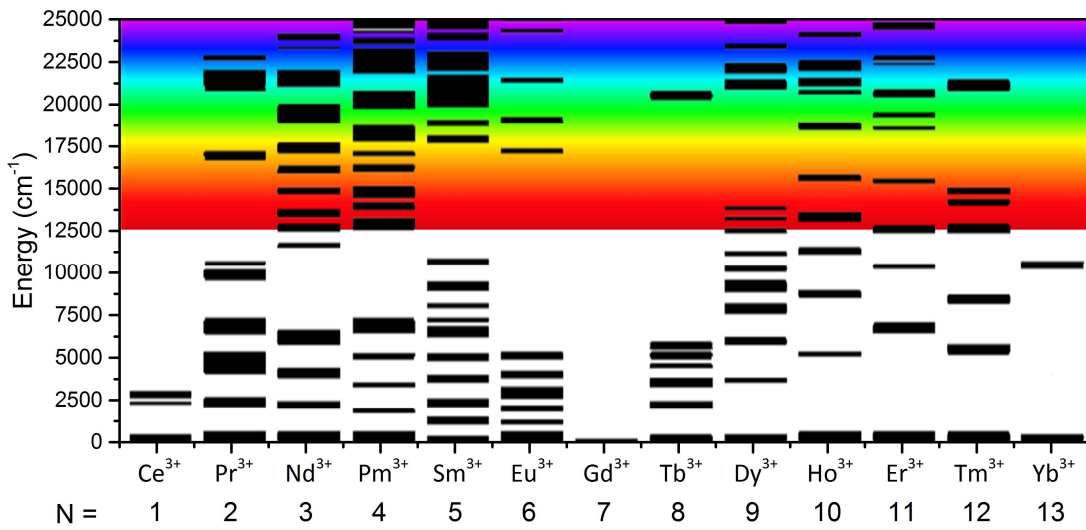
Figure 1.5 $4f^N$ **energy level diagram of trivalent lanthanide ions in LaF₃ (after [32]).**

Despite the fact that these visible emission bands have early been exploited for illumination and fluorescence sensor, they did not attract much attention with respect to visible laser application as introduced before. Difficulties in laser operation on the visible emission lines of lanthanide ions can be accounted for by several reasons compared to that in the infrared which is well developed. First, to generate visible emission directly, pumping into higher energy levels is required, whereas efficient and cheap pump sources providing UV and visible excitation were lacking in the past. Second, many of the emission and ground-state absorption transitions at visible frequencies are spin-forbidden ($\Delta S = 1$). This leads to low transition probabilities and hence small transition cross-sections. In contrast, most of the infrared emitting lasers are operated on the spin-allowed transitions ($\Delta S = 0$), such as the $^4F_{3/2} \rightarrow {}^4I_{11/2}$ transition of Nd^{3+} at 1 µm. Furthermore, pumping and lasing in the visible spectral range require better transparency of the gain material. Color centers of crystal, whose absorption bands usually appear in the visible spectral range, would be critical for the laser performance. The last but not the least, energy levels of lanthanide ions are dense in the UV spectral region. During the visible laser operation, the energetically low lying $4f^{N-1}5d^1$ and/or $4f^N$ states can be reached by a stepwise

absorption process. This can significantly deplete the pump energy and increase the loss of stimulated emission.

In spite of the intrinsic disadvantages discussed above, numerous efforts were made on this issue over the last few decades. Laser operations on the visible emission transitions of Pr^{3+} [33–39], Sm^{3+} [40–42], Eu^{3+} [43], Tb^{3+} [44–46], Dy^{3+} [47–49], Ho^{3+} [50–52], Er^{3+} [53,54], and Tm^{3+} [55–57] have been documented. These results are selectively presented in Table 1.1. It should be noticed that these lasers were mainly pumped with low-efficient Xenon lamps, bulky Ar^+ lasers, or expensive dye lasers. Some were operated in cryogenic conditions that restrict any practical applications.

Table 1.1   Direct visible lasers based on Ln^{3+} ions reported in the last century.

Active ions	Laser transitions	Host material	Pumping condition	Reference
Pr^{3+}	$^3P_0 \rightarrow {}^3H_4$, 479 nm	LiYF$_4$ crystal	Dye laser, 300 K	[38]
	$^3P_1 \rightarrow {}^3H_5$, 522 nm	LiGdF$_4$ crystal	Dye laser, 300 K	[39]
	$^3P_0 \rightarrow {}^3H_5$, 545 nm			
	$^3P_0 \rightarrow {}^3H_6$, 604/607 nm			
	$^3P_0 \rightarrow {}^3F_2$, 639 nm			
Sm^{3+}	$^4G_{5/2} \rightarrow {}^6H_{7/2}$, ~600 nm	TbF$_3$ crystal	Flash lamp, 110 K	[40]
	$^4G_{5/2} \rightarrow {}^6H_{9/2}$, 651 nm	Silicate glass	Ar$^+$ laser, 300 K	[42]
Eu^{3+}	$^5D_0 \rightarrow {}^7F_2$, 611 nm	Y$_2$O$_3$ crystal	Flash lamp, 220 K	[43]
Tb^{3+}	$^5D_4 \rightarrow {}^7F_5$, 544 nm	Gd:LiYF$_4$ crystal	Flash lamp, 300 K	[46]
Dy^{3+}	$^4F_{9/2} \rightarrow {}^6H_{13/2}$, 574 nm	KY(WO$_4$)$_2$ crystal	Flash lamp, 180 K	[49]
	$^4F_{9/2} \rightarrow {}^6H_{11/2}$, 664 nm		Flash lamp, 110 K	
	$^4F_{9/2} \rightarrow {}^6H_{9/2} + {}^6F_{11/2}$, 750 nm	LiNbO$_3$ crystal	Dye laser	[47]
Ho^{3+}	$^5S_2 \rightarrow {}^5I_8$, ~545 nm	YAlO$_3$ crystal	Flash lamp, 300 K	[52]
	$^5S_2 \rightarrow {}^5I_7$, ~750 nm			
Er^{3+}	$^4S_{3/2} \rightarrow {}^4I_{15/2}$, 551 nm	LiYF$_4$ crystal	Ar$^+$ laser, 300 K	[54]
Tm^{3+}	$^1G_4 \rightarrow {}^3F_4$, 649 nm	Ba$_2$Y$_2$F$_8$ crystal	Ti:sapphire, 300K	[57]

In 2004, A. Richter et al. reported the first blue LD-pumped solid-state laser using Pr^{3+}-doped LiYF$_4$ crystal as gain medium [58]. The crystal was pumped at 442 nm, providing visible laser output at 640 nm originating from the $^3P_0 \rightarrow {}^3F_2$ transition. This opened a new page to the subject of blue semiconductor-pumped visible laser.

Nowadays, progressive development of semiconductor pump sources has been made. In terms of maximum output power, it has been remarkably improved from 25 mW, output power of the pump used in A. Richter's demonstration in 2004, to more than 10 W. Moreover, choices of the output wavelength have been greatly expanded to nearly a full cover of the visible spectral region. Benefiting from the more powerful and versatile pumps, an ascending amount of Ln^{3+}-based visible transitions are being exploited to produce laser emission. This motivates us to investigate the potential of each Ln^{3+} ion for efficient semiconductor-pumped direct visible laser applications.

Although the simple electronic structure of Ce^{3+} does not allow any $4f \rightarrow 4f$ transitions in the visible, it features energetically low-lying $4f^0 5d^1$ states, which are sensitive to the crystal field. Thus, Ce^{3+} can provide intense visible emission bands originating from the inter-configurational $5d^1 4f^0 \rightarrow 4f^1$ transitions in suitable host materials [59,60]. However, the stimulated emission was found to show significant optical loss owing to the parity-allowed excited-state absorption (ESA) into energetically higher $5d$ configuration [61,62]. Laser operation on the $5d^1 4f^0 \rightarrow 4f^1$ transitions would be difficult.

Nd^{3+} can exhibit orange fluorescence deriving from the $^4G_{5/2} \rightarrow {}^4I_{9/2}$ transition [63]. However, the closely spaced multiplets lying below the $^4G_{5/2}$ manifold with intervals less than 2000 cm^{-1} indicate inevitable and pronounced non-radiative processes from the upper laser level. Up to now there are very few reports regarding its direct laser performance out of the infrared [64].

Ho^{3+} is mainly known for its laser emission at 2 µm using the $^5I_7 \rightarrow {}^5I_8$ transition. A couple of multiplets located in the blue spectral range support semiconductor pumping. After being pumped into these levels, the populations would be transported rapidly to the overlapped $^5F_4$ and $^5S_2$ manifolds at around 535 nm via multi-phonon relaxation. Radiative relaxation to the terminal levels of $^5I_7$ and $^5I_8$ provide visible emission transitions around and 750 nm and 540 nm, respectively. However, the $^5I_7$ level separated from the ground state $^5I_8$ by about 5000 cm^{-1} shows radiative lifetime up to 10 ms [65]. This might cause unwanted population accumulation on the laser terminal level if phonon-assisted relaxation is not efficient from the $^5I_7$ level. Unfortunately, using host materials which support higher phonon energy would cause even more severe quenching on the $^5F_4$, $^5S_2$ upper laser levels, since they were separated from the next lower energy level by ca. 3000 cm^{-1}. This contradiction impedes lasing on the deep red $^5F_4$, $^5S_2 \rightarrow {}^5I_7$ transitions. On the other hand, laser operation on the green $^5F_4$, $^5S_2 \rightarrow {}^5I_8$ ground-state transition bears in a high laser threshold energy stemming from the quasi-three-level system. In 2014, F. Reichert *et al.* reports the first laser demonstration of the green $^5F_4$, $^5S_2 \rightarrow {}^5I_8$ transition [66]. The Ho:LaF$_3$ gain medium was pumped by OPSL at 479 nm. Due to the low absorption efficiency of the pump and the quasi-three-level character, the laser threshold energy was more than 2 W whereas the maximum output was merely 7.7 mW upon incident pump power of 4 W in the best configuration. Using Ho:LiLuF$_4$, laser performance of the $^5F_4$, $^5S_2 \rightarrow {}^5I_7$ transitions was detected but poor as well. Only self-pulsed output with power less than 1 mW could be observed under 4-Watt OPSL pumping [67]. Therefore, Ho^{3+} is not interesting for this subject owing to its intrinsic disadvantages.

Except for the well-established infrared lasers at 1.5 and 3 µm, Er^{3+} is also known for its green emission deriving from the $^4S_{3/2} \rightarrow {}^4I_{15/2}$ transition. Laser oscillation using this transition can be achieved with

pumping in upconversion schemes or a direct-pumping approach. F. Moglia and co-workers demonstrated green laser emission using the gain crystal of Er:LiLuF$_4$ [68]. Laser outputs could be realized with either a Ti:sapphire laser or an OPSL as pump source. The Ti:sapphire pumped Er^{3+}-laser in an upconversion pumping scheme gave peak slope efficiencies around 20%, while this value is more than 50% upon OPSL pumping. However, due to the small energy gap (ca. 3000 cm^{-1}) from $^4S_{3/2}$ to the next lower level, Er^{3+} is not suitable for lasing in oxide matrices.

Tm^{3+} has only a few transitions in the visible spectral range. The $^1G_4$ manifold situated around 21300 cm^{-1} (470 nm) can serve as pump and upper laser level. Unfortunately, its ground-state absorption wavelength does not match the output wavelengths of common LDs or OPSLs, though an upconversion pumping scheme can be employed [69]. Radiative transitions from energy level of $^1G_4$ to $^3H_6$ and $^3F_4$ provide blue and red emission, respectively. The former, as a ground-state transition, foresees a large laser threshold energy for laser operation. The branching ratio of the latter is, however, found to be only around 5% [70–72]. Furthermore, cross-relaxation channels from the $^1G_4$ state, $^1G_4 + {}^3H_6 \rightarrow {}^3H_4 + {}^3H_5$ and $^1G_4 + {}^3H_6 \rightarrow {}^3H_5 + {}^3H_4$, could be problematic. Thus, Tm^{3+} is not very promising for visible laser application.

Further excluding Pm^{3+} which lacks stable isotopes and Gd^{3+} as well as Yb^{3+} which do not provide any visible emissions, Pr^{3+}, Sm^{3+}, Eu^{3+}, Dy^{3+}, and Tb^{3+} are considered to be potentially suitable for direct visible laser application. Their spectroscopic and laser properties will be discussed in detail.

1.3.1 Praseodymium(III)

Trivalent praseodymium (Pr^{3+}) is the most well-developed Ln^{3+} active ion for yielding direct visible lasers [73]. The energy level scheme of Pr^{3+} is shown in Figure 1.6. Several ground-state transitions can be found in the blue spectral range. They feature large absorption cross-sections in the order of 10^{-20} cm^2 to 10^{-19} cm^2. Their wavelengths match with the commercial semiconductor lasers. For example, the $^3P_2$ multiplet at 445 nm and the $^3P_0$ multiplet at 480 nm can be reached by LD and OPSL pumping, respectively. Fluorescence lines spread throughout the visible spectral range, originating from emission transitions starting from the ^3P_J and $^1I_6$ multiplets. They exhibit emission cross-sections in the order of 10^{-21} cm^2 to 10^{-20} cm^2.

Visible lasers activated by Pr^{3+} have been achieved using emission transitions ranging from the cyan to the deep red spectral region [73]. Except for the cyan transition which suffers reabsorption, watt-level outputs have been realized on these transitions with maximum slope efficiencies exceeding 50% [73]. In addition to the abundant output wavelengths, visible laser operations of Pr^{3+} have been realized in various matrices, both fluoride-based and oxide-based. Fluoride crystals including LiREF$_4$ (RE = Y, Gd, and Lu) [74], KYF$_4$ [75], β-NaGdF$_4$ [76], KY$_3$F$_{10}$ [77], BaY$_2$F$_8$ [78], CaF$_2$ [79], and Y$_{0.5}$Gd$_{0.5}$F$_3$ [76] have been utilized for hosting Pr^{3+}. Among them Pr:LiYF$_4$ provides the best results. Laser emissions at 523 nm or 640 nm with slope efficiencies around 70% can be produced using Pr:LiYF$_4$ as gain medium [80]. With regard to the oxides, stimulated emission of Pr^{3+} could be observed in YAlO$_3$ [81], CaAl$_{12}$O$_{19}$ [82],

SrAl$_{12}$O$_{19}$ [83], LaMgAl$_{11}$O$_{19}$ [84], and Sr$_{0.7}$La$_{0.3}$Mg$_{0.3}$Al$_{11.7}$O$_{19}$ [85]. The Pr:YAlO$_3$ gain crystal can yield a decent slope efficiency of 45% for the laser operation at 747 nm.

In spite of these successes, the issue of direct visible laser cannot totally rely on Pr^{3+} because it does not provide laser emissions in the yellow spectral range. It also shows a couple of intrinsic disadvantages that may impede actual applications of Pr^{3+}-lasers. First, the energy gap between the upper laser level ^{3}P$_0$ and the next lower energy level ^{1}D$_2$ is around 4000 cm^{-1}. Efficient and detrimental multi-phonon relaxation from the upper laser level is possible if the host lattice supports large phonon energy [86]. Second, ESA transitions from the upper laser levels cannot be overlooked owing to the energetically low-lying $4f^15d^1$ configuration [87,88]. These two characters restrict the scope of host materials for Pr^{3+}-activated visible lasers. Moreover, cross-relaxation channels starting from the upper laser level limit the doping concentration of Pr^{3+} in the matrix. The last but not the least, the short upper-level lifetime, which is typically a few tens of micro-seconds, results in relatively high laser threshold energy and difficulty in Q-switched operation.
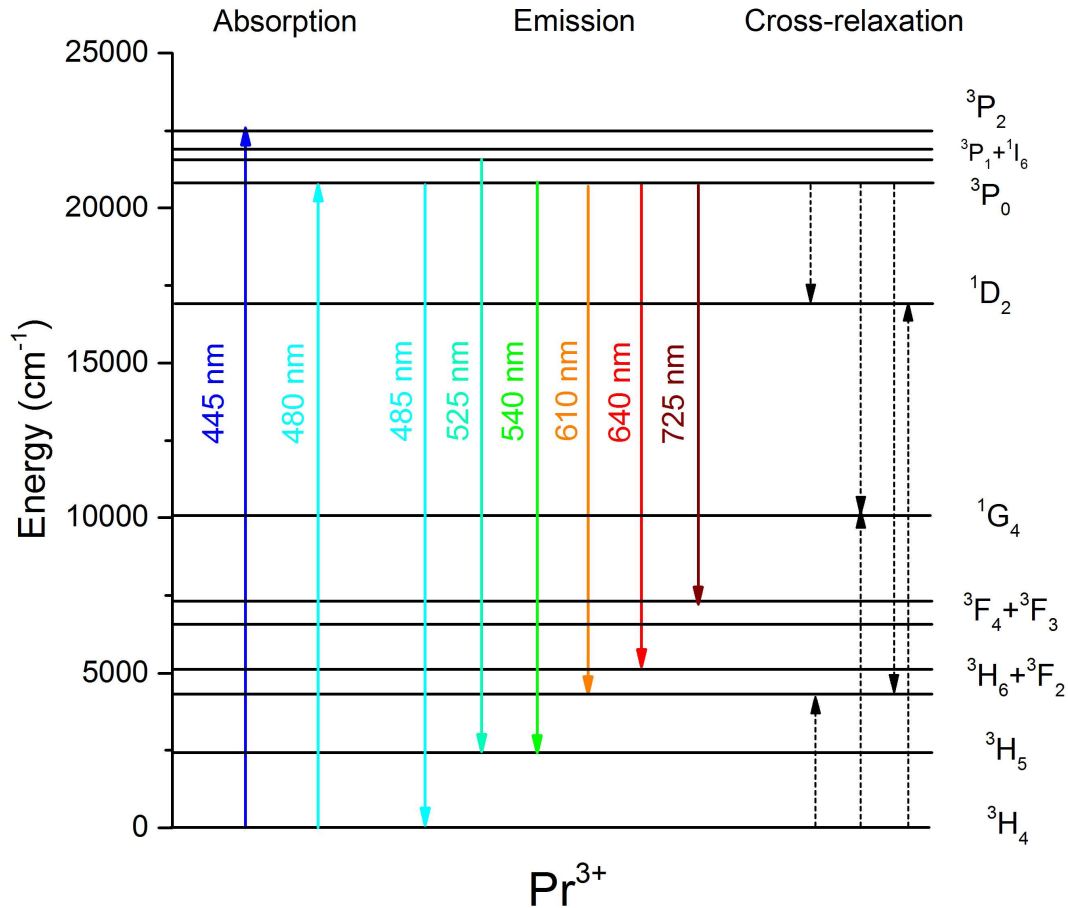
Figure 1.6 **Simplified energy level diagram of Pr^{3+}. Solid and dot arrows represent radiative and possible cross-relaxation process, respectively.**

1.3.2 Samarium(III)

As is shown in Figure 1.7, Sm^{3+} displays a complicated energy-level scheme. The ground-state absorption transitions around 405 nm are suitable for commercial GaN LD pumping. It can provide absorption cross-sections up to several 10^{-20} cm^2. Besides, a couple of absorption transitions can also be found in the energetically lower blue spectral region, which enables LD or OPSL pumping. However, these transitions are spin-forbidden and show much smaller cross-sections than the $^6H_{5/2} \rightarrow ^6P_{5/2}$ spin-allowed transition around 405 nm. Emission bands in the visible are attributed to the $^4G_{5/2} \rightarrow ^6H_{5/2}$, $^6H_{7/2}$, $^6H_{9/2}$, and $^6H_{11/2}$ transitions. They are located in the yellow-green, orange, red, and deep red spectral regions, respectively. All these transitions suffer a spin flip and thus show weak transition cross-sections in the order of 10^{-22} cm^2. The $^4G_{5/2} \rightarrow ^6H_{7/2}$ transition at around 600 nm usually gives the largest branching ratio. Research interest regarding the laser property of Sm^{3+} mainly focuses on this transition as it can generate orange laser emission, which is difficult to obtain by conventional frequency conversion of Nd^{3+} or Yb^{3+}. Despite that the $^4G_{5/2} \rightarrow ^6H_{7/2}$ transition can provide unique yellow-green emission at ca. 560 nm, a high laser threshold using this transition is expected as it terminates on the ground state.
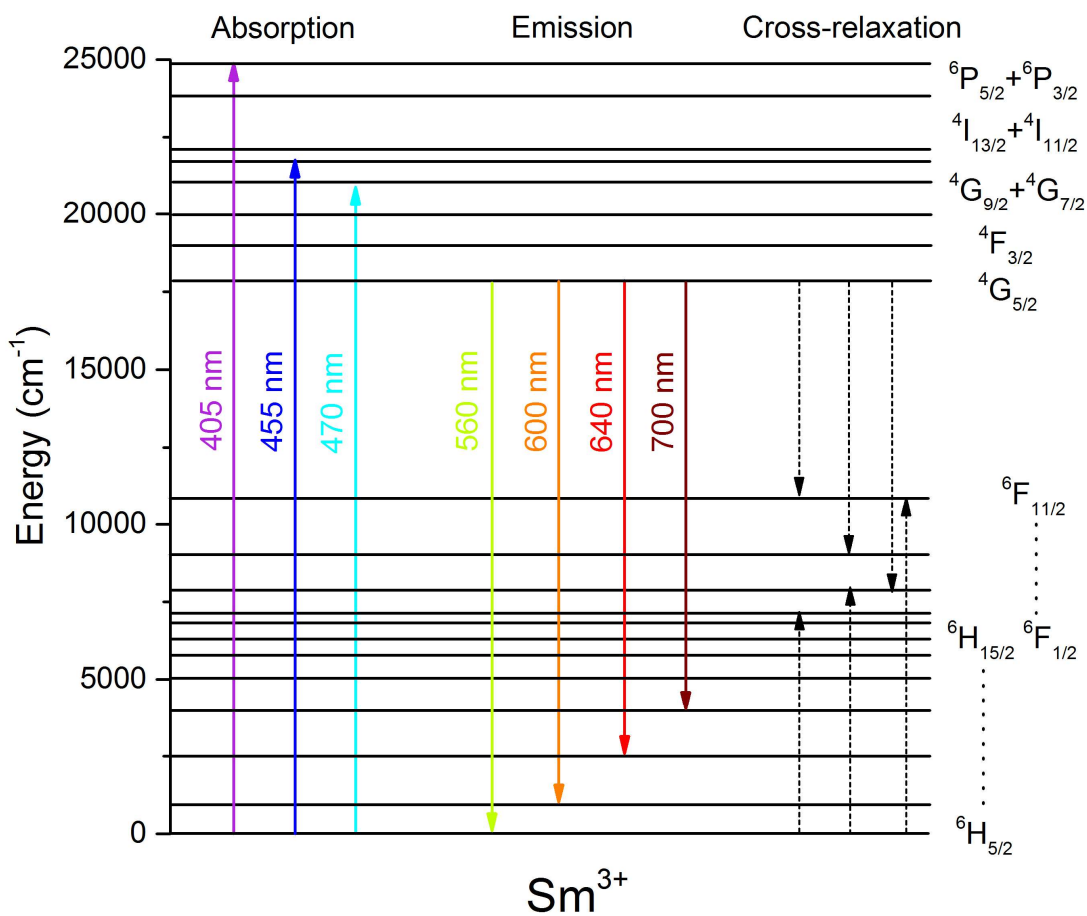
Figure 1.7 **Simplified energy level diagram of Sm^{3+}. Some less important energy levels with weak absorption intensity are neglected for clarity.**

The upper laser level $^4G_{5/2}$ was separated from the next lower energy level by about 7000 cm^{-1}. Therefore, multi-phonon relaxation from the $^4G_{5/2}$ manifold is considered to be unlikely. Moreover, the energetic position of the lowest $5d$ configuration is ca. 14000 cm^{-1} higher than that of Pr^{3+} [87]. Thus, deleterious ESA process into the $5d$ states is not a main issue for Sm^{3+}-lasers. These characters make it feasible to lase Sm^{3+} in oxide-based matrices. However, the closely spaced energy levels lying between the $^4G_{5/2}$ upper laser level and the ground state allow cross-relaxation [89]. As a result, doping concentration should be limited in order to circumvent the non-radiative loss.

Visible laser oscillation have been realized using Sm:LiLuF$_4$ and Sm,Mg:SrAl$_{12}$O$_{19}$ crystals via in-band pumping to the $^4G_{5/2}$ upper laser level [90]. The OPSL pump source emitting at 480 nm provided absorption efficiencies around 30%. The former gain crystal was able to lase at 606 and 648 nm while the latter at 593 and 703 nm. With regard to the orange laser operation, Sm:LiLuF$_4$ showed slope efficiency of 13% which is apparently larger than that of 1.2% using Sm,Mg:SrAl$_{12}$O$_{19}$. In these demonstrations, the laser outputs were prone to show self-pulsing behaviors and delivered power less than 100 mW. It is deduced that the self-pulsing is due to ESA, probably terminated at the higher-energy $4f^5$ manifolds, at the lasing wavelengths.

1.3.3 Europium(III)

Europium complexes are widely used as emitter in many fields taking advantage of the intense red luminescence. Figure 1.8 illustrates the energy level scheme of Eu^{3+}. Absorption transitions in the visible start from the thermally coupled $^7F_0$ and $^7F_1$ manifolds and terminate at the ^5D_J ($J = 0, 1, 2, 3$) multiplets. Unfortunately, none of the absorption lines match with the wavelengths of common semiconductor lasers. In Eu^{3+}-doped tungstate crystals, the $^7F_0\rightarrow^5D_2$ transition around 465 nm exhibits large absorption cross-sections approaching 10^{-19} cm^2 despite the requirement of spin flip [91,92]. Fluorescence lines from the $^5D_0$ manifold are mainly situated in the orange and red spectral region. The $^5D_0\rightarrow^7F_2$ and $^5D_0\rightarrow^7F_4$ emission transitions show cross-sections in the order of 10^{-20} cm^2 in tungstate compounds [91–93]. The most intense $^5D_0\rightarrow^7F_2$ transition at around 615 nm can give branching ratio up to 86% [91]. The $^5D_0\rightarrow^7F_1$ transition located in the orange spectral region is a pure magnetic dipole transition with significantly weaker intensity than the electric dipole transitions. An advantage of Eu^{3+} as active ion is that the $^5D_0$ multiplet is free from multi-phonon transitions and cross-relaxation channels. This enables large doping ratio of Eu^{3+} without dramatically decreasing the fluorescence lifetime [94]. In addition, the energy of the lowest $5d$ level of free-ion Eu^{3+} is ca. 85000 cm^{-1} [87], thus ESA to the $5d$ configuration is unlikely for visible laser operation.

Despite that the $^5D_0\rightarrow^7F_2$ transition seems to be the most promising for laser operation, it is found that its peak wavelength in KRE(WO$_4$)$_2$ host materials is identical to that of the $^5D_0\rightarrow^5F_4$, a super-intense intra-configurational ESA transition. As a result, optical gain offered by the $^5D_0\rightarrow^7F_2$ transition is greatly suppressed by ESA [93]. P. A. Loiko, V. Dashkevich, and the co-workers characterized the laser performance of Eu^{3+}-doped KRE(WO$_4$)$_2$ crystals upon pumping at 534 nm, which corresponds to the $^7F_1\rightarrow^5D_1$ transition [95,96]. Laser oscillations have been realized only on the deep red $^5D_0\rightarrow^7F_4$

transition. Due to the lack of efficient pump sources and existence of color centers in the crystals, the optical-to-optical efficiencies were no more than 2% in their demonstrations.

Nevertheless, it should be noted that a novel LD emitting at 465 nm with output power up to 16 W is commercially available [97]. This pump source matches the wavelength of the intense $^7F_0 \rightarrow {}^5D_2$ ground-state transition. In addition, using host materials with smaller crystal field strengths might circumvent the intra-configurational ESA transition and enable laser operation using the most interesting $^5D_0 \rightarrow {}^7F_2$ transition.
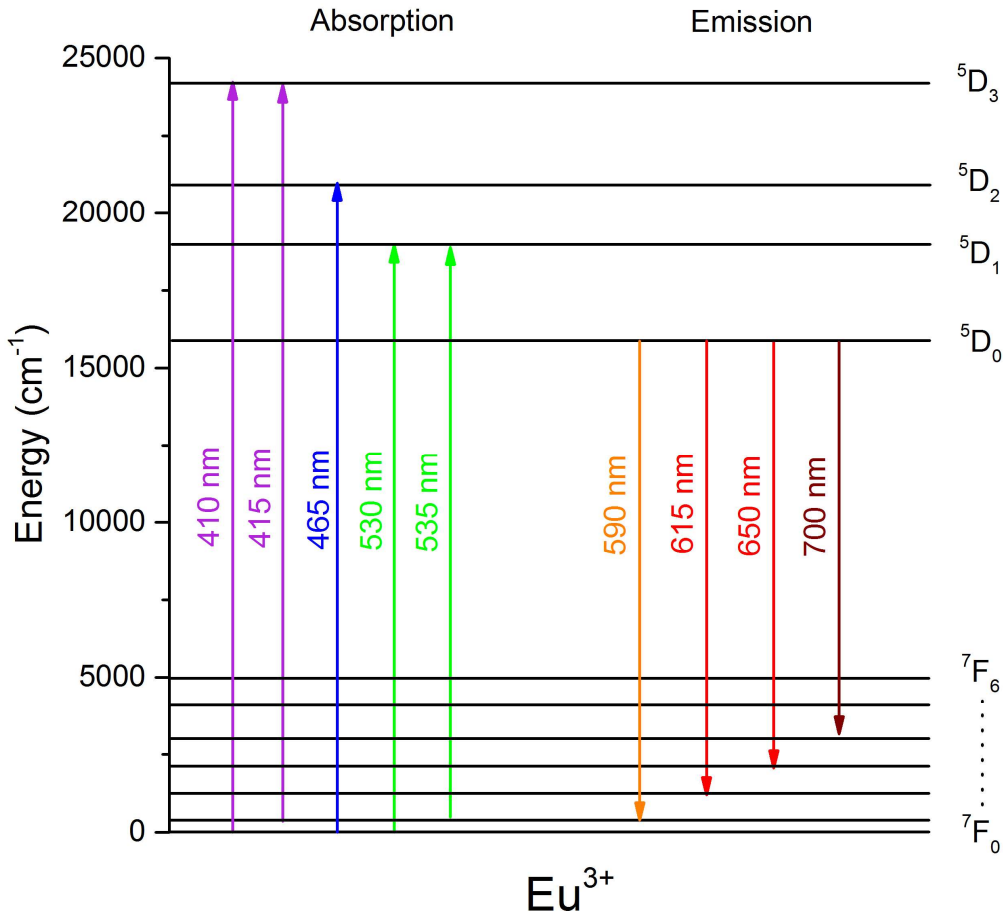
Figure 1.8   **Simplified energy level diagram of Eu³⁺.**

1.3.4 Terbium(III)

The energy level diagram of Tb³⁺ (Figure 1.9) is similar to Eu³⁺, since the $4f$ shell of the former is filled with six $4f$ "holes" while the latter has the same number of $4f$ electrons. The ground state is the $^7F_6$ multiplet. It can be excited to the $^5D_4$ manifold with OPSL or novel LD pumps in the cyan spectral range. Unfortunately, this spin-forbidden transition exhibits fairly low cross-sections in the order of a few 10^{-22} cm². Emission transitions terminating at the ^7F_J $(J = 0 - 6)$ multiplets spread throughout the visible spectral range. The $^5D_4 \rightarrow {}^7F_5$ transition around 545 nm is the most promising for laser operation

as it usually shows the largest branching ratio and emission cross-sections. The $^5D_4{\rightarrow}^7F_4$ transition around 585 nm, which can provide rare yellow laser emission, also attracts attention. Transitions in the red spectral region are much weaker, thus they are not interesting for visible laser applications. Due to the long radiative lifetime up to several milliseconds of the $^5D_4$ manifold, though favorable for storing energy on this level, even the strongest emission transition of $^5D_4{\rightarrow}^7F_5$ features low cross-sections in the order of 10^{-22} to 10^{-21} cm^2.
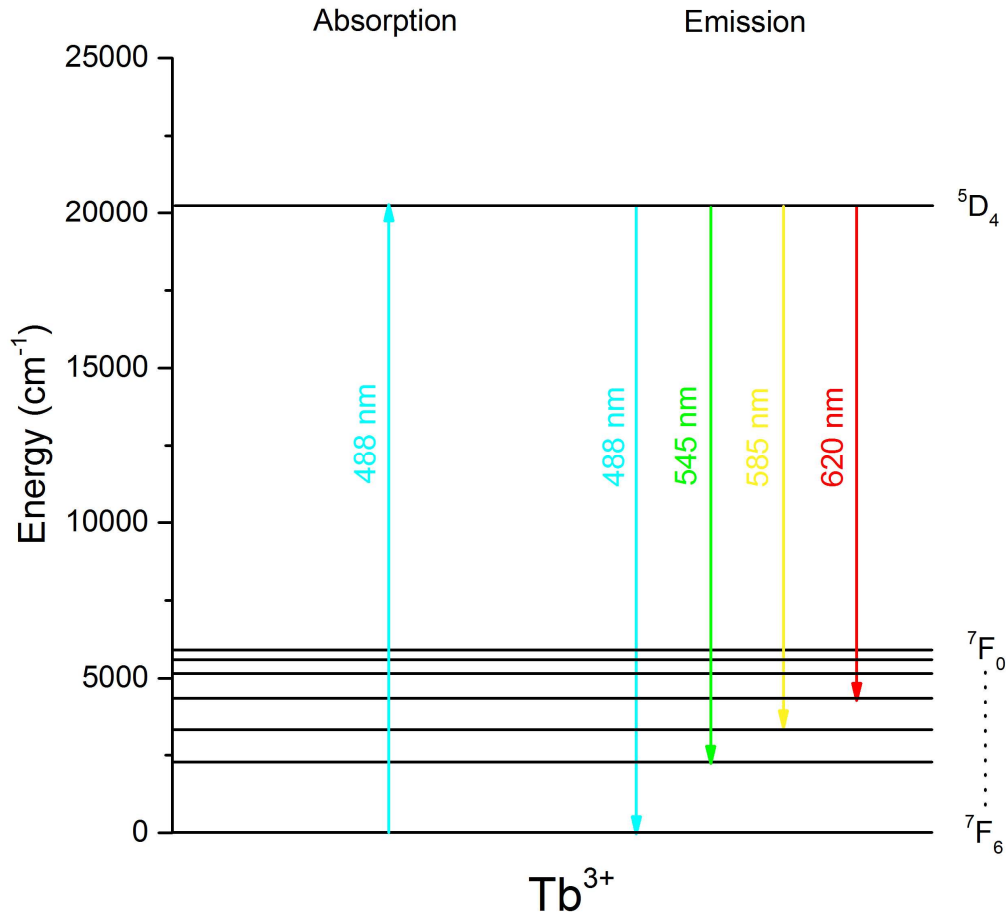
Figure 1.9   **Simplified energy level diagram of Tb^{3+}.**

In 2015, C. Kränkel et al. performed systematic laser experiments using Tb^{3+}-doped fluoride crystals as gain medium and cyan OPSLs as pump source. They were able to demonstrate Tb^{3+}-based visible lasers via efficient semiconductor pumping for the first time [98]. Spectroscopic studies of the fabricated Tb^{3+}-doped fluoride crystals, including Tb:LiLuF$_4$, Tb:LiYF$_4$, LiTbF$_4$, Tb:KY$_3$F$_{10}$, Tb:β-BaLu$_2$F$_8$, and Tb:LaF$_3$, showed that the absorption efficiency at the pump wavelengths varies from 10 to 70%. Laser operation on the green $^5D_4{\rightarrow}^7F_5$ transition were succeeded for all the mentioned gain materials. Benefiting from the long radiative lifetime, the typical threshold power were found to be a few tens of milliwatts. The largest slope efficiency of 58% was observed by using a 11-mm-long 14 at% Tb:LiLuF$_4$ crystal. The 21-mm-long 28 at% Tb:LiLuF$_4$ crystal yielded the largest output power of 1.13 W and the highest optical-to-optical efficiency, with respect to incident pump power, of 44%. This value is comparable to

the well-developed frequency-doubled Nd^{3+}-lasers emitting at 532 nm [99]. Continuous-wave laser operation on the yellow $^5D_4 \rightarrow {}^7F_4$ transition was also achieved. Best results were obtained by the Tb:LiYF$_4$ crystal, giving a slope efficiency of 22% and the maximum output power of 71 mW at 587 nm. Furthermore, wavelength tuning in the green spectral region has also been realized [100].

In spite of the impressive results of these Tb^{3+}-lasers, their utility is limited to academic level since bulky and expensive OPSLs were employed as pump source. The emergence of novel LD with emission around 488 nm offers a much cheaper choice for the pump source [101]. Evaluating the possibility for this substitute could be interesting. Q-switched operation of Tb^{3+} is also prospective, considering the long fluorescence lifetime that is favorable for energy storage.

1.3.5 Dysprosium(III)

Achieving laser emissions in the yellow spectral range is not facile. Sum frequency mixing or frequency doubling of Nd^{3+}-doped gain media can generate yellow laser emission, whereas the typical slope efficiency is merely a few percent [102,103]. Dy^{3+}, which exhibits characteristic yellow fluorescence under UV irradiation, is considered as a candidate to deliver yellow laser emissions. The layout of the energy diagram of Dy^{3+}, depicted in Figure 1.10, resembles Sm^{3+} to some extent, since the number of $4f$ holes in Dy^{3+} is identical to the number of $4f$ electrons in Sm^{3+}. There are three energy levels residing in the blue spectral range. Among them, the $^6H_{15/2} \rightarrow {}^4I_{15/2}$ transition which corresponds the output wavelength of common InGaN LDs and features the largest cross-section of a few 10^{-21} cm^2 is the most promising for pumping. After excitation, population on the $^4I_{15/2}$ multiplets rapidly relax to the $^4F_{9/2}$ level via phonon emission. Inband pumping to the $^4F_{9/2}$ manifold by cyan OPSL is also possible, but this transition shows an order of magnitude weaker cross-section than the $^6H_{15/2} \rightarrow {}^4I_{15/2}$ transition centered at around 450 nm. Radiative decays from the $^4F_{9/2}$ level to the ^6H_J and ^6F_J multiplets produce several visible emission bands. The yellow $^4F_{9/2} \rightarrow {}^6H_{13/2}$ emission transition usually shows the largest branching ratio over 50% and emission cross-section in the order of 10^{-21} to 10^{-20} cm^2 [104–108]. The $^4F_{9/2} \rightarrow {}^6F_{11/2} + {}^6H_{9/2}$ and $^4F_{9/2} \rightarrow {}^6F_{9/2} + {}^6H_{7/2}$ transitions in the red spectral range typically exhibit a factor of 2 to 4 weaker emission cross-sections, which are less interesting for laser application.

It is worth mentioning that, except for the $^4F_{9/2} \rightarrow {}^6H_{15/2}$ ground state transition, all the emission transitions depopulate into the terminal level $^6H_{13/2}$, which separates from the ground state by about 3500 cm^{-1}. Host materials with too-small phonon energy, such as fluorides, may suffer undesirable population accumulation on the $^6H_{13/2}$ multiplets, since the population cannot be efficiently quenched via electron-phonon coupling and the radiative lifetime of this level is estimated to be up to several tens of milliseconds [109,110].
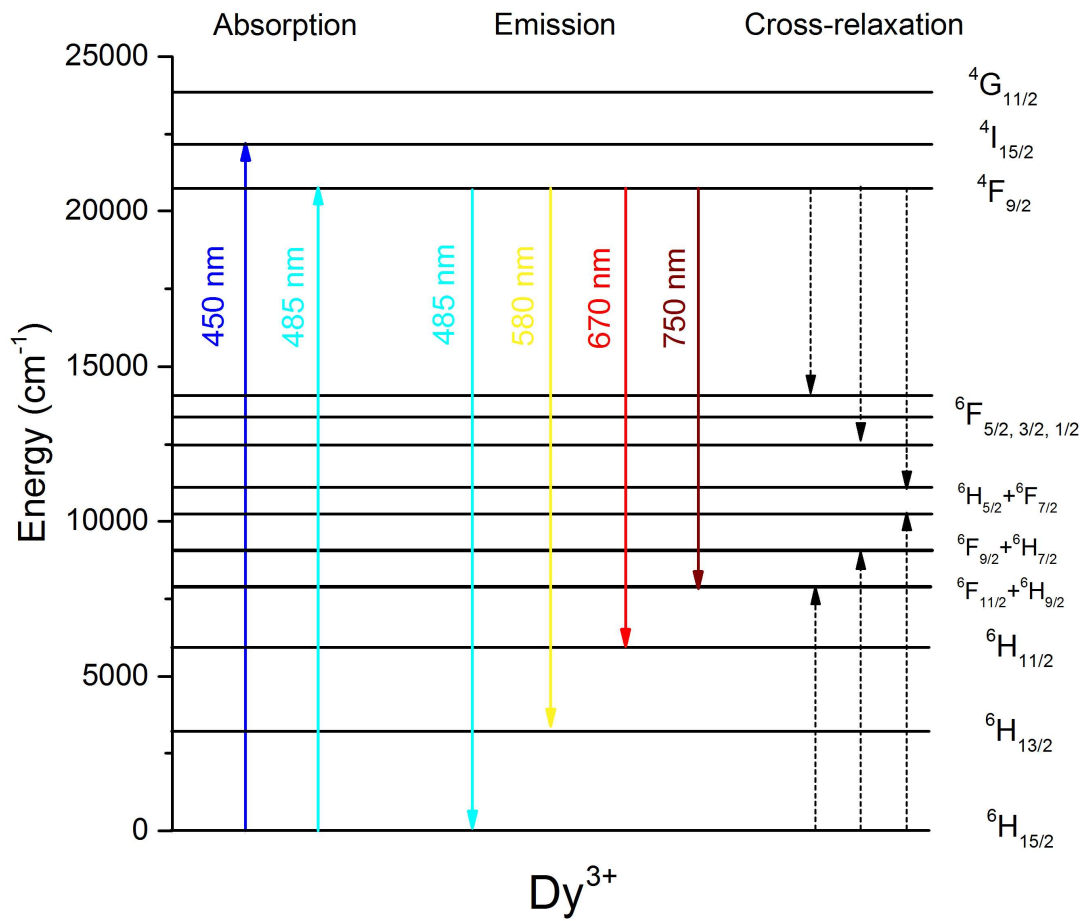
Figure 1.10   Simplified energy level diagram of Dy³⁺.

In 2010, Fujimoto et al. demonstrated yellow laser operation in a Dy^{3+}-doped fluoro-aluminate glass fiber by LD pumping for the first time [111]. Under excitation at 399 nm, a maximum output power of 10.3 mW was obtained. 2 years later, diode-pumped laser operation in bulk crystal material was first reported, using Dy:YAG as gain medium [112]. The gain crystal was pumped by a pulse GaN LD at 447 nm and laser output at 583 nm was observed. Best results were obtained with about 2% output coupling at the lasing wavelength, giving a slope efficiency of 12.5% and maximum output power of 150 mW. Continuous-wave pumping by a 450-nm LD using $Dy:ZnWO_4$ as gain medium presents similar results [113]. Maximum cw output power of 110 mW was observed at 575 nm with a slope efficiency around 13%. Yellow laser performance in $Dy,Tb:LiLuF_4$ crystal was reported by G. Bolognesi and co-workers [114]. The Tb^{3+} co-dopant is to facilitate depletion of population on the laser terminal level via energy transfer to the $^7F_4$ manifold of Tb^{3+}. The laser threshold power was found to be 320 mW, pumped by a blue emitting LD at 450 nm. The maximum output was 55 mW at 574 nm upon absorbed pump power of ca. 730 mW, resulting in a slope efficiency of 13.4%. In these demonstrations, the efficiencies of Dy^{3+}-lasers have surpassed the conventional frequency-converted Nd^{3+}-lasers. Yellow lasers based on direct emission of Dy^{3+} is prospective. Besides, LD-pumped laser operations on the other visible emission bands, viz. those around 670 and 750 nm, have not been demonstrated to date.

1.3.6 Summary of the state-of-the-art investigation

In this section, we investigated the potential of each Ln^{3+} species as active ion for direct visible laser usages. A summary of these novel lasers is presented in Table 1.2. The investigation especially focused on Pr^{3+}, Sm^{3+}, Eu^{3+}, Dy^{3+}, and Tb^{3+} ions. Among these candidates, Pr^{3+}-doped fluoride gain materials have been maturely developed. On the other hand, due to the tendency of multiphonon relaxation from the upper laser levels, oxide-based materials with large phonon energy, such as phosphates and borates, are not promising for Pr^{3+}-activated lasers. However, to circumvent the ESA process, materials with small crystal field strengths are favorable for hosting Pr^{3+}, whereas most of them are phosphates or borates. Direct visible lasers have also been demonstrated using Sm^{3+}- and Eu^{3+}-doped oxide-based crystals. However, the quasi-cw output behaviors in these laser operations indicate intrinsic ESA processes of Sm^{3+} and Eu^{3+} ions.

Tb^{3+}-doped fluorides are able to lase efficiently with green and yellow emissions, while the oxide domain is at the moment a blank as Tb^{3+}-based gain material. With regard to Dy^{3+}, yellow laser operations in direct pumping schemes have been achieved using both fluoride- and oxide-based crystals giving moderate efficiency. It would be interesting to study stimulated emission of Dy^{3+} in a variety range of materials to acquire a better insight into the structure-property relationship of Dy^{3+}-lasers. Finally, it has to be accentuated again that Tb^{3+} and Dy^{3+} can produce lasers emitting in the unique yellow spectral region. These considerations lead to the theme of this PhD thesis.

Table 1.2   Selected Ln^{3+}-based direct visible lasers. For clarity, the data not given in the literature are denoted "-".

Active ion	Host material	Pol.	Laser transition	λ_{em} (nm)	η_{slope} (%)	$P_{thres.}$ (mW)	$P_{max.}$ (mW)	Operation mode	Pump	Ref.
Pr^{3+}	LiYF$_4$	π	$^3P_0 \rightarrow ^3H_4$	523	72	52	2900	cw	OPSL	[80]
	LiYF$_4$	π	$^3P_0 \rightarrow ^3H_6$	640	68	17	2800	cw	OPSL	[80]
	SrAl$_{12}$O$_{19}$	σ	$^3P_0 \rightarrow ^3H_6$	643	44	60	549	cw	OPSL	[83]
	Sr$_{0.7}$La$_{0.3}$Mg$_{0.3}$Al$_{11.7}$O$_{19}$	σ	$^3P_0 \rightarrow ^3H_6$	643	27	200	234	cw	OPSL	[85]
	Sr$_{0.7}$La$_{0.3}$Mg$_{0.3}$Al$_{11.7}$O$_{19}$	σ	$^3P_0 \rightarrow ^3F_4$	725	37	350	300	cw	OPSL	[85]
	YAlO$_3$	π	$^3P_0 \rightarrow ^3F_4$	747	45	620	91	cw	LD	[81]
Sm^{3+}	LiLuF$_4$	π	$^4G_{5/2} \rightarrow ^6H_{7/2}$	606	13	46	86	quasi-cw	OPSL	[76,90]
	LiLuF$_4$	π	$^4G_{5/2} \rightarrow ^6H_{9/2}$	648	15	147	93	quasi-cw	OPSL	[76,90]
	SrAl$_{12}$O$_{19}$	-	$^4G_{5/2} \rightarrow ^6H_{7/2}$	593	1.2	99	44	quasi-cw	OPSL	
	SrAl$_{12}$O$_{19}$	-	$^4G_{5/2} \rightarrow ^6H_{9/2}$	703	7	200	7	quasi-cw	OPSL	
Eu^{3+}	KY(WO$_4$)$_2$	N$_m$	$^5D_0 \rightarrow ^7F_4$	702	1	640	19	quasi-cw	Nd:KGW	[95]
Tb^{3+}	LiYF$_4$	σ/π	$^5D_4 \rightarrow ^7F_5$	544/542	55	8	158	cw	OPSL	[98]
	LiYF$_4$	π	$^5D_4 \rightarrow ^7F_4$	587	22	32	71	cw	OPSL	
	LiLuF$_4$	σ/π	$^5D_4 \rightarrow ^7F_5$	544/542	58	35	613	cw	OPSL	
	LiLuF$_4$	π	$^5D_4 \rightarrow ^7F_4$	587	14	107	82	cw	OPSL	
	KY$_3$F$_{10}$		$^5D_4 \rightarrow ^7F_5$	545	34	25	793	cw	OPSL	
	KY$_3$F$_{10}$		$^5D_4 \rightarrow ^7F_4$	584	5	38	18	cw	OPSL	
	β-BaLu$_2$F$_8$	-	$^5D_4 \rightarrow ^7F_5$	546	46	18	270	cw	OPSL	
	LaF$_3$	-	$^5D_4 \rightarrow ^7F_5$	543	33	41	64	quasi-cw	OPSL	
Dy^{3+}	Y$_3$Al$_5$O$_{12}$		$^4F_{9/2} \rightarrow ^6H_{13/2}$	583	12	725	150	pulse	LD	[112]
	ZnWO$_4$	-	$^4F_{9/2} \rightarrow ^6H_{13/2}$	575	13	550	110	cw	LD	[113]
	LiLuF$_4$[a]	σ	$^4F_{9/2} \rightarrow ^6H_{13/2}$	574	13	320	55	cw	LD	[114]
Ho^{3+}	LaF$_3$	π	$^5F_4, ^5S_2 \rightarrow ^6H_{13/2}$	549	0.4	2000	8	quasi-cw	OPSL	[66]
Er^{3+}	LiLuF$_4$	π	$^4F_{9/2} \rightarrow ^6H_{13/2}$	552	24	188	58	quasi-cw	OPSL	[68]

[a] co-doped with Tb^{3+}.

1.4   Criteria of host materials for direct visible laser application

The performance of a gain medium greatly depends on the physical properties of the matrix. The host material defines the coordination environment of the active ion, and as a part of the resonator, its macroscopic property impacts the optical actions within the cavity. Criteria of a suitable laser host material depends on its actual application. In general, the crystal structure, site symmetry, and ligand field which directly modify the spectroscopic properties of the active ion play the main role. Nevertheless, its macroscopic optical, thermal, mechanical, and chemical properties that can give rise to practical problems have to be taken into consideration as well.

Fluoride-based single crystals are excellent gain media for visible laser operation. As a matter of fact, most of the direct visible lasers discussed above are based on fluorides. This is mainly due to their wide optical transparency range, low phonon energy, small crystal field strength, and large band gap energy in contrast with the oxides. However, their thermal and mechanical properties, chemical stability, as well as facility for crystal growth are eclipsed by oxide single crystals. To be more specific, they have relative large thermal expansion, leading to a small thermal shock resistance. They are softer than oxides and thus vulnerable to fracture and mechanical damage. For example, $LiYF_4$ has a Moh's hardness of 4-5, which is at the same level as glass. The hygroscopicity reduces the lifetime of usage and further protection might be needed. The crystal growth requires complicated protection atmosphere such as CF_4 and it is quite difficult to obtain high quality single crystals. These deficiencies impede the large-scale production and industrial usage of fluoride crystals [115].

1.4.1 Host materials for Tb³⁺-activated visible lasers

Tb^{3+}-doped fluorides have made great success as laser gain medium, whereas there is no report on a Tb^{3+}-laser based on oxides up till now. To achieve this goal, selection of a suitable oxide host material must be paid utmost attention to. A critical factor that fetters laser performance of Tb^{3+} in solids is the possibility of ESA into the $4f^7 5d^1$ configuration while lasing. The stability of the half-filled $4f$ shell results in energetically low lying $4f^7 5d^1$ levels (see also Figure 1.3). As is illustrated in figure 1.11, the lowest $4f^7 5d^1$ energy levels consist of a low-spin state with ^{7}D configuration and a high-spin state with ^{9}D configuration [116]. Although the latter is located at a lower position, the ESA transition from energy level of $^5D_4$ to ^{9}D is doubly spin-forbidden ($\Delta S = 2$) and is expected to have very small transition rate. Therefore, inter-configurational ESA into the ^{9}D states is considered to be negligible. Such ESA loss, which can be recognized by a non-linear gain behavior, has been detected in Tb^{3+}-doped fluoride fibers [117].

Nonetheless, stemming from the well shielded $4f$ electrons by the external $5s$ and $5p$ orbitals, the $4f^8$ ground state of Tb^{3+} is not significantly affected by the coordination environment, contrary to $4f^7 5d^1$ states. This means the energetic position of the $4f^7 5d^1$ states with respect to the $4f^8$ states is strongly matrix-dependent. Selecting a suitable host material with a small crystal field strength can

enlarge this energy gap and circumvent the ESA process. The energetic position of the lowest ^{7}D state can be estimated by the crystal-field depression of the host material [87]:
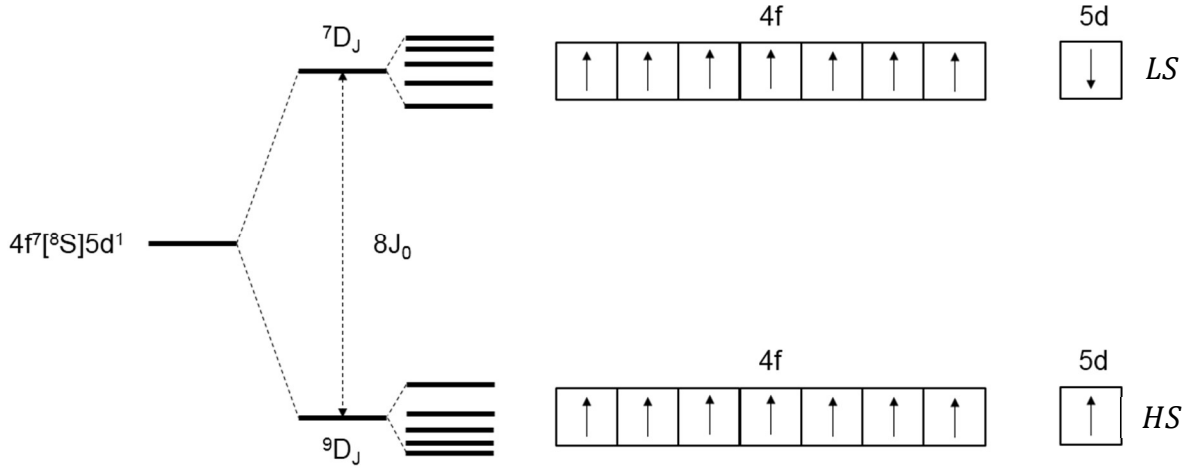
Figure 1.11   The high-spin (^{9}D$_J$) and low-spin (^{7}D$_J$) states of the $4f^7 5d^1$ configuration of Tb^{3+}.

$$E(4f^7 5d^1, LS) = 62540 \ cm^{-1} - D(A) \qquad (1.22)$$

Assume that the wavelength of the pump is 486 nm ($\sim$20600 cm^{-1}). To avoid any efficient ESA, the depression value of the matrix should be less than 21000 cm^{-1} so that $E(4f^7 5d^1, LS)$ is more than the pump photon energy plus the laser photon energy.

Charge transfer from the $4f$ states to the conduction band, though it is usually situated in an energetically higher position than the $5d$ states, should also be considered. The location of the $4f$ states with respect to the conduction band can be reflected by the energy of the inter-valence charge transfer (IVCT) band, which stems from the photo-induced electron transfer process from a lanthanide ion to another cation constituting the conduction-band bottom [118–120]:

$$Ln^{3+} + M^{n+} \rightarrow Ln^{4+} + M^{(n-1)+} \qquad (1.23)$$

Generally ,this charge transfer process takes place between Ln^{3+} that is prone to lose an electron such as Tb^{3+}, and M^{n+} that tends to accept an electron, e.g. transition metal ions in high oxidation states (Ti^{4+}, V^{5+}, W^{6+}, etc.). Quenching phenomenon of the green emission deriving from Tb^{3+} have been observed in CaTiO$_3$, YVO$_4$, and YNbO$_4$ while is absent in YPO$_4$ [121]. Therefore, compounds containing cations with relatively large electronegativity should be ruled out for hosting Tb^{3+}. One should notice the difference between IVCT and the charge transfer process from the valence band to Ln^{3+} (also known as O^{2-}→Ln^{3+} charge transfer) [122]. The latter does not have a direct impact on the dynamics of the excited state of lanthanide ion. In any cases, the band gap energy of the matrix should be as large as possible.

The last but not the least, host materials that can provide high doping level of Tb^{3+} are favorable. As is shown in the energy diagram of Tb^{3+} (see also Figure 1.9), the ^{5}D$_4$ manifold is greatly separated with

the next lower energy state (> 14000 cm^{-1}). This results in negligible non-radiative phonon relaxation from this level. The simple energy level scheme does not support any cross-relaxation channels from the $^5D_4$ energy level as well. Thus, the weak transition cross-sections can be partially compensated by using highly concentrated gain materials, without significantly decreasing the fluorescence lifetime. For example, the TbF$_3$ crystal with a Tb^{3+} concentration as large as 2.2×10^{22} cm^{-3} provides a satisfying absorption coefficient at the pump wavelength of more than 5 cm^{-1}, in contrast to its poor absorption cross-section of 1×10^{-22} cm^{-3}. What's more, it still keeps a fluorescence lifetime around 2 ms [98].

Based on these considerations, Table 1.3 summarizes some oxide compounds that satisfy the requirements mentioned above. It should be noted that, since the upper laser level is unlikely to suffer multi-phonon relaxation, the phonon energy of the matrix does not need to be evaluated.

Besides the structure-dependent properties, the possibility to grow a single crystal with sufficient size and good optical quality should also be regarded. Among these compounds, TbB$_3$O$_9$, LiTb(PO$_3$)$_4$, TbPO$_4$, K$_3$Tb(PO$_4$)$_2$, and TbAl$_3$(BO$_3$)$_4$ do not melt congruently and thus flux growth methods have to be employed. It is difficult to obtain a large size crystal by this technique, whereas to compensate the weak absorption at the pump wavelength, a long crystal is necessary to increase the absorption efficiency. Moreover, the growth process is complicated and time-consuming. Based on these considerations, compounds of Ba$_3$Tb(PO$_4$)$_3$, Sr$_3$Tb(BO$_3$)$_3$, Li$_6$Tb(BO$_3$)$_3$, and TbCa$_4$O(BO$_3$)$_3$ were selected for crystal fabrication in this PhD thesis. Collaborating with Dr. D. Rytz from FEE GmbH, Germany, who is expert in the flux growth techniques, crystals of TbAl$_3$(BO$_3$)$_4$ and KTb(WO$_4$)$_2$ are also available for study.

Table 1.3 **Potentially suitable oxide-based materials for Tb^{3+}-lasers.**

Compound	Space group	Concentration of Tb (10^{20} cm^{-3})	$D(A)$ [a]
TbB$_3$O$_6$	$C2/c$	102	12526
TbMgB$_5$O$_{10}$	$P2_1/c$	63	12568
LiTb(PO$_3$)$_4$	$C2/c$	45	13369
TbPO$_4$	$I4_1/amd$	137	16007
TbAlO$_3$	$Pnma$	194	16537
K$_3$Tb(PO$_4$)$_2$	$P2_1/m$	59	16959
Ba$_3$Tb(PO$_4$)$_3$	$I\bar{4}3d$	35	17594
TbAl$_3$(BO$_3$)$_4$	$R32$	55	18259
Sr$_3$Tb(BO$_3$)$_3$	$R\bar{3}$	48	20521
Li$_6$Tb(BO$_3$)$_3$	$P2_1/c$	52	20559
TbCa$_4$O(BO$_3$)$_3$	Cm	44	20659

[a] $D(A)$ values are estimated from the isostructural RE^{3+}-based species [87].

1.4.2 Host materials for Dy^{3+}-activated visible lasers

The low-spin $4f^8 5d^1$ configuration (^{6}H(2)) of Dy^{3+} is located at a high energy position. The energy of the ground-state transition to this level is around 74400 cm^{-1} in free-ion Dy^{3+} (Equation 1.24, [87]) and was measured to be less than 200 nm (50000 cm^{-1}) in Dy^{3+}-doped borates [123,124]. Moreover, since the optical transitions from the potential upper laser level ^{4}F$_{9/2}$ to the $4f^8 5d^1$ states are doubly or even quadruply spin-forbidden, their ESA cross-sections are considered to be small. Assuming that the pump wavelength is 450 nm (22000 cm^{-1}), the maximum crystal-field depression to circumvent ESA should be around 30000 cm^{-1}. As a matter of fact, Dy:YAG, which shows a large crystal-field depression of 26700 cm^{-1}, is the first reported gain material of Dy^{3+}-based visible laser. Host materials with $D(A)$ values lower than YAG should be safe from such ESA processes.

$$E(4f^8 5d^1, LS) = 74400 \ cm^{-1} - D(A) \qquad (1.24)$$

On the other hand, charge transfer into the conduction band is as well less likely than Tb^{3+}. According to the P. Dorenbos' research, in the same host material, the energetic position of the $4f$ ground state with respect to the conduction band of Dy^{3+} is 1.65 eV (13400 cm^{-1}) larger than that of Tb^{3+} (Figure 1.12) [125]. This makes Dy^{3+} less probable to undergo an IVCT process. Therefore, the scope of suitable host material for lasing Dy^{3+} is much larger than Tb^{3+}. Besides the reported laser gain media of Dy:YAG, Dy:ZnWO$_4$, and Dy,Tb:LiLuF$_4$ crystals, optical gain of the yellow emission band is observed in a number of matrices, such as Dy:LiNbO$_3$ crystal and Dy:Ba$_2$TiSi$_2$O$_8$ glass ceramic [126,127]. The phonon energy is a minor factor as well, owing to the large energy gap between the upper and terminal laser levels of Dy^{3+}.
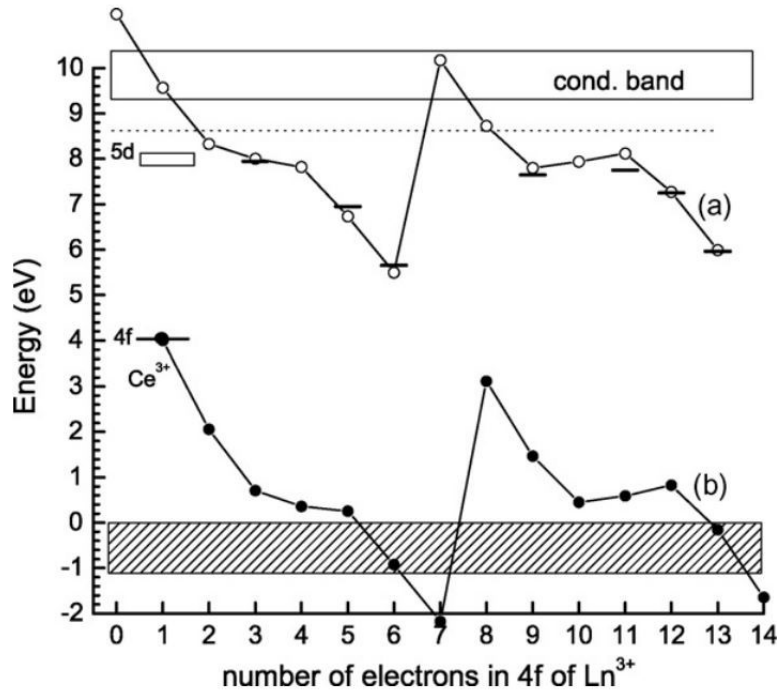

Figure 1.12 The ground-state level location of lanthanide ions (solid dots: Ln^{3+}, hollow dots: Ln^{2+}) in YPO$_4$, after [125].

Another issue is the doping site in the matrix. A cation site with a comparable radius to Dy^{3+} results in smaller stress within the crystal and a segregation coefficient closer to unity, which leads to a lower concentration gradient in the crystal. Concerning this, Y^{3+} ($r = 90.0\,pm$), and Gd^{3+} ($r = 93.8\,pm$) would be suitable for doping Dy^{3+} ($r = 91.2\,pm$) (effective ionic radii (6-coordinate) are used in this thesis, reported in [128]). However, the ^6D_J manifolds of Gd^{3+} have about twice the energy of the upper laser level $^4F_{9/2}$ of Dy^{3+}. Cooperative energy transfer processes might take place during the laser operation. Thus, Y^{3+}-based matrices are more favorable.

The energetic gap around 7000 cm^{-1} between the $^4F_{9/2}$ and $^6F_{1/2}$ manifolds indicates inefficient multi-phonon relaxation from the $^4F_{9/2}$ upper laser level. The complex energy levels below $^4F_{9/2}$, however, give rise to cross-relaxation. Therefore, it is of great importance to balance the simultaneously increasing gain and loss deriving from the rising Dy^{3+}-concentration. In this regard, the doping concentration of Dy^{3+} should be carefully sought after via preliminary experiments. Also, host materials with weak crystal field strengths would be preferred as the splitting of stark levels can be to some extent lessen. This can help to inhibit the detrimental cross-relaxation process which is sensitive to the energy matching of the stark levels. Based on these considerations, we chose $CaYAlO_4$ ($D(A) = 22500$), $YCa_4O(BO_3)_3$ ($D(A) = 20659$), and $Ca_2Al_2SiO_7$ ($D(A) = 19413$) for hosting Dy^{3+}, which meet the aforementioned requirements, and whose crystal growth techniques have been maturely developed in our group.

The selected and available materials discussed in this section for hosting Tb^{3+} or Dy^{3+} ions are briefly summarized in Table 1.4.

Table 1.4   Selected and available oxide-based materials for this PhD thesis.

Active ion	Compound	Abbreviation	Space group	Congruent melting	$D(A)$
Tb^{3+}	$Ba_3Tb(PO_4)_3$	BTP	$I\bar{4}3d$	yes	17594
	$Sr_3Tb(BO_3)_3$	STB	$R\bar{3}$	yes	20559
	$TbAl_3(BO_3)_4$	TAB	$R32$	no	18259
	$Li_6Tb(BO_3)_3$	LTB	$P2_1/c$	yes	20521
	$TbCa_4O(BO_3)_3$	TbCOB	Cm	yes	20659
	$KTb(WO_4)_2$	KTW	$C2/c$	no	16959
Dy^{3+}	$CaYAlO_4$	CYA	$I\bar{4}3d$	yes	22500
	$Ca_2Al_2SiO_7$	CAS	$P\bar{4}2_1m$	yes	19413
	$YCa_4O(BO_3)_3$	YCOB	Cm	yes	20659

1.5   Conclusion of Chapter 1 and objective of this thesis

Visible lasers have very mature applications due to the particular utility of this spectral range. The ongoing demands for developing efficient solid-state visible lasers with more attainable output wavelengths are driven by the sciences and technologies on the cutting edge. Direct visible lasers are capable of circumventing the energy loss during the frequency conversion of the traditional Nd^{3+}- or Yb^{3+}-lasers. They are also able to provide more output wavelengths, as more laser transitions of various lanthanide ions in various host materials can be exploited. Especially after the development of blue emitting semiconductor lasers, viz. LDs and OPSLs, new laser channels have been progressively discovered using them as pump source.

In view of the promising perspective of this subject, and based on the state-of-the-art investigation, this work aims at developing Tb^{3+}- as well as Dy^{3+}-activated oxide single crystals for direct visible laser application. This will mainly be done by characterizing their thermal and optical spectroscopic properties. As a subject of material science, the synthesis procedures will be discussed in detail and optimized to obtain eligible single crystalline materials.

References of Chapter 1

[1]   P. M.B. Walker, Chambers Science & Technology Dictionary, (1988) 1940: 914.

[2]   A. Partovi, D. Peale, M. Wuttig, C.A. Murray, G. Zydzik, L. Hopkins, K. Baldwin, W.S. Hobson, J. Wynn, J. Lopata, L. Dhar, R. Chichester, J.H.-J. Yeh, High-power laser light source for near-field optics and its application to high-density optical data storage, Appl. Phys. Lett. 75 (1999) 1515–1517. doi:10.1063/1.124740.

[3]   C.E. Webb, J.D.C. Jones, eds., Handbook of laser technology and applications, Philadelphia : Institute of Physics, Bristol, 2004.

[4]   W. DEMTRODER, LASER SPECTROSCOPY: basic concepts and instrumentation., SPRINGER, CHAM, 2003.

[5]   H. Jelínková, ed., Lasers for medical applications: diagnostics, therapy, and surgery, WP/Woodhead Publishing, Oxford ; Philadelphia, 2013.

[6]   Y.-C. Chi, D.-H. Hsieh, C.-T. Tsai, H.-Y. Chen, H.-C. Kuo, G.-R. Lin, 450-nm GaN laser diode enables high-speed visible light communication with 9-Gbps QAM-OFDM, Opt. Express. 23 (2015) 13051. doi:10.1364/OE.23.013051.

[7]   D. Tsonev, S. Videv, H. Haas, Towards a 100 Gb/s visible light wireless access network, Opt. Express. 23 (2015) 1627. doi:10.1364/OE.23.001627.

[8]   R.C. Hilldale, D. Raff, Assessing the ability of airborne LiDAR to map river bathymetry, Earth Surf. Process. Landf. 33 (2008) 773–783. doi:10.1002/esp.1575.

[9]   Brian E. Kruschwitz, Andrew F. Kurtz, Laser projection display system, US6594090B2, 2001. https://patents.google.com/patent/US6594090B2/en.

[10]   A. Adan, G. Alizada, Y. Kiraz, Y. Baran, A. Nalbant, Flow cytometry: basic principles and applications, Crit. Rev. Biotechnol. 37 (2017) 163–176. doi:10.3109/07388551.2015.1128876.

[11]   M. Arrigoni, G. Nigel, M. Darryl, P. Volker, S. Matthias, Lasers for Microscopy: Major Trends, Photonics Spectra. (2017).

[12]   Kebes, Absorption spectrum of liquid water, (n.d.). https://commons.wikimedia.org/wiki/File:Absorption_spectrum_of_liquid_water.png.

[13]   T.H. Maiman, Stimulated Optical Radiation in Ruby, Nature. 187 (1960) 493–494. doi:10.1038/187493a0.

[14]   G.H. Dieke, H.M. Crosswhite, The Spectra of the Doubly and Triply Ionized Rare Earths, Appl. Opt. 2 (1963) 675. doi:10.1364/AO.2.000675.

[15]   P. Dorenbos, The 5d level positions of the trivalent lanthanides in inorganic compounds, J. Lumin. 91 (2000) 155–176. doi:10.1016/S0022-2313(00)00229-5.

[16]   P. Dorenbos, The transitions of the trivalent lanthanides in halogenides and chalcogenides, J. Lumin. 91 (2000) 91–106. doi:10.1016/S0022-2313(00)00197-6.

[17]   B.R. Judd, Optical Absorption Intensities of Rare-Earth Ions, Phys. Rev. 127 (1962) 750–761. doi:10.1103/PhysRev.127.750.

[18]   G.S. Ofelt, Intensities of Crystal Spectra of Rare-Earth Ions, J. Chem. Phys. 37 (1962) 511–520. doi:10.1063/1.1701366.

[19]   M. Born, E. Wolf, Principles of optics: electromagnetic theory of propagation, interference and diffraction of light, Cambridge University Press, Cambridge; New York, 1999. http://dx.doi.org/10.1017/CBO9781139644181 (accessed September 3, 2018).

[20]   B.M. Walsh, Judd-Ofelt theory: principles and practices, in: B. Di Bartolo, O. Forte (Eds.), Adv. Spectrosc. Lasers Sens., Springer Netherlands, Dordrecht, 2006: pp. 403–433. doi:10.1007/1-4020-4789-4_21.

[21]   M. Tanaka, G. Nishimura, T. Kushida, Contribution of J mixing to the $^5D_0 - {^7}F_0$ transition of Eu^{3+} ions in several host matrices, Phys. Rev. B. 49 (1994) 16917–16925. doi:10.1103/PhysRevB.49.16917.

[22]   M. Burresi, D. van Oosten, T. Kampfrath, H. Schoenmaker, R. Heideman, A. Leinse, L. Kuipers, Probing the Magnetic Field of Light at Optical Frequencies, Science. 326 (2009) 550–553. doi:10.1126/science.1177096.

[23]   M. Kasperczyk, S. Person, D. Ananias, L.D. Carlos, L. Novotny, Excitation of Magnetic Dipole Transitions at Optical Frequencies, Phys. Rev. Lett. 114 (2015). doi:10.1103/PhysRevLett.114.163903.

[24]   T.H. Taminiau, S. Karaveli, N.F. van Hulst, R. Zia, Quantifying the magnetic nature of light emission, Nat. Commun. 3 (2012) 979. doi:10.1038/ncomms1984.

[25]   C.M. Dodson, J.A. Kurvits, D. Li, M. Jiang, R. Zia, Magnetic dipole emission of Dy^{3+}:Y_2O_3 and Tm^{3+}:Y_2O_3 at near-infrared wavelengths, Opt. Mater. Express. 4 (2014) 2441. doi:10.1364/OME.4.002441.

[26]   C.M. Dodson, R. Zia, Magnetic dipole and electric quadrupole transitions in the trivalent lanthanide series: Calculated emission rates and oscillator strengths, Phys. Rev. B. 86 (2012). doi:10.1103/PhysRevB.86.125102.

[27]   M.P. Hehlen, M.G. Brik, K.W. Krämer, 50th anniversary of the Judd–Ofelt theory: An experimentalist's view of the formalism and its application, J. Lumin. 136 (2013) 221–239. doi:10.1016/j.jlumin.2012.10.035.

[28]   F.S. Richardson, Selection rules for lanthanide optical activity, Inorg. Chem. 19 (1980) 2806–2812. doi:10.1021/ic50211a063.

[29]   D.L. Dexter, A Theory of Sensitized Luminescence in Solids, J. Chem. Phys. 21 (1953) 836–850. doi:10.1063/1.1699044.

[30]   T. Kushida, Energy Transfer and Cooperative Optical Transitions in Rare-Earth Doped Inorganic Materials. I. Transition Probability Calculation, J. Phys. Soc. Jpn. 34 (1973) 1318–1326. doi:10.1143/JPSJ.34.1318.

[31]   S.A. Egorov, J.L. Skinner, On the theory of multiphonon relaxation rates in solids, J. Chem. Phys. 103 (1995) 1533–1543. doi:10.1063/1.469775.

[32]   P.S. Peijzel, A. Meijerink, R.T. Wegh, M.F. Reid, G.W. Burdick, A complete energy level diagram for all trivalent lanthanide ions, J. Solid State Chem. 178 (2005) 448–453. doi:10.1016/j.jssc.2004.07.046.

[33]   K.R. German, A. Kiel, H. Guggenheim, Stimulated emission from $PrCl_3$, Appl. Phys. Lett. 22 (1973) 87–89. doi:10.1063/1.1654573.

[34]   R. Solomon, L. Mueller, STIMULATED EMISSION AT 5985 Å FROM Pr^{+3} IN LaF_3, Appl. Phys. Lett. 3 (1963) 135–137. doi:10.1063/1.1753902.

[35]   A.A. Kaminskii, S.E. Sarkisov, Stimulated-emission spectroscopy of Pr^{3+} ions in monoclinic BaY_2F_8 fluoride, Phys. Status Solidi A. 97 (1986) K163–K168. doi:10.1002/pssa.2210970253.

[36]   F. Varsanyi, Surface Lasers, Appl. Phys. Lett. 19 (1971) 169–171. doi:10.1063/1.1653870.

[37]   A.A. Kaminskii, Stimulated emission spectroscopy of Ln^{3+} ions in tetragonal $LiLuF_4$ fluoride, Phys. Status Solidi A. 97 (1986) K53–K58. doi:10.1002/pssa.2210970145.

[38]   L. Esterowitz, R. Allen, M. Kruer, F. Bartoli, L.S. Goldberg, H.P. Jenssen, A. Linz, V.O. Nicolai, Blue light emission by a Pr:LiYF$_4$ – laser operated at room temperature, J. Appl. Phys. 48 (1977) 650–652. doi:10.1063/1.323648.

[39]   T. Danger, T. Sandrock, E. Heumann, G. Huber, B. Chai, Pulsed laser action of Pr:GdLiF$_4$ at room temperature, Appl. Phys. B Photophysics Laser Chem. 57 (1993) 239–241. doi:10.1007/BF00334541.

[40]   B. N. Kazakov, M. S. Orlov, M. V. Petrov, A. L. Stolov, and A. M. Tkachuk, Induced emission of Sm^{3+} ions in the visible region of the spectrum, Opt Spectrosc. 47 (1979) 676.

[41]   H. P. Jenssen, Visible (orange) laser emission from Sm doped LiTbF$_4$ in Advanced Solid-State Lasers, OSA Technical Digest, (Optical Society of America, 1995), Washington DC, 1995.

[42]   M.C. Farries, P.R. Morkel, J.E. Townsend, Samarium^{3+} -doped glass laser operating at 651 nm, Electron. Lett. 24 (1988) 709–711. doi:10.1049/el:19880479.

[43]   N.C. Chang, Fluorescence and Stimulated Emission from Trivalent Europium in Yttrium Oxide, J. Appl. Phys. 34 (1963) 3500–3504. doi:10.1063/1.1729247.

[44]   S. I. Andreev, M. R. Bedilov, G. O. Karapetyan, and V. M., The stimulated emission of terbium-activated glass, Sov J Opt Technol. 34 (1967) 819.

[45]   S. Bjorklund, G. Kellermeyer, C.R. Hurt, N. McAvoy, N. Filipescu, LASER ACTION FROM TERBIUM TRIFLUOROACETYLACETONATE IN p -DIOXANE AND ACETONITRILE AT ROOM TEMPERATURE, Appl. Phys. Lett. 10 (1967) 160–162. doi:10.1063/1.1754892.

[46]   H. Jenssen, D. Castleberry, D. Gabbe, A. Linz, Stimulated emission at 5445 Å in Tb^{3+} : YLF, IEEE J. Quantum Electron. 9 (1973) 665–665. doi:10.1109/JQE.1973.1077559.

[47]   M. Malinowski, P. Myziak, R. Piramidowicz, I. Pracka, T. Łukasiewicz, B. Surma, S. Kaczmarek, K. Kopczyński, Z. Mierczyk, Spectroscopic and Laser Properties of LiNbO$_3$:Dy^{3+} Crystals, Acta Phys. Pol. A. 90 (1996) 181–189. doi:10.12693/APhysPolA.90.181.

[48]   A.A. Kaminskii, U. Hömmerich, D. Temple, J.T. Seo, A.A. Pavlyuk, New Laser Potential of Monoclinic KR(WO$_4$)$_2$:Ln^{3+} Tungstates (R = Y and Ln), Phys. Status Solidi A. 174 (1999) R7–R8. doi:10.1002/(SICI)1521-396X(199907)174:1<R7::AID-PSSA99997>3.0.CO;2-P.

[49]   A. Kaminskii, U. Hömmerich, D. Temple, J.T. Seo, K. Ueda, S. Bagayev, A. Pavlyulk, Visible Laser Action of Dy^{3+} Ions in Monoclinic KY(WO$_4$)$_2$ and KGd(WO$_4$)$_2$ Crystals under Xe-Flashlamp Pumping, Jpn. J. Appl. Phys. 39 (2000) L208–L211. doi:10.1143/JJAP.39.L208.

[50]   Yu. K. Voronko, A. A. Kaminskii, V. V. Osiko, and A. M. Prokhorov, Stimulated emission of Ho^{3+} in CaF$_2$ at lambda= 5512 Å, JETP Lett. 1 (1965) 3.

[51]   I. G. Podkolzina, A. M. Tkachuk, V. A. Fedorov, and P. P. Feofilov, Multifrequency generation of stimulated emission of Ho^{3+} ion in LiYF$_4$ crystals, Opt Spectrosc. 40 (1976) 111.

[52]   A. A. Kaminskii, V. M. Garmash, G. E. Ermakov, V. A. Akkerman, A. A. Filimonov, and K. Kurbanov, Luminescence and stimulated radiation of a rhomboidal crystal YAlO$_3$-Ho^{3+}, Inorg Mater. 22 (1986) 1567.

[53]   L.F. Johnson, H.J. Guggenheim, New Laser Lines in the Visible from Er^{3+} Ions in BaY$_2$F$_8$, Appl. Phys. Lett. 20 (1972) 474–477. doi:10.1063/1.1654022.

[54]   R. Brede, T. Danger, E. Heumann, G. Huber, B. Chai, Room-temperature green laser emission of Er:LiYF$_4$, Appl. Phys. Lett. 63 (1993) 729–730. doi:10.1063/1.109942.

[55]   B. M. Antipenko, S. P. Voronin, and T. A. Privalova, New laser channels of the Tm^{3+} ion, Opt Spectrosc. 68 (1990) 164.

[56]   R. M. Macfarlane, R. Wannemacher, T. Hebert, and W. Lenth, IQEC-90 Technical Digest (OSA/IEEE, Anaheim, CA, 1990), n.d.

[57] R.J. Thrash, L.F. Johnson, Upconversion laser emission from Yb^{3+}-sensitized Tm^{3+} in BaY_2F_8, J. Opt. Soc. Am. B. 11 (1994) 881. doi:10.1364/JOSAB.11.000881.

[58] A. Richter, E. Heumann, E. Osiac, G. Huber, W. Seelert, A. Diening, Diode pumping of a continuous-wave Pr^{3+}-doped $LiYF_4$ laser, Opt. Lett. 29 (2004) 2638. doi:10.1364/OL.29.002638.

[59] R. Yongfeng, Z. Shouchao, L. Shuhua, L. Guanghui, L. Wenrun, L. Jingwang, Growth and Spectrum Properties of $Ce:YVO_4$ Single Crystal, J. Rare Earths. 25 (2007) 122–124. doi:10.1016/S1002-0721(07)60538-9.

[60] J.A. Mares, M. Nikl, K. Blazek, Green emission band in Ce^{3+}-doped yttrium aluminium perovskite, Phys. Status Solidi A. 127 (1991) K65–K68. doi:10.1002/pssa.2211270146.

[61] W.J. Miniscalco, J.M. Pellegrino, W.M. Yen, Measurements of excited-state absorption in Ce^{3+}: YAG, J. Appl. Phys. 49 (1978) 6109–6111. doi:10.1063/1.324531.

[62] R.R. Jacobs, W.F. Krupke, M.J. Weber, Measurement of excited-state-absorption loss for Ce^{3+} in $Y_3Al_5O_{12}$ and implications for tunable $5d \rightarrow 4f$ rare-earth lasers, Appl. Phys. Lett. 33 (1978) 410–412. doi:10.1063/1.90395.

[63] K. Jayanthi, S.V. Manorama, S. Chawla, Observation of Nd^{3+} visible line emission in $ZnO:Nd^{3+}$ prepared by a controlled reaction in the solid state, J. Phys. Appl. Phys. 46 (2013) 325101. doi:10.1088/0022-3727/46/32/325101.

[64] R.M. Macfarlane, F. Tong, A.J. Silversmith, W. Lenth, Violet cw neodymium upconversion laser, Appl. Phys. Lett. 52 (1988) 1300–1302. doi:10.1063/1.99681.

[65] P. Koopmann, S. Lamrini, K. Scholle, M. Schäfer, P. Fuhrberg, G. Huber, Holmium-doped Lu_2O_3, Y_2O_3, and Sc_2O_3 for lasers above 21 µm, Opt. Express. 21 (2013) 3926. doi:10.1364/OE.21.003926.

[66] F. Reichert, F. Moglia, P.W. Metz, A. Arcangeli, D.-T. Marzahl, S. Veronesi, D. Parisi, M. Fechner, M. Tonelli, G. Huber, Prospects of Holmium-doped fluorides as gain media for visible solid state lasers, Opt. Mater. Express. 5 (2015) 88. doi:10.1364/OME.5.000088.

[67] C. Kränkel, P. W. Metz, F. Reichert, F. Moglia, D. T. Marzahl, and G. Huber, ASSL, Shanghai, 2014.

[68] F. Moglia, S. Müller, F. Reichert, P.W. Metz, T. Calmano, C. Kränkel, E. Heumann, G. Huber, Efficient upconversion-pumped continuous wave $Er^{3+}:LiLuF_4$ lasers, Opt. Mater. 42 (2015) 167–173. doi:10.1016/j.optmat.2015.01.004.

[69] R. Paschotta, N. Moore, W.A. Clarkson, A.C. Tropper, D.C. Hanna, G. Maze, 230 mW of blue light from a thulium-doped upconversion fiber laser, IEEE J. Sel. Top. Quantum Electron. 3 (1997) 1100–1102. doi:10.1109/2944.649548.

[70] E. Cavalli, C. Meschini, A. Toncelli, M. Tonelli, M. Bettinelli, Optical spectroscopy of Tm^{3+} doped in $KLa(MoO_4)_2$ crystals, J. Phys. Chem. Solids. 58 (1997) 587–595. doi:10.1016/S0022-3697(96)00170-9.

[71] M. Song, L. Wang, N. Zhang, X. Tai, G. Wang, Crystal Growth and Spectroscopic Investigations of $Tm^{3+}:Li_3Ba_2Gd_3(MoO_4)_8$ Crystal, Materials. 7 (2014) 496–507. doi:10.3390/ma7010496.

[72] W. Guo, Y. Chen, Y. Lin, X. Gong, Z. Luo, Y. Huang, Spectroscopic analysis and laser performance of $Tm^{3+}: NaGd(MoO_4)_2$ crystal, J. Phys. Appl. Phys. 41 (2008) 115409. doi:10.1088/0022-3727/41/11/115409.

[73] C. Kränkel, D.-T. Marzahl, F. Moglia, G. Huber, P.W. Metz, Out of the blue: semiconductor laser pumped visible rare-earth doped lasers: Out of the blue: semiconductor laser pumped visible rare-earth, Laser Photonics Rev. 10 (2016) 548–568. doi:10.1002/lpor.201500290.

[74] F. Cornacchia, A. Di Lieto, M. Tonelli, A. Richter, E. Heumann, G. Huber, Efficient visible laser emission of GaN laser diode pumped Pr-doped fluoride scheelite crystals, Opt. Express. 16 (2008) 15932. doi:10.1364/OE.16.015932.

[75] B. Xu, F. Starecki, D. Pabœuf, P. Camy, J.L. Doualan, Z.P. Cai, A. Braud, R. Moncorgé, P. Goldner, F. Bretenaker, Red and orange laser operation of Pr:KYF$_4$ pumped by a Nd:YAG/LBO laser at 469.1 nm and a InGaN laser diode at 444 nm, Opt. Express. 21 (2013) 5567. doi:10.1364/OE.21.005567.

[76] Philip Werner Metz, Visible lasers in rare earth-doped fluoride crystals, Universit¨at Hamburg, 2014.

[77] B. Xu, P. Camy, J.-L. Doualan, Z. Cai, R. Moncorgé, Visible laser operation of Pr^{3+}-doped fluoride crystals pumped by a 469 nm blue laser, Opt. Express. 19 (2011) 1191. doi:10.1364/OE.19.001191.

[78] A. Sottile, D. Parisi, M. Tonelli, Multiple polarization orange and red laser emissions with Pr:BaY$_2$F$_8$, Opt. Express. 22 (2014) 13784. doi:10.1364/OE.22.013784.

[79] H. Yu, D. Jiang, F. Tang, L. Su, S. Luo, X. Yan, B. Xu, Z. Cai, J. Wang, Q. Ju, J. Xu, Enhanced photoluminescence and initial red laser operation in Pr:CaF$_2$ crystal via co-doping Gd^{3+} ions, Mater. Lett. 206 (2017) 140–142. doi:10.1016/j.matlet.2017.07.019.

[80] P.W. Metz, F. Reichert, F. Moglia, S. Müller, D.-T. Marzahl, C. Kränkel, G. Huber, High-power red, orange, and green Pr^{3+}:LiYF$_4$ lasers, Opt. Lett. 39 (2014) 3193. doi:10.1364/OL.39.003193.

[81] M. Fibrich, H. Jelínková, J. Šulc, K. Nejezchleb, V. Škoda, Visible cw laser emission of GaN-diode pumped Pr:YAlO$_3$ crystal, Appl. Phys. B. 97 (2009) 363–367. doi:10.1007/s00340-009-3679-5.

[82] F. Reichert, D.-T. Marzahl, G. Huber, Spectroscopic characterization and laser performance of Pr,Mg:CaAl$_{12}$O$_{19}$, J. Opt. Soc. Am. B. 31 (2014) 349. doi:10.1364/JOSAB.31.000349.

[83] D.-T. Marzahl, F. Reichert, P.W. Metz, M. Fechner, N.-O. Hansen, G. Huber, Efficient laser operation of diode-pumped Pr^{3+},Mg^{2+}:SrAl$_{12}$O$_{19}$, Appl. Phys. B. 116 (2014) 109–113. doi:10.1007/s00340-013-5655-3.

[84] Marzahl, D.T., Reichert, F., Fechner, M., Hansen, N.O., Petermann, K. and Huber, G., Laser Operation and Spectroscopy of P^{r3+}: LaMgAl$_{11}$O$_{19}$, in: Stockholm, Sweden, 2012: p. paper ThP.3.

[85] S. Sattayaporn, P. Loiseau, G. Aka, D.-T. Marzahl, C. Kränkel, Crystal growth, spectroscopy and laser performances of Pr^{3+}:Sr$_{0.7}$La$_{0.3}$Mg$_{0.3}$Al$_{11.7}$O$_{19}$ (Pr:ASL), Opt. Express. 26 (2018) 1278. doi:10.1364/OE.26.001278.

[86] C. De Mello Donegá, A. Meijerink, G. Blasse, Non-radiative relaxation processes of the Pr^{3+} ion in solids, J. Phys. Chem. Solids. 56 (1995) 673–685. doi:10.1016/0022-3697(94)00183-9.

[87] P. Dorenbos, The 5d level positions of the trivalent lanthanides in inorganic compounds, J. Lumin. 91 (2000) 155–176. doi:10.1016/S0022-2313(00)00229-5.

[88] S. Nicolas, M. Laroche, S. Girard, R. Moncorgé, Y. Guyot, M.F. Joubert, E. Descroix, A.G. Petrosyan, 4f^2 to 4f5d excited state absorption in Pr^{3+}:YAlO$_3$, J. Phys. Condens. Matter. 11 (1999) 7937–7946. doi:10.1088/0953-8984/11/40/317.

[89] C. Gheorghe, L. Gheorghe, A. Achim, S. Hau, R.D. Avram, G. Stanciu, Optical properties of Sm^{3+} doped strontium hexa-aluminate single crystals, J. Alloys Compd. 622 (2015) 296–302. doi:10.1016/j.jallcom.2014.10.033.

[90] D.-T. Marzahl, P.W. Metz, C. Kränkel, G. Huber, Spectroscopy and laser operation of Sm^{3+}-doped lithium lutetium tetrafluoride (LiLuF$_4$) and strontium hexaaluminate (SrAl$_{12}$O$_{19}$), Opt. Express. 23 (2015) 21118. doi:10.1364/OE.23.021118.

[91] P.A. Loiko, E.V. Vilejshikova, X. Mateos, J.M. Serres, E.B. Dunina, A.A. Kornienko, K.V. Yumashev, M. Aguiló, F. Díaz, Europium doping in monoclinic KYb(WO$_4$)$_2$ crystal, J. Lumin. 183 (2017) 217–225. doi:10.1016/j.jlumin.2016.11.046.

[92] T. Koubaa, M. Dammak, M.C. Pujol, M. Aguiló, F. Díaz, Optical spectroscopy of Eu^{3+} ions doped in KLu(WO$_4$)$_2$ single crystals, J. Lumin. 168 (2015) 7–13. doi:10.1016/j.jlumin.2015.07.015.

[93]   P.A. Loiko, V.I. Dashkevich, S.N. Bagaev, V.A. Orlovich, A.S. Yasukevich, K.V. Yumashev, N.V. Kuleshov, E.B. Dunina, A.A. Kornienko, S.M. Vatnik, A.A. Pavlyuk, Spectroscopic and photoluminescence characterization of Eu^{3+}-doped monoclinic $KY(WO_4)_2$ crystal, J. Lumin. 153 (2014) 221–226. doi:10.1016/j.jlumin.2014.03.037.

[94]   P.A. Loiko, E.V. Vilejshikova, X. Mateos, J.M. Serres, V.I. Dashkevich, V.A. Orlovich, A.S. Yasukevich, N.V. Kuleshov, K.V. Yumashev, S.V. Grigoriev, S.M. Vatnik, S.N. Bagaev, A.A. Pavlyuk, Spectroscopy of tetragonal $Eu:NaGd(WO_4)_2$ crystal, Opt. Mater. 57 (2016) 1–7. doi:10.1016/j.optmat.2016.04.003.

[95]   V.I. Dashkevich, S.N. Bagayev, V.A. Orlovich, A.A. Bui, P.A. Loiko, K.V. Yumashev, A.S. Yasukevich, N.V. Kuleshov, S.M. Vatnik, A.A. Pavlyuk, Red $Eu,Yb:KY(WO_4)_2$ laser at ~702 nm, Laser Phys. Lett. 12 (2015) 085001. doi:10.1088/1612-2011/12/8/085001.

[96]   P.A. Loiko, V.I. Dashkevich, S.N. Bagaev, V.A. Orlovich, A.S. Yasukevich, K.V. Yumashev, N.V. Kuleshov, E.B. Dunina, A.A. Kornienko, S.M. Vatnik, A.A. Pavlyuk, Spectroscopic characterization and pulsed laser operation of $Eu^{3+}:KGd(WO_4)_2$ crystal, Laser Phys. 23 (2013) 105811. doi:10.1088/1054-660X/23/10/105811.

[97]   465nm Blue Diode Laser. http://www.cnilaser.com/blue_laser465.htm.

[98]   P.W. Metz, D.-T. Marzahl, A. Majid, C. Kränkel, G. Huber, Efficient continuous wave laser operation of Tb^{3+}-doped fluoride crystals in the green and yellow spectral regions: Efficient continuous wave laser operation…, Laser Photonics Rev. 10 (2016) 335–344. doi:10.1002/lpor.201500274.

[99]   Y.Q. Zheng, H.Y. Zhu, L.X. Huang, H.B. Chen, Y.M. Duan, R.B. Su, C.H. Huang, Y. Wei, J. Zhuang, G. Zhang, Efficient 532 nm laser using high gray-tracking resistance KTP crystal, Laser Phys. 20 (2010) 756–760. doi:10.1134/S1054660X10070406.

[100] P.W. Metz, D.-T. Marzahl, G. Huber, C. Kränkel, Performance and wavelength tuning of green emitting terbium lasers, Opt. Express. 25 (2017) 5716. doi:10.1364/OE.25.005716.

[101] Single-Mode LD, SkyBlue. http://www.nichia.co.jp/en/product/laser.html.

[102] M.L. Rico, J.L. Valdés, J. Martínez-Pastor, J. Capmany, Continuous-wave dual-wavelength operation at 1062 and 1338 nm in $Nd^{3+}:YAl_3(BO_3)_4$ and observation of yellow laser light generation at 592 nm by their self-sum-frequency-mixing, Opt. Commun. 282 (2009) 1619–1621. doi:10.1016/j.optcom.2008.12.065.

[103] Y.F. Lü, W.B. Cheng, Z. Xiong, J. Lu, L.J. Xu, G.C. Sun, Z.M. Zhao, Efficient CW laser at 559 nm by intracavity sum-frequency mixing in a self-Raman $Nd:YVO_4$ laser under direct 880 nm diode laser pumping, Laser Phys. Lett. 7 (2010) 787–789. doi:10.1002/lapl.201010064.

[104] W. Zhao, W.-W. Zhou, B. Wei, Y. Yu, G.-F. Wang, J.-M. Du, H.-J. Yu, Z.-C. Lv, Y.-H. Chen, Spectroscopic assessment of $Dy^{3+}:LiLa(MoO_4)_2$ crystal as an active medium for all-solid-state direct yellow-emitting lasers, J. Alloys Compd. 538 (2012) 136–143. doi:10.1016/j.jallcom.2012.05.109.

[105] W.-W. Zhou, B. Wei, W. Zhao, G.-F. Wang, X. Bao, Y.-H. Chen, F.-W. Wang, J.-M. Du, H.-J. Yu, Intense yellow emission in Dy3+-doped LiGd(MoO4)2 crystal for visible lasers, Opt. Mater. 34 (2011) 56–60. doi:10.1016/j.optmat.2011.07.006.

[106] W. Zhao, W. Zhou, M. Song, G. Wang, J. Du, H. Yu, J. Chen, Spectroscopic investigation of Dy^{3+}-doped $Li_2Gd_4(MoO_4)_7$ crystal for potential application in solid-state yellow laser, J. Alloys Compd. 509 (2011) 3937–3942. doi:10.1016/j.jallcom.2010.12.176.

[107] K. Ning, X. He, L. Zhang, Y. Liu, J. Yin, P. Zhang, G. Chen, X. Wang, Z. Chen, C. Shi, J. Hong, Y. Hang, Spectroscopic characteristics of $GdVO_4:Dy^{3+}$ crystal, Opt. Mater. 37 (2014) 745–749. doi:10.1016/j.optmat.2014.08.022.

[108] B. Liu, J. Shi, Q. Wang, H. Tang, J. Liu, H. Zhao, D. Li, J. Liu, X. Xu, Z. Wang, J. Xu, Crystal growth and yellow emission of Dy:YAlO$_3$, Opt. Mater. 72 (2017) 208–213. doi:10.1016/j.optmat.2017.06.005.

[109] P. Van Do, V.P. Tuyen, V.X. Quang, N.T. Thanh, V.T.T. Ha, H. Van Tuyen, N.M. Khaidukov, J. Marcazzó, Y.-I. Lee, B.T. Huy, Optical properties and Judd–Ofelt parameters of Dy^{3+} doped K$_2$GdF$_5$ single crystal, Opt. Mater. 35 (2013) 1636–1641. doi:10.1016/j.optmat.2013.04.014.

[110] M.G. Brik, T. Ishii, A.M. Tkachuk, S.E. Ivanova, I.K. Razumova, Calculations of the transitions intensities in the optical spectra of Dy^{3+}:LiYF$_4$, J. Alloys Compd. 374 (2004) 63–68. doi:10.1016/j.jallcom.2003.11.142.

[111] Y. Fujimoto, O. Ishii, M. Yamazaki, Yellow laser oscillation in Dy^{3+}-doped waterproof fluoro-aluminate glass fibre pumped by 398.8 nm GaN laser diodes, Electron. Lett. 46 (2010) 586. doi:10.1049/el.2010.0488.

[112] S.R. Bowman, S. O'Connor, N.J. Condon, Diode pumped yellow dysprosium lasers, Opt. Express. 20 (2012) 12906. doi:10.1364/OE.20.012906.

[113] Z. Xia, F. Yang, L. Qiao, F. Yan, End pumped yellow laser performance of Dy^{3+} :ZnWO$_4$, Opt. Commun. 387 (2017) 357–360. doi:10.1016/j.optcom.2016.12.008.

[114] G. Bolognesi, D. Parisi, D. Calonico, G.A. Costanzo, F. Levi, P.W. Metz, C. Kränkel, G. Huber, M. Tonelli, Yellow laser performance of Dy^{3+} in co-doped Dy,Tb:LiLuF$_4$, Opt. Lett. 39 (2014) 6628. doi:10.1364/OL.39.006628.

[115] LEE LASER, Nd:YLF as an Alternative to Nd:YAG Advantages and Disadvantages, n.d. http://www.leelaser.com/pdf/Nd-YLF%20vs%20Nd-YAG.pdf.

[116] P. Dorenbos, Exchange and crystal field effects on the 4f^{n}5d levels of Tb^{3+}, J. Phys. Condens. Matter. 15 (2003) 6249–6268. doi:10.1088/0953-8984/15/36/313.

[117] T. Yamashita, Y. Ohishi, Amplification and Lasing Characteristics of Tb^{3+}-doped Fluoride Fiber in the 0.54 μm Band, Jpn. J. Appl. Phys. 46 (2007) L991–L993. doi:10.1143/JJAP.46.L991.

[118] P. Boutinaud, E. Cavalli, M. Bettinelli, Emission quenching induced by intervalence charge transfer in Pr^{3+}- or Tb^{3+}-doped YNbO$_4$ and CaNb$_2$O$_6$, J. Phys. Condens. Matter. 19 (2007) 386230. doi:10.1088/0953-8984/19/38/386230.

[119] P. Dorenbos, A.H. Krumpel, E. van der Kolk, P. Boutinaud, M. Bettinelli, E. Cavalli, Lanthanide level location in transition metal complex compounds, Opt. Mater. 32 (2010) 1681–1685. doi:10.1016/j.optmat.2010.02.021.

[120] E. Cavalli, P. Boutinaud, R. Mahiou, M. Bettinelli, P. Dorenbos, Luminescence Dynamics in Tb^{3+}-Doped CaWO$_4$ and CaMoO$_4$ Crystals, Inorg. Chem. 49 (2010) 4916–4921. doi:10.1021/ic902445c.

[121] P. Boutinaud, P. Putaj, R. Mahiou, E. Cavalli, A. Speghini, M. Bettinelli, Quenching of Lanthanide Emission by Intervalence Charge Transfer in Crystals Containing Closed Shell Transition Metal Ions, Spectrosc. Lett. 40 (2007) 209–220. doi:10.1080/00387010701247019.

[122] P. Dorenbos, Systematic behaviour in trivalent lanthanide charge transfer energies, J. Phys. Condens. Matter. 15 (2003) 8417–8434. doi:10.1088/0953-8984/15/49/018.

[123] G. Dominiak-Dzik, W. Ryba-Romanowski, L. Kovács, E. Beregi, Effect of temperature on luminescence and VUV to visible conversion in the YAl$_3$(BO$_3$)$_4$:Dy^{3+} (YAB:Dy) crystal, Radiat. Meas. 38 (2004) 557–561. doi:10.1016/j.radmeas.2004.03.015.

[124] H.C. Yang, C.Y. Li, H. He, Y. Tao, J.H. Xu, Q. Su, VUV–UV excited luminescent properties of LnCa$_4$O(BO$_3$)$_3$:RE^{3+} (Ln=Y, La, Gd; Re=Eu, Tb, Dy, Ce), J. Lumin. 118 (2006) 61–69. doi:10.1016/j.jlumin.2005.06.007.

[125] P. Dorenbos, Lanthanide charge transfer energies and related luminescence, charge carrier trapping, and redox phenomena, J. Alloys Compd. 488 (2009) 568–573. doi:10.1016/j.jallcom.2008.09.059.

[126] P. Haro-González, L.L. Martín, I.R. Martín, G. Grazyna Dominiak-Dzik, W. Ryba-Romanowski, Pump and probe measurements of optical amplification at 584 nm in dysprosium doped lithium niobate crystal, Opt. Mater. 33 (2010) 196–199. doi:10.1016/j.optmat.2010.07.017.

[127] L.L. Martin, P. Haro-González, I.R. Martín, Optical properties of transparent Dy^{3+} doped $Ba_2TiSi_2O_8$ glass ceramic, Opt. Mater. 33 (2011) 738–741. doi:10.1016/j.optmat.2010.11.027.

[128] R.D. Shannon, Revised effective ionic radii and systematic studies of interatomic distances in halides and chalcogenides, Acta Crystallogr. Sect. A. 32 (1976) 751–767. doi:10.1107/S0567739476001551.

CHAPTER 2   STRUCTURE, SYNTHESIS, AND THERMAL PROPERTIES OF SINGLE CRYSTALS

This first section of this chapter describes the crystal structure and synthesis procedure of all the selected materials. Each material occupies one subsection and each subsection comprises discussion about: (1) crystal structure and coordination environment of the active ions; (2) preparation methods of the polycrystalline starting materials, which impacts the quality of the single crystals to be grown; (3) single crystal growth process; (4) optical quality of the as-grown crystals with the assistance of microscopes. Problems during the crystal fabrication are analyzed, followed by further optimization of the growth conditions. The second section deals with the color centers observed in the Tb^{3+}-based crystals grown in air. The origin of the color centers is analyzed by electron paramagnetic resonance spectroscopy. Characterization of the thermal properties, including the thermal conductivity and thermal expansion coefficients along the crystallographic axes, is presented in the third section.

2.1 Structure and crystal growth

The structure-property relationship is one of the most important issues of material science. An aforehand investigation into the structure of the single crystal material on atomic level can not only provide information related to the fabrication procedure, but also predict its physical properties. Tightly related to the spectroscopic properties, the coordination environments of Tb^{3+} or Dy^{3+} ions in the crystals will be discussed in detail.

At a practical level, the laser performance of a single crystalline material is impacted by its optical quality. Since light oscillates through the gain medium during the laser operation, any scattering centers or color centers in its path would be devastating. The good optical quality is also a prerequisite for an accurate spectroscopic study of a single crystal.

The crystal quality is directly related to the purity of the starting material and the configuration for the growth. In this work, we used polycrystalline materials with the same composition as the designated single crystals as starting material. The polycrystals were prepared by solid-state reactions at high temperature. The incompletely reacted raw materials or parasitic phases formed during the solid-state reactions might form inclusions in the crystal and modify its optical property. The preparation methods and X-ray diffraction analysis of the polycrystalline products will be presented in this section.

The crystal growth process is often influenced by the physical properties of the material itself, such as the congruent-melting behavior, viscosity and volatility of the melt, and thermal properties of the crystal. For example, a high viscosity of the melt is prone to form inclusions in the crystal and a crystal with a large anisotropy of the thermal expansion tends to crack during the growth. To circumvent these inconveniences, the conditions for the single crystal fabrication, including the atmosphere, setup of the furnace, orientation of the seed, parameters for the growth program have to be adapted.

Compounds of $Ba_3Tb(PO_4)_3$ (BTP), $Sr_3Tb(BO_3)_3$ (STB), $Li_6Tb(BO_3)_3$ (LTB), $TbCa_4O(BO_3)_3$ (TbCOB), Dy:$CaYAlO_4$ (CYA), Dy:$Ca_2Al_2SiO_7$ (CAS), and Dy:$YCa_4O(BO_3)_3$ (YCOB) exhibit a congruent-melting behavior and are thus suitable to be grown via the Czochralski technique. The Czochralski growth is a practical and facile approach to obtain high-quality single crystalline material. To be more specific, the crystallization takes place on the interface of the melt and the atmosphere without contacting the crucible, which remarkably reduces the stress on the crystal and prevents parasitic nucleation on the crucible wall. Real-time monitoring of the growth process is possible. This makes the growth process controllable. Moreover, the duration of fabrication is relatively short. These advantages have made it the most widely used technique for high-quality bulk single crystal fabrication.

Owing to the similarity of the synthesis processes of these compounds, general experimental procedures for preparing the polycrystalline raw materials and the Czochralski crystal growth are given in Appendix B. The atomic coordinates of all the studied materials are also presented in Appendix B. Syntheses of $TbAl_3(BO_3)_4$ (TAB), $KTb(WO_4)_2$ (KTW), and Dy:CAS were not performed in this PhD study and will not be discussed in detail.

2.1.1 Ba$_3$Tb(PO$_4$)$_3$ (BTP)

Phosphates having a general chemical formula M$^{II}_3$M^{III}(PO$_4$)$_3$ (M^{II} = Ba^{2+}, Sr^{2+}, Ca^{2+}, Pb^{2+}, etc., and M^{II} = Ln^{3+}, Bi^{3+}, etc.) belong to the eulytite (Bi$_4$(SiO$_4$)$_3$) family. They crystalize in the non-centrosymmetric space group of $I\bar{4}3d$. The crystallographic data of BTP based on single crystal X-ray diffraction refinement are listed in Table 2.1.

The eulytites have several interesting features for optical applications. The cubic symmetry leads to an isotropic thermal expansion, which can avoid cracking during the growth as well as the laser operations. The optical isotropy can also facilitate the processing of the single crystal. The absorption edge of its analogue, Sr$_3$Gd(PO$_4$)$_3$, was found to be around 7 eV (177 nm) in the far-UV zone, indicating a large band gap energy [1]. More importantly, the Ba$_3$Ln(PO$_4$)$_3$ eulytite phosphate shows a weak crystal-field depression of 17594 cm^{-1}. This value is comparable to that of KY$_3$F$_{10}$ ($D(A) = 16084$), using which as host material of Tb^{3+}, visible lasers were able to achieve. In light of these features, BTP is a favorable candidate for Tb^{3+}-based gain material.

Table 2.1   Crystallographic data and selective physical properties of BTP [2].

Chemical formula	Ba$_3$Tb(PO$_4$)$_3$
Formula weight	855.82 g·mol^{-1}
Crystal system	Cubic
Space group	$I\bar{4}3d$
Unit cell parameters (Å)	$a = 10.4484$
Unit cell volume (Å^3)	1140.6
Z	4
Theoretical density	4.984 g·cm^{-3}
Melting point	>1950°C
Mohs hardness	5.5 Moh

The crystal structure is schematically shown in Figure 2.1. The structure refinement reveals that barium and terbium atoms occupy the same cationic site with a Wyckoff position of 16c. Their lattice coordinates are slightly separated ($\sim$0.3 Å). This is probably due to the large difference of their ionic radii, which are 135 pm and 92.3 pm for Ba^{2+} and Tb^{3+}, respectively. The eulytite phosphates are known to exhibit rotational disorder of the tetrahedral [PO$_4$] group. Nevertheless, such disorder can vary with the species of metal ions in its general formula M$^{II}_3$M^{III}(PO$_4$)$_3$ [3,4]. In terms of BTP, the oxygen atoms of the [PO$_4$] polyhedron are distributed over two sites O1 and O2 with site occupancies of 0.75 and 0.25, respectively (Figure 2.1 (b)). The P—O1 and P—O2 bonds are identical in length and the O1—P—O2 angle is 40.3°.

The Tb atom is surrounded by six oxygen atoms and has the lowest C_1 symmery. Resulting from the disorder, the two oxygen sites give different bond lengths to the Tb atom (Figure 2.1 (c)). Each oxygen

site generates two sets of equivalent Tb−O bonds (3×2.40 Å, 3×2.74 Å for Tb−O1 and 3×2.64 Å, 3×2.79 Å for Tb−O2). The averaged Tb−O distance is 2.61 Å. This value is relatively large and indicates a small crystal field strength. It is worth pointing out that in some eulytite structure the metal ion is considered to have a 6+3 coordinate number with three longer M−O bonds compared to ordinary values. According to the structure refinement of BTP, the distance between terbium and the next closer oxygen atoms is around 3.2 Å. Therefore, it is reasonable to suppose a 6-coordinate Tb site in this compound.
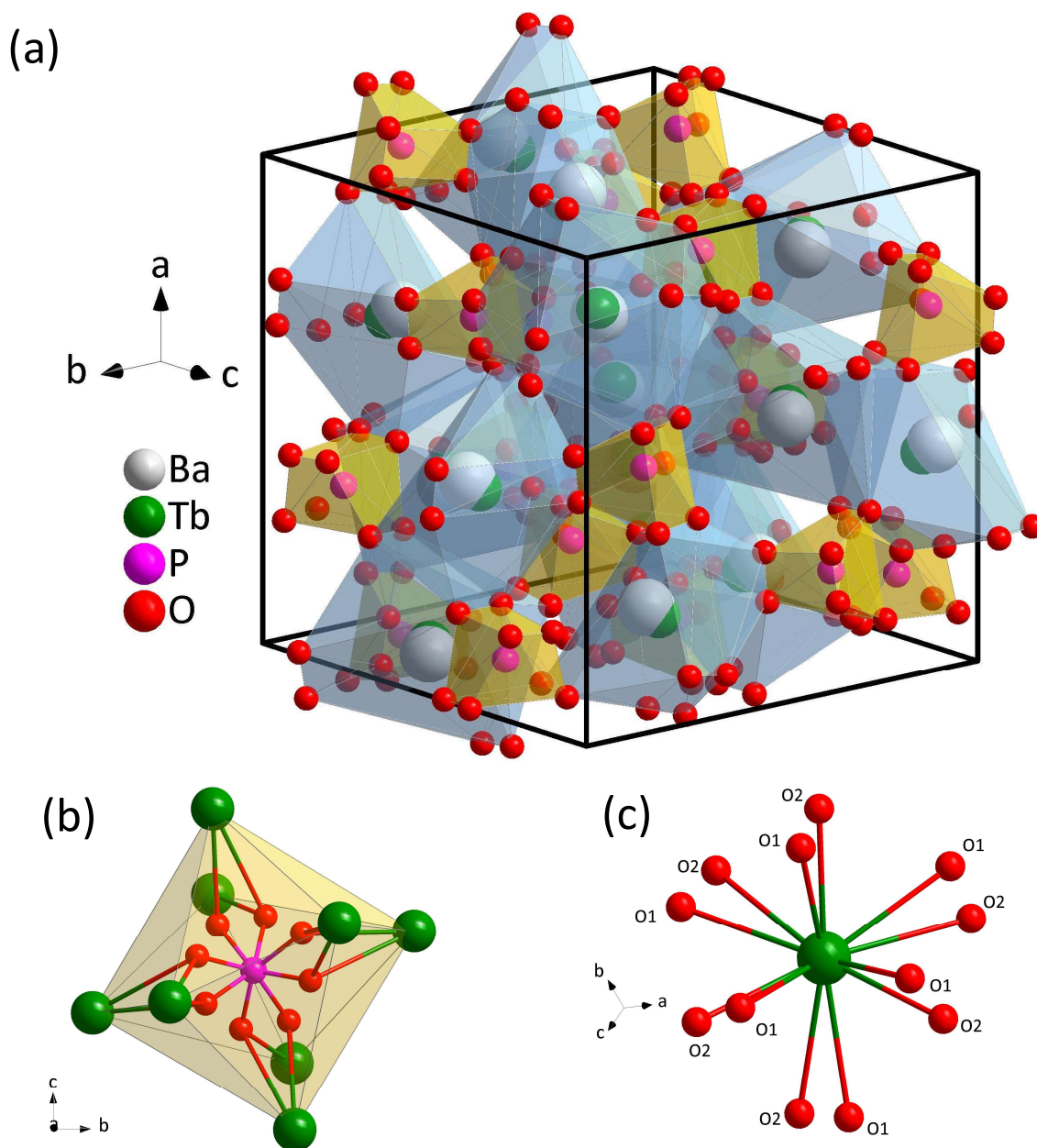
Figure 2.1 **Graphics showing: (a) crystal structure of the $Ba_3Tb(PO_4)_3$ unit cell (blue: MO_6 polyhedron; yellow: $[PO_4]$ polyhedron); (b) disorder of the $[PO_4]$ anion and bonding of the oxygen atoms with the adjacent terbium atoms; (c) coordination environment of the Tb site.**

BTP shows a congruent-melting behavior allowing for crystal growth by Czochralski technique. The polycrystalline raw material was synthesized by conventional solid-state reaction of ground and mixed chemicals of Tb_4O_7 (4N), $BaCO_3$ (2N5), and $(NH_4)H_2PO_4$ (2N) as follows:

$$\frac{1}{4}Tb_4O_7 + 3BaCO_3 + 3(NH_4)H_2PO_4 \xrightarrow{1200°C} Ba_3Tb(PO_4)_3 + \frac{1}{8}O_2 \uparrow + 3CO_2 \uparrow + 3NH_3 \uparrow + \frac{9}{2}H_2O \uparrow$$
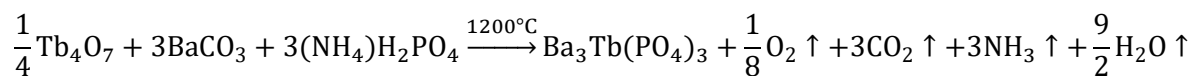
An excess amount (1.5 wt%) of P_2O_5 was added to compensate its evaporation during the sintering. Due to the large quantity of gaseous products, the reaction temperature was first slowly increased to 250°C at a rate of 1°C/h and then to 1200°C at a faster rate of 2.5°C/h. The temperature was then kept for 48h and cooled down to room temperature at a rate of 5°C/h. Powder X-ray diffraction (PXRD) of the as-sintered sample, follow by a semi-quantification analysis, revealed that the final product contains ca. 4% of $Ba_2P_2O_7$ phase and 1% of $TbPO_4$ phase (Figure 2.2). The formation of the pyrophosphate $Ba_2P_2O_7$ phase is probably due to the excessive P_2O_5 reactant.
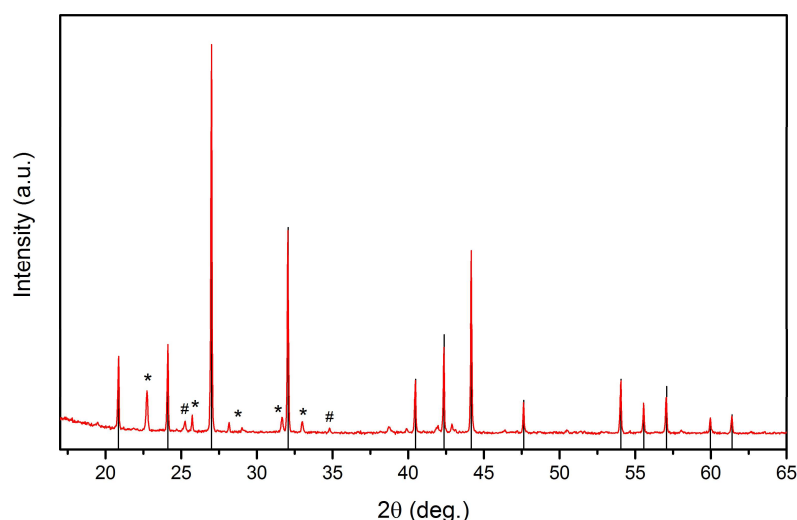
Figure 2.2   Powder X-ray diffraction pattern of the polycrystalline BTP (reference ICCD code: 00-043-0640; * hexagonal $Ba_2P_2O_7$ phase; # tetragonal $TbPO_4$ phase).

The Czochralski crystal growth of BTP was performed in static argon atmosphere. An iridium crucible was employed, which was 50 mm in height and 50 mm in diameter. An iridium wire was used as a growth starter. The pulling rate was 1.5 mm/h and the rotation was 12 rpm. These two parameters were kept constant throughout the growth process. It should be pointed out that the melting point of BTP was reported to be around 1650°C [2] whereas the temperature of the melt was estimated to be at least 1950°C using a pyrometer during the growth process. According to the phase diagram of BaO-Y_2O_3-P_2O_5, the melting point of its isostructural compound $Ba_3Y(PO_4)_3$ is also 1950°C [5], which backs our observation. Despite the high melting temperature, no significant evaporation of the P_2O_5 species could be observed. This further proves the congruent melting behavior of BTP. After the separation from the melt, the crystal was cooled down to room temperature in 48 h. The boule crystal was annealed in argon atmosphere at 1400°C for 24 h and cooled down to room temperature at a rate of 2°C/h to remove the stress during the growth.

Photographs of the as-grown crystal and the cut and polished samples are shown in Figure 2.3. The color is faintly yellow, owing to a weak absorption band of Tb^{3+} in the blue spectral range. The boule is free from cracks. Its quality was checked by passing a laser beam through the crystal. No scattering centers could be observed in the transparent part. Optical microscopy did not detect any noticeable inclusions in the crystal sample as well. PXRD analysis of the sample from the bottom part showed additional peaks originating from the cubic Tb_2O_3 phase. This impure phase was not detected in the sample from the transparent part. Thus, the bulk inclusions at the bottom could be attributed to this secondary phase.
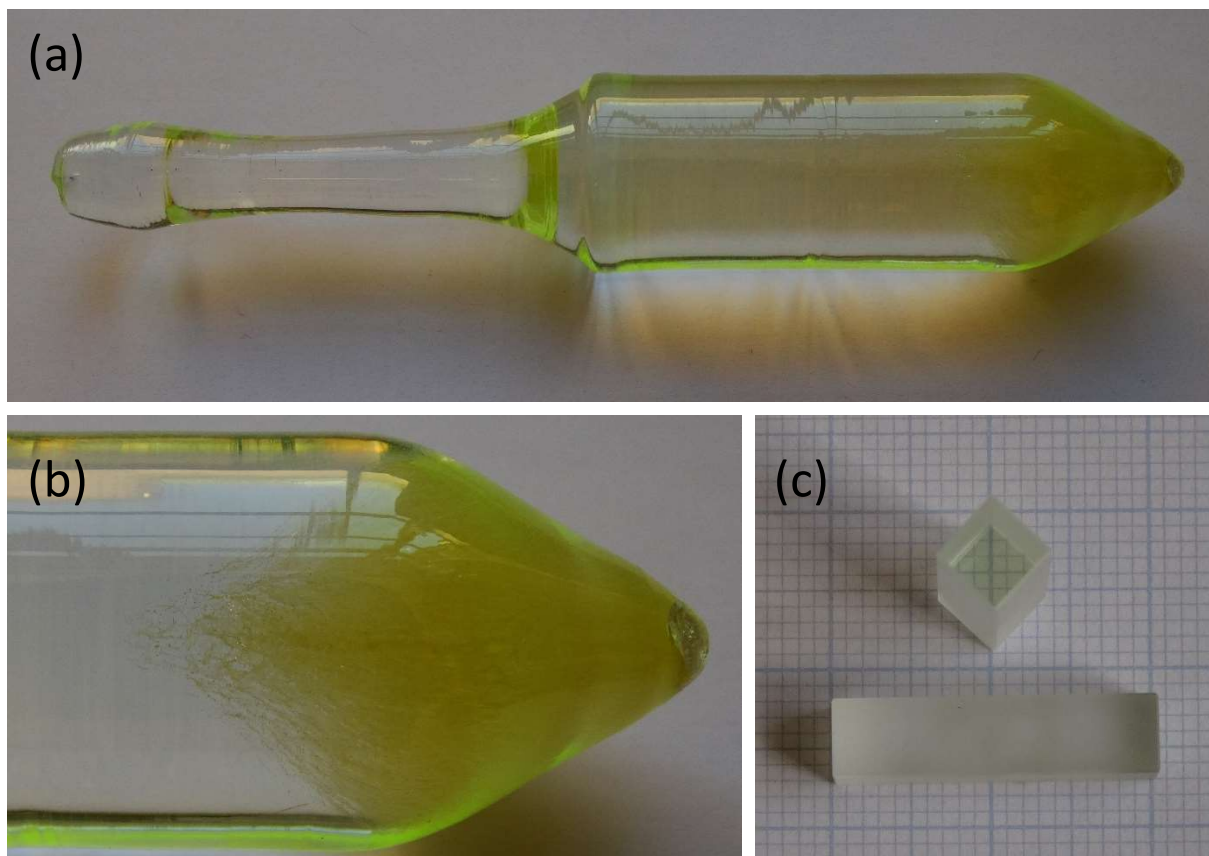
Figure 2.3 **(a) as-grown crystal of BTP; (b) bulk inclusions in the bottom part of the boule; (c) cut and polished samples from the transparent part of the crystal (dimension: 5×5×20 mm).**

As it belongs to the cubic crystal system, BTP is expected to show an isotropic optical property. However, when the crystal sample was observed in plane polarized light between crossed polarizers under an optical microscope, it exhibited some irregular patterns (Figure 2.4). Such optical anisotropy could not be eliminated by annealing the crystal in different atmospheres, including hydrogen, argon, and oxygen. It is reported that the eulytite compound of $Pb_3V(PO_4)_3$ shows a rhombohedral super structure on its original electron diffraction patterns [6], which might account for this optical inhomogeneity.
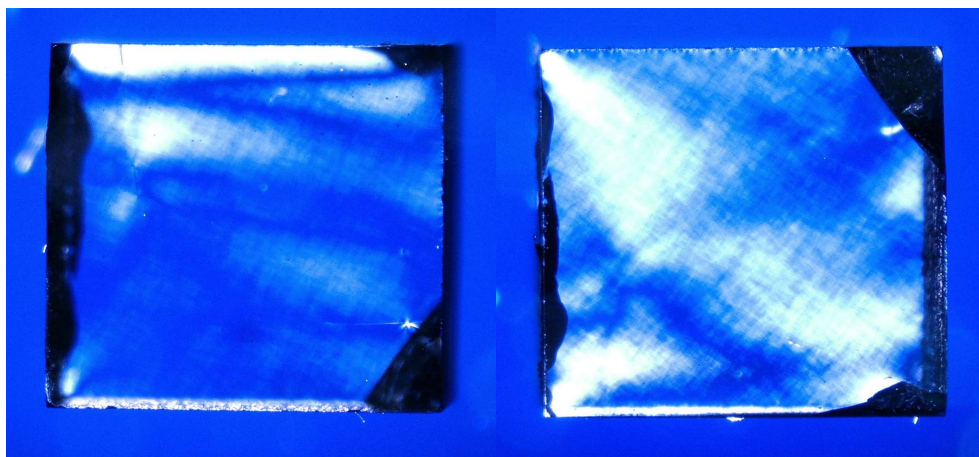
Figure 2.4 **Microphotograph of a polished BTP crystal in plane polarized light between two crossed polarizers.**
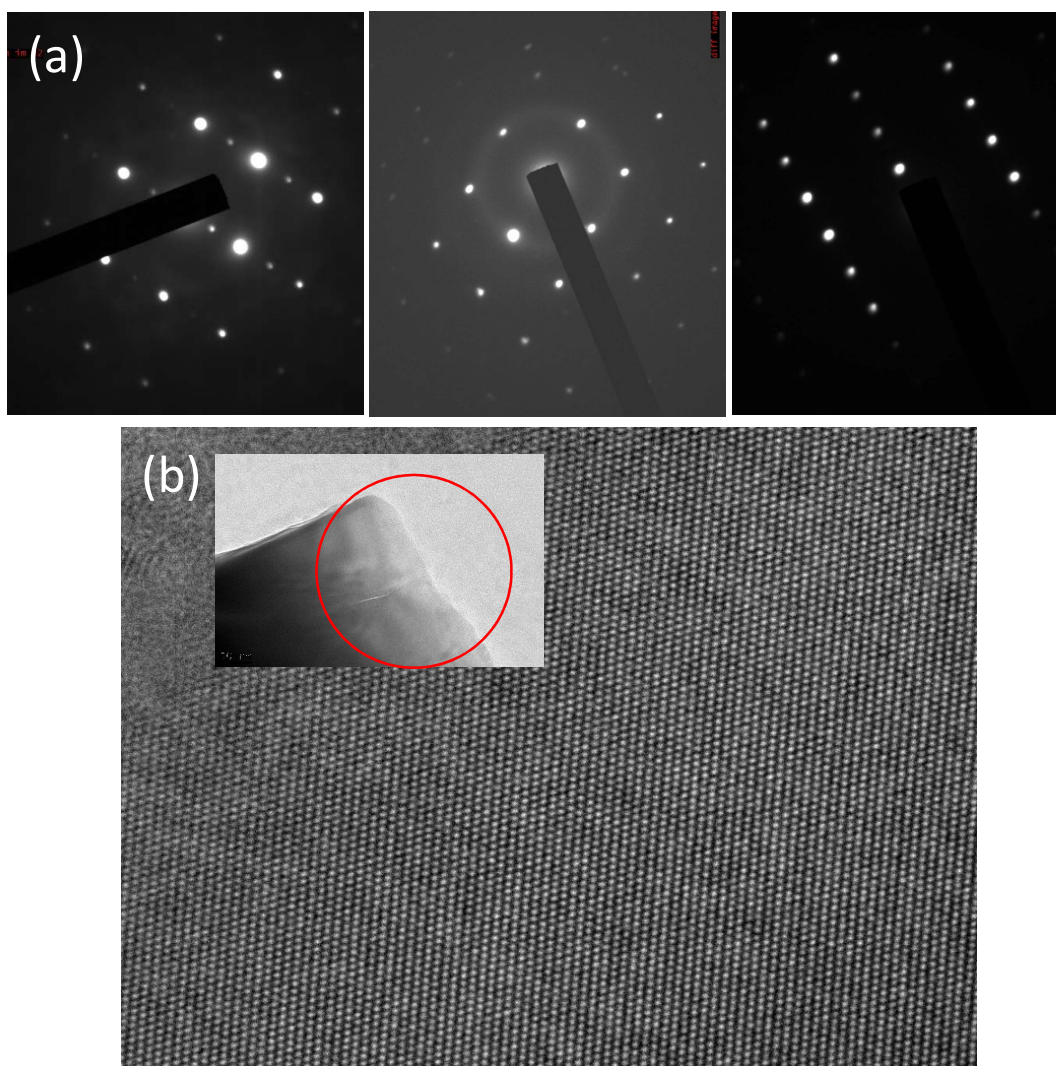
Figure 2.5 **(a) Electron diffraction patterns of three BTP crystal samples with arbitary orientation; (b) high resolution electron microscopy image with the inset showing the recorded area on a crystal slice.**

Transmission electron microscopy was carried out using a Jeol 2011 electron microscope operating at 200 kV accelerating voltage with several single crystalline slices prepared from the BTP as-grown crystal. Electron diffraction patterns of the BTP samples with three random orientations did not reveal any super structures (Figure 2.5 (a)). High resolution electron microscopy images did not show any twin variants as well (Figure 2.5 (b)). Therefore, this optical inhomogeneity might still come from the internal stress of crystal that cannot be removed by annealing.

2.1.2 Sr₃Tb(BO₃)₃ (STB)

The "STACK" family of borate compounds is derived from the structure of $Sr_3Sc(BO_3)_3$ substituted with a variety of metal ions at the Sr and Sc sites [7]. The general formula is $A_6MM'(BO_3)_6$, where A = Sr^{2+}, Ba^{2+}, Pb^{2+}, or Ln^{3+}, M ranges from Sc^{3+} ($r = 74.5\ pm$) to Sr^{2+} ($r = 118\ pm$), and M' varies from Al^{3+} ($r = 53.5\ pm$) to Gd^{3+} ($r = 93.8\ pm$), in terms of ionic radius. All the STACK compounds belong to the rhombohedral lattice system with space group $R\bar{3}$. Crystallographic data of STB based on the refinement in the literature (ICCD code:04-009-3070) [7] are given in Table 2.2.

Czochralski growth of $Sr_3RE(BO_3)_3$ compounds are reported in the literature [8–12], in which crystals with good optical quality could be obtained. Efficient Yb^{3+}-lasers using $Sr_3Y(BO_3)_3$ and $Sr_3Gd(BO_3)_3$ as host material are documented [13–15]. Furthermore, its crystal field depression is small enough to avoid efficient ESA processes. The optical absorption cutoff wavelengths of its analogue compounds, $Sr_3Gd(BO_3)_3$ and $Ba_3Gd(BO_3)_3$, are around 225 nm, according to the vacuum ultraviolet spectroscopic studies [16,17]. This suggests a quite large band gap energy of STB as well. These features point toward that STB is a suitable material to achieve Tb^{3+}-based laser emissions.

Table 2.2   Crystallographic data selective and physical properties of STB [7,18].

Chemical formula	$Sr_3Tb(BO_3)_3$
Formula weight	598.21 g·mol⁻¹
Crystal system	Trigonal
Space group	$R\bar{3}$
Unit cell parameters (Å)	$a = b = 12.521, c = 9.247$
Unit cell volume (Å³)	1255.4
Z	6
Theoretical density	4.748 g·cm⁻³
Melting point	1351°C
Mohs hardness	5.0
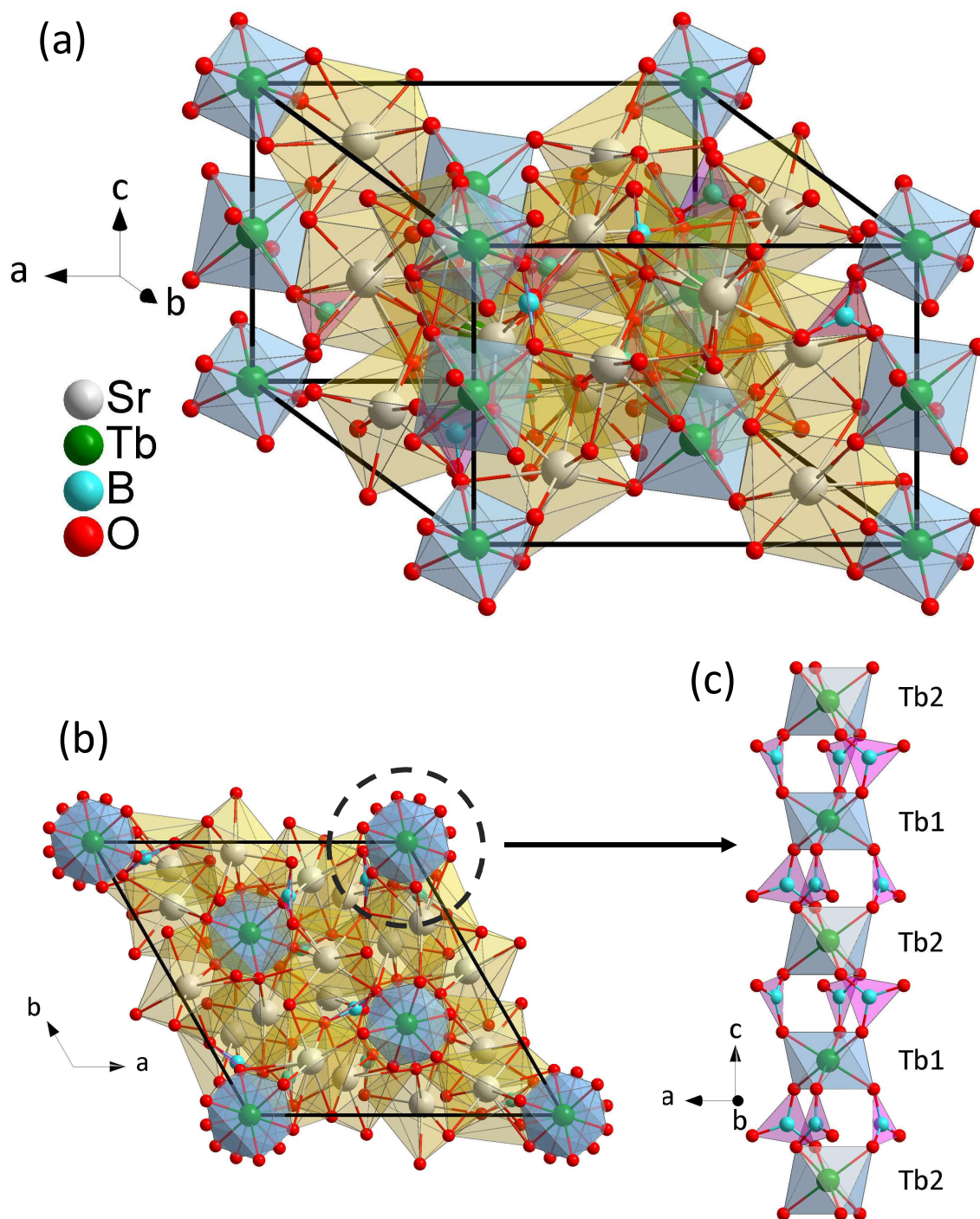
Figure 2.6 **Graphics showing: (a) crystal structure of the Sr$_3$Tb(BO$_3$)$_3$ unit cell (blue: [TbO$_6$] octahedron; yellow: [SrO$_9$] polyhedron; pink: trigonal [BO$_3$] anion); (b) unit cell viewed from the crystallographic c-axis; (c) [TbO$_6$] octahedra arranging alternatively along the c-axis.**

Figure 2.6 (a) illustrates the arrangement of atoms in a unit cell of STB. There are two crystallographic positions of Tb, both of which are 6-coordinate, and one Sr site with a coordination number of 9. The ligand oxygen atoms of the Tb site come from different [BO$_3$] groups. The two Tb sites, Tb1 and Tb2, correspond to, respectively, the M' and M site in the general formula A$_6$MM'(BO$_3$)$_6$. The Tb1 site occupying the vertexes of the crystal cell yields six equivalent Tb−O bonds which are 2.13 Å in length.

55

The Tb2 site also shows identical distance to six adjacent oxygen atoms, which is 2.19 Å. Both Tb sites exhibit a disordered octahedral configuration and a C_1 symmetry. These two [TbO$_6$] groups are connected alternatively with each other along the crystallographic c-axis to form an infinite 1D chain via the trigonal [BO$_3$] groups (Figure 2.6 (b) and (c)). Within this chain, the shortest distance between Tb1 and Tb2 is 4.62 Å while adjacent chains are separated by 7.23 Å. In addition, terbium atoms can also enter the 9-fold strontium site, whose Sr—O bond lengths range from 2.54 to 2.93 Å. Due to the minor occupation of Ln^{3+} in the Sr site, the broadening of spectral lineshape in Ln^{3+}-doped Sr$_3$RE(BO$_3$)$_3$ materials have been observed [9,11,12].

STB melts congruently at a moderate temperature of 1351°C [19] and is thus very suitable for Czochralski growth. The polycrystals of STB were synthesized by sintering the chemicals of Tb$_4$O$_7$ (4N), SrCO$_3$ (2N5), and H$_3$BO$_3$ (5N):

$$\frac{1}{4}\mathrm{Tb_4O_7} + 3\mathrm{SrCO_3} + 3\mathrm{H_3BO_3} \xrightarrow{1200°C} \mathrm{Sr_3Tb(BO_3)_3} + \frac{1}{8}\mathrm{O_2} \uparrow + 3\mathrm{CO_2} \uparrow + \frac{9}{2}\mathrm{H_2O} \uparrow$$
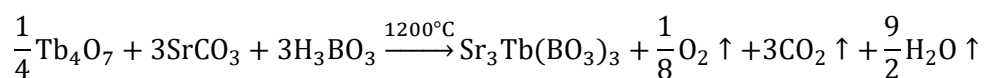
An excess amount (3 wt%) of H$_3$BO$_3$ was added to compensate the evaporation of B$_2$O$_3$ during the solid-state reaction. The heating rate was 2.5°C/h and the sintering temperature was kept at 1200°C for 48h. The as-sintered products show inhomogeneous colors. The majority was orange (~90%) while the other parts were white or black. PXRD was performed on three samples showing different colors (orange, white, and black). The orange polycrystals did not show noticeable parasitic peaks in its XRD pattern, as is shown in Figure 2.7. The other two samples, however, were found to contain incompletely reacted species.
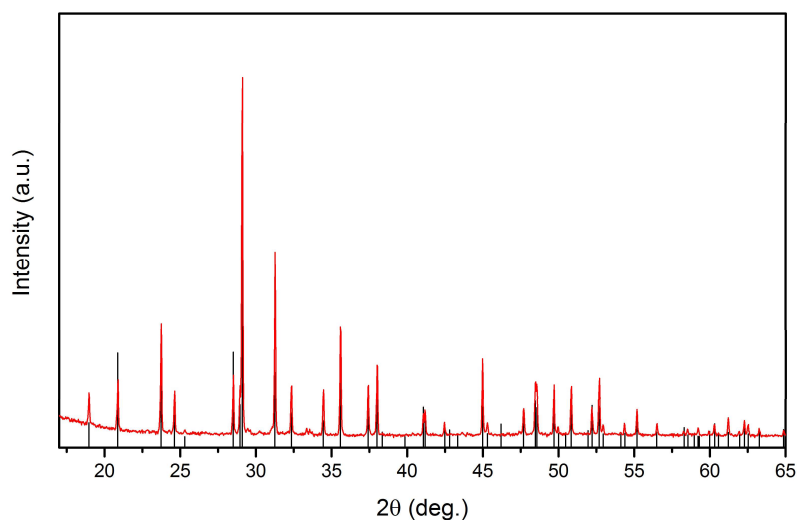
Figure 2.7   **Powder X-ray diffraction pattern of the orange STB polycrystals (reference ICCD code: 04-009-3070).**

The single crystal growth was first performed in air atmosphere using a Pt-Rh crucible which is 50 mm in height and 50 mm in diameter. A platinum wire was used as a growth starter. The pulling rate was 0.7 mm/h and the rotation was 10 rpm. The diameters of the neck and body part were set to be 6 and

22 mm, respectively. Significant evaporation of B_2O_3 from the melt was not observed during the synthesis. The as-grown crystal, denoted STB1, is free from cracks whereas it shows a red color (Figure 2.8 (a)). Considering the fact that the terbium-doped (18%) $Sr_3Gd(BO_3)_3$ crystals grown in N_2 atmosphere were reported to be colorless [20], the red color of STB1 could be attributed to the oxidation of Tb^{3+} into Tb^{4+} in air atmosphere. Identification of this red color by spectroscopic and electron paramagnetic resonance measurements will be presented in next subsection.

Annealing of STB1 in a reducing atmosphere containing 10% H_2 and 90% Ar at 1000°C for 24h turned it into a colorless single crystal (Figure 2.8 (b)). However, this process might generate vacancies in the lattice. To circumvent the unwanted red color of the as-grown crystal, another growth of STB was carried out. The second growth was conducted in the same reducing atmosphere as for the annealing (H_2/Ar). This is also to take into account the fact that oxidation of Tb^{3+} already takes place during the preparation of polycrystalline materials, which exhibit an orange color. The H_2/Ar atmosphere can thus reduce the Tb^{4+} species in the melt in situ. An oriented crystal along the c-axis was cut from the STB1 boule and utilized as a seed for this growth. The pulling rate was set to be 0.5 mm/h, which is slower than the previous growth and the rotation was kept at 10 rpm. The as-grown crystal, denoted as STB2, is colorless and free from bulk inclusions (Figure 2.9 (a)). A small amount of rod-like defects could be observed using an optical microscope (Figure 2.9 (b)). Nevertheless, its optical quality is good overall as no scattering center could be detected by passing a laser beam through the crystal. Figure 2.9 (c) shows the cut and polished samples with a dimension of 5×5×20 ($\|b$) mm.
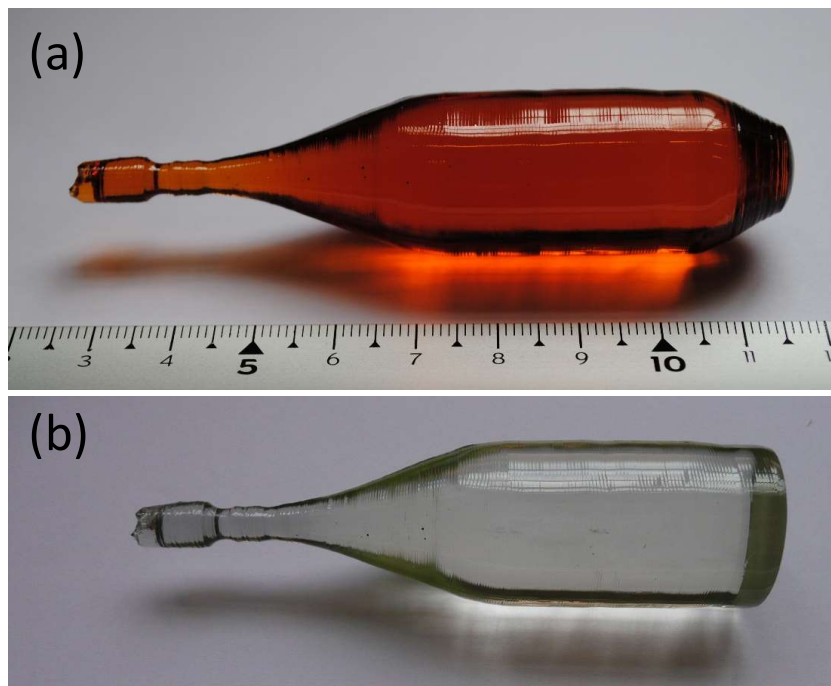
Figure 2.8   **(a) as-grown crystal of STB1; (b) the crystal after annealing in H$_2$/Ar.**
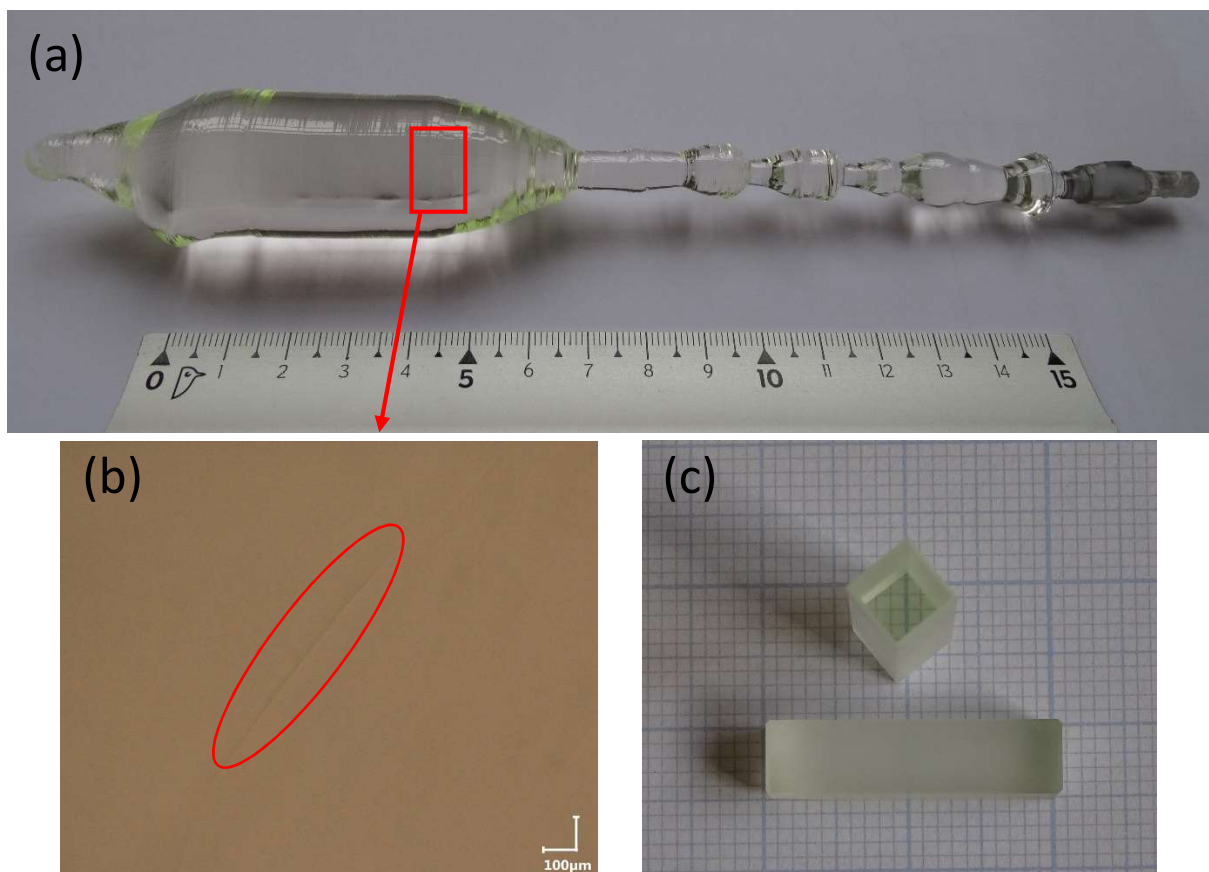
Figure 2.9 **(a) as-grown crystal of STB2; (b) scattering centers observed under a microscope; (c) cut and polished samples from the crystal (dimension: 5×5×20 mm).**

2.1.3 TbAl$_3$(BO$_3$)$_4$ (TAB)

TbAl$_3$(BO$_3$)$_4$ (TAB) crystalizes in the trigonal crystal system with the non-centrosymmetric $R32$ space group (Table 2.3). Figure 2.10 (a) illustrates the positions of atoms in a unit cell, which contains three formula units of TbAl$_3$(BO$_3$)$_4$. The crystal structure yields only one crystallographic position for Tb. This site is closely surrounded by six equivalent oxygen atoms and the Tb$-$O distance is 2.31 Å (Figure 2.10 (b)). The coordination polyhedron generated by these oxygen atoms, which is a slightly disordered triangular prism, yields a D_3 symmetry of the Tb site. The distance between Tb and the surrounded six crystallographically equivalent O3 atoms is 3.06 Å, which is slightly larger than the threshold of a Tb$-$O coordinate bond. The TbO$_6$ polyhedra do not share any coordinate oxygen atoms with each other. As a result, the shortest distance between two Tb atoms is as large as 5.88 Å. This value is greater than those of BTP (3.90 Å), STB (4.62 Å), LTB (3.88 Å), and TbCOB (3.54 Å), even though TAB has larger concentration of Tb^{3+}. Detrimental energy transfer processes among the Tb atoms can be markedly lessen in TAB, as is well-known that the dipole-dipole energy-transfer rate is inversely proportional to the sixth power of atomic distance.

58

Table 2.3   Crystallographic data and selective physical properties of TAB [21,22].

Chemical formula	$TbAl_3(BO_3)_4$
Formula weight	475.11 g·mol^{-1}
Crystal system	Trigonal
Space group	$R32$
Unit cell parameters (Å)	$a = b = 9.293(1), c = 7.249(6)$
Unit cell volume (Å^3)	541.796(1)
Z	3
Theoretical density	4.366 g·cm^{-3}
Melting point	decomposes at ~1200°C
Mohs hardness	~7.5[a]

[a] based on the analogue compound $YAl_3(BO_3)_4$.
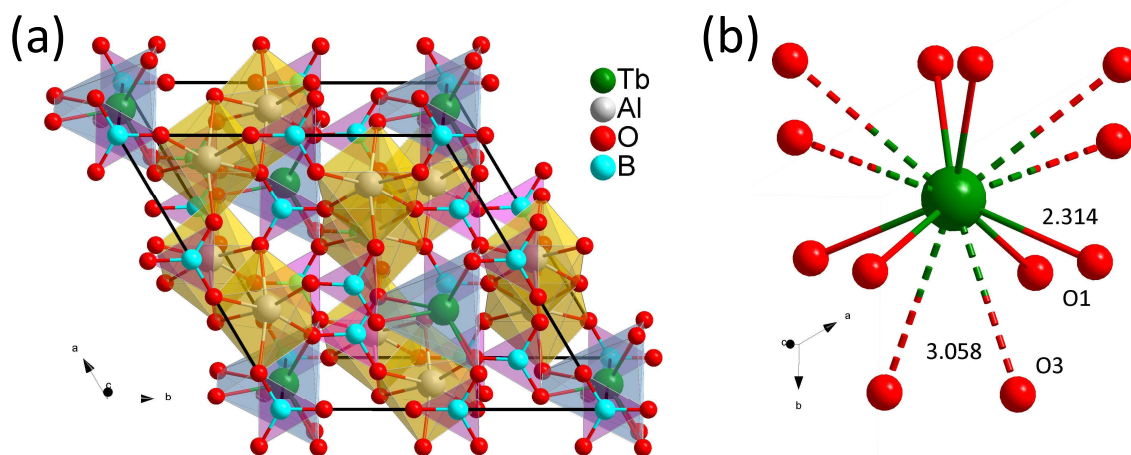
Figure 2.10   Graphics showing: (a) crystal structure of the TbAl$_3$(BO$_3$)$_4$ unit cell (blue: [TbO$_6$] polyhedron; yellow: [AlO$_6$] polyhedron; pink: trigonal [BO$_3$] anion); (b) coordination environment of the Tb site.

The TAB crystal was kindly offered by Dr. D. Rytz. It was synthesized by top-seeded solution growth method. Li$_2$WO$_4$ was used as flux and the growing temperature was ~950°C. A boule crystal of ~8 g was obtained after a growth run of 25 days. The cut and polished TAB sample is shown in Figure 2.11. Although scattering centers can be observed in the sample, the optical quality is sufficient for the following spectroscopic study.
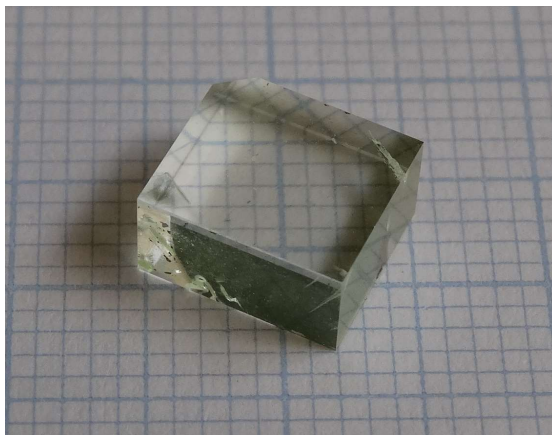
Figure 2.11   **Cut and polished TAB crystal, oriented to the indicatrix axes.**

2.1.4 $Li_6Tb(BO_3)_3$ (LTB)

The lithium borates with a general formula $Li_6RE(BO_3)_3$ (RE = Y, Gd-Lu) are known for their wide transparent zone, which is indispensable for direct visible laser application. Single crystalline $Li_6Y(BO_3)_3$ is transparent into far-UV and has a large band gap energy of 7.04 eV (176 nm) [23]. The crystal field depression is small enough to circumvent efficient ESA processes starting from the $^5D_4$ upper state. The concentration of Tb^{3+} in LTB is estimated to be 5.2×10^{21} cm^{-3}, which is a factor of 1.5 larger than that of BTP (3.5×10^{21} cm^{-3}). The large active-ion density is favorable for compensating the weak absorption cross-section of the $^7F_6\rightarrow^5D_4$ pump transition. These characters makes it a promising candidate for this subject.

Single crystal XRD measurements were carried out in order to perform precise structural refinement of LTB, which are summarized in Table 2.4. The structural solution reveals that LTB belongs to the monoclinic crystal system with space group $P2_1/c$. The refined atomic coordinates and displacement parameters are listed in the appendix section B.2.4. The unit cell comprises four chemical formula units. A graphic representation of the crystal structure is presented in Figure 2.12 (a). The Tb atom is 8-coordinated by oxygen atoms having six different crystallographic symmetries, denoted O1-O6. This cationic site has the lowest C_1 symmetry. The Tb—O bond lengths range from 2.31 to 2.53 Å, yielding an average value of 2.40 Å (Figure 2.12 (b)). The [TbO$_8$] polyhedra connect with each other via common edges formed by O1 and O6 (figure 2.12 (c)). They pile along the crystallographic c-axis and result in a 1D zigzag chain with a distance of 3.88 Å between two Tb atoms. These chains are separated by 7.20 Å with each other by the [LiO$_4$]/[LiO$_5$] groups. This crystal structure leads to a mono-dimensional inter-ionic interaction of the Tb atoms within the 1D chain.

Table 2.4   Crystallographic and structural refinement data of LTB (this work).

Chemical formula	$Li_6Tb(BO_3)_3$
Formula weight	377.00 g·mol^{-1}
Crystal system	Monoclinic
Space group	$P2_1/c$
Unit cell parameters (Å)	$a = 7.2030(2), b = 16.4723(3),$ $c = 6.6678(2), \beta = 105.326(3)$
Unit cell volume (Å^3)	763.00
Z	4
Theoretical density	3.282 g·cm^{-3}
Absorption coefficient	9.293 mm^{-1}
Theta range for data collection	3.401 to 28.274°
Limiting indices	$\|h\| \leq 9, \|k\| \leq 21, \|l\| \leq 8$
Reflections collected/unique	10108/1891
R(int)	0.0400
Refinement method	Full-matrix least-squares on F^2
Extinction coefficient	0.0223
Final R indices $(I > 2\sigma(I))$[a]	$R_1 = 0.0185, wR_2 = 0.0462$
R indices (all data)	$R_1 = 0.0211, wR_2 = 0.0474$
Goodness-of-fit on F^2	1.143
Highest difference peak and deepest hole	0.867 and -0.849 Å^3

[a] $R_1 = \frac{\sum\|\|F_0\|-\|F_c\|\|}{\sum\|F_0\|}, wR_2 = \left[\frac{\sum w\left(F_0^2 - F_c^2\right)^2}{\sum w\left(F_0^2\right)^2}\right]^{1/2}$

The congruent melting temperature of LTB should be closed to $Li_6Gd(BO_3)_3$, which is as low as 848°C [24]. As a result, the $Li_6RE(BO_3)_3$ melt exhibits high viscosity and large super cooling effect (~200°C), which further bring about a couple of practical problems. To be more specific, problems such as macroscale defects, bulk inclusions, concave interface growth, and spiral growth have been reported [24–29]. In addition, the tendency of cleavage and cracking along the three cleavage planes, viz. (102), (010), and (121), may bother the fabrication and processing of LTB crystals. Therefore, the growth parameters must be thought over in order to obtain good quality LTB crystals with sufficient size.
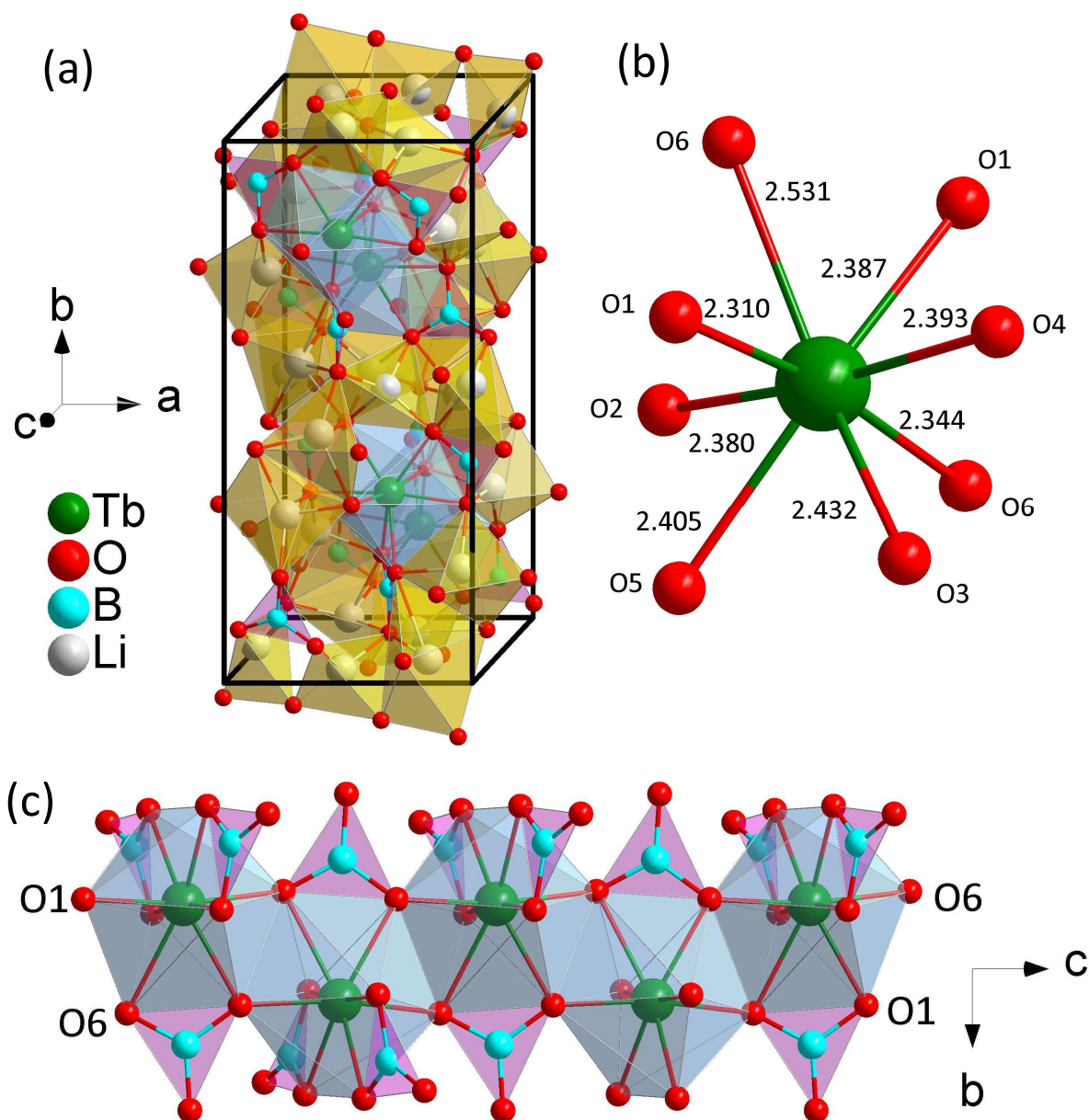
Figure 2.12 **Graphics showing: (a) crystal structure of the Li₆Tb(BO₃)₃ unit cell (blue: [TbO₈] polyhedron; yellow: [LiO₄]/[LiO₅] polyhedron; pink: trigonal BO₃ anion); (b) coordination environment of the Tb site; (c) [TbO₈] polyhedra stacking along the *c*-axis in an edge-sharing scheme.**

It is found that after melting the polycrystalline starting material, the incompletely reacted species during the solid-state reaction, such as lithium pyroborates, tend to enter the growing Li₆RE(BO₃)₃ crystal and remain as bulk inclusions [26,28]. Therefore, purity of the starting material for the single crystal growth has to be particularly taken care. The polycrystalline material of LTB was synthesized by a solid-state reaction of Tb₄O₇ (4N), Li₂CO₃ (5N), and H₃BO₃ (5N) as below:

$$\frac{1}{4}Tb_4O_7 + 3Li_2CO_3 + 3H_3BO_3 \xrightarrow{750°C} Li_6Tb(BO_3)_3 + \frac{1}{8}O_2 \uparrow + 3CO_2 \uparrow + \frac{9}{2}H_2O \uparrow$$
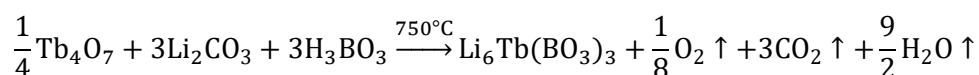
Unlike the syntheses of other borate polycrystals in this study, no excess of B_2O_3 was added before the sintering because of the relatively low reaction temperature. The raw materials were slowly heated to 750°C at a rate of 1°C/h. The duration of sintering was 48h. The appearance of the as-synthesized polycrystalline pieces was white overall, with a small amount with color in black. The PXRD pattern of the white polycrystals reveals an almost pure phase (Figure 2.13). The parasitic peak at around 29° is probably from the TbO_x species. On the other hand, the black products contained several parasitic phases. They showed aggregation effect on the rim of the polycrystalline cylinder were removed manually.
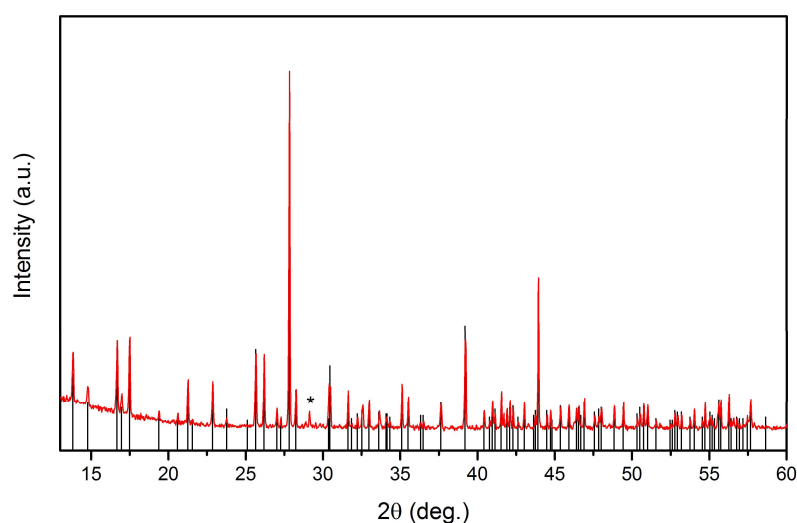
Figure 2.13   Powder X-ray diffraction pattern of the white LTB polycrystals (reference ICCD code: 00-061-0412).

The control of thermal gradients in the crystal growth circumstance of LTB is crucial. Low thermal gradients were found to produce spiral growth or uncontrollably rapid growth behaviors [24–26]. Too-high thermal gradients, however, might lead to cracking of the crystal. The furnace setup for growing LTB crystals were modified from the typical one. The zirconia grains surrounding the crucible as well as the cone above the crucible were removed in order to increase the thermal gradients (see also Figure B.1 in Appendix B).

The initial growth of LTB was carried out in air atmosphere with a platinum crucible. The crucible is slightly deformed, with a diameter of 38 mm on top and 42 mm at bottom. A $Li_6Gd(BO_3)_3$ crystal with a random orientation perpendicular to the b-axis was kindly offered by Dr. P. Veber from ICMCB, Bordeaux. It was used as a seed crystal for this growth. A slow pulling rate of 0.5 mm/h was adopted to circumvent formation of gas inclusions. A slow rotation was suggested in the previous works in order to prevent the forced convection and stabilize the growth [25,26]. Thus, the crystal rotation was maintained constantly at 5 rpm. The diameters of the neck and body part were set to be 8 and 22 mm, respectively. Notable evaporation of B_2O_3 from the melt was not observed after completely melting the polycrystals. After being separated from the melt, the boule crystal was allowed to cool down in

25 h. Considering the low melting temperature, this cooling rate should be slow enough. Nevertheless, a part of the boule underwent cleavage during the cooling procedure.
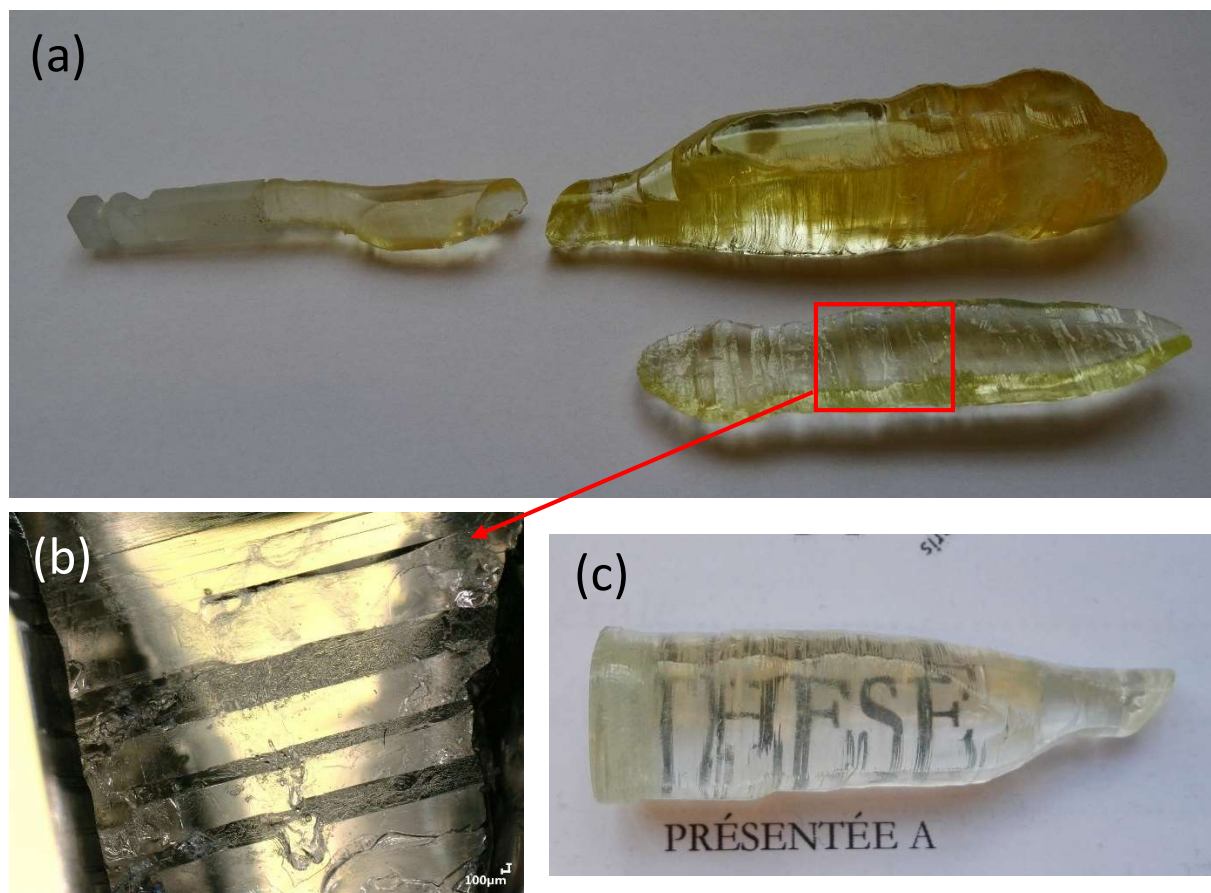
Figure 2.14   (a) as-grown crystal of LTB1; (b) cleavage planes observed under a microscope; (c) the crystal after annealing in H$_2$/Ar.

Photos of the as-grown crystals, denoted LTB1, are shown in Figure 2.14 (a). The cleavage, showing a stepwise structure, took place from the shoulder part. The perfect cleavage planes (Figure 2.14 (b)), as well as the noticeable natural facets on the boule crystal, were found to be (010). The as-grown crystal exhibited a yellow color, which could be assigned to the oxidation of Tb^{3+} in the air. This is supported by a similar behavior to STB discussed in subsection 2.1.2. After annealing in a reducing atmosphere (H$_2$/Ar, 750°C for 48 h), the LTB crystal turned almost colorless. The upper part of the boule had a low density of scattering centers inside. With regard to the lower part, however, a vast amount of cloudy inclusions could be observed by naked eyes.

The unfavorable cleavage behavior can be circumvented by using a suitably oriented seed. A new seed crystal was fabricated from LTB1. The orientation is designed to have an angle as large as possible with respect to ⟨102⟩, ⟨010⟩, and ⟨121⟩, which is around ⟨4-32⟩. Another growth of LTB was performed with this seed crystal. Setup of the Czochralski furnace was similar to the first growth, except that the reducing atmosphere was employed. This is the same strategy to avoid color-center formation as for STB. The growth rate, rotation speed, and diameter of the body part were set to be 0.5 mm/h, 5 rpm, and 25 mm, respectively. The cooling duration of the crystal was elongated to 36 h.

The grown crystals, denoted as LTB2, are shown in Figure 2.15 (a). The color is much paler than LTB1. Unfortunately, the boule crystal cracked severely during the growth process (before cooling). Here we proposed two possible reasons. First, it can be due to the highly deformed crucible (not used for the previous growths). Its diameter on top is 44 mm while that of the inflated part is 56 mm (Figure 2.15 (b)). Such irregular shape could result in asymmetric temperature field and a large axial thermal gradient, since the coupling efficiency to the RF coil differs with crucible diameter. This unfavorable growing environment might had caused the cracking of the crystal. Second, the diameter of the body part was increased by 3 mm compared to the first growth. The diameter of the crystal impacts the convection mode of the melt. The forced convection mode is promoted as the crystal diameter increases [26,30]. It transports melt from the lower part, which has higher temperature, to the upper part of the crucible. This process might had also lead to the cracking.

On the other hand, LTB2 is free from cleavages which took place in LTB1. This indicates that the orientation of the seed crystal was suitable. The much paler color than LTB1 proves that the oxidation of Tb^{3+} was suppressed owing to the reducing atmosphere. A small amount of scattering centers can be observed in the upper body part of LTB2 with a laser pointer or an optical microscope. A microscope image showing a typical inclusion in LTB2 is presented in Figure 2.15 (c).
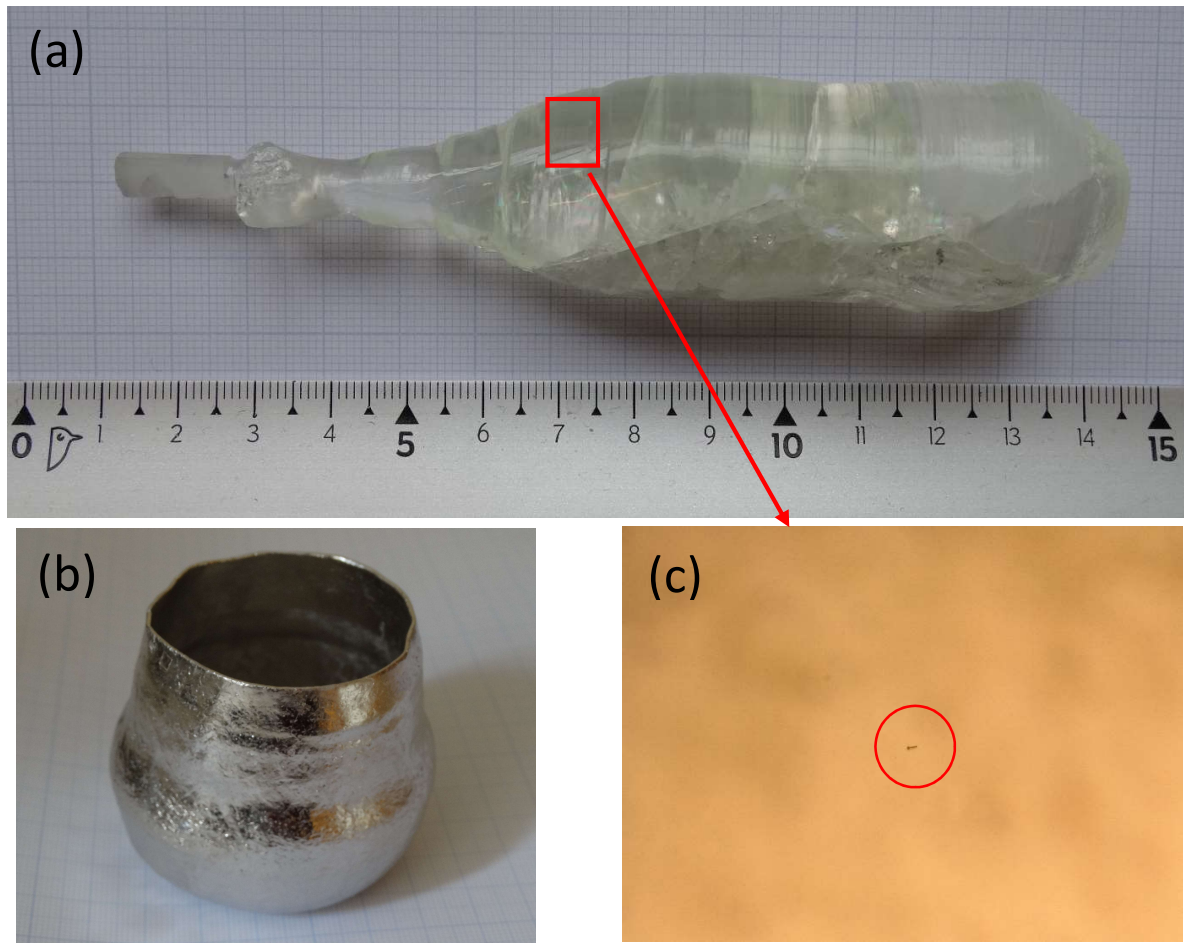
Figure 2.15   **(a) as-grown crystal of LTB2; (b) the deformed crucible used for the growth of LTB2; (c) observation of the scattering center in the upper part of the boule under a microscope.**

Growth conditions were further optimized in the third run. To avoid the unfavorable temperature field, a more regular crucible was employed, which had been used for the growth of LTB1. The diameter of the body part was reduced to be 20 mm to lessen the forced convection. The pulling speed was further decreased to 0.4 mm/h. The growth program was modified as well (see also appendix section B.1.3). The pulling was not immediately stopped after the end of bottom part. The purpose is to gradually transport the boule away from the melt. In this way, the thermal shock exerted to the boule crystal can be minimized during the separation and cooling processes. Finally, the cooling rate was further extended to 48 h to avoid cracking.

The as-grown crystal of LTB3 is shown in Figure 2.16 (a). It is free from cracks and cleavages. However, a low density of scattering centers can still be found in the upper body part of the boule, which have the same morphology as those of LTB2 (Figure 2.16 (b)). Similar to the previous two as-grown LTB crystals, the density and size of the inclusion increase drastically at end of the body part. A polished crystal sample is shown in Figure 2.16 (c).
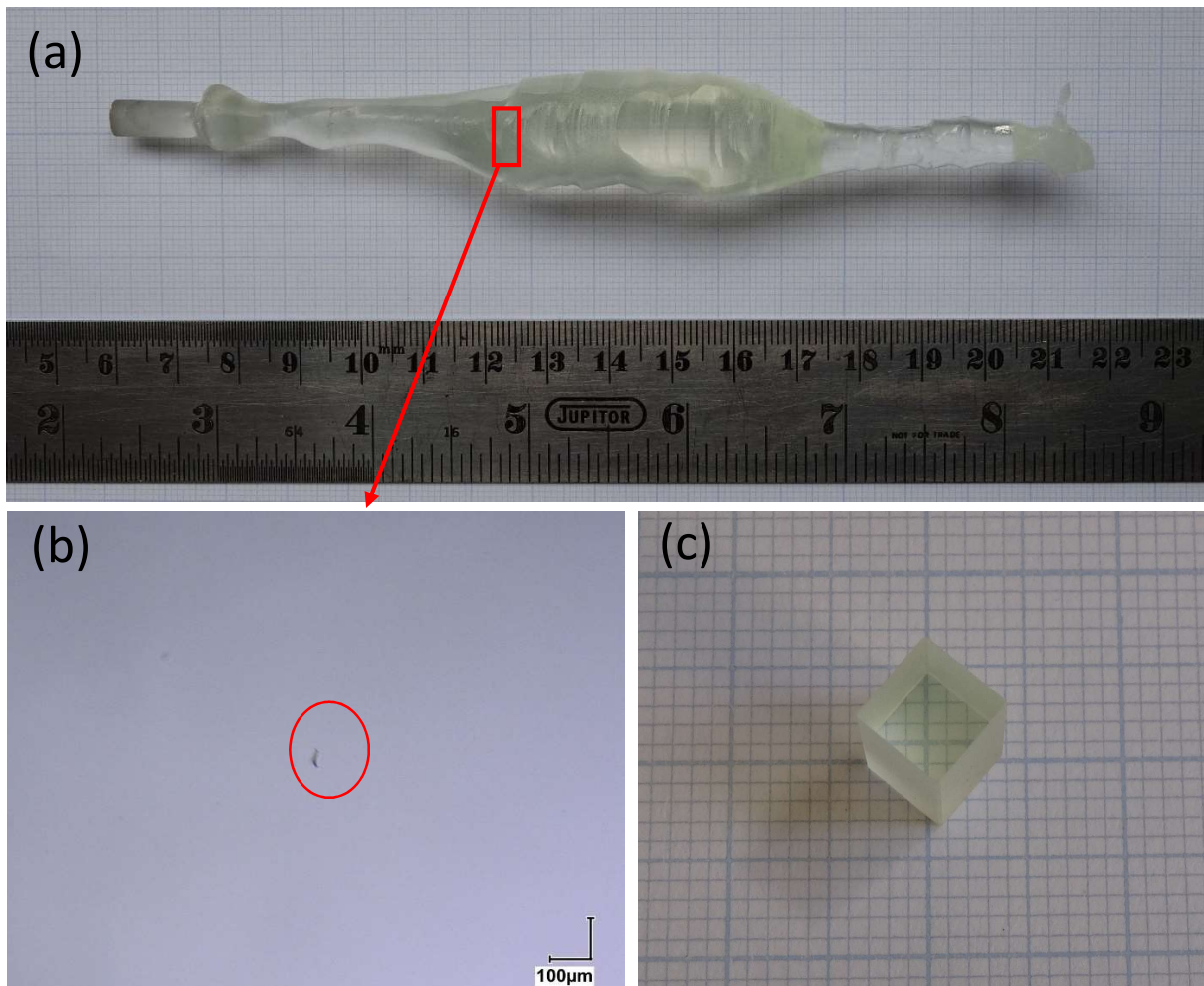
Figure 2.16   (a) as-grown crystal of LTB3; (b) observation of the scattering center in the upper part of the boule under a microscope; (c) cut and polished samples from the crystal (dimension: 5×5×11 mm).

2.1.5 TbCa₄O(BO₃)₃ (TbCOB)

$TbCa_4O(BO_3)_3$ (TbCOB) crystalizes in a non-centrosymmetric C_m space group. The crystallographic information of TbCOB is given in Table 2.5. Its isostructural compounds YCOB and GdCOB have been extensively used as laser gain medium and non-linear optical material on account of the broad transparent range and facileness to grow a high quality single crystal. The absorption edge of YCOB is reported to be 220 nm [31]. The crystal field depression of TbCOB is similar to those of STB and LTB discussed above. These advantages motivate us to study the physical properties of TbCOB.

Table 2.5   Crystallographic data and selective physical properties of TbCOB [32,33].

Chemical formula	$TbCa_4O(BO_3)_3$
Formula weight	509.89 g·mol⁻¹
Crystal system	Monoclinic
Space group	Cm
Unit cell parameters (Å)	$a = 8.0715, b = 16.0000, c = 3.5454, \beta = 101.2550$
Unit cell volume (Å³)	449.06
Z	2
Theoretical density	3.771 g·cm⁻³
Melting point	1498°C
Mohs hardness	5.65 on (010)
Refractive index[a]	$n^2(\lambda) = A + \dfrac{B}{\lambda^2 - C} - D\lambda^2$

[a] Sellmeier coefficients: $A_x = 2.809$; $A_y = 2.900$; $A_z = 2.930$; $B_x = 22330\ nm^2$, $B_y = 23340\ nm^2$, $B_z = 23730\ nm^2$; $C_x = 16130\ nm^2$, $C_y = 17290\ nm^2$, $C_z = 15680\ nm^2$; $D_x = 5890\ nm^{-2}$, $D_y = 11040\ nm^{-2}$, $D_z = 11980\ nm^{-2}$.

The crystal structure of TbCOB is illustrated in Figure 2.17 (a), which is based on the single crystal diffraction refinement data [33]. A unit cell provides three metallic sites, one is occupied only by Ca, while the other two are distributed with Ca and Tb. Nevertheless, occupation of Tb in the Ca1/Tb1 site was found to be predominant over the Ca2/Tb2 site (0.96 for the Ca1/Tb1 site) [32,34]. The Ca1/Tb1 site has a C_s symmetry with a mirror plane passing through the O1 and O3 atoms while the other two metallic sites give a C_1 symmetry. As is depicted in Figure 2.17 (b) and (c), both Tb sites are six-coordinated. The average Tb−O bond lengths of the Tb1 and Tb2 sites are found to be 2.33 and 2.34 Å, respectively. The eight-fold Ca site gives an average Ca−O distance of 2.55 Å. The [Ca1/Tb1O₆] octahedra are connected to the neighboring units by common edges and the [Ca2/Tb2O₆] octahedra display a similar edge-sharing approach (Figure 2.17 (d)). The 4-coordinate O1 atom, which is independent from the borate groups, bonds with two [Ca1/Tb1O₆] octahedra and two [Ca2/Tb2O₆] octahedra at the same time. The three parallel [Ca/TbO₆] chains stack along the crystallographic c-axis (Figure 2.17 (e)). The minimum Tb−Tb distance within the same chain is 3.54 Å.
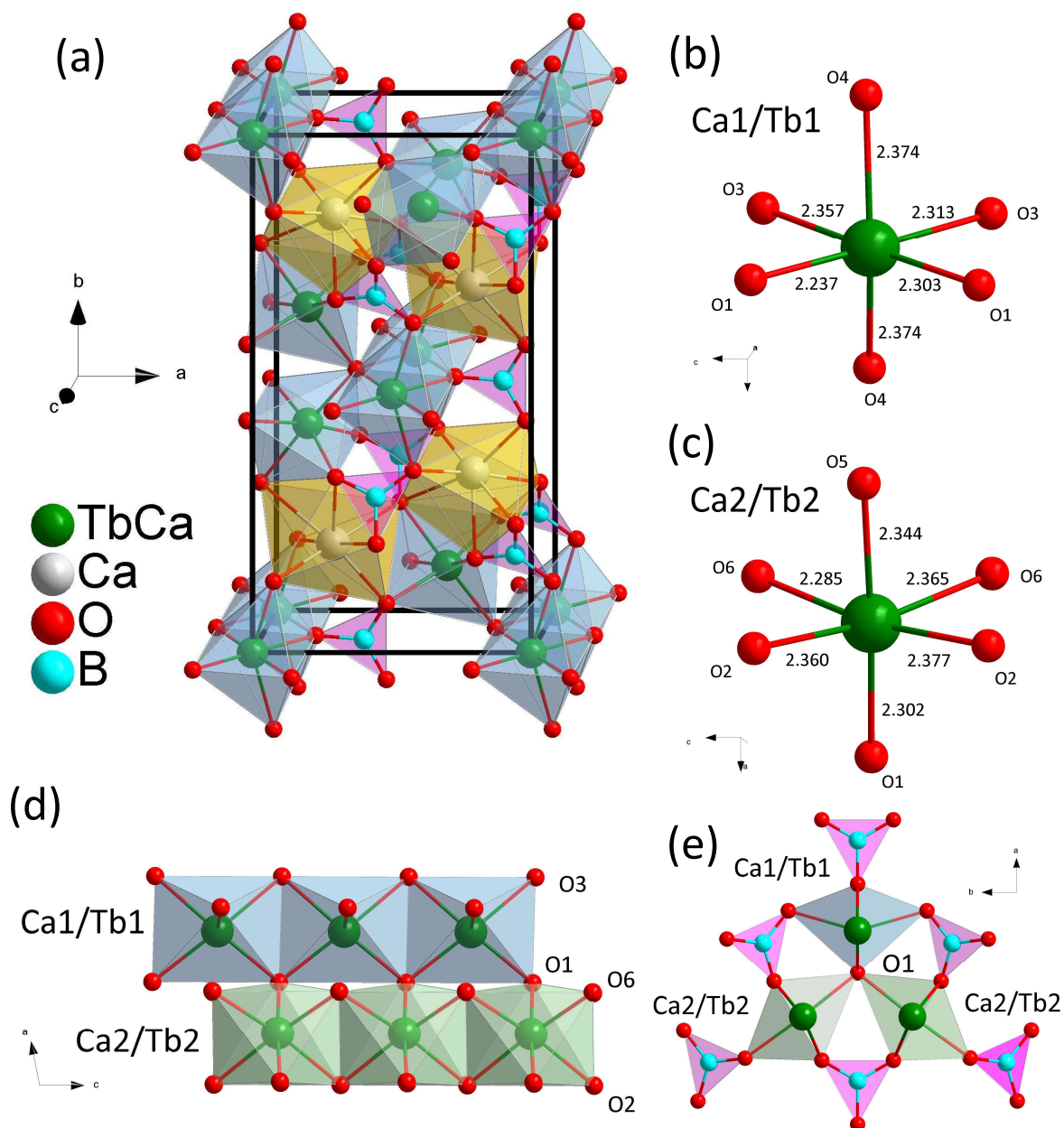
Figure 2.17   Graphics showing: (a) crystal structure of the TbCa$_4$O(BO$_3$)$_3$ unit cell (blue: [TbO$_6$] octahedron; yellow: [CaO$_8$] polyhedron; pink: trigonal [BO$_3$] anion); (b)(c) coordination environment of the Tb sites; (d) stacking of the [Ca/TbO$_6$] octahedra along the c-axis; (e) the [Ca/TbO$_6$] chains viewed from the c-axis.

TbCOB melts congruently at around 1500°C [32]. The polycrystalline TbCOB raw materials were synthesized by sintering the chemicals of Tb$_4$O$_7$ (4N), CaCO$_3$ (2N5), and H$_3$BO$_3$ (5N):

$$\frac{1}{4}\mathrm{Tb_4O_7} + 4\mathrm{CaCO_3} + 3\mathrm{H_3BO_3} \xrightarrow{1300°C} \mathrm{Ca_4TbO(BO_3)_3} + \frac{1}{8}\mathrm{O_2}\uparrow + 4\mathrm{CO_2}\uparrow + \frac{9}{2}\mathrm{H_2O}\uparrow$$
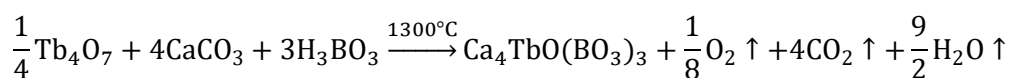
An excess amount (4 wt%) of H$_3$BO$_3$ was added to compensate the loss of B$_2$O$_3$ via evaporation. The starting materials were heated up to 1300°C at a rate of 2.5°C/h .The sintering lasted for 36h. The as-

synthesized polycrystalline cylinder was overall pale yellow. A small amount of brown stain was observed on the surface. Such partial dark color was also observed in the STB and LTB polycrystals products. They tend to aggregate on the rim and surface of the polycrystalline cylinder. PXRD was carried out on the pale yellow and brown samples. The pale yellow sample does not show any obvious secondary phases, as is shown in Figure 2.18. The sample with color in brown, however, exhibits many parasitic peaks in its diffraction pattern. They were removed manually from the pure pale yellow products.
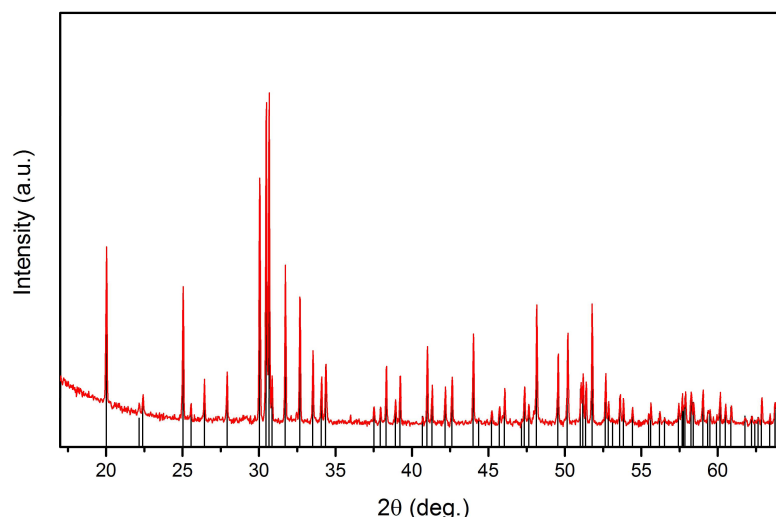
Figure 2.18 **Powder X-ray diffraction pattern of the pale yellow TbCOB polycrystals (reference ICCD code: 04-009-0602).**

TbCOB crystals grown in argon atmosphere showed a yellow color, which derives from a broad absorption band starting from around 500 nm to middle UV zone [33] (see also Figure 2.19 (b)). This unwanted broadband absorption, probably stems from existence of tetravalent terbium, covers the pump transition at around 486 nm and must be circumvented. Based on the previous experiences in growing terbium-based crystals, TbCOB was grown directly in the reducing atmosphere (10% H_2 and 90% Ar). A b-oriented YCOB seed crystal and an iridium crucible (50 mm in height and 50 mm in diameter) were used for the Czochralski growth.

As expected, the as-grown crystal of TbCOB shows its natural pale color in contrast with the yellow TbCOB crystal grown in argon (Figure 2.19 (a)). The natural facets of the as-grown crystal were found to be $(\bar{2}01)$ by Laue diffraction. Despite that the bottom part has a rough surface and bulk inclusions, this TbCOB crystal has the best optical quality among all the terbium-based crystals fabricated in this work. No scattering center could be detected in a polished sample cut from the upper body part of the boule. The fabricated single crystal rods of TbCOB are shown in Figure 2.19 (c).
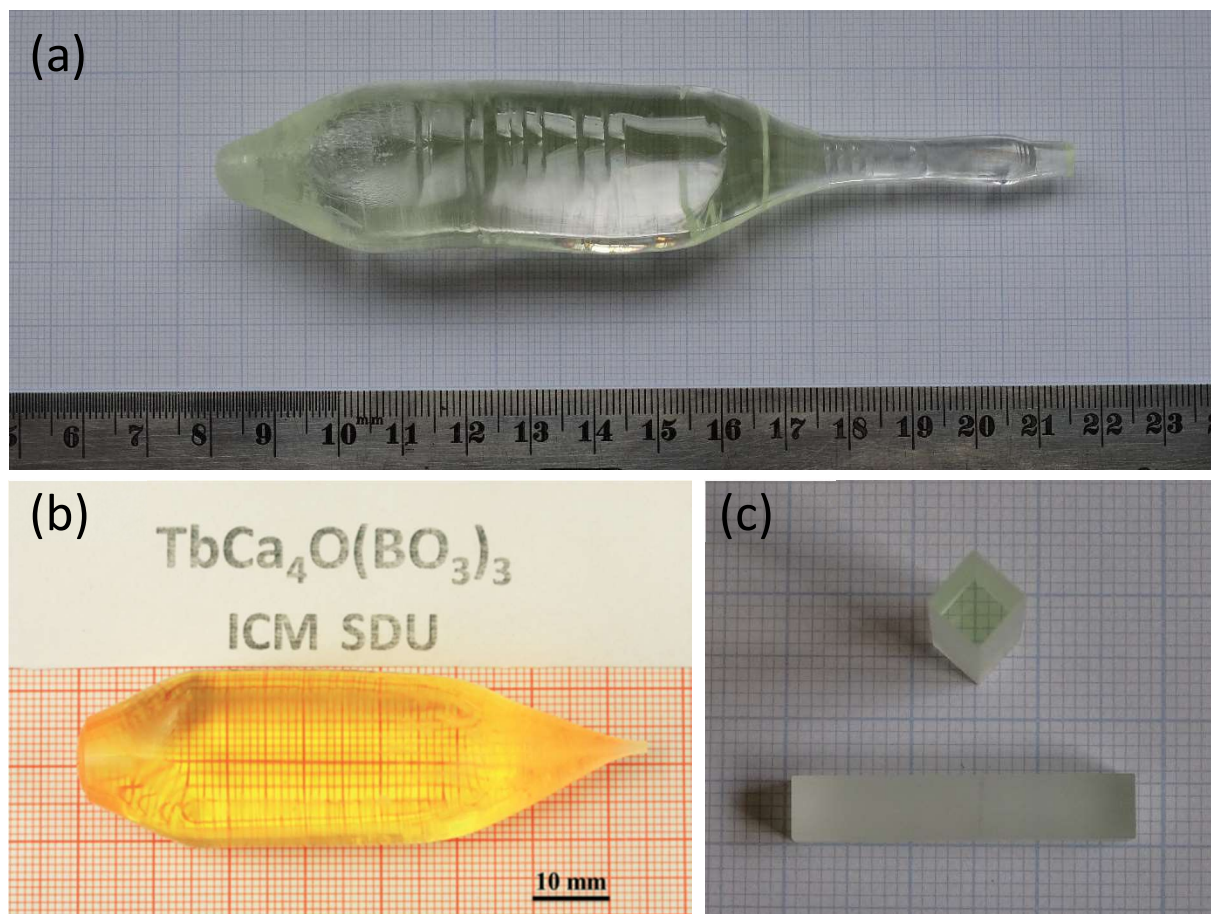
Figure 2.19 **(a) as-grown crystal of TbCOB; (b) TbCOB grown in argon atmosphere in the literature [33]; (c) cut and polished samples from the crystal (dimension: 5×5×26.7 mm).**

2.1.6 KTb(WO₄)₂ (KTW)

The monoclinic tungstate crystals KRE(WO$_4$)$_2$ (RE = Y, Gd-Lu) are interesting as laser gain medium mainly because of their relatively small lattice phonon energy ($\sim$900 cm^{-1}) and that the doping active ion usually shows exceptionally large transition cross-sections [35,36]. However, the preliminary investigation in Chapter 1 reveals that hexavalent tungsten-based materials are not compatible for hosting Tb^{3+} for visible laser applications due to the risk of charge transfer process that depletes the excite-state population during laser operation. Nevertheless, the terbium-based tungstate of KTb(WO$_4$)$_2$ (KTW) is worth studying since it can offer knowledge about excited-state absorption of Tb^{3+} to the host bands. Its crystallographic information is given in Table 2.6.

Table 2.6   **Crystallographic data and selective physical properties of KTW [37,38].**

Chemical formula	$KTb(WO_4)_2$
Formula weight	693.72 g·mol^{-1}
Crystal system	Monoclinic
Space group	$C2/c$
Unit cell parameters (Å)	$a = 10.6586(5)$, $b = 10.4073(4)$, $c = 7.5762(3)$, $\beta = 130.754(5)$
Unit cell volume (Å^3)	636.6
Z	4
Theoretical density	7.238 g·cm^{-3}
Melting point	decomposes at ~1010°C
Mohs hardness[a]	4-5

[a] Based on the analogue compound $KY(WO_4)_2$.
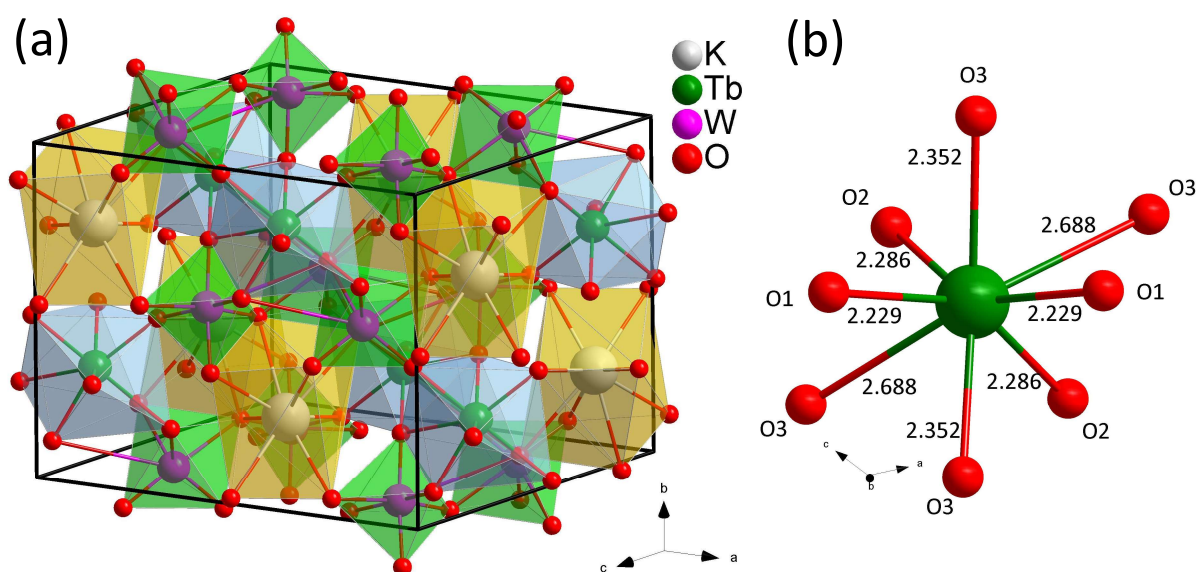
Figure 2.20   **Graphics showing: (a) crystal structure of the TbAl$_3$(BO$_3$)$_4$ unit cell (blue: [TbO$_8$] polyhedron; yellow: [KO$_8$] polyhedron; green: [WO$_6$] octahedron); (b) coordination environment of the Tb site.**

Single crystal XRD refinement of KTW has been conducted by S. Schwung et al [37]. It belongs to the monoclinic space group of $C2/c$. The crystal structure is shown in Figure 2.20 (a). It gives only one crystallographic position of Tb. The Tb site is surrounded by eight O atoms and has the $C2$ point symmetry. The Tb—O bond lengths range from 2.23 to 2.69 Å (Figure 2.20 (b)). The [TbO$_8$] polyhedra connect with each other via an edge-sharing scheme and form a 1D chain. The eight coordinate oxygen atoms of the Tb site bond with eight adjacent W atoms. The minimum distance between a terbium

and a tungsten atom is only 3.55 Å. The closely spaced Tb and W sites enables the charge transfer process. It is worth mentioning that site exchange of K and Tb atoms, both are 8-fold, can take place. This may lead to broad spectral lines.

The KTW crystal received from Dr. D. Rytz was grown from $K_2W_2O_7$ flux at ca. 900°C. The processed crystal sample shown in Figure 2.21 is almost colorless and has good optical quality.
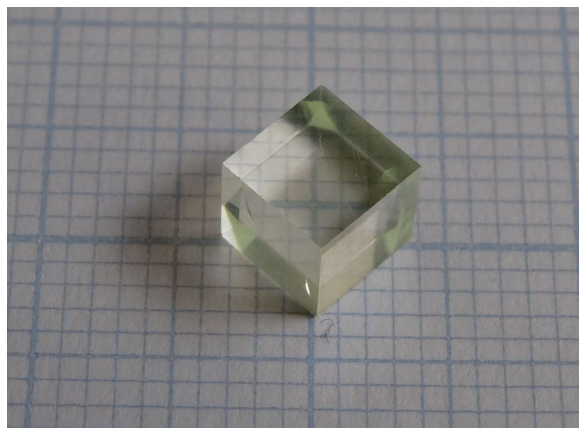
Figure 2.21   **Cut and polished KTW crystal, oriented to the indicatrix axes.**

2.1.7 Dy:CaYAlO₄ (Dy:CYA)

The $^6H_{15/2} \rightarrow {}^4I_{15/2}$ ground-state transition of Dy^{3+} around 450 nm fits the output wavelength of commercial InGaN LD pump sources, which usually exhibit broad band emissions with FWHM of 1.5-2 nm. Thus, host materials with suitably disordered rare-earth sites, which lead to inhomogeneously broaden spectral lines of the doping active ion, would be beneficial to increase the absorption efficiency of the pump. The tetragonal $CaYAlO_4$ (CYA) compound features a random distribution of Ca^{2+} and Y^{3+} over the same cation sites. Taking advantage of the inhomogeneous broadening, CYA has been extensively studied as host material for broad-band tunable Yb^{3+}-lasers [39,40]. In addition, single crystalline CYA has good thermal and mechanical properties. It has a moderate Mohs hardness around 7 making it easy to be processed. The small anisotropy of the thermal conductivities along a and c crystallographic axis, which are 3.7 and 3.3 $W \cdot m^{-1} \cdot K^{-1}$, respectively, plays down the possibility of cracking during the laser operation. Dy:CYA is thus considered as a promising laser gain medium for blue LD pumping. The crystallographic parameters as well as thermal and mechanical properties of CYA are summarized in Table 2.7.

Table 2.7   Crystallographic data selective physical properties of CYA [41–43].

Chemical formula	$CaYAlO_4$
Formula weight	219.96 g·mol^{-1}
Crystal system	Tetragonal
Space group	$I4/mmm$
Unit cell parameters (Å)	$a = 3.6451(1), c = 11.8743(6)$
Unit cell volume (Å^3)	157.77
Z	2
Theoretical density	4.640 g·cm^{-3}
Melting point	1810°C
Mohs hardness[a]	7.23 on (100) and 6.86 on (001)
Thermal expansion coefficient (10^{-6} K^{-1})	8 (along a-axis); 11 (along c-axis)
Thermal conductivity (W·m^{-1}·K^{-1})	3.7 (along a-axis); 3.3 (along c-axis)
Specific heat	0.593 J·g^{-1}·K^{-1}
Refractive index[b]	$n^2(\lambda) = 1 + A\lambda^2/(\lambda^2 - B)$

[a] Based on the analogue compound $CaGdAlO_4$.

[b] Sellmeier coefficients: $A_o = 2.64$; $A_e = 2.53$; $B_o = 11400\ nm^2$, and $B_e = 14400\ nm^2$.

The unit cell structure of CYA is illustrated in Figure 2.22 (a). The Al atoms occupy the vertices and body-centers of the unit cell and are coordinated with 6 oxygen atoms. The slightly disordered [AlO$_6$] octahedra orthogonally connect with each other in a vertex-sharing scheme and form a 2-D network, which is perpendicular to the c-axis. The Ca and Y atoms share the same 9-fold site with a C_{4v} symmetry. It yields two sets of four identical Ca/Y—O bonds (4×2.480 Å and 4×2.594 Å) and a unique Ca/Y—O bond with the shortest length of 2.259 Å (Figure 2.22 (b)). The [Ca/YO$_9$] polyhedra stack compactly via the 6-coordinate oxygen atoms within the [AlO$_6$] 2-D sheets. The Ca/Y atom is closely surrounded by the other nine Ca/Y atoms with distances ranging from 3.377 to 3.633 Å, as is shown in Figure 2.22 (c).
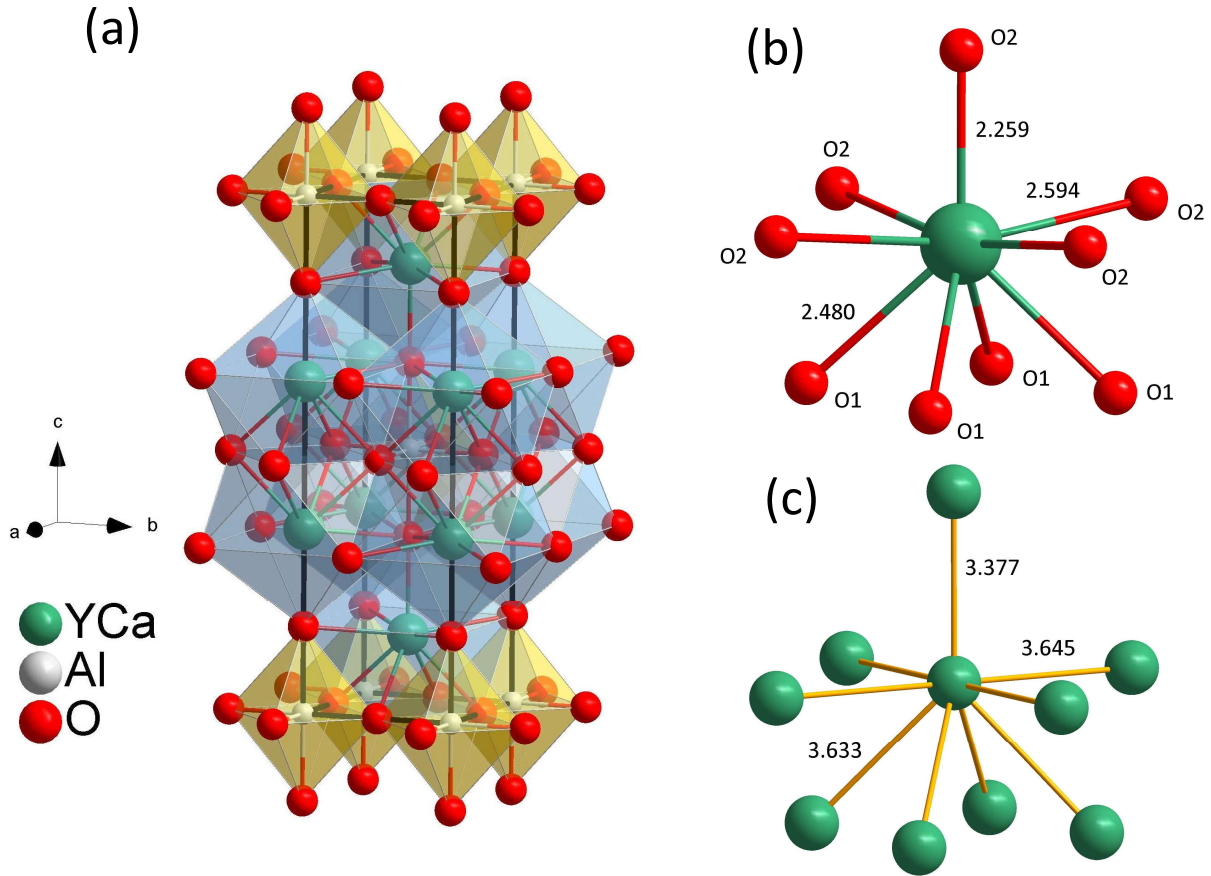
Figure 2.22 **Graphics showing: (a) crystal structure of the CaYAlO$_4$ unit cell (blue: [Ca/YO$_9$] polyhedron; yellow: [AlO$_6$] octahedron); (b) coordination environment of the Ca/Y site; (c) distances between the adjacent Ca/Y sites.**

To suppress the cross-relaxation processes, the doping concentration of Dy^{3+} has to be taken care. The designated doping concentration of Dy^{3+} in Dy:CYA was set to be 4.5×10^{20} cm^{-3}, which corresponds to a doping level of 3.54 at%. This value is designed to be similar to those in the reported Dy^{3+}-doped gain media [44–46]. The Dy:CYA polycrystals were synthesized by solid-state reaction. The powders of Dy$_2$O$_3$ (4N), Y$_2$O$_3$ (4N), CaCO$_3$ (2N5), and Al$_2$O$_3$ (4N) were ball milled, pressed, and sintered at 1400°C:

$$\frac{0.0354}{2} \text{Dy}_2\text{O}_3 + \frac{0.9646}{2}\text{Y}_2\text{O}_3 + \text{CaCO}_3 + \frac{1}{2}\text{Al}_2\text{O}_3 \xrightarrow{1400°C} \text{CaY}_{0.9646}\text{Dy}_{0.0354}\text{AlO}_4 + \text{CO}_2 \uparrow$$
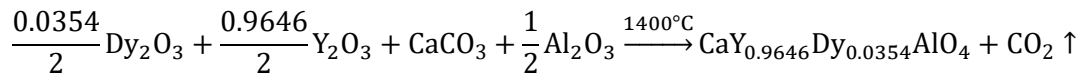
The duration of the sintering was 48 h. The as-synthesized polycrystalline materials exhibited a homogeneous brown color and their purity were verified by PXRD. The diffraction pattern indicates a pure phase, which is shown in Figure 2.23.
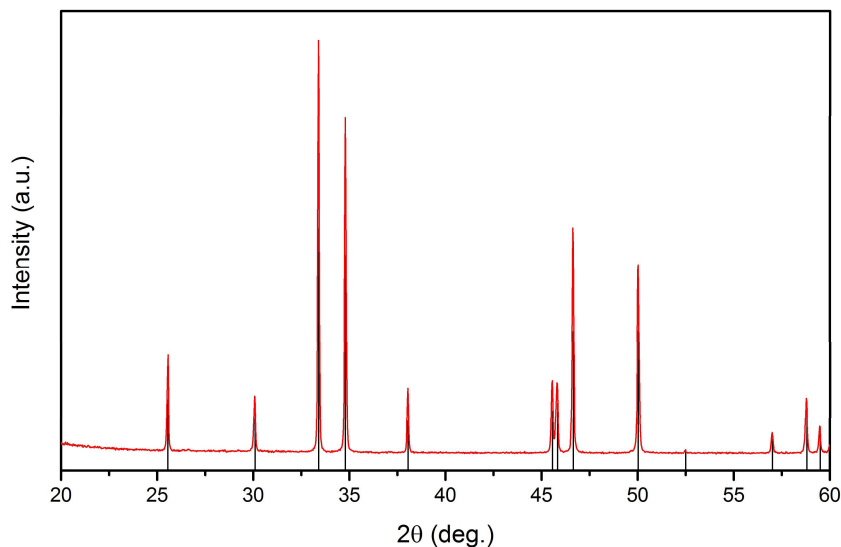
Figure 2.23   Powder X-ray diffraction pattern of the brown Dy:CYA polycrystals (reference ICCD code: 04-011-4753).

CYA has a congruent melting temperature around 1810°C. It is, however, prone to form color centers during the growth even in N_2 atmosphere [47–51]. The natural colorless crystal of CYA exhibits a wide transparency into middle UV spectral range (~200 nm) whereas the crystal with color center shows an additional absorption band starting from 600 nm to the UV [42]. During the laser operation, these color centers can not only absorb the pump and emission energy but also cause additional thermal effects. Xutang T. et. al. studied the origin of such color center formation, which universally takes place in the $ABCO_4$ (A= Ca, Sr, Ba; B = Y, Ln; C = Al, Ga) compounds [43]. Based on the experimental and calculated data, they were able to assign the additional absorption band to interstitial oxygen atoms in the lattice, as its absorption intensity increases with the increase of O interstitials, whereas decreases with the increase of O vacancies.

In order to circumvent the detrimental coloration, the Czochralski growth of Dy:CYA was performed in H_2/Ar reducing atmosphere. An iridium wire was used as a growth starter. The crucible was 50 mm in height and 50 mm in diameter. The pulling rate was controlled to gradually decrease from 1.0 mm/h (at the beginning of the neck part) to 0.6 mm/h (at the end of the shoulder part). Then the pulling rate was maintained to be 0.6 mm/h for the growth of body part. The rotation speed was kept constantly at 12 rpm. Noticeable fuming behavior of the melt was observed during the growth, which might be due to the evaporation of Al_2O_3 at high temperature. The cooling of the crystal lasted for 48 h after being separated from the melt.

The as-grown crystals are shown in Figure 2.24, which exhibit a naturally pale yellow color originating from Dy^{3+}. The growth orientation was found to be perpendicular to the crystallographic c-axis by X-ray diffraction. No scattering centers could be observed when passing a laser beam through the Dy:CYA crystals. However, a small amount of inclusions with particle size of a few microns could be observed inside the crystal under an optical microscope (Figure 2.24 (b)). These small-size inclusions, as well as

the rough surface of the boule, might be due to the evaporation during the growth process. The processed crystal samples are shown in Figure 2.24 (c).
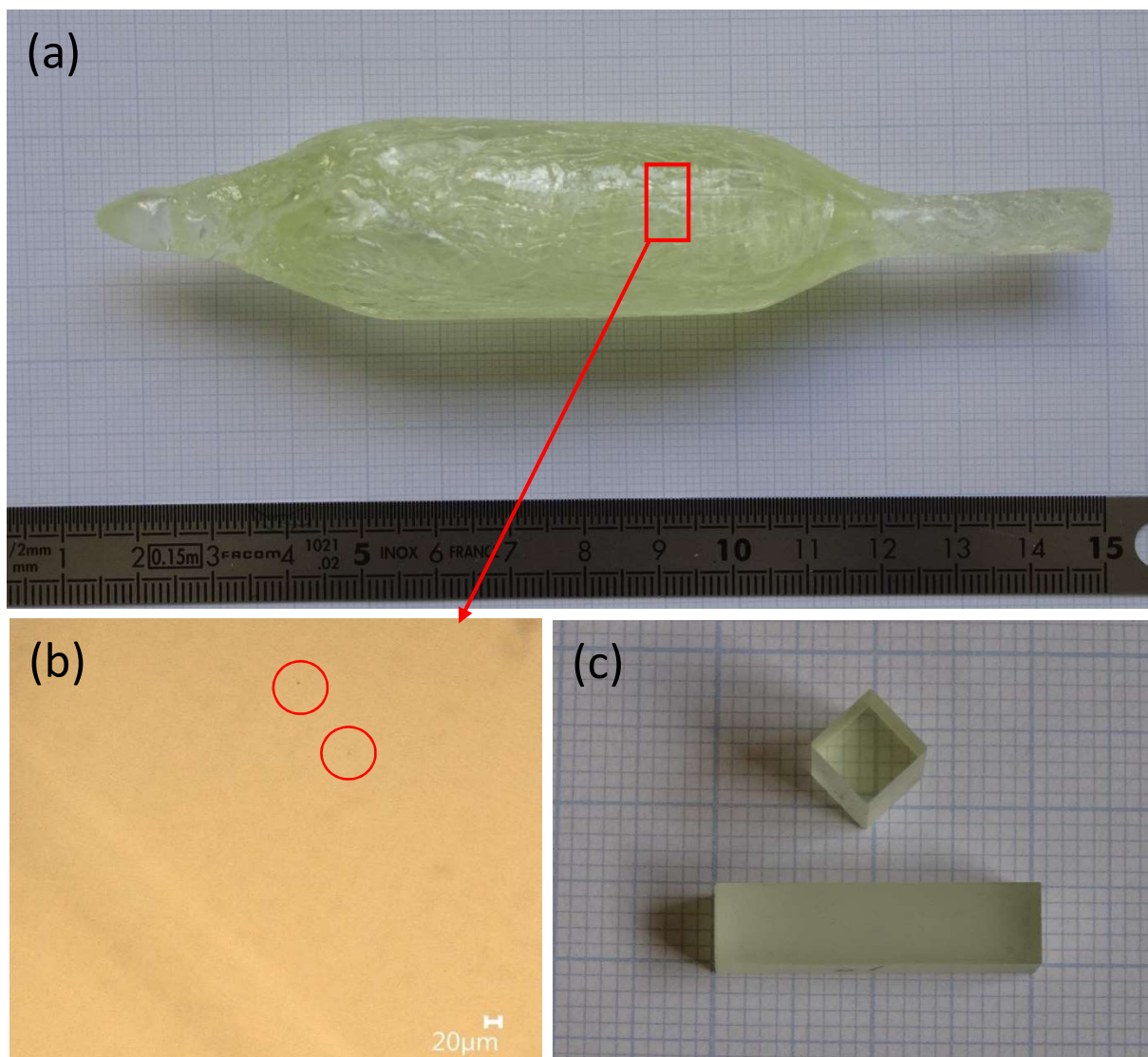
Figure 2.24 **(a) as-grown crystal of Dy:CYA; (b) observation of the small-size inclusions under a microscope; (c) cut and polished samples from the crystal (dimension: 5×5×10; 5×5×20 mm).**

Elementary analysis of the as-grown Dy:CYA crystals was performed by electron probe micro-analysis (EPMA). The Dy^{3+} concentrations of samples from different parts of the boule are summarized in Table 2.8. The segregation coefficient of Dy^{3+} ion in the CYA matrix was calculated to be 1.06 using the equation: $k = c_s/c_0$, where c_s is the concentration in the neck part and c_0 is the initial concentration in the melt. The segregation coefficient close to 1 suggests that the CYA matrix is very suitable for hosting Dy^{3+}. It results in a smooth concentration gradient and small stress inside the Dy:CYA crystals. The crystal sample for the spectroscopic studies was cut from the upper body part of the boule. The Dy^{3+} concentration in this sample was estimated to be 4.67×10^{20} cm^{-3}, corresponding to a doping level of 3.68 at%.

Table 2.8 **Concentration (in units of 10^{20} cm^{-3}) and doping level of dysprosium in different parts of the boule. The doping level was determined as the ratio of the dysprosium atoms to the total of the dysprosium and yttrium atoms.**

	Dy^{3+} concentration	Doping level (at%)
Neck	4.75	3.74
Upper part of body	4.67	3.68
Lower part of body	4.44	3.48
Residue melt	4.36	3.40

2.1.8 Dy:Ca$_2$Al$_2$SiO$_7$ (Dy:CAS)

Broadening of spectral lines in Dy^{3+}-activated materials would be beneficial for LD pumping owing to a better overlap of the optical bands. Lanthanide-doped gehlenite Ca$_2$Al$_2$SiO$_7$ (CAS) compounds are known for their broad spectral lineshape stemming from the disordered structure [52,53]. This character motivates us to study the spectroscopic property of Dy^{3+} in this matrix.

Table 2.9 **Crystallographic data and selective physical properties of CAS [54–57].**

Chemical formula	Ca$_2$Al$_2$SiO$_7$
Formula weight	219.96 g·mol^{-1}
Crystal system	Tetragonal
Space group	$P\bar{4}2_1m$
Unit cell parameters (Å)	$a = 7.685, c = 5.064$
Unit cell volume (Å^3)	299.05
Z	2
Theoretical density	3.045 g·cm^{-3}
Melting point	1583°C
Thermal expansion coefficient (10^{-6} K^{-1})	7.6 (along a-axis); 12.1 (along c-axis)
Thermal conductivity (W·m^{-1}·K^{-1})	2.2 (along c-axis)
Refractive index[a]	$n^2(\lambda) = 1 + A\lambda^2/(\lambda^2 - B)$

[a] Sellmeier coefficients: $A_o = 1.888$; $A_e = 1.857$; $B_o = 15389\ nm^2$, and $B_e = 14139\ nm^2$.

CAS crystallizes in the tetragonal $P\bar{4}2_1m$ space group (Table 2.9). The unit cell structure of CAS is illustrated in Figure 2.25 (a). The Al1 site, which occupies the vertex of the unit cell, yields four identical Al−O bonds and forms a regular tetrahedron. Another tetrahedral site is shared by Si and Al atoms with the same occupancy. This site connects to one O1, one O2, and two O3 atoms, and shows a C_s symmetry. The [AlO$_4$] and [Si/AlO$_4$] tetrahedra extend into a 2-D sheet along the a-b crystallographic

plane. The crystal structure of CAS can then be simply described as an alternative stacking of this 2-D network with that constituted by the [CaO$_8$] polyhedra (Figure 2.25 (b)). The 8-fold Ca site, which allows for doping with Ln^{3+}, exhibits a C_s symmetry (Figure 2.25 (c)). The average Ca$-$O bond length is 2.57 Å. The additional positive charge arising from introducing trivalent lanthanide ions to the divalent calcium ion site could be compensated by increasing the occupancy of Al in the Si/Al site in the following approach: $Ca_{2-x}Ln_xAl^1Al^2_{1+x}Si_{1-x}O_7$ (The superscript denotes Al atoms in different sites).

The Dy:CAS crystals, with a nominal doping level of 10%, were grown by N. Britos, a former PhD in our lab, with a slow pulling rate of 0.5 mm/h and fast rotations of 35-40 rpm [58]. Although containing noticeable scattering centers, the Dy:CAS crystal from the upper body part of the boule have enough good optical quality for the following spectroscopic studies. Based on the EPMA results, the Dy^{3+} concentration in the sample cut from the upper body part of the boule is 8.07 × 10^{20} cm^{-3}, corresponding to a doping level of 12.1 at%.
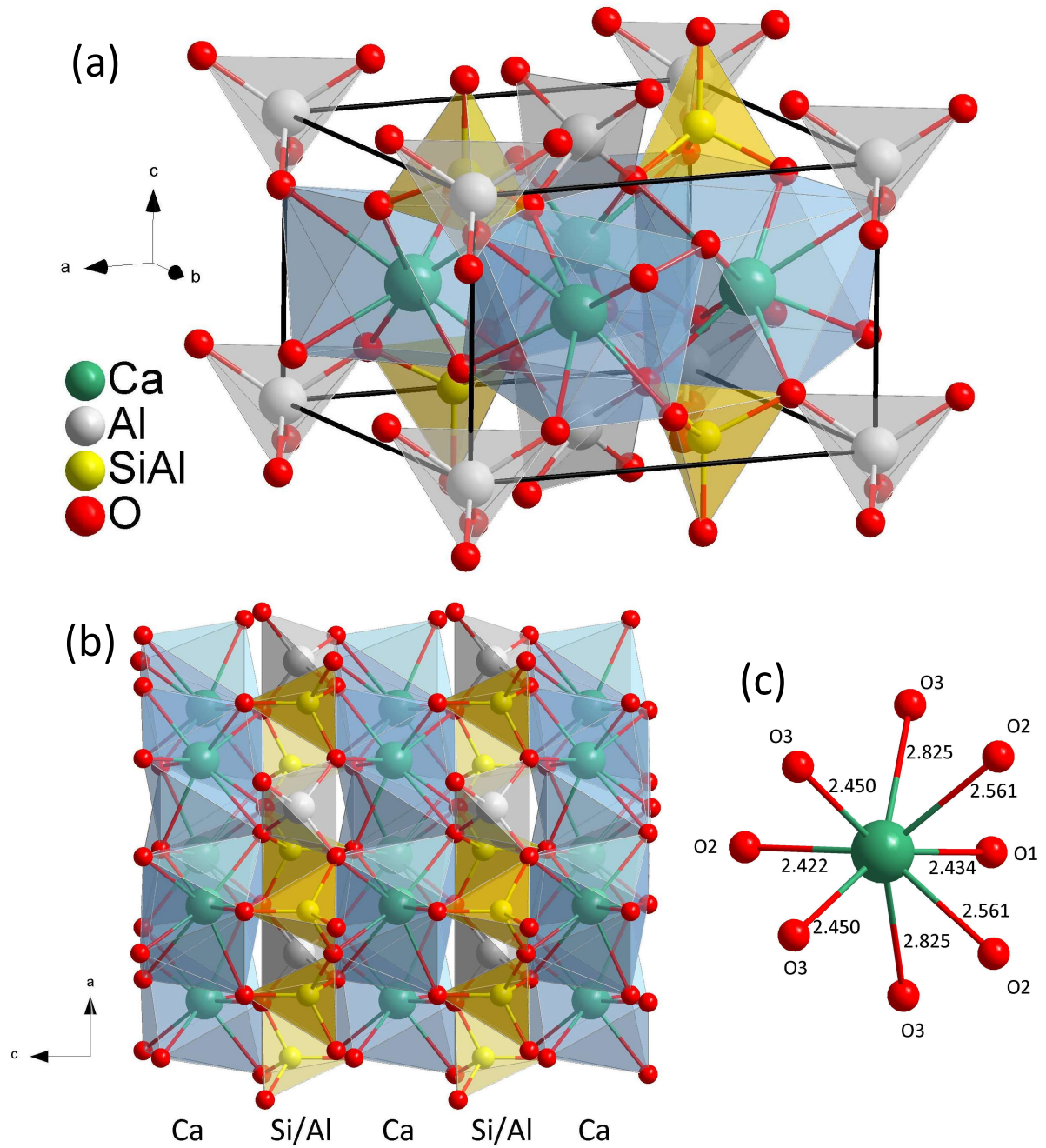
Figure 2.25 **Graphics showing: (a) crystal structure of the $Ca_2Al_2SiO_7$ unit cell (blue: $[CaO_8]$ polyhedron; grey: $[AlO_4]$ tetrahedron; yellow: $[Si/AlO_4]$ tetrahedron); (b) stacking mode of the $[CaO_8]$, $[AlO_4]$, and $[Si/AlO_4]$ polyhedra; (c) coordination environment of the Ca site.**

2.1.9 Dy:$Ca_4YO(BO_3)_3$ (Dy:YCOB)

$YCa_4O(BO_3)_3$ (YCOB) is isostructal to $TbCa_4O(BO_3)_3$, the crystallographic properties of which have been discussed in subsection 2.1.5. The crystallographic data and thermal properties of YCOB can be found in Table 2.10. Here we directly introduce the fabrication procedure of Dy:YCOB. The polycrystalline

79

materials were synthesized with a nominal doping ratio of Dy^{3+} of 10%, which corresponds to a concentration of 4.5×10^{20} cm^{-3} in the matrix. The solid-state reaction can be described by the chemical formula below:

$$\frac{0.1}{2}Dy_2O_3 + \frac{0.9}{2}Y_2O_3 + 4CaCO_3 + 3H_3BO_3 \xrightarrow{1300°C} Ca_4Y_{0.9}Dy_{0.1}(BO_3)_3 + 4CO_2 \uparrow + \frac{9}{2}H_2O \uparrow$$
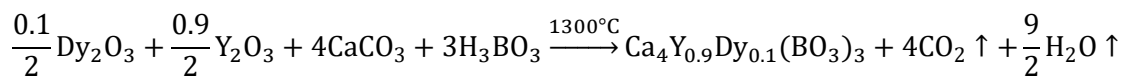
The synthesis was carried out with an additional amount (4 wt%) of H_3BO_3 to compensate the evaporation of B_2O_3 during the sintering. The as-sintered products showing a color in orange were found to be almost pure phase by PXRD. The pattern is shown in Figure 2.26. The weak parasitic peaks could be attributed to incompletely reacted Y_2O_3 species.

Table 2.10   Crystallographic data and selective physical properties of YCOB [59–62].

Chemical formula	$YCa_4O(BO_3)_3$
Formula weight	441.64 g·mol^{-1}
Crystal system	Monoclinic
Space group	Cm
Unit cell parameters (Å)	$a = 8.094, b = 15.959, c = 3.517, \beta = 101.19$
Unit cell volume (Å^3)	446.93
Z	2
Theoretical density	3.310 g·cm^{-3}
Melting point	1510°C
Mohs hardness	6.0-6.5
Thermal expansion coefficient (10^{-6} K^{-1})	9.9 (along a); 8.2 (along b); 12.8 (along c)
Thermal conductivity (W·m^{-1}·K^{-1})	1.83 (along a); 1.72 (along b); 2.17 (along c)
Specific heat	0.730 J·g^{-1}·K^{-1} (373 K)
Refractive index^a	$n^2(\lambda) = A + \dfrac{B}{\lambda^2 - C} - D\lambda^2$

^{a} Sellmeier coefficients: $A_x = 2.767$; $A_y = 2.873$; $A_z = 2.911$; $B_x = 20470\ nm^2$, $B_y = 22590\ nm^2$, $B_z = 22420\ nm^2$; $C_x = 18630\ nm^2$, $C_y = 17100\ nm^2$, $C_z = 18730\ nm^2$; $D_x = 6250\ nm^{-2}$, $D_y = 9210\ nm^{-2}$, $D_z = 12350\ nm^{-2}$.
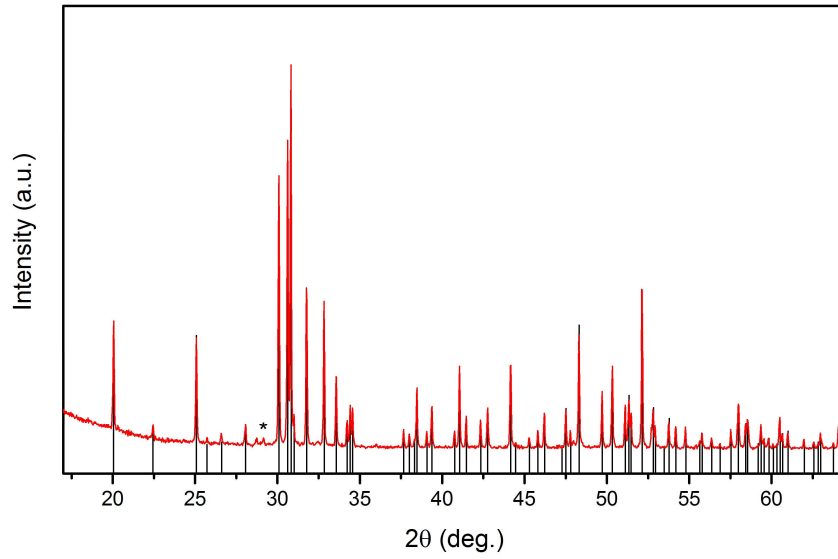
Figure 2.26   **Powder X-ray diffraction pattern of the brown Dy:YCOB polycrystals (reference ICCD code: 01-070-8121; * cubic Y_2O_3 phase).**

The growth conditions of Dy:YCOB are very similar to those of TbCOB, except that pure argon was used as protection atmosphere. Photographs showing the Dy:YCOB crystals are presented in Figure 2.27. The as-grown crystal has an overall good optical quality. However, some particle-like inclusions could be observed in the upper body part of the boule under a microscope. Similar to TbCOB, we found significant bulk scattering centers aggregating at the end of the body part and the bottom part.
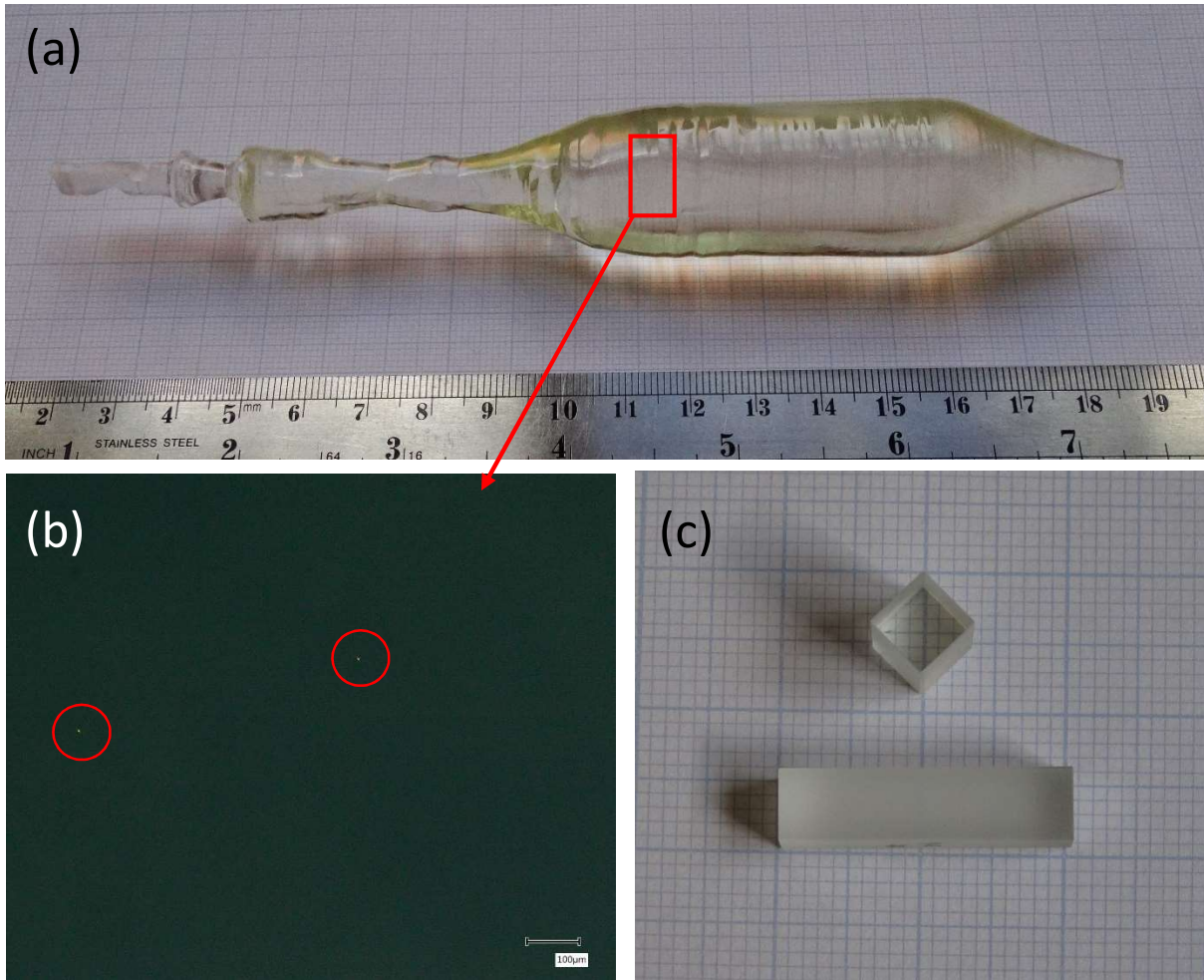
Figure 2.27 **(a) as-grown crystal of Dy:YCOB; (b) under a microscope; (c) cut and polished samples from the crystal (dimension: 5×5×10; 5×5×20 mm).**

EPMA was performed on different parts of the Dy:YCOB boule crystal to estimate the chemical compositions. The resulting data are summarized in Table 2.11. The segregation coefficient of Dy^{3+} was estimated to be 0.86 by comparing the concentration in the neck part and the initial concentration in the melt. It is worth noting that this value is smaller than 1, while the segregation coefficient of Dy^{3+} in CYA is slightly larger than 1. The crystal sample for the spectroscopic studies was cut from the upper body part of the boule, the Dy^{3+} concentration of which is around 3.86×10^{20} cm^{-3}.

Table 2.11 **Concentration (in units of 10^{20} cm^{-3}) and doping level of dysprosium in different parts of the boule. The doping level was determined as the ratio of the dysprosium atoms to the total of the dysprosium and yttrium atoms.**

	Dy^{3+} concentration	Doping level (at%)
Neck	0.385	8.59
Upper part of body	0.386	8.61
Lower part of body	0.401	8.94
Residue melt	0.431	9.60

2.2 Color center formation

Formation of color centers were observed during the growth of terbium-based crystals in the air atmosphere. The additional absorption bands in the visible range can dissipate the excitation energy, quench the luminescent emission, and cause detrimental thermal effects. Therefore, for visible laser or luminescence applications using Tb^{3+}-activated materials, absence of any color centers is required. As a matter of fact, all the polycrystalline raw materials, synthesized in air, showed more or less some yellow or orange color. The phenomena of a dark color, rather than the original color of the compound itself, have been widely reported in crystals that tend to form lattice defects, such as $REAlO_3$ and $CaREAlO_4$ [42,63,64]. This character, however, does not depend on the rare-earth ion in the lattice. The crystal growths of the analogue compounds of STB and LTB under air atmosphere are documented, such as $Sr_6GdSc(BO_3)_6$ and $Li_6Gd(BO_3)_3$ [28,65]. The as-grown crystals in these literatures did not exhibit such color-center formation. This could exclude that the dark color is derived from crystal defects. Terbium-based crystals grown in air, on the other hand, were reported to feature color in yellow or red, such as TAB, KTW, $NaTb(MoO_4)_2$, and $Na_2Tb_4(MoO_4)_7$ [22,66–68]. Therefore, in the first place, we attribute the dark color to the oxidation of Tb^{3+} to metastable Tb^{4+} ion during the crystal preparation.

After annealing as-grown crystals of STB1 and LTB1 under H_2/Ar reducing atmosphere, a change of the color could be observed. The absorption spectra of the crystals before and after annealing are shown in Figure 2.28. The STB and LTB crystals grown in air show broad absorption bands rising from around 600 nm into the UV, which disappeared after annealing in H_2/Ar. The LTB crystal before annealing, which is pale yellow in color, showed much weaker intensity of this absorption band compared to the red STB. This could be explained by the much lower reaction and growing temperature of LTB than STB. Free-ion Tb^{4+}, which has the same electronic structure as Gd^{3+}, does not possess any $4f \rightarrow 4f$ transitions in the visible spectral range [69]. However, similar broad absorption bands can be found in solid or aqueous tetravalent terbium compounds, such as $SrTbO_3$ and TbP_4O_{12}, and are considered to be derived from Tb^{4+} [70–72]. Nevertheless, it should be pointed out that these additional absorption bands can also originate from the lattice defects induced by Tb^{4+} with an excessive positive charge.
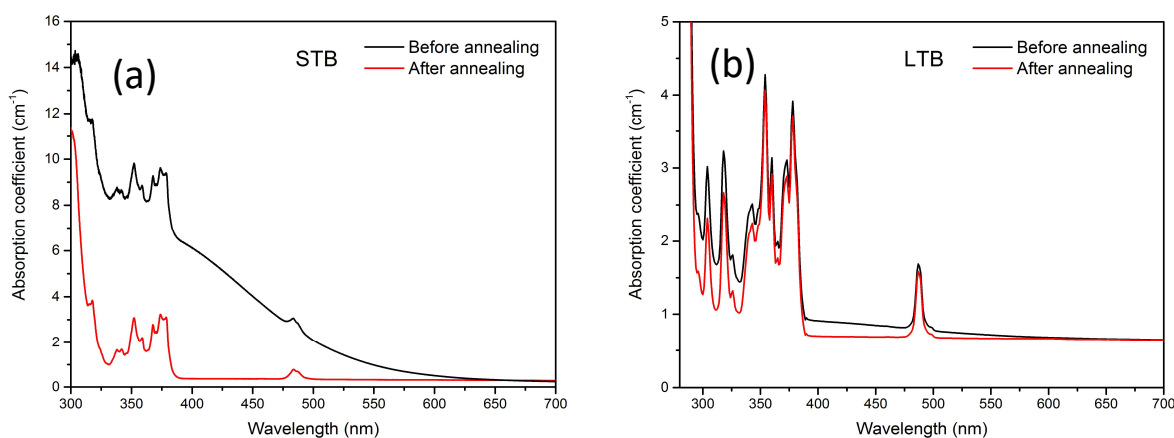
Figure 2.28 **Absorption spectra of the crystals before and after annealing in H_2/Ar atmosphere: (a) STB; (b) LTB.**

83

To figure out the origin of the color centers, electron paramagnetic resonance (EPR) spectroscopy characterization was performed. The EPR signals of all the Ln^{3+} ions except Gd^{3+}, can be detected only under cryogenic conditions because of the well-known rapid spin-lattice relaxation [73]. Gd^{3+}, as well as its isoelectronic Tb^{4+}, is a Kramers ion that possess a half-filled $4f$ orbital with a ground-state term of ^8S. This makes it possible to measure the EPR spectrum of Tb^{4+} at room temperature. On the other hand, the Tb^{3+} ion existing in these matrices is not EPR-active at room temperature. Therefore, the presence of Tb^{4+} could be verified from the EPR spectroscopy of the crystals.
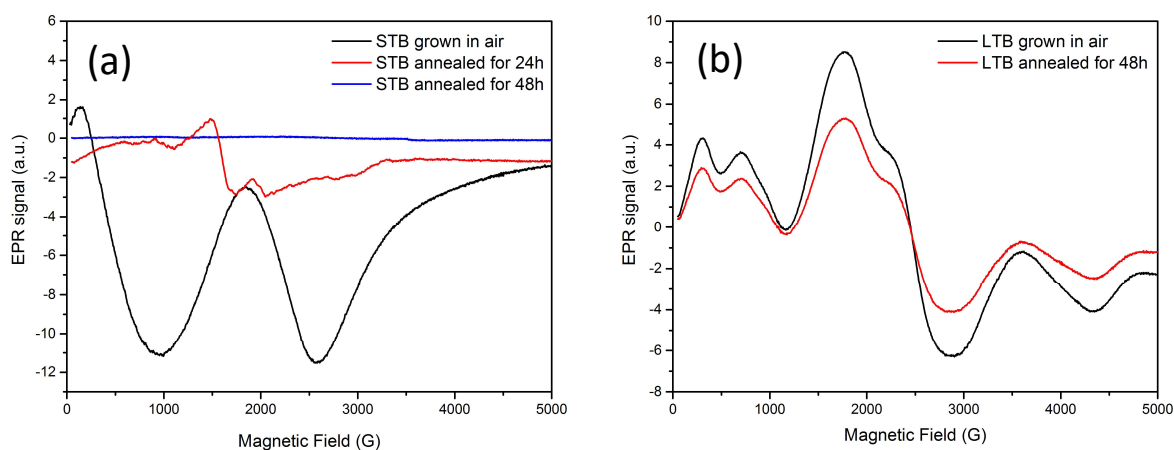
Figure 2.29 **Room-temperature EPR spectra of the ground crystals before and after annealing in H₂/Ar atmosphere: (a) STB; (b) LTB.**

X-band EPR spectra (Bruker ELEXSYS E500) were recorded at room temperature using ground powder samples from different batches of the growth. The measurements were performed under the same condition and the spectral intensities were calibrated so that the resulting data are comparable. EPR spectra of STB1 and LTB1, which were grown in air, and their annealed samples are illustrated in Figure 2.29. The as-grown crystals show intense broad-band signals. Referring to the EPR spectra of the tetravalent terbium compounds of $BaTbO_3$ and $SrTbO_3$, the signals originating from Tb^{4+} have linewidth more than 1000 G [74]. After annealing in H₂/Ar atmosphere for 48 h, the EPR bands of the STB sample disappeared whereas those of LTB became weaker. Measurements were also carried out using the BTP sample grown in argon, as well as STB2, LTB2, and TbCOB crystals grown in the reducing atmosphere. The resulting data are shown in Figure 2.30. No significant broad-band signals could be detected. This suggests the absence of Tb^{4+} in these samples, which is in line with the observation that they are almost colorless. From these results, we can draw the conclusion that the formation of color centers is related to the oxidation of Tb^{3+} to Tb^{4+}.

The actual mechanism of the oxidation of Tb^{3+} in the crystalline matrices is complicated and could be structure-dependent. Tb^{4+} ions can enter the lattice while crystallization. The additional positive charge generated by Tb^{4+} occupying the Tb^{3+} site could be compensated by introducing lower-valence ions, in our cases, Ba^{2+}, Sr^{2+}, or Ca^{2+} into the Tb^{3+} site. Take STB as an example, the actual composition might be $Sr_{(3+x)}Tb_{(1-x)}(III, IV)(BO_3)_3$ with additional Sr^{2+} occupying the Tb^{3+} site. Also, Tb^{3+} in the crystals may be oxidized in air at a high temperature, accompanying the formation of interstitial oxygen. Here, we

propose a feasible scheme expressed by Kröger–Vink notation (the interstitial oxygen could occur in various forms):

$$\mathrm{Tb}^{\times}_{\mathrm{Tb}^{3+}} + \frac{1}{4}\mathrm{O}_2 \rightarrow \mathrm{Tb}^{\bullet}_{\mathrm{Tb}^{3+}} + \frac{1}{2}\mathrm{O}''_i$$

or

$$\mathrm{Tb}^{\times}_{\mathrm{Tb}^{3+}} + \frac{1}{2}\mathrm{O}_2 \rightarrow \mathrm{Tb}^{\bullet}_{\mathrm{Tb}^{3+}} + \mathrm{O}'_i$$
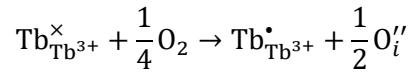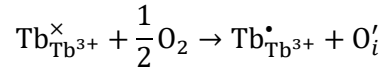
The reducing process by H_2 could be written as:

$$\mathrm{Tb}^{\bullet}_{\mathrm{Tb}^{3+}} + \frac{1}{2}\mathrm{O}''_i + \frac{1}{2}\mathrm{H}_2 \rightarrow \mathrm{Tb}^{\times}_{\mathrm{Tb}^{3+}} + \frac{1}{2}\mathrm{H}_2\mathrm{O}$$

or

$$\mathrm{Tb}^{\bullet}_{\mathrm{Tb}^{3+}} + \frac{1}{2}\mathrm{O}^{\times}_{\mathrm{O}^{2-}} + \frac{1}{2}\mathrm{H}_2 \rightarrow \mathrm{Tb}^{\times}_{\mathrm{Tb}^{3+}} + \frac{1}{2}\mathrm{V}^{\bullet\bullet}_{\mathrm{O}^{2-}} + \frac{1}{2}\mathrm{H}_2\mathrm{O}$$
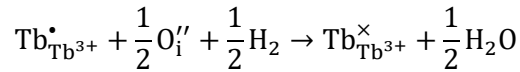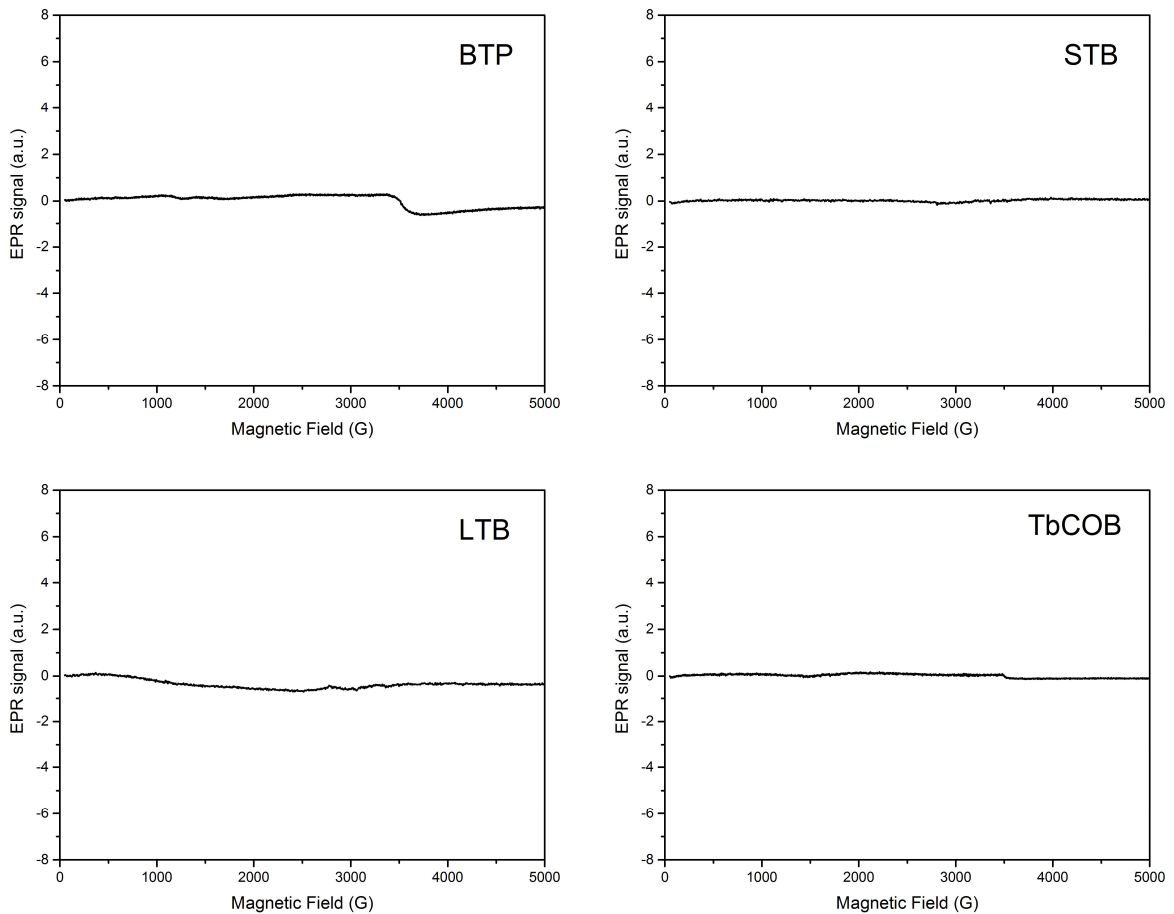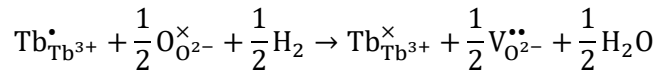
Figure 2.30   **EPR spectra of (a) the BTP crystal grown in argon; (b), (c), (d) the STB, LTB, TbCOB crystals grown in H₂/Ar atmosphere.**

85

2.3 Thermal properties

The thermal properties of a laser gain material are of great important, especially thermal conductivity and thermal expansion. Heating of the gain medium during the laser operation can be problematic. The gain material with a small thermal conductivity leads to a large radial thermal gradient perpendicular to the lasing direction, which further gives rise to detrimental thermal lensing effects or even cracking. A large thermal conductivity is favorable particularly for high-power lasers. On the other hand, the thermal shock resistance parameter is inversely proportional to the second power of thermal expansion coefficient. Thus, a too-large thermal expansion of the gain materials makes it vulnerable to thermal shocks. A significant anisotropy with respect to the thermal expansion coefficients may also result in cracking. Detailed experimental procedures in this section are given in Appendix B.

2.3.1 Thermal conductivity, effusivity and specific heat capacity

Thermal conductivity as well as effusivity of the bulk crystal samples were measured at room temperature by a TCi thermal conductivity analyzer. The resulting data are listed in Table 2.12. With these values, the specific heat capacity was calculated via the following formula:

$$e = (\kappa \cdot \rho \cdot C_p)^{1/2} \tag{2.1}$$

where e is the thermal effusivity, κ is the thermal conductivity, ρ is the theoretical density, and C_p is the specific heat capacity.

Table 2.12   **Thermal conductivity, effusivity, and specific heat capacity of the terbium-based single crystals at room temperature.**

Matrices	Thermal conductivity (W·m^{-1}·K^{-1})	Thermal effusivity (kW·s$^{-1/2}$·m^{-2}·K^{-1})	Specific heat capacity (J·kg^{-1}·K^{-1})
BTP	0.65	1.17	427
STB (along c-axis)	1.11	1.46	402
LTB (arbitrary orientation)	2.97	2.48	628
TbCOB (along b-axis)	1.92	1.92	510

The thermal conductivity of BTP was measured to be as low as 0.65 W·m^{-1}·K. However, LTB gives a decent value of 2.97 W·m^{-1}·K^{-1}, which is greater than many other borates such as GdCa$_4$O(BO$_3$)$_3$ (2.2 W·m^{-1}·K^{-1}), Ca$_3$La$_2$(BO$_3$)$_4$ (0.5 W·m^{-1}·K^{-1}), Sr$_3$Y$_2$(BO$_3$)$_4$ (0.8 W·m^{-1}·K^{-1}), and β-BaB$_2$O$_4$ (1.4 W·m^{-1}·K^{-1}) [75–78]. R. Gaumé and co-workers developed a model for estimating the thermal conductivity of insulating crystals with overall relative errors less than 50%. The relationship between thermal conductivity and a couple of physical properties is found to be [79]:

$$\kappa = \frac{1}{T} \cdot \frac{A}{\gamma^2 \varepsilon^3} \cdot T_{mp}^{3/2} \cdot \rho^{2/3} \cdot M^{1/3} \cdot n^{-1/3} \cdot \mu^{-3/2} \qquad (2.2)$$

where $\frac{A}{\gamma^2 \varepsilon^3}$ is a constant of 7.53×10^{-7} for ionocovalent materials, T_{mp} is the melting temperature, M is the molar mass, n is number of atoms per formula unit, and μ is the reduced mass, which is the harmonic average of all ion masses of the formula unit (covalent groups like $[PO_4]^{3-}$ and $[BO_3]^{3-}$ are treated as entity).

Based on the equation 2.2, the thermal conductivity of BTP, STB, LTB, and TbCOB at 293 K were calculated to be, respectively, 0.71, 0.78, 5.2, and 1.7 W·m^{-1}·K. These values are overall consistent with the experimental data. One can also notice that according to Gaumé's model, κ is inversely proportional to the reduced mass to 1.5th power, which plays a main role in determining the value of κ. This could explain the exceptionally large thermal conductivity of LTB by the large contribution from the light Li atoms to its chemical formula unit. Moreover, LTB also features the largest thermal effusivity, which characterizes the capability of a material to exchange thermal energy with its surroundings.

2.3.2 Thermal expansion

Thermal expansion refers to a change in size of matter in response to a change in temperature. It is usually quantified by the linear or volumetric thermal expansion coefficients defined as:

$$\alpha_L = \frac{1}{L}\frac{dL}{dT} \qquad (2.3)$$

and
$$\alpha_V = \frac{1}{V}\frac{dV}{dT} \qquad (2.4)$$

They can be calculated from the variation of crystallographic unit cell parameters at different temperatures. This method starts with the measurements of PXRD patterns at different temperatures. Then the temperature-dependent lattice parameters can be obtained by profile-matching refinement of the PXRD patterns. As an example, the PXRD patterns of BTP obtained from 298 to 1073 K are depicted in Figure 2.31. All the recorded diffraction peaks exhibit shifts to smaller 2θ with increasing temperature. This indicates that the lattice intervals in BTP increase simultaneously at higher temperature.
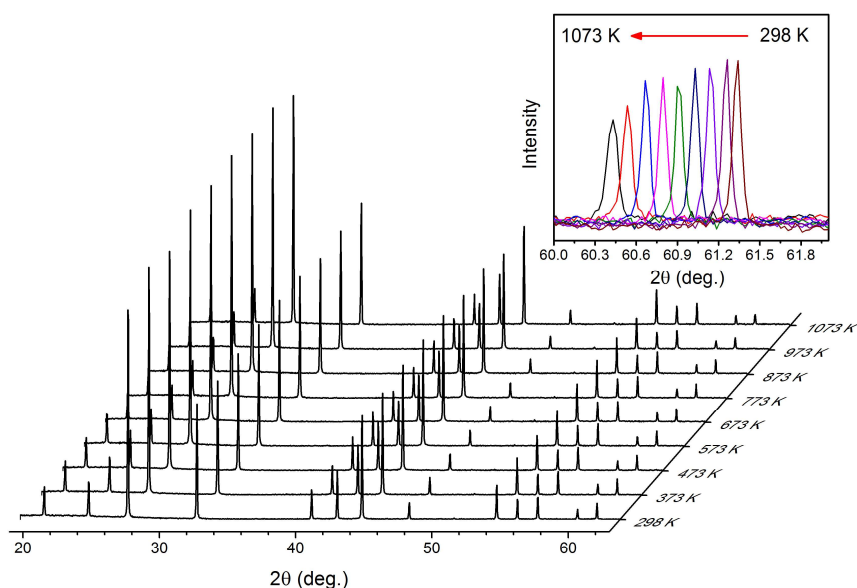
Figure 2.31   **PXRD patterns of BTP at different temperatures; the inset shows the variation of the (444) diffraction peak.**

The refined cell parameters of BTP, STB, TAB, LTB, TbCOB, and KTW at different temperatures are shown in sequence in Figure 2.32 to Figure 2.37. All the samples for the PXRD measurements were prepared from the single crystals. The thermal expansion coefficient of BTP along the crystallographic axis, which exhibits a linear behavior within the measured temperature range, was calculated to be 17.6×10^{-6} K^{-1} at room temperature. This value is comparable to the other eulytite phosphates such as Sr:Ba$_3$La(PO$_4$)$_3$ (17.7×10^{-6} K^{-1}) and Ba$_4$(PO$_4$)$_2$SO$_4$ (18.2×10^{-6} K^{-1}) [80,81]. However, it is larger than the other well-developed cubic materials such as Y$_3$Al$_5$O$_{12}$ (6.13×10^{-6} K^{-1}), Gd$_3$Ga$_5$O$_{12}$ (9.0×10^{-6} K^{-1}), and KY$_3$F$_{10}$ (14.5×10^{-6} K^{-1}) [82–84].

A linear fit of the cell parameter a of STB yields an expansion coefficient of 19.4×10^{-6} K^{-1} at room temperature. However, the variation of cell parameter c features significant nonlinear behavior at $T > 873\,K$. This phenomenon was not observed in its analogue compounds such as Er:Sr$_3$Y(BO$_3$)$_3$ and Yb:Sr$_6$ScY(BO$_3$)$_6$ [85,86]. Excluding the data at $T > 873$ K, the thermal expansion coefficient along c-axis was fitted to be 6.8×10^{-6} K^{-1}. The obtained α_L values along a- and c-axis are close to those measured with Er:Sr$_3$Y(BO$_3$)$_3$ in the literature [85], which are 19.6×10^{-6} K^{-1} and 7.1×10^{-6} K^{-1}, respectively. The volumetric coefficient α_V was calculated to be 45.1×10^{-6} K^{-1}.

The cell parameter b of LTB exhibits a constant growth in the measured temperature range. On the other hand, the cell parameter a shows an accelerating augment at higher temperatures whereas c displays a decelerating augment. This trend was also observed with Li$_6$Eu(BO$_3$)$_3$ [87], indicating that it is probably irrelevant to the oxidation of Tb^{3+} in air. In spite of this, the expansion of the cell volume is linear, yielding $\alpha_V = 47.8 \times 10^{-6}$ K^{-1}. The expansion coefficients along the crystallographic axes at room temperature were calculated to be $\alpha_a = 12.7 \times 10^{-6}$ K^{-1}, $\alpha_b = 22.5 \times 10^{-6}$ K^{-1}, and $\alpha_c = 15.9 \times 10^{-6}$ K^{-1}. These values are quite large and might account for the cracking of the LTB2 crystal.

The thermal expansion coefficients of TAB, TbCOB, and KTW are listed in Table 2.13, together with those of the above compounds. These data exhibit an overall linear behavior and are comparable to those of their analogue compounds of $YAl_3(BO_3)_4$ ($\alpha_a = 3.88 \times 10^{-6}$ K^{-1}, $\alpha_c = 12.5 \times 10^{-6}$ K^{-1}), GdCOB ($\alpha_a = 10.5 \times 10^{-6}$ K^{-1}, $\alpha_b = 8.3 \times 10^{-6}$ K^{-1}, $\alpha_c = 14.7 \times 10^{-6}$ K^{-1}), and KGdW ($\alpha_a = 13.6 \times 10^{-6}$ K^{-1}, $\alpha_b = 2.8 \times 10^{-6}$ K^{-1}, $\alpha_c = 22.8 \times 10^{-6}$ K^{-1}) [88–90].

Table 2.13   Linear and volumetric thermal expansion coefficients (valid for T $<$ 673 K, in unit of 10^{-6} K^{-1}).

Matrices	α_a	α_b	α_c	α_V
BTP	17.6	17.6	17.6	52.8
STB	19.4	19.4	6.8	45.1
TAB	3.9	3.9	11.9	19.7
LTB	12.7	22.5	15.9	47.8
TbCOB	12.1	7.7	14.2	32.9
KTW	13.7	2.2	25.1	37.2

Among these six terbium-based materials, TAB has the smallest α_V and the thermal expansion coefficients of TbCOB feature the smallest anisotropy (except for BTP). These two matrices should be less likely to suffer cracking during the crystal growth or laser operation. On the other hand, the thermal expansion coefficients STB, LTB, and KTW are relatively large and strongly anisotropic. The anisotropy of α is particularly pronounced along the b- and c-axis of KTW with more than an order of magnitude's difference. Control of the incident power and cooling of these crystals during the laser operation should be concerned.
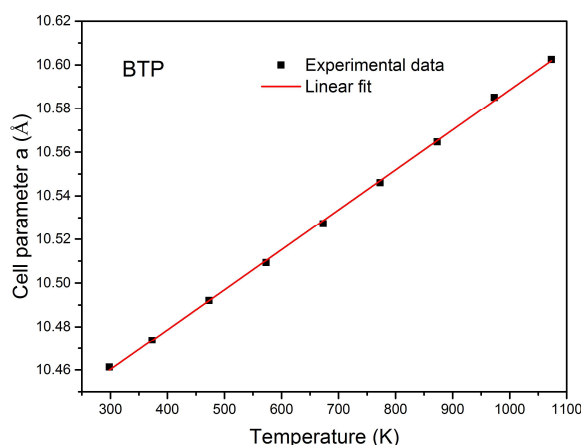
Figure 2.32   Variation of the cell parameter of BTP with temperature.
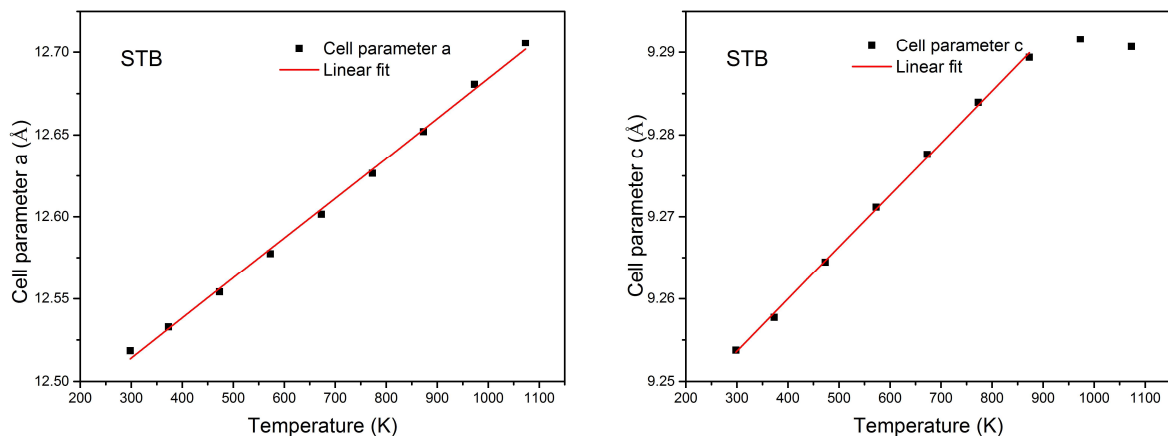
Figure 2.33   **Variation of the cell parameters of STB with temperature.**
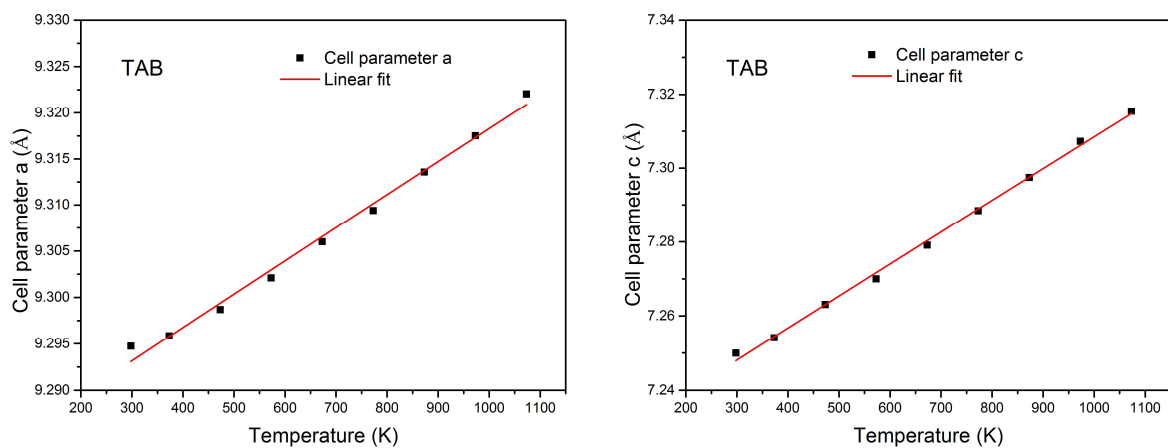
Figure 2.34   **Variation of the cell parameters of TAB with temperature.**
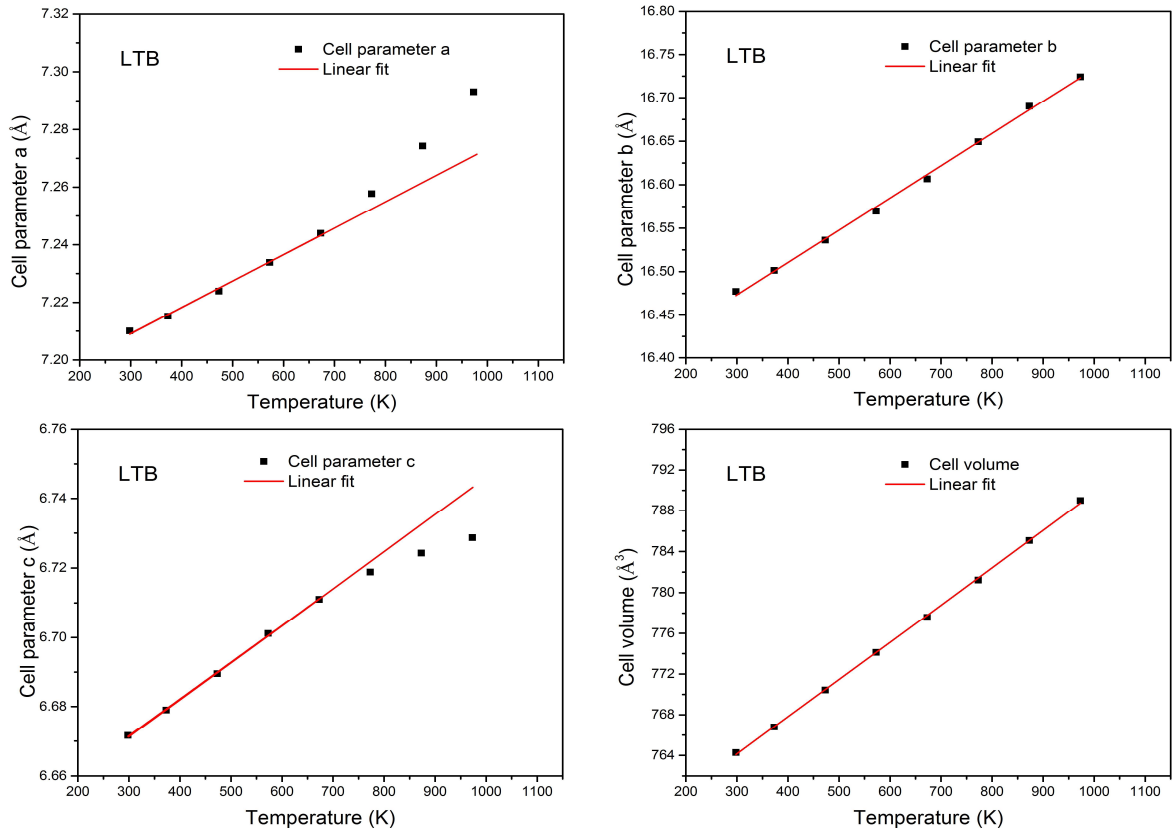
Figure 2.35   Variation of the cell parameters of LTB with temperature.
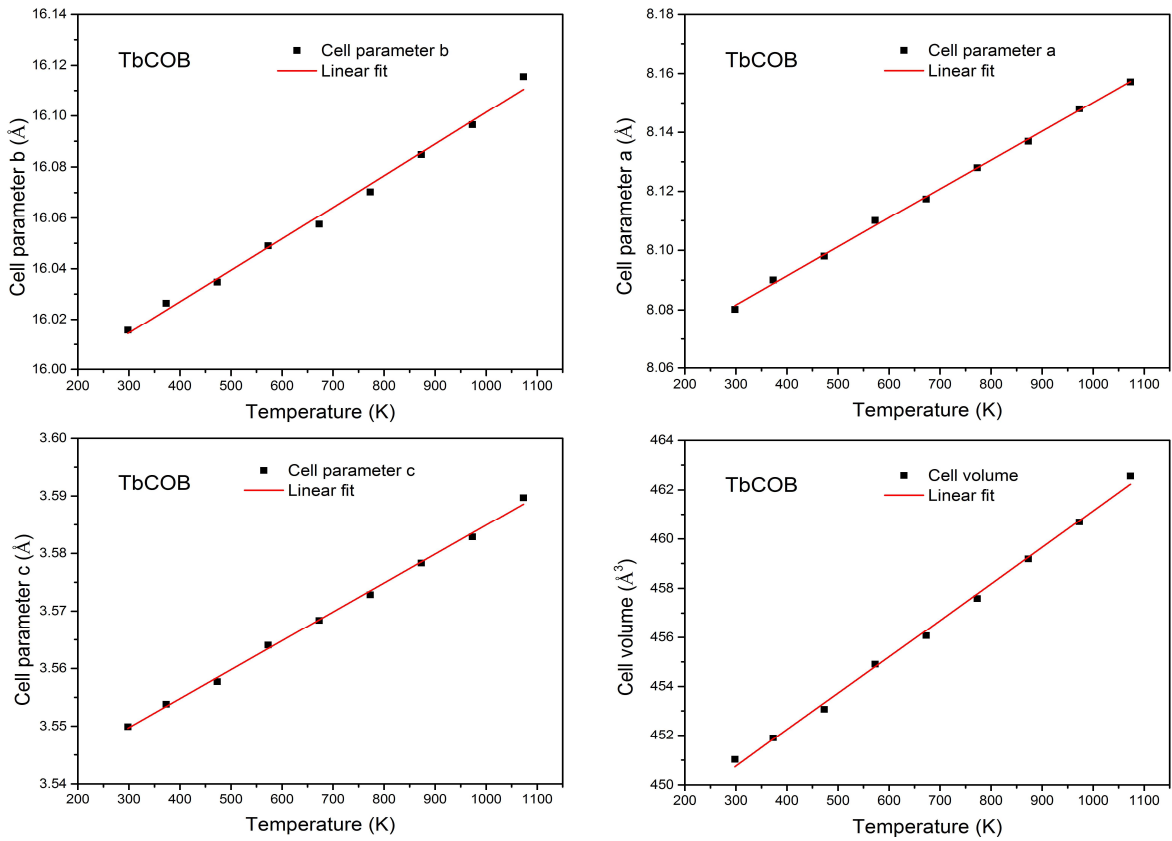
Figure 2.36   Variation of the cell parameters of TbCOB with temperature.
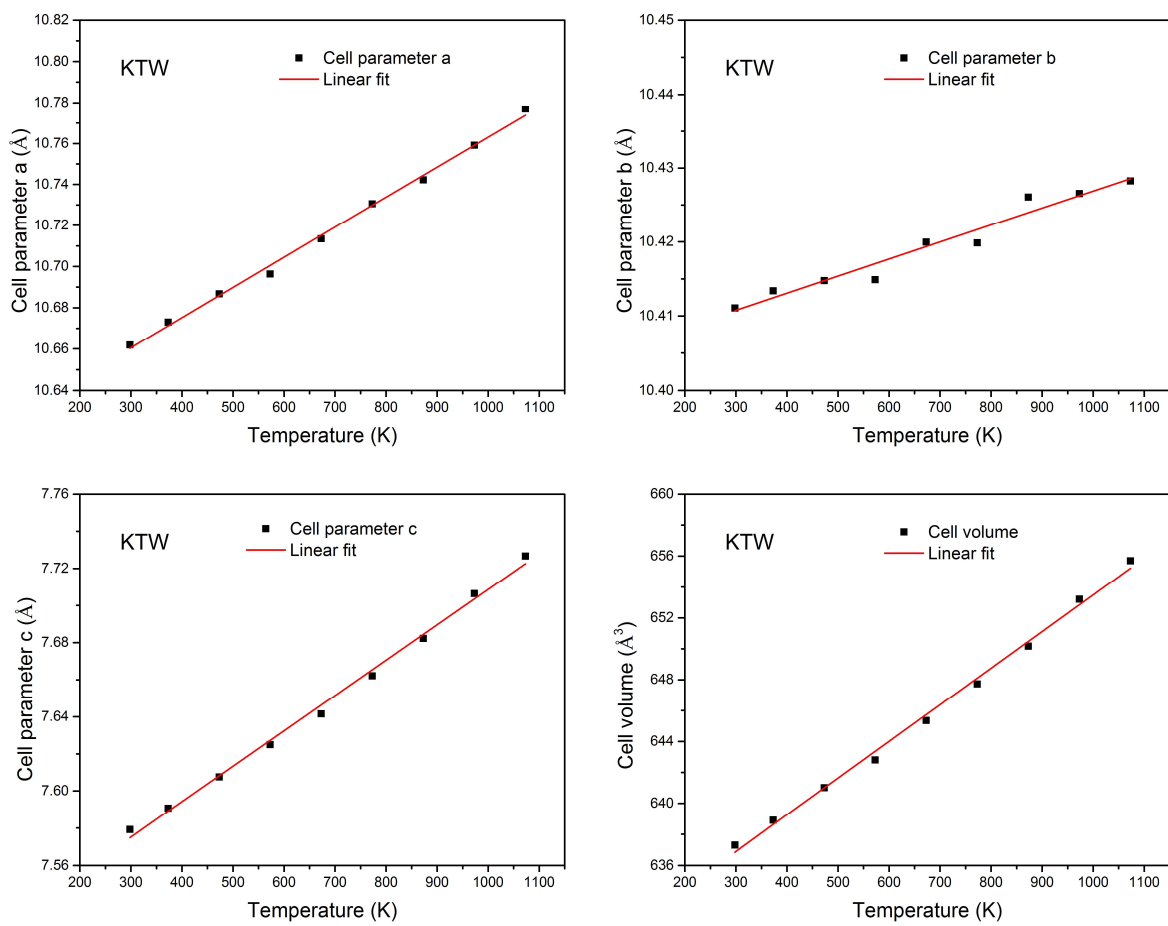
Figure 2.37   **Variation of the cell parameters of KTW with temperature.**

2.4   Conclusion of Chapter 2

Several Tb^{3+}- as well as Dy^{3+}-activated single crystalline materials were synthesized. Phase purity of the polycrystalline starting materials were verified with PXRD. The majority did not exhibit significant secondary phases. Crystal growth of BTP, STB, LTB, TbCOB, Dy:CYA, and Dy:YCOB were carried out using the Czochralski technique. The growth conditions, including the crucible, pulling speed, and rotation were optimized and the atmosphere was taken care. Efforts were particularly made on the crystal growth of LTB to circumvent the cleavage and cracking of this material. Finally, single crystals with good optical quality and sufficient size were obtained, which are free from bulk scattering centers. In addition, single-crystal XRD refinement of LTB was studied for the first time.

The concentrations of Dy^{3+} in the matrices of CYA, CAS, and YCOB were determined with electron probe micro-analysis. They were found to be 4.67×10^{20} cm^{-3}, 8.07×10^{20} cm^{-3} and 3.86×10^{20} cm^{-3} at the upper body part of the boule. The segregation coefficients of Dy^{3+} in CYA and YCOB were calculated to be 1.06 and 0.86, respectively.

To better understand the formation of color centers in terbium-based crystals, EPR spectroscopic measurements were performed. The dark-color samples of STB and LTB showed intense signals in their EPR spectra at room temperature, which could be assigned to the EPR-active Tb^{4+} ion. Thus, we are able to attribute the color centers to the oxidation of Tb^{3+} to Tb^{4+} ion in the lattice. These results accentuate the importance of using a reducing atmosphere to grow Tb^{3+}-activated crystals to get rid of the color centers.

Thermal conductivities and thermal expansion coefficients of the terbium-based compounds were measured. LTB gives the largest thermal conductivity of 2.97 $W \cdot m^{-1} \cdot K^{-1}$. Thermal expansion coefficients along the crystallographic axes were obtained from XRD measurements at a couple of temperatures. Those of TbCOB exhibit the smallest anisotropy. The crystallographic structural and thermal properties of these crystals are summarized in Table 2.14.

Table 2.14   **Crystallographic structural and thermal properties of the terbium-based crystals and the host materials for doping dysprosium.**

Matrices	$Ba_3Tb(PO_4)_3$	$Sr_3Tb(BO_3)_3$	$TbAl_3(BO_3)_4$	$Li_6Tb(BO_3)_3$	$TbCa_4O(BO_3)_3$	$KTb(WO_4)_2$	$CaYAlO_4$	$Ca_2Al_2SiO_7$	$YCa_4O(BO_3)_3$
Crystal system	Cubic	Trigonal	Trigonal	Monoclinic	Monoclinic	Monoclinic	Tetragonal	Tetragonal	Monoclinic
Space group	$I\bar{4}3d$	$R\bar{3}$	$R32$	$P/2_1c$	Cm	$C2/c$	$I4/mmm$	$P\bar{4}2_1m$	Cm
Theoretical density	4.98 g·cm^{-3}	4.75 g·cm^{-3}	4.37 g·cm^{-3}	3.28 g·cm^{-3}	3.77 g·cm^{-3}	7.24 g·cm^{-3}	4.64 g·cm^{-3}	3.04 g·cm^{-3}	3.31 g·cm^{-3}
Melting point	>1950°C	1351°C	~1200°C[a]	~850°C	1498°C	~1010°C[a]	1810°C	1583°C	1510°C
Active-ion conc. (10^{20} cm^{-3})	35	48	55	52	44	63	4.67	8.07	3.86
Coordination number	6	6	6	8	6	8	9	8	6
Avg. Ln—O bond length	2.61 Å	2.13/2.19 Å	2.31 Å	2.40 Å	2.33/2.34 Å	2.39 Å	2.51 Å	2.57 Å	2.32/2.34 Å
Site symmetry	C_1	C_i	D_3	C_1	C_s/C_1	C_2	C_{4v}	C_s	C_s/C_1
Thermal conductivity (W·m^{-1}·K^{-1})	0.65 (arb.)	1.11 (∥c)	~5.3[b]	2.97 (arb.)	1.92 (∥b)	~3.5[c]	3.7 (∥a); 3.3 (∥c)	2.2 (∥c)	1.8 (∥a); 1.7 (∥b); 2.8 (∥c)
Specific heat (J·kg^{-1}·K^{-1})	427	402	~770[a]	628	510	~360[c]	593	-	730
Thermal expansion coefficients (10^{-6} K^{-1})	19.4	17.6 (∥a); 6.8 (∥c)	3.9 (∥a); 11.9 (∥c)	12.7 (∥a); 22.5 (∥b); 12.9 (∥c)	12.1 (∥a); 7.7 (∥b); 14.2 (∥c)	13.7 (∥a); 2.2 (∥b); 25.1 (∥c)	8 (∥a); 11 (∥c)	7.6 (∥a); 12.1 (∥c)	9.9 (∥a); 8.2 (∥b); 12.8 (∥c)

[a] Decomposition temperature.

[b] Data of the analogue compound $GdAl(BO_3)_4$.

[c] Data of the analogue compound $KGd(WO_4)_2$.

References of Chapter 2

[1] L. Schwarz, B. Finke, M. Kloss, A. Rohmann, U. Sasum, D. Haberland, Investigations on the electronic structure of double phosphates of the type M3RE(PO4)2 (RE = rare earths, lanthanides), J. Lumin. 72–74 (1997) 257–259. doi:10.1016/S0022-2313(97)00091-4.

[2] X. Chen, Z. Gong, Q. Wan, S. Wu, F. Guo, N. Zhuang, J. Chen, $Ba_3Tb(PO_4)_3$: Crystal growth, structure, magnetic and magneto-optical properties, Opt. Mater. 44 (2015) 48–53. doi:10.1016/j.optmat.2015.02.029.

[3] J. Barbier, Structural refinements of eulytite-type $Ca_3Bi(PO_4)_3$ and $Ba_3La(PO_4)_3$, J. Solid State Chem. 101 (1992) 249–256. doi:10.1016/0022-4596(92)90181-T.

[4] K. Fukuda, T. Iwata, T. Niwa, Crystal structure and phase transformations of calcium yttrium orthophosphate, $Ca_3Y(PO_4)_3$, J. Solid State Chem. 179 (2006) 3420–3428. doi:10.1016/j.jssc.2006.07.013.

[5] Szuszkiewicz W., Phase Equilibria in the YPO_4 -- $Ba_3(PO_4)_2$ System, Pol. J. Chem. 76 (2002) 23–27.

[6] R.V. Shpanchenko, R.V. Panin, J. Hadermann, C. Bougerol, E. Takayama-Muromachi, E.V. Antipov, Synthesis and structure investigation of the $Pb_3V(PO_4)_3$ eulytite, J. Solid State Chem. 178 (2005) 3715–3721. doi:10.1016/j.jssc.2005.09.045.

[7] K.I. Schaffers, P.D. Thompson, T. Alekel, J.R. Cox, D.A. Keszler, STACK Crystal Chemistry, Chem. Mater. 6 (1994) 2014–2022. doi:10.1021/cm00047a022.

[8] J. Pan, S. Wu, G. Wang, Crystal growth and spectral properties of Nd^{3+}:$Sr_3Gd(BO_3)_3$ crystal, Opt. Mater. 28 (2006) 391–394. doi:10.1016/j.optmat.2004.12.022.

[9] D. Zhao, Z. Hu, Z. Lin, G. Wang, Growth and spectral properties of Er^{3+}/Yb^{3+}-codoped $Sr_3Y(BO_3)_3$ crystal, J. Cryst. Growth. 277 (2005) 401–405. doi:10.1016/j.jcrysgro.2005.01.081.

[10] J. Pan, Z. Hu, Z. Lin, G. Wang, Growth and spectral properties of Nd^{3+}-doped $Sr_3Y(BO_3)_3$ crystal, J. Cryst. Growth. 260 (2004) 456–459. doi:10.1016/j.jcrysgro.2003.08.057.

[11] X. Meng, L. Zhang, G. Wang, Growth and spectral properties of Tm^{3+}-doped $Sr_3Y(BO_3)_3$ crystal, J. Alloys Compd. 481 (2009) 354–357. doi:10.1016/j.jallcom.2009.02.136.

[12] H. Xia, J. Feng, Y. Ji, J. Xu, Z. Zhu, Y. Wang, Z. You, J. Li, H. Wang, C. Tu, Crystal growth and spectroscopic properties of Sm^{3+}:$Sr_3Gd(BO_3)_3$ crystal, J. Lumin. 149 (2014) 7–11. doi:10.1016/j.jlumin.2013.12.048.

[13] F. Druon, S. Chénais, P. Raybaut, F. Balembois, P. Georges, R. Gaumé, G. Aka, B. Viana, S. Mohr, D. Kopf, Diode-pumped Yb:$Sr_3Y(BO_3)_3$ femtosecond laser, Opt. Lett. 27 (2002) 197. doi:10.1364/OL.27.000197.

[14] H. Xia, J. Xu, J. Feng, C. Tu, Diode-pumped multi-wavelength laser operation of Yb^{3+}: $Sr_3Gd(BO_3)_3$ crystal, Mater. Lett. 131 (2014) 97–99. doi:10.1016/j.matlet.2014.05.143.

[15] S. Chénais, F. Druon, F. Balembois, P. Georges, R. Gaumé, P.H. Haumesser, B. Viana, G.P. Aka, D. Vivien, Spectroscopy and efficient laser action from diode pumping of a new broadly tunable crystal: Yb^{3+}:$Sr_3Y(BO_3)_3$, J. Opt. Soc. Am. B. 19 (2002) 1083. doi:10.1364/JOSAB.19.001083.

[16] W. Zhao, S. Gao, S. An, B. Fan, S. Li, The luminescence properties of $Sr_3Gd(BO_3)_3$: Tb^{3+} phosphors under vacuum ultraviolet excitation, Chin. Sci. Bull. 57 (2012) 4513–4516. doi:10.1007/s11434-012-5418-2.

[17] D.-Y. Wang, T.-M. Chen, B.-M. Cheng, Host Sensitization of Tb^{3+} Ions in Tribarium Lanthanide Borates $Ba_3Ln(BO_3)_3$ (Ln = Lu and Gd), Inorg. Chem. 51 (2012) 2961–2965. doi:10.1021/ic202241h.

[18] J. Lu, F. Guo, J. Chen, Growth and characteristic of $Sr_3Tb(BO_3)_3$ crystal, J. Cryst. Growth. 314 (2011) 157–162. doi:10.1016/j.jcrysgro.2010.12.018.

[19] J. Lu, F. Guo, J. Chen, Growth and characteristic of $Sr_3Tb(BO_3)_3$ crystal, J. Cryst. Growth. 314 (2011) 157–162. doi:10.1016/j.jcrysgro.2010.12.018.

[20] L. Junye, C. Jianzhong, Growth and magnetic-optical properties of $Sr_3Gd(BO_3)_3$ and $Sr_3Tb_xGd_{1-x}(BO_3)_3$ single crystals, Cryst. Res. Technol. 45 (2010) 1137–1140. doi:10.1002/crat.201000417.

[21] D. Rytz, A. Gross, S. Vernay, V. Wesemann, $YAl_3(BO_3)_4$: a novel NLO crystal for frequency conversion to UV wavelengths, in: J.A. Terry, T. Graf, H. Jelínková (Eds.), 2008: p. 699814. doi:10.1117/12.780027.

[22] J. Lu, C. Fu, J. Chen, Structure, growth, and optical properties of $TbAl_3(BO_3)_4$ single crystal, Appl. Opt. 50 (2011) 116. doi:10.1364/AO.50.000116.

[23] R.P. Yavetskiy, A.V. Tolmachev, E.F. Dolzhenkova, V.N. Baumer, Thermally stimulated luminescence mechanism of $Li_6Y(BO_3)_3$:Eu^{3+} single crystals, J. Alloys Compd. 429 (2007) 77–81. doi:10.1016/j.jallcom.2006.04.040.

[24] J.-P. Chaminade, O. Viraphong, S. Miyazawa, One possible mechanism of spiral/footing growth of Cz-grown $Li_6Gd(BO_3)_3$, J. Cryst. Growth. 237–239 (2002) 864–868. doi:10.1016/S0022-0248(01)02029-2.

[25] J.P. Chaminade, O. Viraphong, F. Guillen, C. Fouassier, B. Czirr, Crystal growth and optical properties of new neutron detectors Ce^{3+}:$Li_6R(BO_3)_3$ (R=Gd,Y), IEEE Trans. Nucl. Sci. 48 (2001) 1158–1161. doi:10.1109/23.958742.

[26] F. Yang, S.K. Pan, D.Z. Ding, G.H. Ren, Problems in the growth of Ce^{3+}-doped $Li_6Gd(BO_3)_3$ crystals by Czochralski method, Cryst. Res. Technol. 44 (2009) 141–145. doi:10.1002/crat.200800194.

[27] R.P. Yavetskii, E.F. Dolzhenkova, M.F. Dubovik, T.I. Korshikova, A.V. Tolmachev, Growth of single crystals of Li_6Y_{1-x} $Eu_x(BO_3)_3$ (x = 0–1) solid solutions by the Czochralski method, Crystallogr. Rep. 50 (2005) S88–S91. doi:10.1134/1.2133979.

[28] A.. Shekhovtsov, A.. Tolmachev, M.. Dubovik, E.. Dolzhenkova, T.. Korshikova, B.. Grinyov, V.. Baumer, O.. Zelenskaya, Structure and growth of pure and Ce3+-doped Li6Gd(BO3)3 single crystals, J. Cryst. Growth. 242 (2002) 167–171. doi:10.1016/S0022-0248(02)01137-5.

[29] F. Yang, S.K. Pan, D.Z. Ding, G.H. Ren, Problems in the growth of Ce^{3+}-doped $Li_6Gd(BO_3)_3$ crystals by Czochralski method, Cryst. Res. Technol. 44 (2009) 141–145. doi:10.1002/crat.200800194.

[30] J.C. Brice, Crystal growth processes, Blackie ; Halsted Press, Glasgow : New York, 1986.

[31] R. Arun Kumar, Borate Crystals for Nonlinear Optical and Laser Applications: A Review, J. Chem. 2013 (2013) 1–6. doi:10.1155/2013/154862.

[32] Yuan Dongsheng, Equipment development and single crystal growth of micro-pulling-down, and the synthesis and investigations of functional crystal TbCOB, Shandong University, 2016.

[33] D. Yuan, Z. Jia, J. Wang, Z. Gao, J. Zhang, X. Fu, J. Shu, Y. Yin, Q. Hu, X. Tao, Bulk growth, structure, and characterization of the new monoclinic $TbCa_4O(BO_3)_3$ crystal, CrystEngComm. 16 (2014) 4008–4015. doi:10.1039/C4CE00051J.

[34] Ilyukhin, A.B. and Dzhurinskii, B.F., Crystal structures of binary oxoborates $LnCa_4O(BO_3)_3$ (Ln=Gd, Tb, and Lu) and $Eu_2CaO(BO_3)_2$, Russ. J. Inorg. Chem. 38 (1993) 847–850.

[35] A. Jayaraman, B. Batlogg, L.G. VanUitert, High-pressure Raman study of alkaline-earth tungstates and a new pressure-induced phase transition in $BaWO_4$, Phys. Rev. B. 28 (1983) 4774–4777. doi:10.1103/PhysRevB.28.4774.

[36] P.A. Loiko, E.V. Vilejshikova, X. Mateos, J.M. Serres, E.B. Dunina, A.A. Kornienko, K.V. Yumashev, M. Aguiló, F. Díaz, Europium doping in monoclinic $KYb(WO_4)_2$ crystal, J. Lumin. 183 (2017) 217–225. doi:10.1016/j.jlumin.2016.11.046.

[37] S. Schwung, D. Rytz, B. Heying, U.C. Rodewald, O. Niehaus, D. Enseling, T. Jüstel, R. Pöttgen, The crystal structure and luminescence quenching of poly- and single-crystalline KYW_2O_8:Tb^{3+}, J. Lumin. 166 (2015) 289–294. doi:10.1016/j.jlumin.2015.05.052.

[38] A.A. Kaminskii, A.F. Konstantinova, V.P. Orekhova, A.V. Butashin, R.F. Klevtsova, A.A. Pavlyuk, Optical and nonlinear laser properties of the χ(3)-active monoclinic α-$KY(WO_4)_2$ crystals, Crystallogr. Rep. 46 (2001) 665–672. doi:10.1134/1.1387135.

[39] F. Pirzio, S.D.D.D. Cafiso, M. Kemnitzer, A. Guandalini, F. Kienle, S. Veronesi, M. Tonelli, J. Aus der Au, A. Agnesi, Sub-50-fs widely tunable Yb:$CaYAlO_4$ laser pumped by 400-mW single-mode fiber-coupled laser diode, Opt. Express. 23 (2015) 9790. doi:10.1364/OE.23.009790.

[40] Z. Gao, J. Zhu, J. Wang, Z. Wang, Z. Wei, X. Xu, L. Zheng, L. Su, J. Xu, Diode-pumped Kerr-lens mode-locked Yb:$CaGdAlO_4$ laser with tunable wavelength, Laser Phys. Lett. 13 (2016) 015302. doi:10.1088/1612-2011/13/1/015302.

[41] A.A. Kaminskii, X. Xu, O. Lux, H. Rhee, H.J. Eichler, J. Zhang, D. Zhou, A. Shirakawa, K. Ueda, J. Xu, High-order stimulated Raman scattering in tetragonal CaYAlO4 crystal-host for Ln^{3+}-lasant ions, Laser Phys. Lett. 9 (2012) 306–311. doi:10.1002/lapl.201110135.

[42] Q. Hu, Z. Jia, C. Tang, N. Lin, J. Zhang, N. Jia, S. Wang, X. Zhao, X. Tao, The origin of coloration of $CaGdAlO_4$ crystals and its effect on their physical properties, CrystEngComm. 19 (2017) 537–545. doi:10.1039/C6CE02411D.

[43] R.D. Shannon, R.A. Oswald, J.B. Parise, B.H.T. Chai, P. Byszewski, A. Pajaczkowska, R. Sobolewski, Dielectric constants and crystal structures of $CaYAlO_4$, $CaNdAlO_4$, and $SrLaAlO_4$, and deviations from the oxide additivity rule, J. Solid State Chem. 98 (1992) 90–98. doi:10.1016/0022-4596(92)90073-5.

[44] S.R. Bowman, S. O'Connor, N.J. Condon, Diode pumped yellow dysprosium lasers, Opt. Express. 20 (2012) 12906. doi:10.1364/OE.20.012906.

[45] Z. Xia, F. Yang, L. Qiao, F. Yan, End pumped yellow laser performance of Dy^{3+} :$ZnWO_4$, Opt. Commun. 387 (2017) 357–360. doi:10.1016/j.optcom.2016.12.008.

[46] G. Bolognesi, D. Parisi, D. Calonico, G.A. Costanzo, F. Levi, P.W. Metz, C. Kränkel, G. Huber, M. Tonelli, Yellow laser performance of Dy^{3+} in co-doped Dy,Tb:$LiLuF_4$, Opt. Lett. 39 (2014) 6628. doi:10.1364/OL.39.006628.

[47] W. Wang, X. Yan, X. Wu, Z. Zhang, B. Hu, J. Zhou, Study of single-crystal growth of Tm^{3+}:$CaYAlO_4$ by the floating-zone method, J. Cryst. Growth. 219 (2000) 56–60. doi:10.1016/S0022-0248(00)00590-X.

[48] S. Lv, Y. Wang, Z. Zhu, Z. You, J. Li, S. Gao, H. Wang, C. Tu, Spectroscopic analysis of Pr^{3+}:$CaYAlO_4$ crystal, Appl. Phys. B. 116 (2014) 83–89. doi:10.1007/s00340-013-5651-7.

[49] J.Q. Di, X.D. Xu, C.T. Xia, L.H. Zheng, G. Aka, H.H. Yu, Q.L. Sai, X.Y. Guo, L. Zhu, Crystal growth, polarized spectra, and laser performance of Yb:$CaGdAlO_4$ crystal, Laser Phys. 26 (2016) 045803. doi:10.1088/1054-660X/26/4/045803.

[50] D. Li, X. Xu, Y. Cheng, S. Cheng, D. Zhou, F. Wu, C. Xia, J. Xu, J. Zhang, Crystal growth and spectroscopic properties of Yb:$CaYAlO_4$ single crystal, J. Cryst. Growth. 312 (2010) 2117–2121. doi:10.1016/j.jcrysgro.2010.04.028.

[51] Anael JAFFRES, Matériaux laser dopés terres rares impulsionnels dans la gamme spectrale 1 μm et 1,5 μm: efforts sur la montée en puissance et en cadence, Paris 6, 2013.

[52] B. Simondi-Teisseire, B. Viana, D. Vivien, A.M. Lejus, Optical Investigation of Er:$Ca_2Al_2SiO_7$ and Yb:$Ca_2Al_2SiO_7$ for Laser Applications in the Near Infrared, Phys. Status Solidi A. 155 (1996) 249–262. doi:10.1002/pssa.2211550125.

[53] A.M. Lejus, N. Pelletier-Allard, R. Pelletier, D. Vivien, Site selective spectroscopy of Nd ions in gehlenite ($Ca_2Al_2SiO_7$), a new laser material, Opt. Mater. 6 (1996) 129–137. doi:10.1016/0925-3467(96)00041-9.

[54] I. Swainson, M. Dove, W. Schmahl, A. Putnis, Neutron powder diffraction study of the Akermanite-gehlenite solid solution series, Phys. Chem. Miner. 19 (1992). doi:10.1007/BF00202107.

[55] A.M. Lejus, A. Kahn-Harari, J.M. Benitez, B. Viana, Crystal growth, characterization and structure refinement of neodymium^{3+} doped gehlenite, a new laser material [$Ca_2Al_2SiO_7$], Mater. Res. Bull. 29 (1994) 725–734. doi:10.1016/0025-5408(94)90197-X.

[56] M. Merlini, M. Gemmi, G. Artioli, Thermal expansion and phase transitions in åkermanite and gehlenite, Phys. Chem. Miner. 32 (2005) 189–196. doi:10.1007/s00269-005-0458-7.

[57] Z. Burshtein, Y. Shimony, I. Levy, A.M. Lejus, J.M. Benitez, F. Mougel, Refractive-index studies in $Ca_2Ga_2SiO_7$ and $SrLaGa_3O_7$ melilite-type compounds, J. Opt. Soc. Am. B. 13 (1996) 1941. doi:10.1364/JOSAB.13.001941.

[58] Nathalie Britos, Les gehlenites ($Ca_2Al_2SiO_7$) activees par des ions lanthanides Ln3+, nouveaux materiaux laser potentiels: cristallogenese et etude specctroscopique, Paris 6, 1995.

[59] M. Iwai, T. Kobayashi, H. Furuya, Y. Mori, T. Sasaki, Crystal Growth and Optical Characterization of Rare-Earth (Re) Calcium Oxyborate $ReCa_4O(BO_3)_3$ (Re = Y or Gd) as New Nonlinear Optical Material, Jpn. J. Appl. Phys. 36 (1997) L276–L279. doi:10.1143/JJAP.36.L276.

[60] Q. Ye, B.H.T. Chai, Crystal growth of YCa4O(BO3)3 and its orientation, J. Cryst. Growth. 197 (1999) 228–235. doi:10.1016/S0022-0248(98)00947-6.

[61] J. Luo, S.J. Fan, H.Q. Xie, K.C. Xiao, S.X. Qian, Z.W. Zhong, G.X. Qiang, R.Y. Sun, J.Y. Xu, Thermal and Nonlinear Optical Properties of $Ca_4YO(BO_3)_3$, Cryst. Res. Technol. 36 (2001) 1215. doi:10.1002/1521-4079(200111)36:11<1215::AID-CRAT1215>3.0.CO;2-Z.

[62] F. Mougel, G. Aka, F. Salin, D. Pelenc, B. Ferrand, A. Kahn-Harari, D. Vivien, Accurate Second Harmonic Generation phase matching angles prediction and evaluation of non linear coefficients of Ca4YO(BO3)3 (YCOB) crystal, in: OSA, 2001: p. WB11. doi:10.1364/ASSL.1999.WB11.

[63] D. Sugak, A. Matkovskii, D. Savitskii, A. Durygin, A. Suchocki, Y. Zhydachevskii, I. Solskii, I. Stefaniuk, F. Wallrafen, Growth and Induced Color Centers in YAlO3-Nd Single Crystals, Phys. Status Solidi A. 184 (2001) 239–250. doi:10.1002/1521-396X(200103)184:1<239::AID-PSSA239>3.0.CO;2-I.

[64] Y.V. Zorenko, A.S. Voloshinovskiĭ, I.V. Konstankevych, Luminescence of F + and F centers in $YAlO_3$, Opt. Spectrosc. 96 (2004) 532–537. doi:10.1134/1.1719141.

[65] Z. Hu, Z. Lin, G. Wang, Growth and spectroscopic characterization of $Nd^{3+}:Sr_6GdSc(BO_3)_6$ crystal, J. Solid State Chem. 177 (2004) 3028–3031. doi:10.1016/j.jssc.2004.05.015.

[66] J. Li, J. Wang, S. Han, Y. Guo, Y. Wang, Growth, structural, thermal properties and spectroscopic characteristics of $KTb(WO_4)_2$ single crystal, J. Rare Earths. 30 (2012) 967–971. doi:10.1016/S1002-0721(12)60162-8.

[67] F. Guo, J. Ru, H. Li, N. Zhuang, B. Zhao, J. Chen, Growth and magneto-optical properties of $NaTb(MoO_4)_2$ crystals, J. Cryst. Growth. 310 (2008) 4390–4393. doi:10.1016/j.jcrysgro.2008.07.028.

[68] X. Chen, M. Ruan, F. Guo, J. Chen, Czochralski growth, magnetic and magneto-optical properties of Na2Tb4(MoO4)7 crystal, J. Cryst. Growth. 421 (2015) 8–12. doi:10.1016/j.jcrysgro.2015.04.001.

[69] L.P. Varga, L.B. Asprey, Free Ion 4fn Levels of the Tetravalent Lanthanides. Fluorescence and Absorption Spectra of Cesium Dysprosium (IV) Heptafluoride, J. Chem. Phys. 48 (1968) 139–146. doi:10.1063/1.1664459.

[70] R. Oka, T. Tsukimori, H. Inoue, T. Masui, Perovskite-type $ALnO_3$ (A = Ca, Sr, Ba; Ln = Ce, Pr, Tb) oxides as environmentally friendly yellow pigments, J. Ceram. Soc. Jpn. 125 (2017) 652–656. doi:10.2109/jcersj2.17118.

[71] X. Li, W. Dong, Y. Qi, D. Wang, R. Yang, Studies on the stabilization of terbium(IV) in aqueous tetrametaphosphate solution, Polyhedron. 10 (1991) 1479–1483. doi:10.1016/S0277-5387(00)86069-6.

[72] Y. Ying, Y. Ru-Dong, Synthesis and characterization of tetravalent terbium complexes of alkali terbium hexaoxidoiodates, Polyhedron. 11 (1992) 963–966. doi:10.1016/S0277-5387(00)83348-3.

[73] A. Abragam, B. Bleaney, Electron paramagnetic resonance of transition ions, Oxford University Press, Oxford, 2012.

[74] Y. Hinatsu, Magnetic susceptibility and electron paramagnetic resonance studies of tetravalent terbium ions in $BaTbO_3$ and $SrTbO_3$, J. Solid State Chem. 100 (1992) 136–140. doi:10.1016/0022-4596(92)90163-P.

[75] F. Druon, J. Boudeile, Y. Zaouter, M. Hanna, F. Balembois, P. Georges, J. Petit, P. Golner, B. Viana, New Yb-doped crystals for high-power and ultrashort lasers, in: S.M. Kirkpatrick, R. Stoian (Eds.), 2006: p. 64000D. doi:10.1117/12.690276.

[76] Z. Pan, H. Cai, H. Huang, H. Yu, H. Zhang, J. Wang, Growth, thermal properties and laser operation of a novel disordered $Yb:Ca_3La_2(BO_3)_4$ laser crystal, Opt. Mater. 36 (2014) 2039–2043. doi:10.1016/j.optmat.2013.12.022.

[77] Z. Pan, H. Cong, H. Yu, H. Zhang, J. Wang, R.I. Boughton, Growth, morphology and anisotropic thermal properties of Nd-doped $Sr_3Y_2(BO_3)_4$ crystal, J. Cryst. Growth. 363 (2013) 176–184. doi:10.1016/j.jcrysgro.2012.10.034.

[78] P.A. Popov, N.V. Moiseev, A.E. Kokh, K.A. Kokh, Thermal conductivity and heat capacity of α- and β-BaB_2O_4 single crystals, Inorg. Mater. 47 (2011) 163–166. doi:10.1134/S0020168511020142.

[79] R. Gaumé, B. Viana, D. Vivien, J.-P. Roger, D. Fournier, A simple model for the prediction of thermal conductivity in pure and doped insulating crystals, Appl. Phys. Lett. 83 (2003) 1355–1357. doi:10.1063/1.1601676.

[80] N. Sharova, H. Fjellvåg, T. Norby, Structure, defect chemistry, and proton conductivity in nominally Sr-doped $Ba_3La(PO_4)_3$, Solid State Ion. 180 (2009) 338–342. doi:10.1016/j.ssi.2009.01.002.

[81] V.I. Pet'kov, A.S. Dmitrienko, A.I. Bokov, Thermal expansion of phosphate–sulfates of eulytite structure, J. Therm. Anal. Calorim. (2017). doi:10.1007/s10973-017-6676-7.

[82] Y. Sato, T. Taira, Highly accurate interferometric evaluation of thermal expansion and dn/dT of optical materials, Opt. Mater. Express. 4 (2014) 876. doi:10.1364/OME.4.000876.

[83] K. Friese, H. Krüger, V. Kahlenberg, T. Balić-Žunić, H. Emerich, J.-Y. Gesland, A. Grzechnik, Study of the temperature dependence of the structure of KY_3F_{10}, J. Phys. Condens. Matter. 18 (2006) 2677–2687. doi:10.1088/0953-8984/18/9/007.

[84] H. Zhou, X. Ma, G. Chen, W. Lv, Y. Wang, Z. You, J. Li, Z. Zhu, C. Tu, Tm^{3+}-doped $Gd_3Ga_5O_{12}$ crystal: A potential tunable laser crystal at 2.0 μm, J. Alloys Compd. 475 (2009) 555–559. doi:10.1016/j.jallcom.2008.07.084.

[85] D. Zhao, G. Wang, Growth and spectroscopic characterization of Er^{3+}: $Sr_3Y(BO_3)_3$ crystal, J. Lumin. 130 (2010) 424–428. doi:10.1016/j.jlumin.2009.10.007.

[86] F. Yuan, L. Zhang, Y. Huang, S. Sun, Z. Lin, G. Wang, Growth, thermal and spectral characteristics of $Yb^{3+}:Sr_6YSc(BO_3)_6$ crystal, Mater. Sci. Eng. B. 187 (2014) 32–38. doi:10.1016/j.mseb.2014.04.008.

[87] R. Belhoucif, M. Velázquez, Y. Petit, O. Pérez, B. Glorieux, O. Viraphong, P. de Marcillac, N. Coron, L. Torres, E. Véron, A. Kellou, P. Veber, R. Decourt, H.E. Hafid, Growth and spectroscopic properties

of 6Li- and 10B-enriched crystals for heat-scintillation cryogenic bolometers used in the rare events searches, CrystEngComm. 15 (2013) 3785. doi:10.1039/c3ce40176f.

[88] H. Liu, J. Li, S.H. Fang, J.Y. Wang, N. Ye, Growth of $YAl_3(BO_3)_4$ crystals with tungstate based flux, Mater. Res. Innov. 15 (2011) 102–106. doi:10.1179/143307511X12998222918750.

[89] F. Mougel, A. Kahn-harari, G. Aka, D. Pelenc, Structural and thermal stability of Czochralski grown GdCOB oxoborate single crystals, J. Mater. Chem. 8 (1998) 1619–1623. doi:10.1039/a800492g.

[90] M.C. Pujol, X. Mateos, R. Solé, J. Massons, J. Gavalda, F. Díaz, M. Aguiló, Linear Thermal Expansion Tensor in $KRE(WO_4)_2$ (RE=Gd, Y, Er, Yb) Monoclinic Crystals, Mater. Sci. Forum. 378–381 (2001) 710–717. doi:10.4028/www.scientific.net/MSF.378-381.710.

CHAPTER 3   OPTICAL PROPERTY CHARACTERIZATION

Optical properties of the crystals are characterized and discussed in this chapter. The principal optical directions of the uniaxial and biaxial crystals are determined. The refractive indices of some terbium-based crystals, which are essential for the following spectroscopic study while not reported, are measured experimentally. The following spectroscopic measurements and analysis are performed: ground-state absorption spectra (Section 3.2), Judd-Ofelt calculations (Section 3.3), fluorescence spectra (Section 3.4), and fluorescence decays (Section 3.5). The Tb^{3+}- and Dy^{3+}-activated crystals are discussed separately in the above-mentioned sections. The spectroscopic data related to the potential laser performance are tabulated to give an overview. The excited-state absorption of the Tb^{3+}-based compounds is studied by photon detectors in a pump-probe approach. Laser experiments using the fabricated materials as gain media are attempted with different pump sources. For conciseness, detailed experimental procedures and information about the apparatus are mainly described in the appendix section B.3.

3.1 Optical orientation and refractive index

The refractive index is an essential parameter for further studies of the optical properties. The interaction between light and the lanthanide ions in the medium is influenced by the refractive index that is parallel to the polarization of light. An optically isotropic crystal like BTP does not show birefringence and has one refractive index. Uniaxial crystals that belong to the tetragonal or hexagonal crystal systems, such as STB and Dy:CYA, yield two sets of refractive index. In the case of uniaxial crystals, the optic axis has the same direction as the crystallographic c-axis. Light whose polarization is perpendicular/parallel to the optic axis is governed by, correspondingly, the ordinary/extraordinary refractive index. Monoclinic biaxial crystals generate two optic axes and three orthogonal directions X, Y, and Z of the optical indicatrix. One of these three indicatrix axes is parallel to the crystallographic b-axis while the other two do not coincide with crystallographic directions. In the case of biaxial crystals, the three refractive indices exhibit the sequence of $n_Z(n_g) > n_Y(n_m) > n_X(n_p)$, where the light polarization is parallel to one of the corresponding principal axes of the optical indicatrix.

The uniaxial crystals of STB, TAB, Dy:CYA, and Dy:CAS could be easily oriented with respect to the optic axis (c-axis) by X-ray diffraction. The as-grown crystals of Dy:CYA and Dy:CAS both exhibit natural faceting of (001), which makes this process even more convenient. The two surfaces perpendicular and parallel to the optic axis were polished so that the polarizations of $E \perp c$ and $E \parallel c$ are accessible for the following characterization. The optical orientations were further examined with a polariscope equipped with a conoscopic lens. Photos of these uniaxial media observed with the polariscope utilizing irradiation from a sodium lamp ($\lambda = 589.3\ nm$) are presented in Figure 3.1.

The principal optical directions of a monoclinic biaxial crystal were, on the other hand, much more complicated to be determined. First, the crystal was oriented with respect to the b-axis, which corresponds to one indicatrix axis. The a- or c-axis of this sample was then found by Laue X-ray diffraction with a goniometeric sample holder. Next, with the reported values (those of the analogue compounds can be referred) of the angles between the optical and crystallographic directions, the other two indicatrix directions could be roughly determined. Finally, further polishing on the roughly oriented sample was conducted to obtain the accurate orientation with assistance of a polariscope.

After the crystal is oriented and cut perpendicular the three mutually orthogonal indicatrix axes, an assignment of them to the X, Y, and Z-axis is necessary. This can be fulfilled with assistance of a quartz wedge [1]. In the case of LTB, the Y-axis was found to be along the b-axis and the X- and Z-axis that bisect the two optic axes could be distinguished by their different moving patterns while manipulating the wedge. The optical indicatrix of LTB viewing from the Y-direction is illustrated in Figure 3.2 (b). The determination of the indicatrix axes is backed by refractive index measurements, which will be discussed later. Since the X-axis is the acute bisectrix of the optic axes, LTB is optically negative. The relationship between the optic, indicatrix, and crystallographic axes is depicted in Figure 3.2 (a) and (c). The direction of the Z-axis is approximately along $\langle \bar{2}\ 0\ \bar{1} \rangle$ and that of the X-axis is about 3° from $\langle \bar{7}\ 0\ 10 \rangle$. The angle between the Z-axis and a-axis was calculated to be 40.7°.
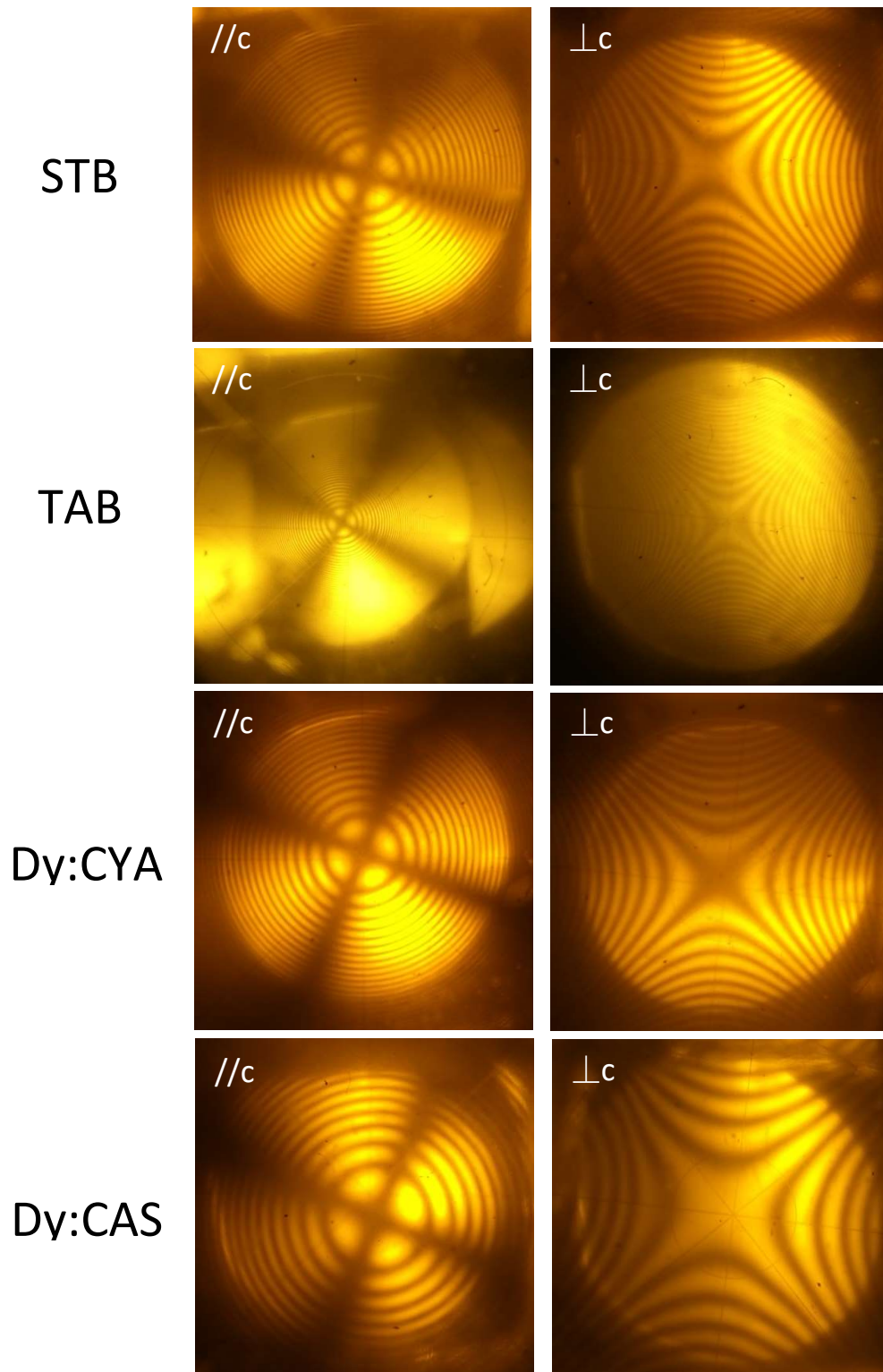
Figure 3.1   **Conoscopic images of the uniaxial crystals. The denoted orientations point toward the viewer.**
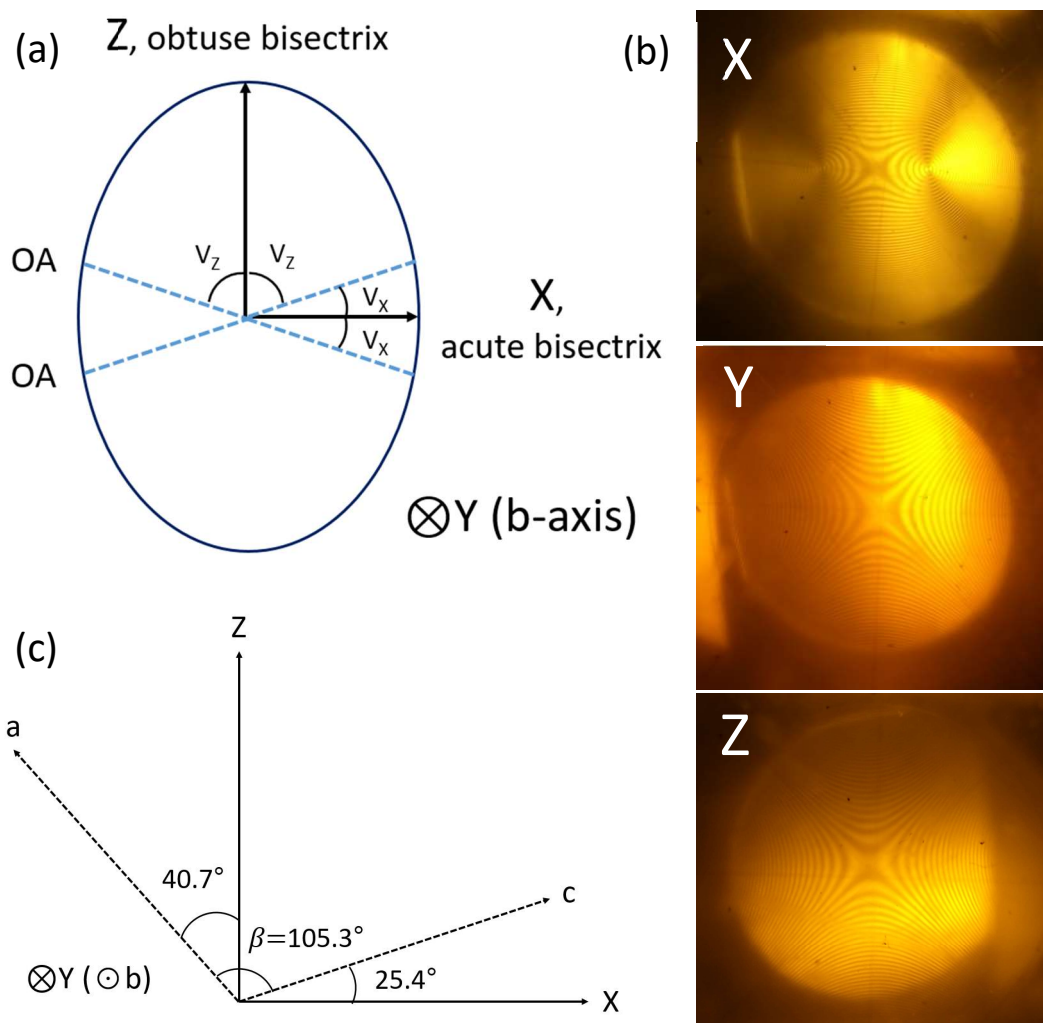
Figure 3.2 **(a) Simplified optical indicatrix of LTB observed along the Y-axis; (b) photos of the LTB crystal oriented to the principal optical directions under a polariscope. The denoted orientations point toward the viewer; (c) relative orientation of the optical indicatrix axes X and Z to the crystallographic axes of LTB.**

The orientation of the monoclinic TbCOB was performed in the same approach. The reported refractive indices of TbCOB are closed to those of GdCOB [2,3]. This indicates that the relationship between the crystallographic and optical directions are similar in TbCOB and GdCOB. According to our observation, the Y-axis is along the crystallographic b-axis and the angle between the Z-axis and a-axis is 23.5°, which is comparable to the reported value of 26° in GdCOB (Figure 3.3).

In the case of KTW, to our surprise, the conoscopic image of one indicatrix direction is irregular in spite of the fact that the crystal is cut orthogonally (Figure 3.3). The crystallographic orientations along the three indicatrix axes were determined. The Y-axis was found to be parallel to the b-axis, which shows an unusual conoscopic pattern. The angle between the Z-axis and c-axis was calculated to be 20° from the Laue X-ray diffraction pattern, which is comparable to the values of 18.5°, 21.5°, and 18.5° in isostructral compounds of KYW, KGdW, and KLuW, respectively [4–6].
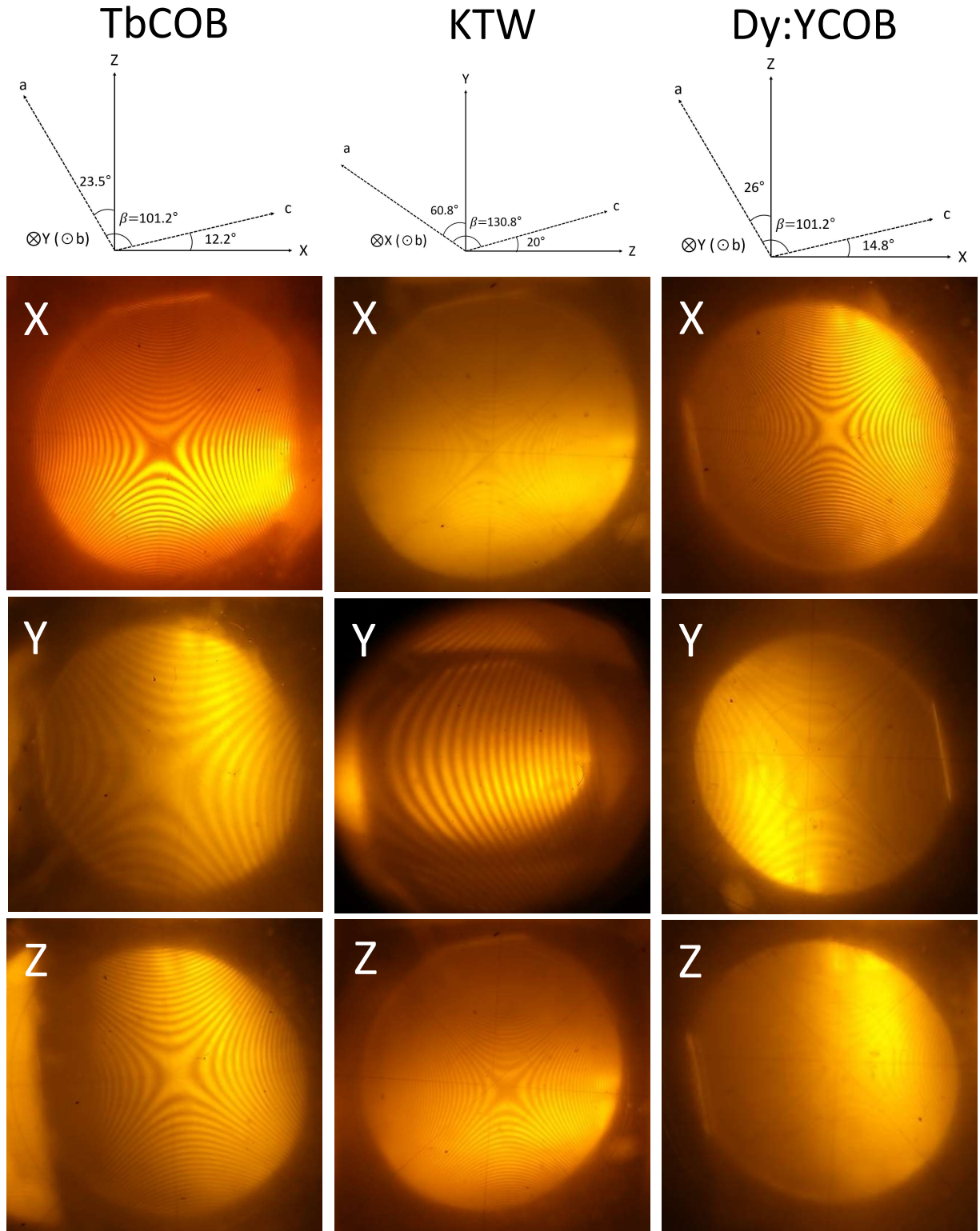
Figure 3.3 **Relationship between optical and crystallographic axes and conoscopic images along indicatrix axes of TbCOB, KTW, and Dy:YCOB. The denoted orientations point toward the viewer.**

The relationship between the crystallographic and optical directions of YCOB was referred to find the three indicatrix axes of Dy:YCOB [7]. According to Laue X-ray diffraction data, the angle between the

Z-axis and a-axis of Dy:YCOB was found to be 23°. This matches exactly with the reported value of YCOB. Conoscopic photos of the oriented crystal of Dy:YCOB are shown in Figure 3.3.

Refractive index measurements of BTP, STB, and LTB were carried out using the standard method of minimum deviation. Prisms of these materials were fabricated. The BTP prism was cut in an arbitrary orientation. The polished surfaces of the STB prism pass through the optic axis (the base of the prism is perpendicular to the two polished surfaces and optic axis) so that the ordinary ($E \perp c$) and extraordinary ($E \parallel c$) refractive indices can be obtained. In order to find the three refractive indices of LTB, two prisms were fabricated, denoted XY prism (X bisects the apex angle and Y is parallel to the polished surfaces) and YZ prism (Y bisects the apex angle and Z is parallel to the polished surfaces). At the minimum deviation angle, the polarization of the incident light can be adjusted to be parallel to one of the two indicatrix directions in an LTB prism. Thus, the refractive indices along the three principal optical orientations can be measured with these two prisms. Photos of the prisms with notation about the optical orientations are presented in Figure 3.4. The apex angles were measured optically to be, respectively, 60.01°, 60.02°, 60.04°, and 59.98° for BTP, STB, LTB (XY), and LTB (YZ).
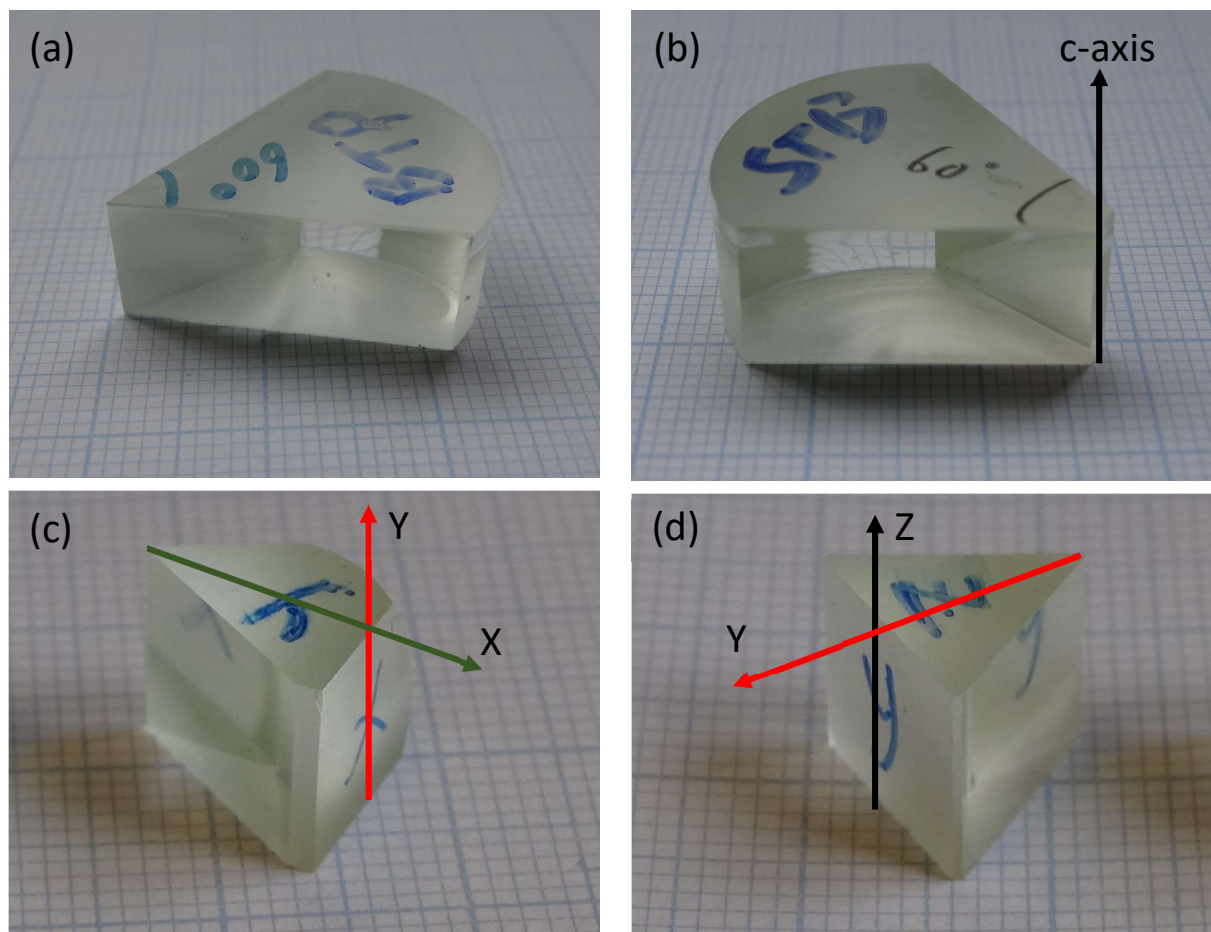
Figure 3.4   Photos showing the prisms of (a) BTP; (b) STB; (c) LTB (XY); (d) LTB (YZ).

The prisms were fixed on a goniometer with minimum accuracy of 1 minute. Polarized spectral lines from different light sources were used to find the minimum angle of deviation. The refractive indices of BTP, STB, and LTB calculated from the minimum deviation angle at each wavelength are summarized

in Table 3.1 and 3.2. The larger value of n_e than n_o points out that STB is an optically positive crystal. The relationship of $n_Z - n_Y < n_Y - n_X$ classifies LTB an optically negative crystal. Using the two prisms of LTB, two sets of n_Y values were obtained. They show a relative deviation of ca. 0.2 %. These experimental errors mainly come from that the two prisms were not perfectly oriented and cut. With the measured refractive indices of LTB, the angle between the Z direction and the optic axis at 589.3 nm can be calculated using the following equation:

$$\sin V_Z = \frac{n_Z(n_Y^2 - n_X^2)^{1/2}}{n_Y(n_Z^2 - n_X^2)^{1/2}} = 0.967 \tag{3.1}$$

It gives V_Z and V_X values around 75° and 15°. This coincide with the observation using the polariscope that the optic axes form a relatively small angle with the X-axis (see also Figure 3.2 (a)).

Table 3.1   **Refractive indices of BTP and STB crystals at different wavelengths.**

Lamp source	Wavelength (μm)	n^{BTP}	n_e^{STB}	n_o^{STB}
HP-Hg	0.4047	1.7147	1.7734	1.7462
HP-Hg	0.4358	1.7092	1.7657	1.7394
Cd	0.4678	1.7047	1.7599	1.7339
Cd	0.4800	1.7031	1.7580	1.7321
Cd	0.5086	1.7000	1.7540	1.7284
HP-Hg	0.5461	1.6967	1.7498	1.7245
HP-Hg	0.5791	1.6946	1.7469	1.7217
Na	0.5893	1.6937	1.7460	1.7212
Cd	0.6438	1.6906	1.7422	1.7173

Table 3.2   **Refractive indices of LTB measured with the XY and YZ prism.**

Lamp source	Wavelength (μm)	$n_X^{XY\ prism}$	$n_Y^{XY\ prism}$	$n_Y^{YZ\ prism}$	$n_Z^{YZ\ prism}$
HP-Hg	0.4047	1.6102	1.6681	-	-
HP-Hg	0.4358	1.6050	1.6625	1.6658	1.6671
Cd	0.4678	1.6011	1.6580	1.6612	1.6624
Cd	0.4800	1.5996	1.6564	1.6597	1.6608
Cd	0.5086	1.5969	1.6534	1.6565	1.6575
HP-Hg	0.5461	1.5938	1.6499	1.6532	1.6541
HP-Hg	0.5791	1.5921	1.6475	1.6508	1.6517
Na	0.5893	1.5913	1.6468	1.6500	1.6509
Cd	0.6438	1.5886	1.6439	1.6469	1.6475

Evolution of the refractive indices to the wavelength can be fitted to two-term Sellmeier dispersion equations. The experimental data as well as fitted curves are presented in Figure 3.5. The fitted equations are given in Table 3.3, where λ is wavelength given in units of micrometer.

Table 3.3   **Fitted Sellmeier dispersion equations.**

BTP	$n^2 = 1 + \dfrac{1.8090\lambda^2}{\lambda^2 - 0.01109}$
STB	$n_e^2 = 1 + \dfrac{1.9697\lambda^2}{\lambda^2 - 0.01333};\ n_o^2 = 1 + \dfrac{1.8897\lambda^2}{\lambda^2 - 0.01274}$
LTB	$n_X^2(XY\ prism) = 1 + \dfrac{1.4821\lambda^2}{\lambda^2 - 0.01136};\ n_Y^2(XY\ prism) = 1 + \dfrac{1.6634\lambda^2}{\lambda^2 - 0.01187}$ $n_Y^2(YZ\ prism) = 1 + \dfrac{1.6630\lambda^2}{\lambda^2 - 0.01201};\ n_Z^2(YZ\ prism) = 1 + \dfrac{1.6641\lambda^2}{\lambda^2 - 0.01231}$
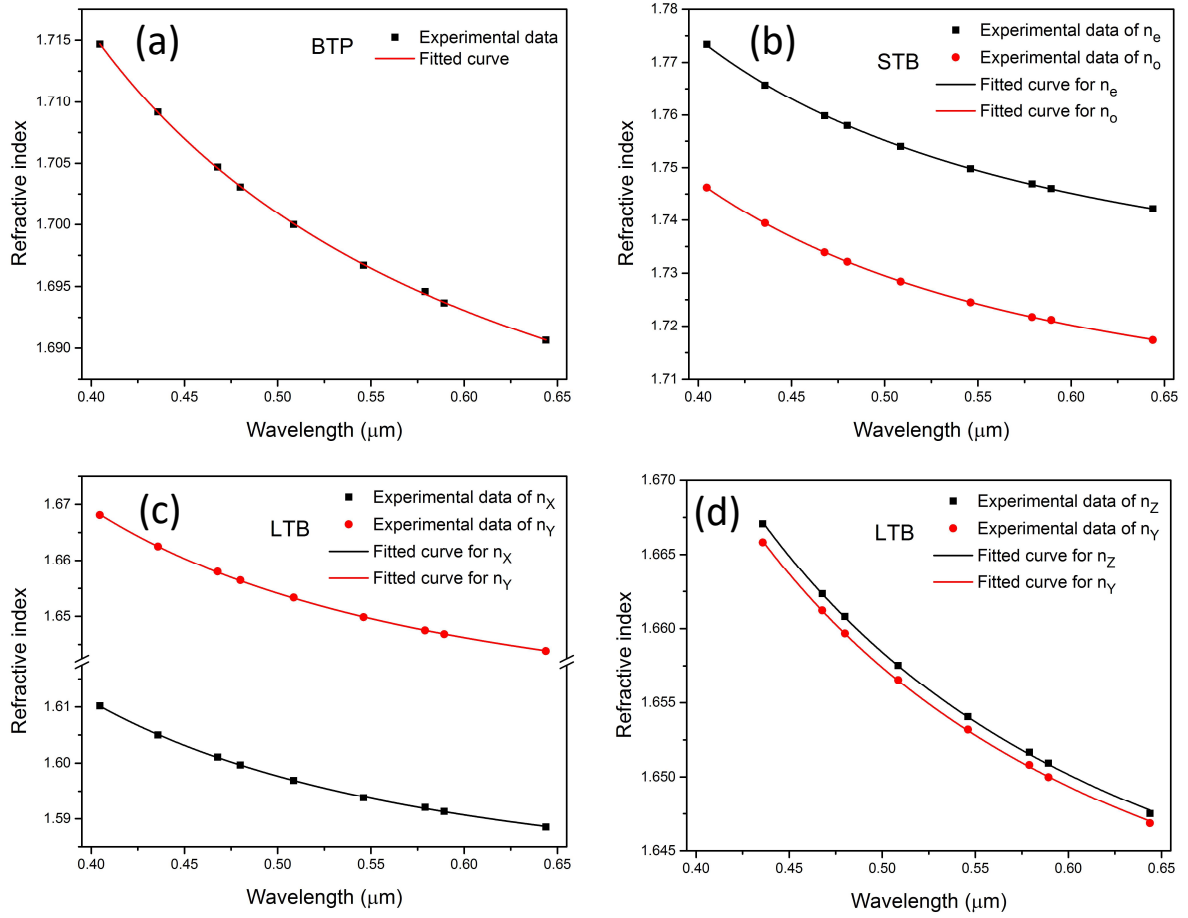
Figure 3.5 **Wavelength-dependent refractive indices measured with the prism of: (a) BTP; (b) STB; (c) LTB (XY); (d) LTB (YZ).**

3.2 Ground-state absorption

The ground-state absorption (GSA) spectroscopy provides useful information of the GSA transitions, such as energetic position and cross-section. The GSA spectra were measured at room temperature in the spectral range of interest for all the Tb^{3+}- as well as Dy^{3+}-activated crystals using a Varian CARY 5000 or CARY 6000i spectrophotometer at room temperature. Detailed experimental procedures are given in the appendix section B.3.7.

First, some theoretical backgrounds of the spectroscopic measurement for lanthanide-based active media should be introduced briefly. A spectroscopic intensity measurement of an atomic transition comprises the light-matter interaction coming from the electric and magnetic multipole moment interactions. Electric dipole (ED) and magnetic dipole (MD) effects are predominant while higher order multipoles, such as electric quatrupole (EQ) and magnetic quatrupole (MQ), are negligible since there is no free charge in a dielectric medium. However, MD transitions deriving from the interaction of the magnetic component of light with matter have also been considered to be very weak compared to ED transitions despite the fact that the energy carried by the electric and magnetic field of light are equivalent followed by the equation $u = \frac{1}{2\mu_0}\boldsymbol{B}^2 + \frac{\varepsilon_0}{2}\boldsymbol{E}^2$. This could be roughly explained by the fact that the force exerted by the magnetic field on the electron is a factor of v/c (v and c are the velocity of the electron and light, respectively) weaker than the electric counterpart [8]. Experimental and theoretical studies indicate that relatively strong MD transitions of lanthanide ions such as Eu^{3+}, Tb^{3+}, and Dy^{3+} could be found at optical frequencies [9–12]. The calculated vacuum MD transition strengths of all the absorption transitions of Tb^{3+} and Dy^{3+} involved in this section are tabulated in the appendix section B.3.8 and some of them should not be neglected. Based on these considerations, the anisotropy of MD transitions was taken into consideration during the spectroscopic measurements by distinguishing the $\boldsymbol{B}$ vector (magnetic field) of light with different principal optical orientations. The polarized spectroscopic measurement methods for uniaxial and biaxial crystals are schematically shown in Figure 3.6. In this approach, three absorption spectra can be obtained for a uniaxial crystal while there are six spectra for a biaxial crystal.
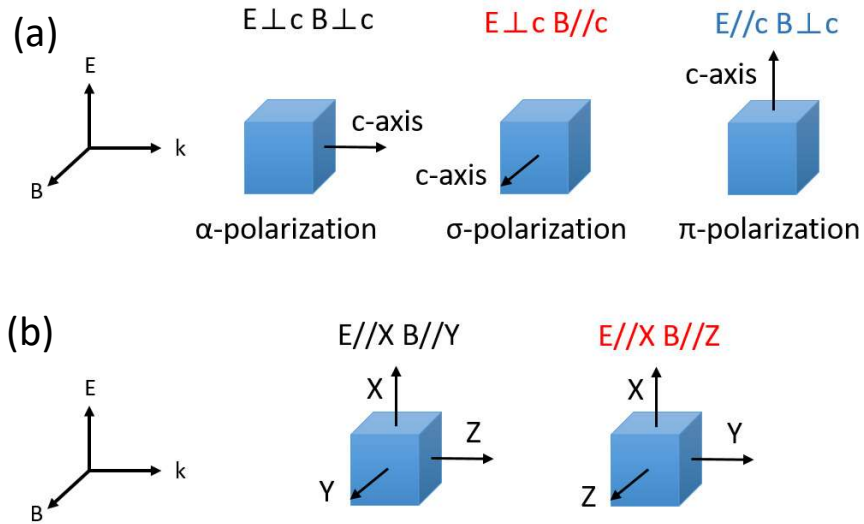
Figure 3.6 **Measurements of polarized spectra for (a) uniaxial crystals; (b) biaxial crystals, the other polarizations, $E \parallel Y\ B \parallel X$, $E \parallel Y\ B \parallel Z$, $E \parallel Z\ B \parallel X$, and $E \parallel Z\ B \parallel Y$, are obtained in the same way.**

Tb^{3+}-activated crystals

The polarized absorption spectra in units of transition cross-section of all the terbium-based crystals are shown in Figure 3.7 to 3.12. The spectral linewidth of BTP and STB are significantly broader than the other host materials. For BTP, it can be accounted for by the disordered [PO$_4$] tetrahedron resulting in dynamic positions of the coordinate oxygen atoms. With regard to STB, the minor occupation of Tb^{3+} in the nine-fold Sr site could be attributed for its spectral-line broadening. The recorded absorption transitions from the ground state $^7F_6$ were assigned according to the literature [13]. Ground-state transitions to the manifolds of $^5L_6$, $^5G_2$, $^5D_1$, and $^5D_0$ are very weak and not necessary to be concerned for this subject.

111
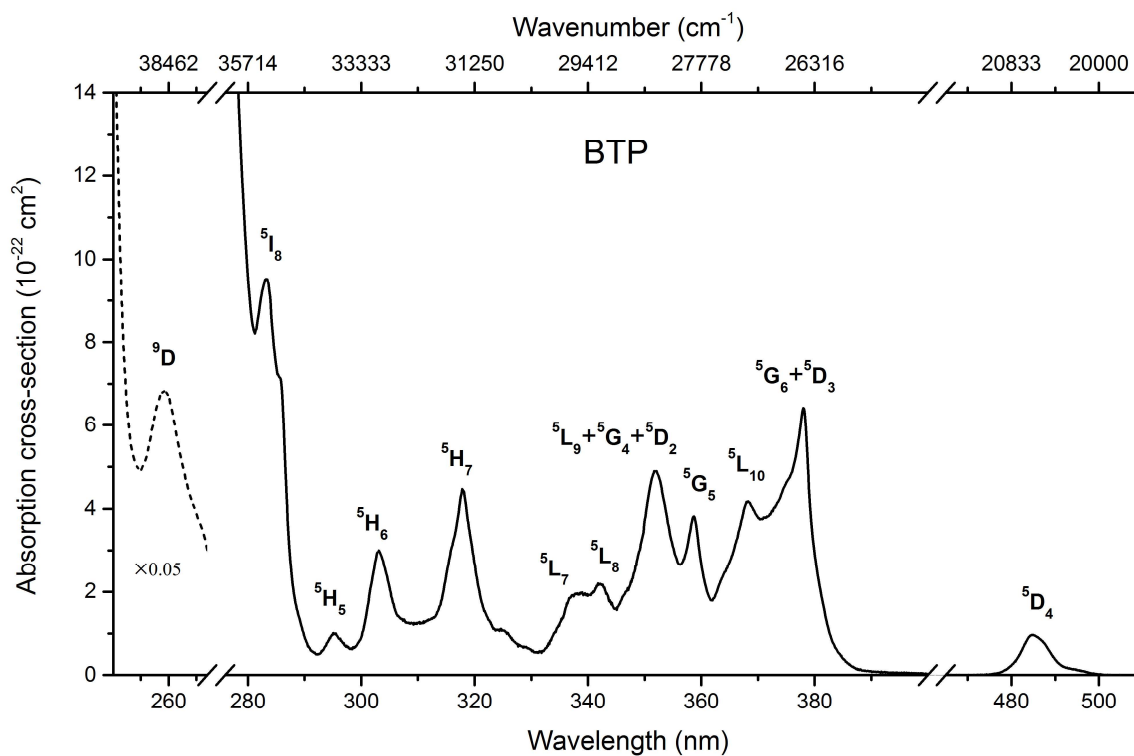
Figure 3.7   Ground-state absorption spectrum of BTP.
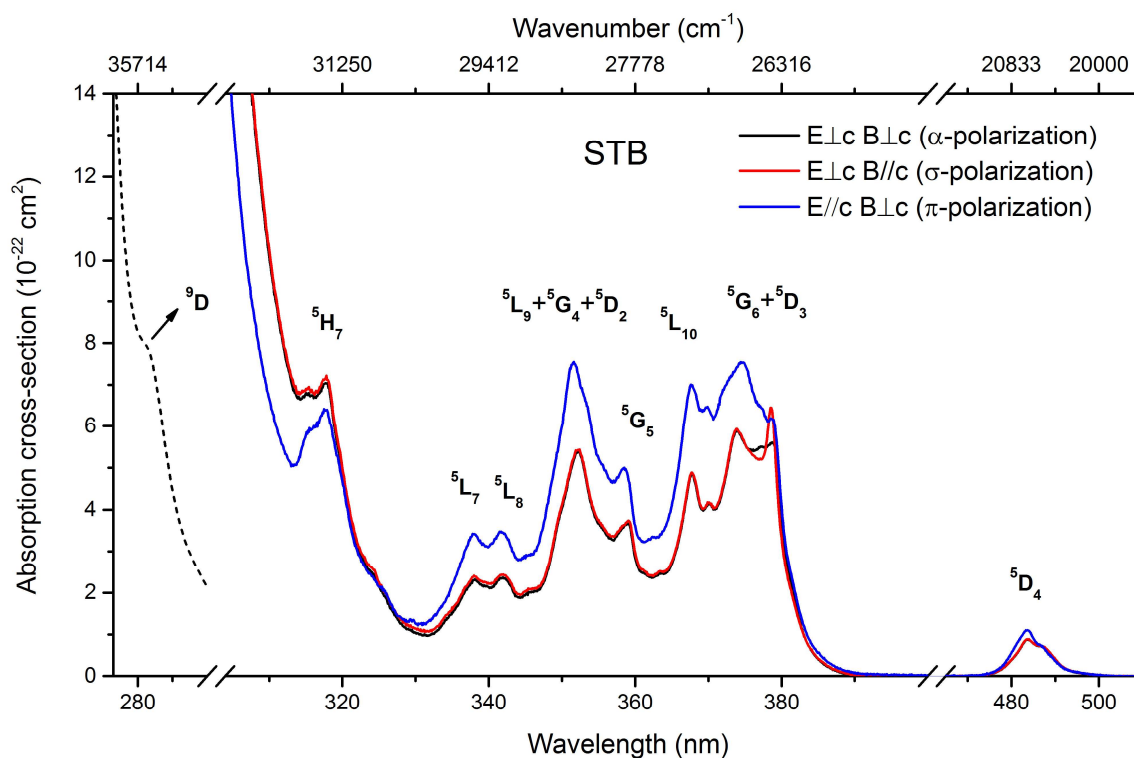
Figure 3.8   Ground-state absorption spectra of STB.
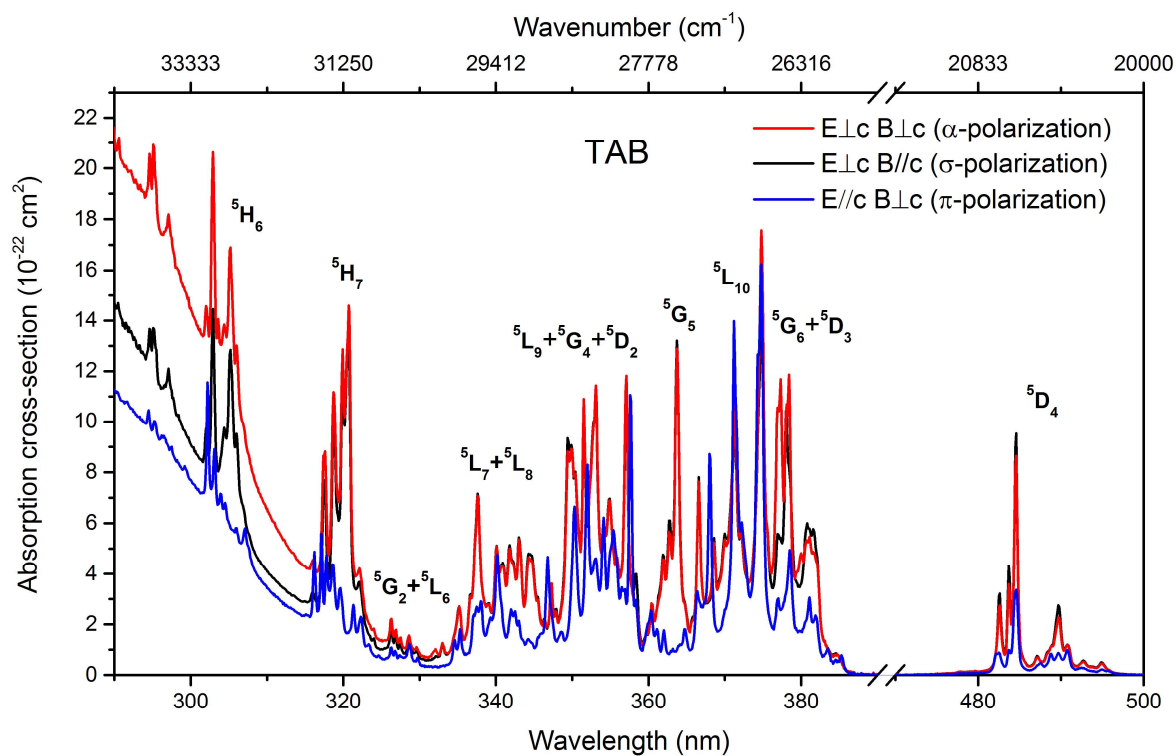
Figure 3.9   **Ground-state absorption spectra of TAB.**

(a) LTB
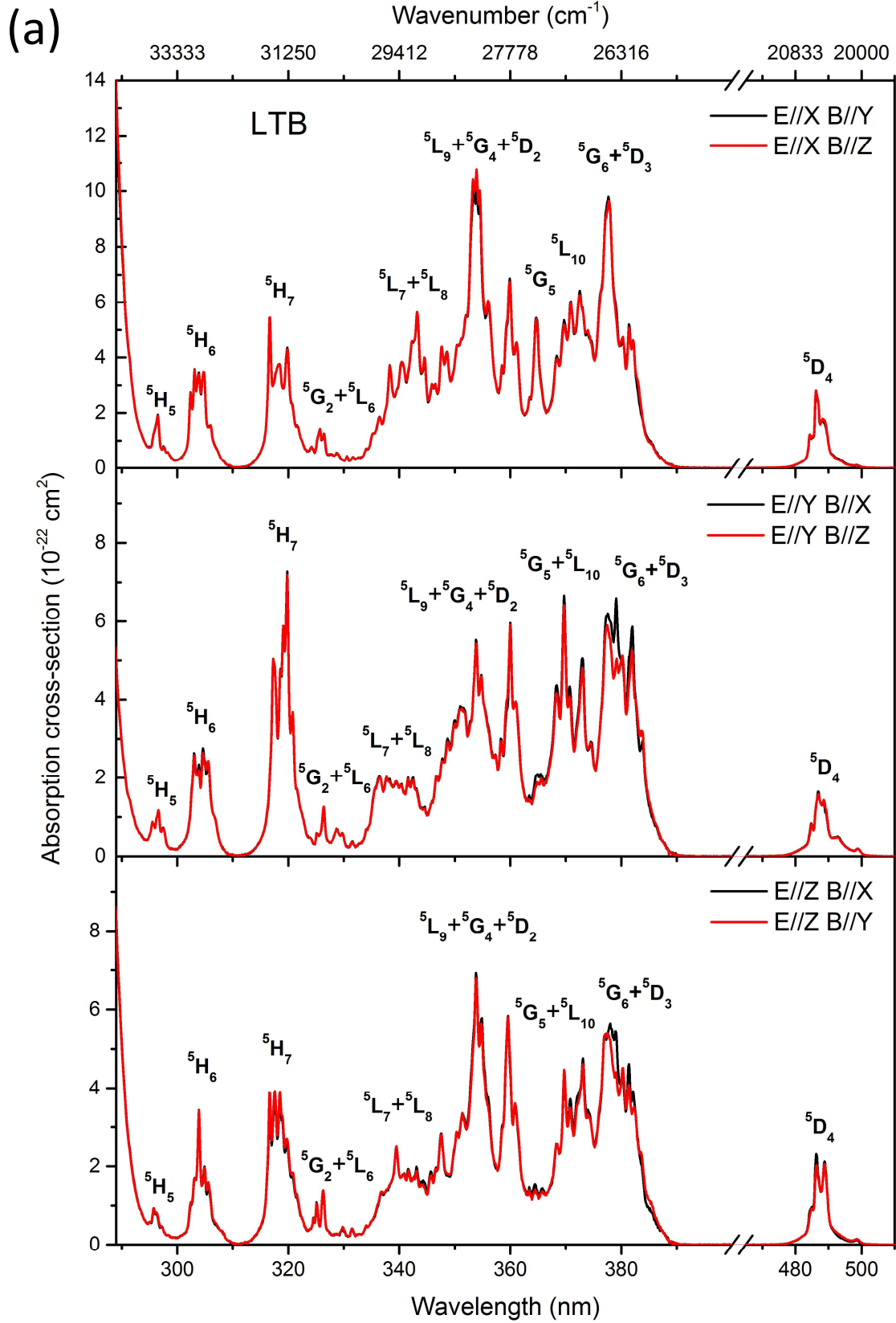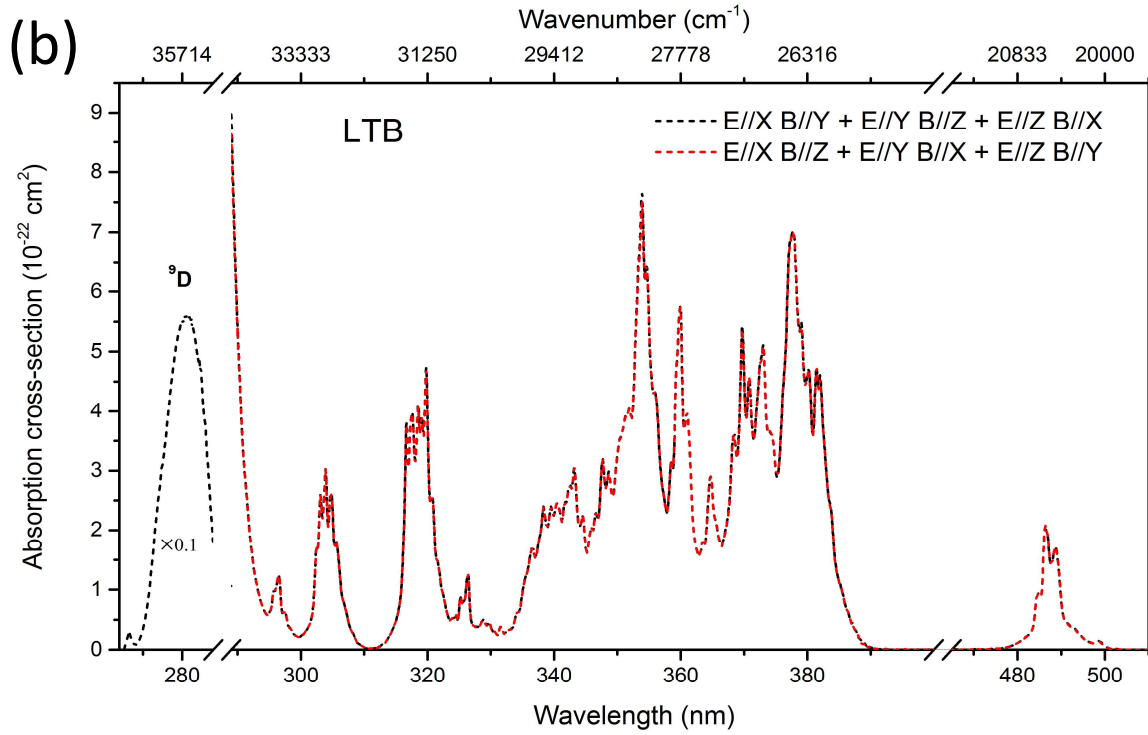
Figure 3.10   (a) Ground-state absorption spectra of LTB; (b) "non-polarized" spectra and position of the $4f \rightarrow 5d$ transitions.

(a)
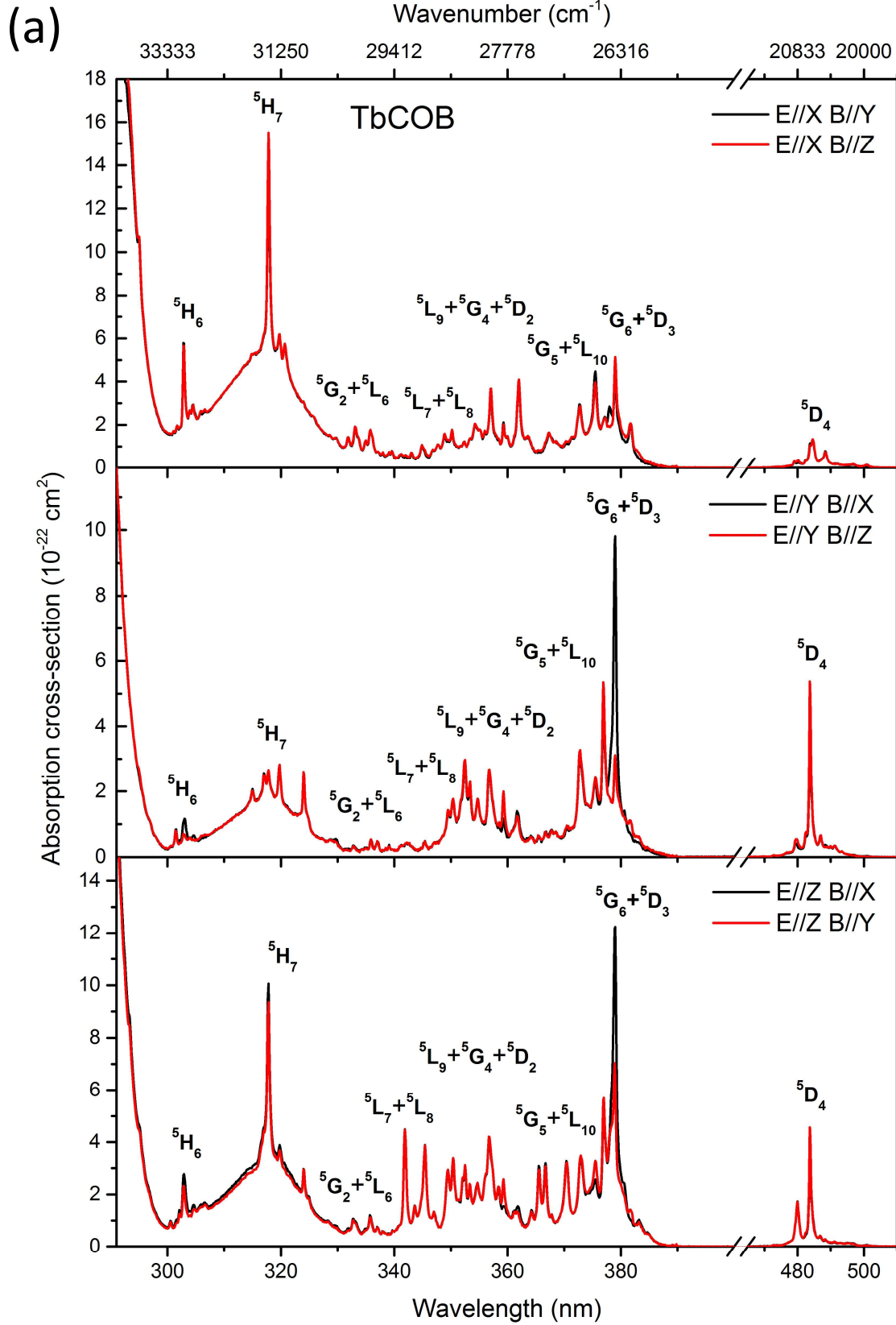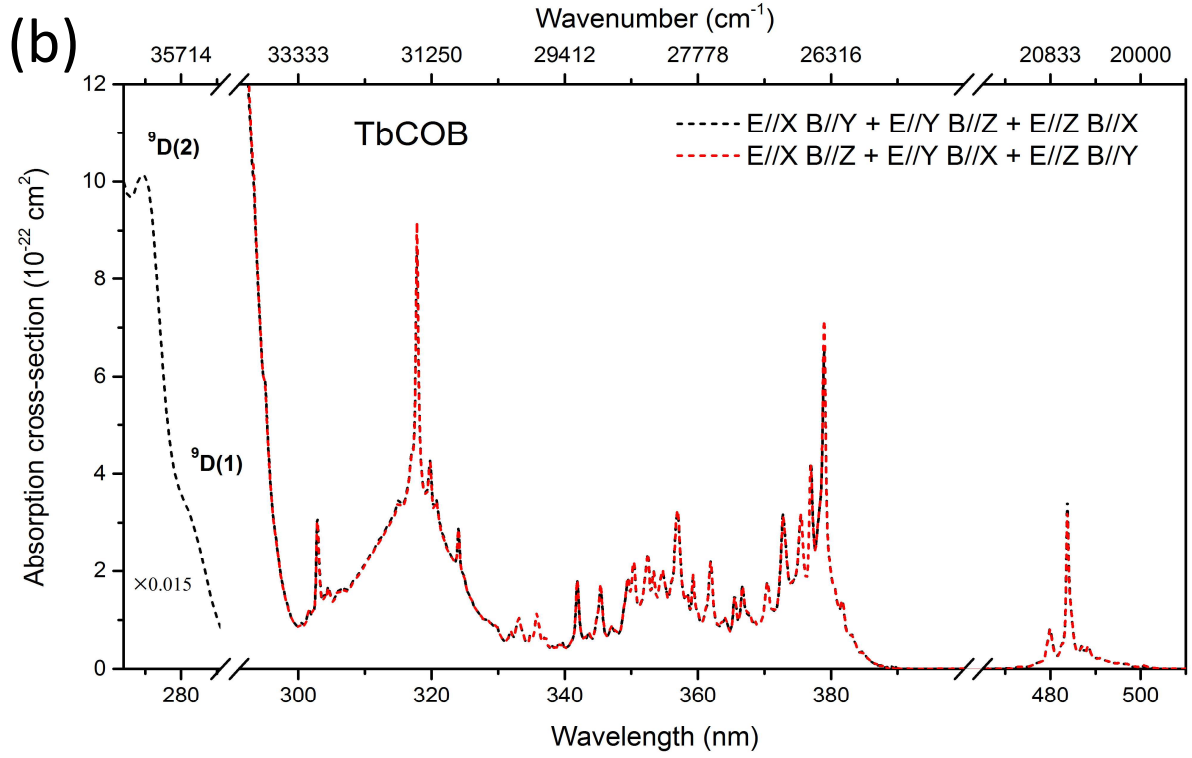
Figure 3.11 **(a) Ground-state absorption spectra of TbCOB; (b) "non-polarized" spectra and position of the $4f \rightarrow 5d$ transitions.**
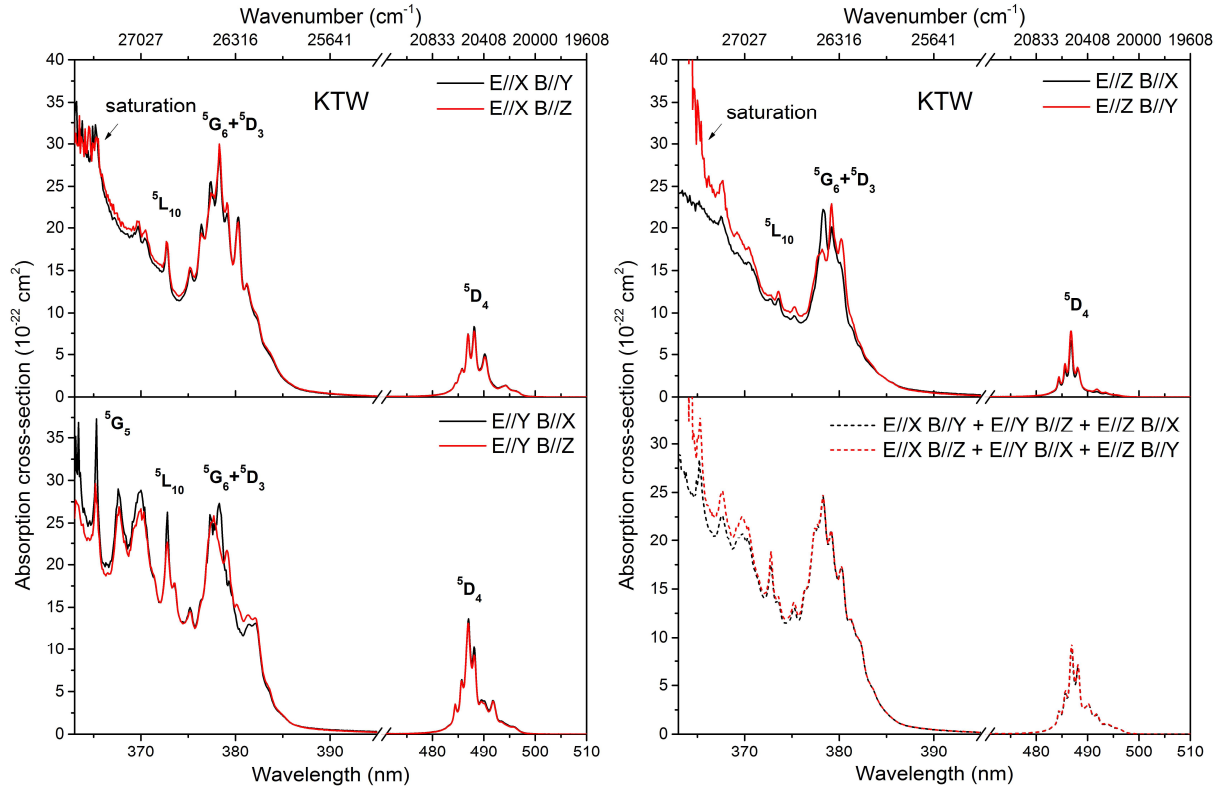
Figure 3.12 **Ground-state absorption spectra of KTW. Notice that the strong intensity of absorption bands in UV results in low accuracy and saturation.**

The intensity of absorption transition in an anisotropic matrix depends on the polarization of light propagating through the medium. The difference between the two polarized spectra with orthogonal directions of E and the same direction of B interpret the anisotropy of ED interactions in the medium. The GSA transitions in STB exhibit overall larger absorption cross-section in $E \parallel c$ polarization than in $E \perp c$ polarization, whereas the situation is the contrary for TAB. This could be partially explained by that STB is optically positive ($n_e > n_o$) while TAB is negative ($n_o > n_e$), and that according to the Lorentz local-field correction, the transition oscillator strength is proportional to the refractive index by a factor of $(n^2 + 2)^2 / 9n$.

Likewise, the anisotropy of MD transitions is reflected by the difference between two polarized spectra with the same direction of E while different directions of B, such as α- and σ-polarization. It can be seen from the GSA spectra of the anisotropic crystals that while transitions without MD interactions are generally well overlapped in polarized spectra with the same electric field orientation, those with non-zero MD oscillator strengths can be different. They are $^7F_6 \rightarrow {}^5G_6$, $^5G_5$, $^5L_7$, $^5L_6$, $^5H_7$, and $^5H_6$. Among them, the $^7F_6 \rightarrow {}^5G_6$ transition gives a relatively large vacuum MD oscillator strength, which is 5.0×10^{-8} (the actual f_{MD} in different matrices is the product of this value and the corresponding refractive index). This value is the same order of magnitude to its ED counterpart. Vacuum oscillator strengths of the other MD transitions are only in the order of 10^{-9} to 10^{-11} thus their anisotropy should be much less pronounced.

The most significant anisotropy of the $^7F_6 \rightarrow {}^5G_6$ MD transition was found between $E \parallel Y \, B \parallel X$ and $E \parallel Y \, B \parallel Z$ polarization of TbCOB. The peak cross-section of the former was measured to be 9.8×10^{-22} cm^2 and the latter 3.1×10^{-22} cm^2. The σ_{abs} at 377.3 nm of TAB also shows a large difference between α- and σ-polarization (12×10^{-22} cm^2 vs. 5.4×10^{-22} cm^2). Besides, MD transitions of $^7F_6 \rightarrow {}^5G_5$ and $^7F_6 \rightarrow {}^5H_6$, although much weaker than the $^7F_6 \rightarrow {}^5G_6$ one, display noticeable anisotropy in TbCOB as well. For example, the spectral line at 359.3 nm attributed to the $^7F_6 \rightarrow {}^5G_5$ transition yields cross-section of 1.6×10^{-22} cm^2 for $E \parallel Z \, B \parallel X$ polarization and 2.6×10^{-22} cm^2 for $E \parallel Z \, B \parallel Y$ polarization. At the wavelength of 303 nm covered by the $^7F_6 \rightarrow {}^5H_6$ transition, the σ_{abs} are 1.2×10^{-22} cm^2 and 0.7×10^{-22} cm^2 in $E \parallel Y \, B \parallel X$ and $E \parallel Y \, B \parallel Z$ polarized spectra, respectively. Viewing from these results, we point out that it is essential to take care of the B vector of light when dealing with relatively strong MD transitions in order to obtain the accurate spectroscopic data. However, it is also worth emphasizing that MD transitions, no matter of their intensities, are not necessary to exhibit anisotropy. For example, spectral lines of LTB in $E \parallel X \, B \parallel Y$ and $E \parallel X \, B \parallel Z$ polarization barely show any differences.

The validity of the polarization-dependent spectral measurement in biaxial crystals can be further verified by the good overlap of the two groups of "non-polarized" spectra, in one of which both the E and B vectors run over all the three principal optical orientations. Taking into account the anisotropy of MD transitions is also the only way to obtain correct "non-polarized" spectra for Judd-Ofelt calculations if strong MD transitions are involved.

The $^7F_6 \rightarrow {}^5D_4$ GSA transition around 486 nm is the only one in the visible spectral range and allows for 2ω-OPSL or LD pumping. Nevertheless, the requirement of a spin flip of electron from the ground state

$^7F_6$ ($S = 3$) to the $^5D_4$ manifold ($S = 2$) results in a low transition probability. The absorption cross-sections of the $^7F_6 \rightarrow ^5D_4$ transition in these crystals are mostly in the order of 10^{-22} cm^2. These values are two orders of magnitude smaller than those of the $^3H_4 \rightarrow ^3P_0$ transition of Pr^{3+} around 485 nm, which is spin-allowed. In an ideal situation for laser operation, the absorption efficiency that quantify the percentage of absorbed photon from the pump in the medium is written as $\eta_{abs} = 1 - exp(-N_c\sigma_{abs}l)$, where N_c is the active-ion concentration. As mentioned before, all these materials were chosen for study in the first place because of their high concentrations of Tb^{3+}, which could greatly compensate the weak absorption capability of the pump energy. The absorption coefficient at maximum absorption wavelength of these oxide crystals, which is the product of N_c and σ_{abs}, ranges from 0.34 cm^{-1} (BTP) to 8.6 cm^{-1} (KTW). For comparison, those of the fluoride gain crystals vary from 0.31 cm^{-1} (12% Tb:LaF$_3$) to 1.2 cm^{-1} (28% Tb:LiLuF$_4$). In fact, except for BTP and STB, the peak absorption cross-sections of TAB, LTB, TbCOB, and KTW are similar or even larger than the highest value of 3×10^{-22} cm^2 among the fluorides (Table 3.4). These results point out that, the oxide crystals have comparable absorption capability of the pump power with the fluorides.

Table 3.4 **Peak wavelengths and absorption cross-sections (in units of 10^{-22} cm^2) of the $^7F_6 \rightarrow ^5D_4$ transition in terbium-based crystals.**

Matrix	Pol.	λ (nm)	σ_{abs}	Matrix	Pol.	λ (nm)	σ_{abs}
BTP	isotropic	484.6	0.96				
STB	α	483.8	0.88		$E \parallel X\ B \parallel Y$	484.6	1.3
	σ	484.0	0.89		$E \parallel X\ B \parallel Z$	484.6	1.3
	π	483.6	1.1	TbCOB	$E \parallel Y\ B \parallel X$	483.7	4.0
TAB	α	484.6	9.5		$E \parallel Y\ B \parallel Z$	483.7	5.4
	σ	484.6	8.6		$E \parallel Z\ B \parallel X$	483.7	3.8
	π	484.6	3.4		$E \parallel Z\ B \parallel Y$	483.7	4.6
LTB	$E \parallel X\ B \parallel Y$	486.2	2.8	KTW	$E \parallel X\ B \parallel Y$	488.1	8.3
	$E \parallel X\ B \parallel Z$	486.2	2.7		$E \parallel X\ B \parallel Z$	488.1	7.8
	$E \parallel Y\ B \parallel X$	486.9	1.7		$E \parallel Y\ B \parallel X$	487.0	14
	$E \parallel Y\ B \parallel Z$	487	1.6		$E \parallel Y\ B \parallel Z$	486.9	13
	$E \parallel Z\ B \parallel X$	486.3	2.3		$E \parallel Z\ B \parallel X$	486.7	6.6
	$E \parallel Z\ B \parallel Y$	486.3	2.1		$E \parallel Z\ B \parallel Y$	486.7	7.7

One may notice that the absorption bands in the UV spectral region are more intense than the $^7F_6 \rightarrow ^5D_4$ transition. A four-level system can be constructed by pumping to the $^5G_6 + ^5D_3$ manifolds around 380 nm. Benefiting from the cross-relaxation channel of $^5D_3 + ^7F_0 \rightarrow ^5D_4 + ^7F_6$, a rapid decay from the

pump level to the upper laser level is anticipated in such Tb^{3+}-concentrated systems. As a matter of fact, the first report of visible stimulated emission of Tb^{3+} was realized by flash-lamp pumping with main output in the spectral range from 300 to 400 nm [14]. However, this approach increases the so-called quantum defect, which is the loss of the pump photon energy. The energy loss due to the non-radiative decay from the pump level to the upper laser level dissipates in the form of lattice vibration and causes detrimental thermal effects. In addition, high-power LD pumps at this wavelength are not available so far and pumping at a high energy level is more likely to result in ESA. This pumping scheme is therefore not more advantageous than the $^7F_6 \rightarrow {}^5D_4$ in-band pumping.

Another important parameter that can be characterized by the GSA spectrum is the energetic position (bary-center energy) of the $4f^7 5d^1$ states of Tb^{3+}, which are considered to be the terminal levels of the ESA processes during the laser operation. Absorption spectra show that the high-spin $4f^7 5d^1$ states with ^9D configuration appear at 259, 280, 281, and 281/269 nm in BTP, STB, LTB, and TbCOB, respectively (see also Figure 3.7, 3.8, 3.10, and 3.11). These results are in good agreement with the predicted values of 263, 285, 285, and 282/274 nm using Dorenbos' semi-empirical method, as well as the experimental values measured with Tb^{3+}-doped polycrystals [15–18]. It should be noted that splitting of the ^9D term into two manifolds is expected, with an energy difference of ca. 1500 cm^{-1} [19]. Transitions above 30000 cm^{-1} in TAB are covered by an additional broad absorption band. This is probably due to the iron impurities, which are typical for this class of material, and makes it difficult to identify the $4f^8 \rightarrow 4f^7 5d^1$ transition in TAB.

It is known that the low-spin $4f^7 5d^1$ state of Tb^{3+} with ^7D configuration is around 6900 cm^{-1} above the energetically lowest ^9D high-spin state. This energy gap does not vary significantly with the host [19]. Therefore, knowing the energy of the high-spin state, that of the low-spin state can be extrapolated. The latter is not realistic to be measured directly since this ground-state transition, which is both parity- and spin-allowed, exhibits fairly strong intensity. The bary-center energies of the low-spin state are thus estimated to be 45500 cm^{-1} for BTP and 42500 cm^{-1} for STB, LTB, and TbCOB based on the experimental data.

It is worth noticing the intense host absorption of KTW arising from a low energy position of around 390 nm (25600 cm^{-1}). This broad absorption band should be derived from Tb^{3+} since the absorption edge of KYW and KGW appears at 330 and 332 nm, respectively [20]. It can be, at least partially, assigned to the inter-valence charge transfer (IVCT) band deriving from the process $Tb^{3+} + W^{6+} \rightarrow Tb^{4+} + W^{5+}$ [21,22]. This strong absorption band makes it impossible to distinguish the inter-configurational $4f^8 \rightarrow 4f^7 5d^1$ transitions in KTW.

Dy^{3+}-activated crystals

GSA spectroscopic measurements for Dy^{3+}-doped single crystals were carried out in a similar approach to the Tb^{3+}-based samples. The polarized GSA spectra of Dy:CYA, Dy:CAS, and Dy:YCOB, scanned from

3333 nm (3000 cm^{-1}) to 312 nm (32000 cm^{-1}), are shown respectively in Figure 3.13, 3.14, and 3.15 in units of absorption cross-section.
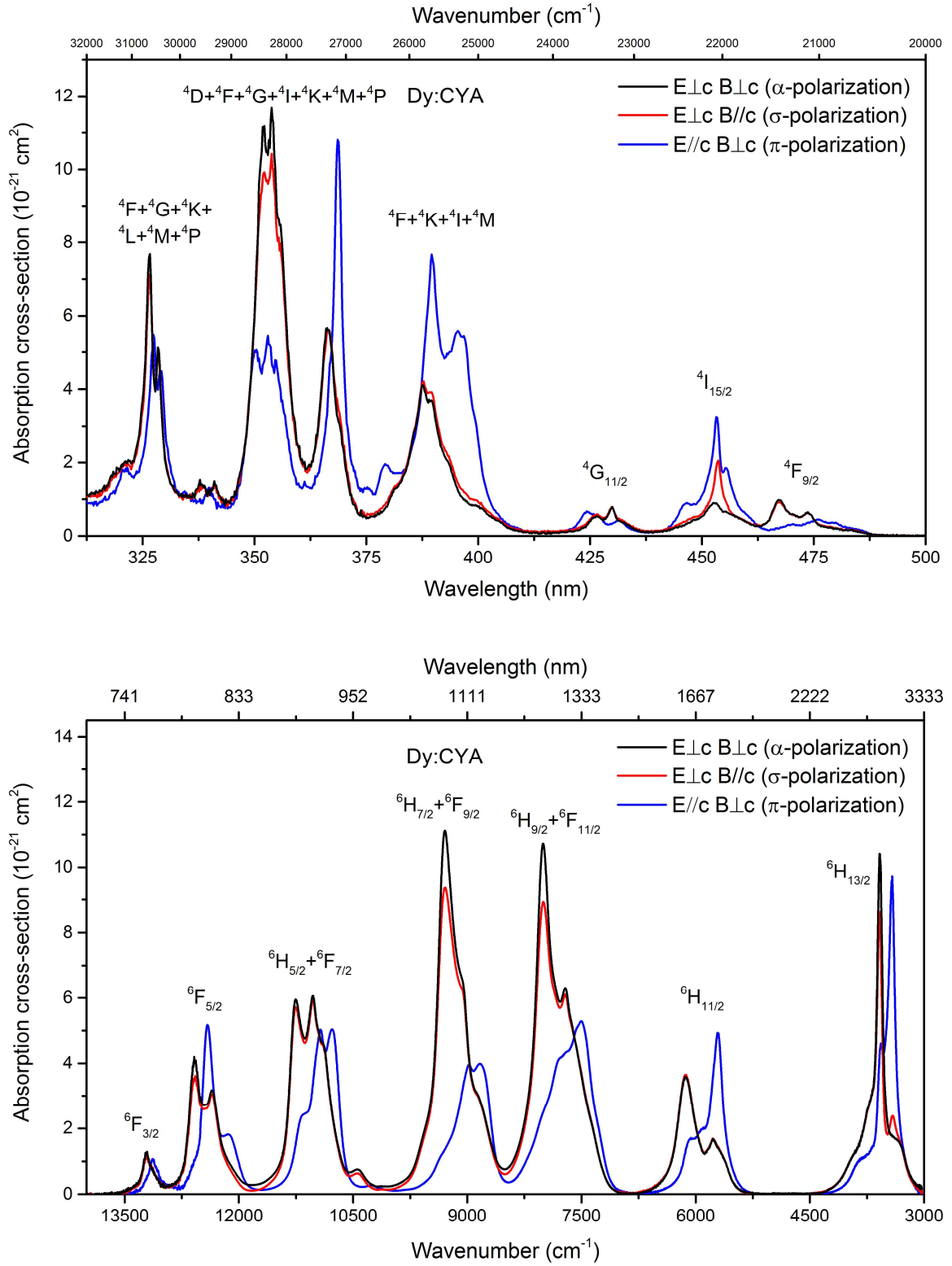
Figure 3.13   **Ground-state absorption spectra of Dy:CYA.**
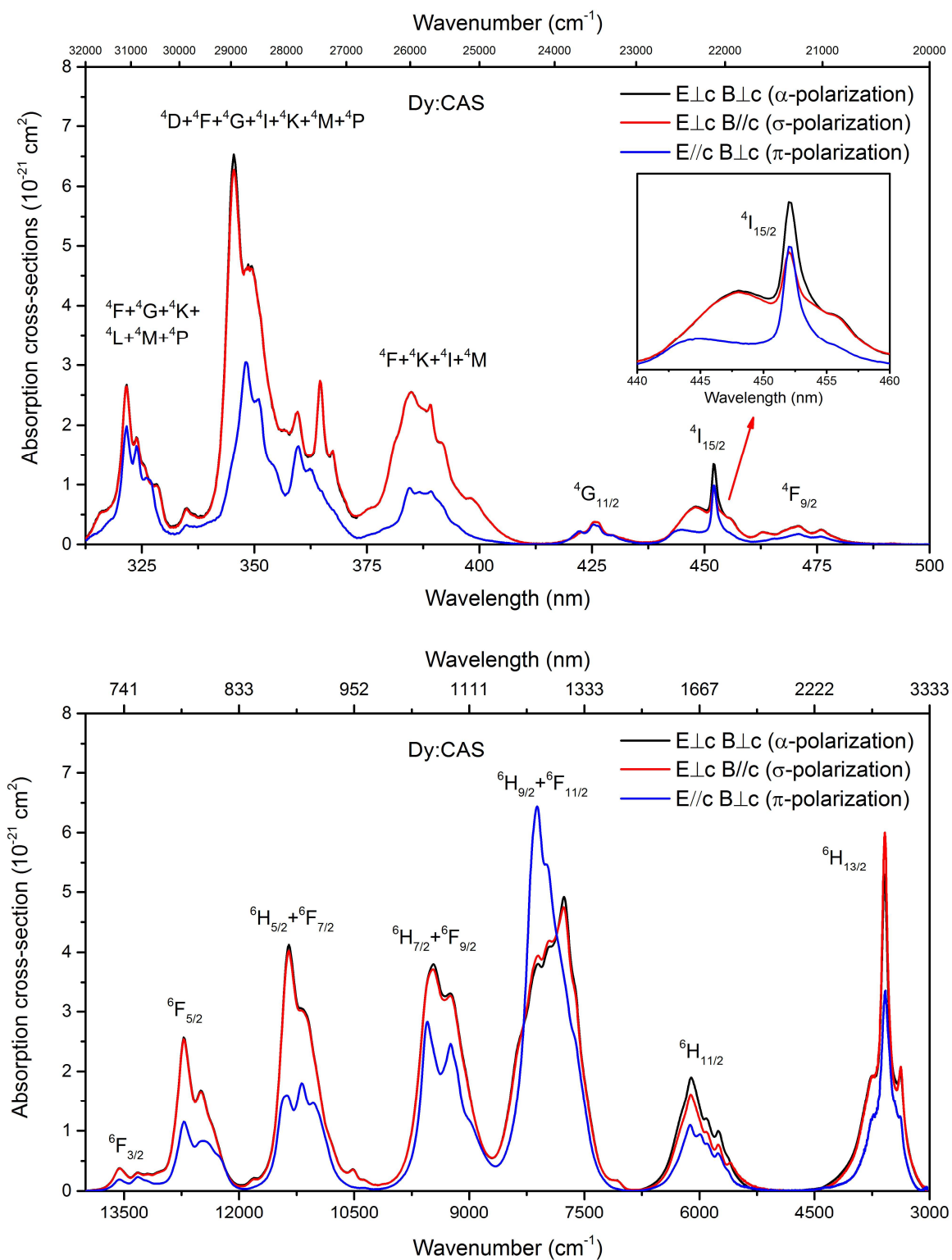
Figure 3.14 **Ground-state absorption spectra of Dy:CAS.**
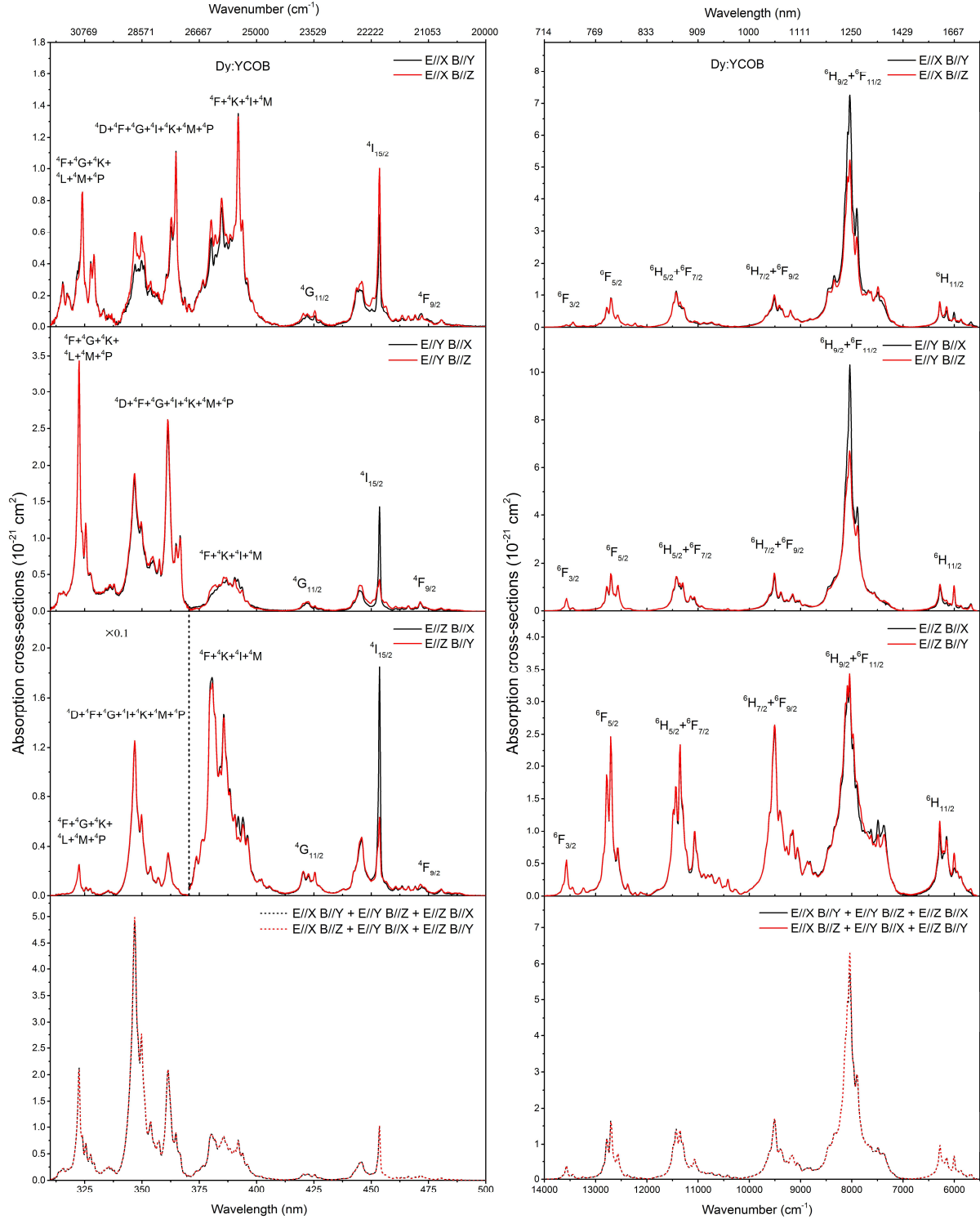
Figure 3.15 **Ground-state absorption spectra of Dy:YCOB in different polarizations. The last two are the "non-polarized" spectra. The $^6H_{15/2} \rightarrow {}^6H_{13/2}$ transition extending over the capable range is not shown.**

It can be seen from the above spectra that the spectral lineshapes of Dy:CYA and Dy:CAS, which feature disordered structures, are broader than that of Dy:YCOB. This is due to the disordered sites in CYA and CAS. The GSA transitions starting from the $^6H_{15/2}$ energy level of Dy^{3+} were assigned according to the

literature [23]. The absorption bands in the infrared ranging from 3000 to 14000 cm^{-1} are spin-allowed transitions from the ground state to the ^6H and ^6F terms. Those around 470 nm, 450 nm, and 425 nm in the visible region could be attributed to GSA transitions to the energy levels of $^4F_{9/2}$, $^4I_{15/2}$, and $^4G_{11/2}$, respectively. They are spin-forbidden and thus show smaller cross-sections than those in the infrared. The energy levels situated in the blue spectral range are potential pump levels for producing visible emissions from the $^4F_{9/2}$ multiplets. Among them, the $^4I_{15/2}$ manifold is the most promising, not only because of its strongest intensity but also due to that it matches the output wavelength of common InGaN-based LD pumps around 450 nm. The near-ultraviolet spectral region comprises more than 20 close-lying manifolds, which can be overall divided into three clusters and are marked in the absorption spectra.

The anisotropy of ED interaction in these Dy^{3+}-activated media is observed. Dy:CAS gives overall higher σ_{abs} values in the $\boldsymbol{E}\perp c$ polarized spectra than in the $\boldsymbol{E}\parallel c$ polarized spectrum since it is optically negative ($n_o > n_e$). The absorption band of Dy:YCOB at 345 nm exhibits a pronounced difference between the $\boldsymbol{E}\parallel Z$ and $\boldsymbol{E}\parallel X$ polarizations. The former give 20 times larger peak σ_{abs} than the latter.

The vacuum MD oscillator strengths of the GSA transitions to $^6H_{15/2}$, $^4I_{15/2}$, $^4F+^4I+^4K+^4M$, and $^4D+^4F+^4G+^4I+^4K+^4M+^4P$, are reported to be, respectively, 2.2×10^{-7}, 5.5×10^{-8}, 6.1×10^{-9}, and 2.4×10^{-9} [11]. Thus, anisotropic behavior of these MD transitions are expected. Among them, the MD transition of $^6H_{15/2}\rightarrow^4I_{15/2}$ shows exceptionally significant anisotropy in these Dy^{3+}-doped crystals. The spectroscopic data focused on the $^6H_{15/2}\rightarrow^4I_{15/2}$ transition is summarized in Table 3.5. The difference between the α- and σ-polarization is a factor of 2.3 in Dy:CYA and of 1.4 in Dy:CAS, in terms of σ_{abs}. The $\boldsymbol{E}\parallel Y\,\boldsymbol{B}\parallel X$ polarized spectrum of Dy:YCOB yields peak cross-section of 1.4×10^{-22} cm^2 at 453.6 nm. In contrast, this value is recorded to be 0.43×10^{-22} cm^2, a factor of 3.3 smaller, in the $\boldsymbol{E}\parallel Y\,\boldsymbol{B}\parallel Z$ polarized spectrum. The accuracy of the spectroscopic measurements of the biaxial Dy:YCOB was verified by the identicalness of the two "non-polarized" spectra (Figure 3.15).

It has to be accentuated again the importance of taking into account the anisotropy of the relatively strong MD transitions during the spectroscopic measurements, since the $^6H_{15/2}\rightarrow^4I_{15/2}$ transition has been used for pumping in the visible laser experiments of Dy^{3+}-activated media. Accurate spectroscopic data for this pump transition is essential for the design of the orientation of the gain crystal. In our cases, to obtain the largest absorption efficiency of the pump, the optimal orientations of the Dy:CYA, Dy:CAS, and Dy:YCOB gain crystals are a-cut, c-cut, and Y-cut, respectively. Routine polarized spectral measurements that only measure σ- and π-polarizations for uniaxial crystals or ambiguous $\boldsymbol{E}\parallel X$, $\boldsymbol{E}\parallel Y$, and $\boldsymbol{E}\parallel Z$ polarizations for biaxial crystals, however, may lead to a different conclusion.

The peak σ_{abs} of the $^6H_{15/2}\rightarrow^4I_{15/2}$ transition in these three crystals, viz. 3.3×10^{-21} cm^2 (Dy:CYA), 1.3×10^{-21} cm^2 (Dy:CAS), and 1.8×10^{-21} cm^2 (Dy:YCOB), are comparable to those of the reported Dy^{3+}-based gain materials (Table 3.5). To precise, they are 1.6×10^{-21} cm^2 in $Dy:Y_3Al_5O_{12}$ and 1.4×10^{-21} cm^2 in $Dy:LiLuF_4$ [24,25]. Thus, these oxide-based crystals, especially Dy:CYA, can provide enough absorption efficiency for blue LD-pumped laser operations.

Table 3.5 **Peak wavelengths and absorption cross-sections (in units of 10^{-21} cm^2) of the $^6H_{15/2} \rightarrow {}^4I_{15/2}$ transition in dysprosium-doped crystals.**

Matrix	Pol.	λ (nm)	σ_{abs}	Matrix	Pol.	λ (nm)	σ_{abs}
	α	452.6	0.92		$\boldsymbol{E} \parallel X\ \boldsymbol{B} \parallel Y$	453.6	0.71
CYA	σ	452.6	2.1		$\boldsymbol{E} \parallel X\ \boldsymbol{B} \parallel Z$	453.6	1.0
	π	452.2	3.3		$\boldsymbol{E} \parallel Y\ \boldsymbol{B} \parallel X$	453.6	1.4
	α	452.0	1.3	YCOB	$\boldsymbol{E} \parallel Y\ \boldsymbol{B} \parallel Z$	453.6	0.43
CAS	σ	452.0	0.9		$\boldsymbol{E} \parallel Z\ \boldsymbol{B} \parallel X$	453.6	1.8
	π	452.0	1.0		$\boldsymbol{E} \parallel Z\ \boldsymbol{B} \parallel Y$	453.6	0.64

3.3 Judd-Ofelt calculations

The Judd-Ofelt theory has been extensively employed to study the intra-configurational $4f \rightarrow 4f$ transitions of lanthanide ions in transparent solid-state materials. It provides great convenience to estimate the transition oscillator strengths, both absorption and emission, by using three Judd-Ofelt phenomenological parameters. Important physical quantities such as excited-state radiative lifetime, fluorescence branching ratio, and quantum efficiency can then be derived from the calculated oscillator strengths of emission transitions, which are difficult to be measured experimentally.

It is worth pointing out that the proper application of the Judd–Ofelt theory should be based on accurate wavelength-dependent refractive index data and high quality wavefunctions of Ln^{3+} for the material system. Using a constant refractive index in calculations for all the involved transitions can cause drastic errors with respect to the calculated ED oscillator strength, which is proportional to the term $(n^2 + 2)^2/9n$. The refractive index dispersion equations of BTP, STB, and LTB were obtained from the accurate measurements in this work and those of TbCOB were reported as well [2]. For the Dy^{3+}-doped crystals, the wavelength-dependent refractive indices of their undoped host materials were used for the calculations, which are reported in [26–28]. This estimation does not cause significant errors due to the low doping level of Dy^{3+} in the matrices.

The Judd-Ofelt calculations in this work were performed using the RELIC software [29]. The host-dependent behavior of atomic wavefunctions can be characterized by the electrostatic and spin-orbit interaction parameters, which are correlated to the $\widehat{H}_e$ and $\widehat{H}_{so}$ Hamiltonians, respectively. The electrostatic interaction parameters $F_{(2)}$, $F_{(4)}$, $F_{(6)}$ quantify the multiplet $^{2S+1}L_J$ barycenter energies while the spin-orbit interaction parameter ζ determines the splitting of each multiplets. These four parameters were fitted to the multiplet barycenter energies determined from their GSA spectra. The results are listed in Table 3.6. They were then used to calculate the intermediate coupling wavefunctions and reduced matrix elements of the ED transitions for each material.

Table 3.6   Fitted electrostatic and spin-orbit interaction parameters in cm⁻¹.

	$F_{(2)}$	$F_{(4)}$	$F_{(6)}$	ζ
BTP	432.7	46.5	8.19	1699.8
STB	432.7	46.5	8.19	1699.7
LTB	432.9	46.7	8.14	1699.6
TbCOB	433.0	46.3	8.18	1699.4
Dy:CYA	406.0	59.8	7.04	1968.0
Dy:CAS	430.6	59.6	7.06	1942.5
Dy:YCOB	423.5	58.1	7.29	1992.6

With the reduced matrix elements, the three Judd-Ofelt intensity parameters $\Omega_\lambda(\lambda = 2, 4, 6)$ can be obtained by a least-square fit of the calculated oscillator strengths to the experimental values. The experimental oscillator strength of an absorption transition is given by [30]:

$$f_{exp} = \frac{4\varepsilon_0 m_e c^2}{e} \int \sigma_{abs}(\bar{v}) \mathrm{d}\bar{v} \tag{3.2}$$

where $\bar{v}$ is wavenumber. In the case of Tb^{3+}, transitions in the UV spectral range are overlapped with each other and their oscillator strengths are difficult to be identified. For the first attempt, the spectral lines of BTP from 390 to 330 nm were fitted to $\sim$20 Gaussian peaks with the same FWHM values and these peaks were assigned according to the energetic positions. Afterwards, we found that it is more convenient and realistic to treat the overlapped transitions as a whole for the fitting, although this could reduce the accuracy to some extent. For comparison, the input and calculated oscillator strengths, the relative root-mean-square deviation for each fitting, and the resulting Judd-Ofelt intensity parameters using these two approaches (marked as SET1 and SET2) are presented in Table 3.7. The relative root-mean-square deviation is defined as:

$$RMS_{rel} = \sqrt{\frac{1}{n-p} \sum_{i=1}^{n} \left(\frac{f_i^{exp} - f_i^{calc}}{f_i^{\mathrm{exp}}} \right)^2} \tag{3.3}$$

where n is the number of transition used for fitting and p is the number of fit parameters, which is 3 in this case.

Table 3.7 **Experimental and calculated oscillator strengths of Tb^{3+} in BTP. The calculated oscillator strength is the sum of the ED and MD counterparts. Values in bracket represent the nonzero MD oscillator strengths.**

Transitions $^7F_6\rightarrow$	$\bar{\lambda}$ (nm)	f_{exp}^{abs} (SET1)	f_{calc}^{abs} (SET1)	f_{exp}^{abs} (SET2)	f_{calc}^{abs} (SET2)
		$\times 10^{-8}$			
$^5D_4$	486	4.19	4.11	4.19	4.08
$^5D_3$	381	2.97	3.40	2.97	3.48
$^5G_6$	376	23.4	25.4 (8.7)	23.4	25.6 (8.7)
$^5L_{10}$	368	31.7	25.0	31.7	25.8
$^5G_5$	358	12.2	11.3 (0.6)	12.2	12.0 (0.6)
$^5D_2$	355	1.17	1.24		
$^5G_4$	353	5.26	5.31	30.7	31.7
$^5L_9$	350	24.3	25.2		
$^5L_8$	343	11.0	9.86	11.0	10.2
$^5L_7$	340	8.40	9.65 (~0)	8.40	9.74 (~0)

$$RMS_{rel} \text{ (SET1)} = 0.130; \ RMS_{rel} \text{ (SET2)} = 0.146$$

SET1: $\Omega_2 = 2.53 \times 10^{-20} cm^2$, $\Omega_4 = 8.56 \times 10^{-20} cm^2$, $\Omega_6 = 1.30 \times 10^{-20} cm^2$

SET2: $\Omega_2 = 2.06 \times 10^{-20} cm^2$, $\Omega_4 = 8.73 \times 10^{-20} cm^2$, $\Omega_6 = 1.35 \times 10^{-20} cm^2$

These two sets of input experimental oscillator strengths result in closed calculated oscillator strengths and comparable Ω_λ parameters. The RMS_{rel} value is larger for SET2 since the number of transition used for fitting is decreased by 2. These results justify the fitting method for overlapped transitions. The input and resulting data for Judd-Ofelt intensity parameters fitting of STB, LTB, TbCOB, Dy:CYA, Dy:CAS, and Dy:YCOB are given in Table 3.8 to 3.13.

Table 3.8   Experimental and calculated oscillator strengths of Tb^{3+} in STB.

Transitions $^7F_6\rightarrow$	$\bar{\lambda}$ (nm)	f_{exp}^{abs}	f_{calc}^{abs}
		$\times 10^{-8}$	
$^5D_4$	486	4.50	4.48
$^5D_3+^5G_6$	378	30.4	31.4 (8.9)
$^5L_{10}$	369	33.7	35.1
$^5G_5$	358	15.9	15.7 (0.6)
$^5D_2+^5G_4+^5L_9$	355	40.8	38.6
$^5L_8$	343	13.3	13.2
$^5L_7$	340	10.5	11.6 ($\sim$0)

$RMS_{rel} = 0.069; \Omega_2 = 2.65 \times 10^{-20} cm^2, \Omega_4 = 7.26 \times 10^{-20} cm^2, \Omega_6 = 1.88 \times 10^{-20} cm^2$

Table 3.9   Experimental and calculated oscillator strengths of Tb^{3+} in LTB.

Transitions $^7F_6\rightarrow$	$\bar{\lambda}$ (nm)	f_{exp}^{abs}	f_{calc}^{abs}
		$\times 10^{-8}$	
$^5D_4$	488	5.77	5.80
$^5D_3+^5G_6$	380	33.3	33.5 (8.5)
$^5L_{10}$	370	32.6	32.8
$^5G_5$	358	15.1	15.4 (0.6)
$^5D_2+^5G_4+^5L_9$	355	40.3	39.6
$^5L_8+^5L_7$	343	22.9	22.5 ($\sim$0)

$RMS_{rel} = 0.019; \Omega_2 = 3.77 \times 10^{-20} cm^2, \Omega_4 = 1.02 \times 10^{-19} cm^2, \Omega_6 = 1.79 \times 10^{-20} cm^2$

Table 3.10   Experimental and calculated oscillator strengths of Tb^{3+} in TbCOB.

Transitions $^7F_6\rightarrow$	$\bar{\lambda}$ (nm)	f_{exp}^{abs}	f_{calc}^{abs}
		$\times 10^{-8}$	
$^5D_4$	484	4.39	2.53
$^5D_3+^5G_6$	379	19.2	19.1 (8.7)
$^5L_{10}$	370	11.3	12.0
$^5G_5$	362	6.23	6.37 (0.6)
$^5D_2+^5G_4+^5L_9$	353	14.4	15.1
$^5L_8$	345	4.07	4.50
$^5L_7$	342	4.32	4.10 ($\sim$0)

$RMS_{rel} = 0.22; \Omega_2 = 1.80 \times 10^{-20} cm^2, \Omega_4 = 4.40 \times 10^{-20} cm^2, \Omega_6 = 6.22 \times 10^{-21} cm^2$

Table 3.11   Experimental and calculated oscillator strengths of Dy^{3+} in CYA.

Transitions $^6H_{15/2}\rightarrow$	$\bar{\lambda}$ (nm)	f_{exp}^{abs}	f_{calc}^{abs}
		$\times 10^{-7}$	
$^6H_{13/2}$	2822	26.0	37.1 (4.3)
$^6H_{11/2}$	1684	19.4	20.9
$^6F_{5/2}$	808	19.1	16.7
$^6F_{3/2}$	757	3.02	3.15
$^4F_{9/2}$	474	4.14	4.12
$^4I_{15/2}$	453	8.12	8.86 (1.14)
$^4G_{11/2}$	428	3.35	3.64

$RMS_{rel} = 0.24; \Omega_2 = 5.05 \times 10^{-20} cm^2, \Omega_4 = 9.95 \times 10^{-20} cm^2, \Omega_6 = 3.12 \times 10^{-20} cm^2$

Table 3.12   Experimental and calculated oscillator strengths of Dy³⁺ in CAS.

Transitions $^6H_{15/2}\rightarrow$	$\bar{\lambda}$ (nm)	f_{exp}^{abs}	f_{calc}^{abs}
		$\times 10^{-7}$	
$^6H_{13/2}$	2789	16.1	15.6 (3.8)
$^6H_{11/2}$	1652	9.50	9.23
$^6H_{9/2}+^6F_{11/2}$	1256	43.2	46.3
$^6H_{7/2}+^6F_{9/2}$	1072	25.3	33.5
$^6H_{5/2}+^6F_{7/2}$	892	20.1	21.4
$^6F_{5/2}$	793	10.5	8.60
$^6F_{3/2}$	746	1.69	1.62
$^4F_{9/2}$	471	1.86	1.93
$^4I_{15/2}$	451	4.21	3.51 (1.0)
$^4G_{11/2}$	426	1.79	1.04

$RMS_{rel} = 0.22; \Omega_2 = 1.96 \times 10^{-20} cm^2, \Omega_4 = 3.58 \times 10^{-20} cm^2, \Omega_6 = 1.92 \times 10^{-20} cm^2$

Table 3.13   Experimental and calculated oscillator strengths of Dy³⁺ in YCOB[a].

Transitions $^6H_{15/2}\rightarrow$	$\bar{\lambda}$ (nm)	f_{exp}^{abs}	f_{calc}^{abs}
		$\times 10^{-7}$	
$^6H_{11/2}$	1623	3.90	4.19
$^6H_{9/2}+^6F_{11/2}$	1246	26.5	27.7
$^6H_{7/2}+^6F_{9/2}$	1059	7.92	9.93
$^6H_{5/2}+^6F_{7/2}$	882	6.47	7.45
$^6F_{5/2}$	787	3.98	3.02
$^6F_{3/2}$	738	0.70	0.57
$^4F_{9/2}$	471	0.58	0.66
$^4I_{15/2}$	449	2.22	2.62 (1.0)
$^4G_{11/2}$	423	0.54	0.26

$RMS_{rel} = 0.29; \Omega_2 = 2.42 \times 10^{-20} cm^2, \Omega_4 = 8.79 \times 10^{-21} cm^2, \Omega_6 = 6.51 \times 10^{-21} cm^2$

[a] The capable spectral range of the spectrophotometer could not completely cover the $^6H_{15/2}\rightarrow^6H_{13/2}$ transition of Dy:YCOB hence it was not used for the calculation.

The resulting Ω_λ parameters of the Tb^{3+}-based compounds exhibit the same order of $\Omega_4 > \Omega_2 > \Omega_6$. Good agreements were obtained for STB and LTB with respect to the experimental and calculated oscillator strengths, while those of TbCOB give a relative large RMS_{rel} of 0.22. It can be seen from Table 2.9 that the discrepancy mainly reside in the $^7F_6 \rightarrow {}^5D_4$ transition. The f_{calc}^{abs} is much smaller than the f_{exp}^{abs} value. This is not surprising viewing from its total oscillator strength. The sum f_{exp}^{abs} of all the used transitions in TbCOB is weaker than that of BTP, STB, and LTB by a factor of 2. This result in the smallest fitted Judd-Ofelt intensity parameters of TbCOB, which define the calculated intensity for all the transitions. However, the f_{exp}^{abs} of the $^7F_6 \rightarrow {}^5D_4$ transition in TbCOB is comparable to the other terbium-based crystals. That is to say, TbCOB exhibits an extraordinarily strong $^7F_6 \rightarrow {}^5D_4$ transition strength that cannot be well accounted for in the framework of Judd-Ofelt theory.

The calculated oscillator strengths of the Dy^{3+}-activated materials are mainly in line with the measured values. However, noticeable discrepancies were observed in transitions of $^6H_{15/2} \rightarrow {}^6H_{13/2}$ (Dy:CYA), $^6H_{15/2} \rightarrow {}^6H_{7/2} + {}^6F_{9/2}$ (Dy:CAS), and $^6H_{15/2} \rightarrow {}^4G_{11/2}$ (Dy:CAS, Dy:YCOB). The large errors observed in the $^6H_{15/2} \rightarrow {}^6H_{13/2}$ transition might be related to its hypersensitive property. The intensity of a hypersensitive transition, which obeys selection rules of $|\Delta J| \leq 2$, $|\Delta L| \leq 2$, and $\Delta S = 0$, is greatly influenced by the coordinate environment [31].

The Judd-Ofelt analysis also provides information about the MD oscillator strengths. The $^7F_6 \rightarrow {}^5G_6$ transition features a large contribution from the MD interaction, as is observed in the absorption spectra of the Tb^{3+}-based crystals. Moreover, the MD transition of $^6H_{15/2} \rightarrow {}^4I_{15/2}$ is found to occupy 13%, 19%, and 38% of its total transition oscillator strength in Dy:CYA, Dy:CAS, and Dy:YCOB, respectively. This is consistent with the spectroscopic results that Dy:YCOB exhibits the most evident anisotropy of this MD transition.

3.4 Fluorescence spectroscopy

The laser performance of an active medium can be predicted by its fluorescence emission spectrum, because the probability of a stimulated emission event at a wavelength is directly related to the intensity of the fluorescence emission at this wavelength. Polarized emission spectra of all the crystals were recorded at room temperature. The excitation source was a tunable pulsed OPO laser (Ekspla NT342B). Several MD transitions are involved in the studied spectral range of these Tb^{3+}- or Dy^{3+}-activated compounds, thus their anisotropic behaviors were taken care. The obtained fluorescence spectra were calibrated owing to the different response of the CCD camera with respect to photon energy. More detailed information about the experimental setup and apparatus can be found in the appendix section B.3.9.

Tb^{3+}-activated crystals

Trivalent terbium ion is known for its intense visible fluorescence originating from radiative decay of the $^5D_4$ level. Figure 3.16 shows the spontaneous emission of the six terbium-based crystals under excitation of 365 and 486 nm. In spite of the large Tb^{3+}-concentration in these materials, the characteristic fluorescence could be well observed because non-radiative quenching effects, viz. cross relaxation and multiphonon relaxation, are negligible from the $^5D_4$ excited state. However, the fluorescence of KTW is remarkably weaker than the others under UV excitation. The fluorescence intensity at 542 nm excited at 365 nm was measured to be around an order of magnitude weaker than that excited at 486 nm for KTW. This is anticipated since the excitation wavelength of 365 nm well enters the IVCT absorption band of KTW, which makes no contribution to the fluorescence of Tb^{3+}.
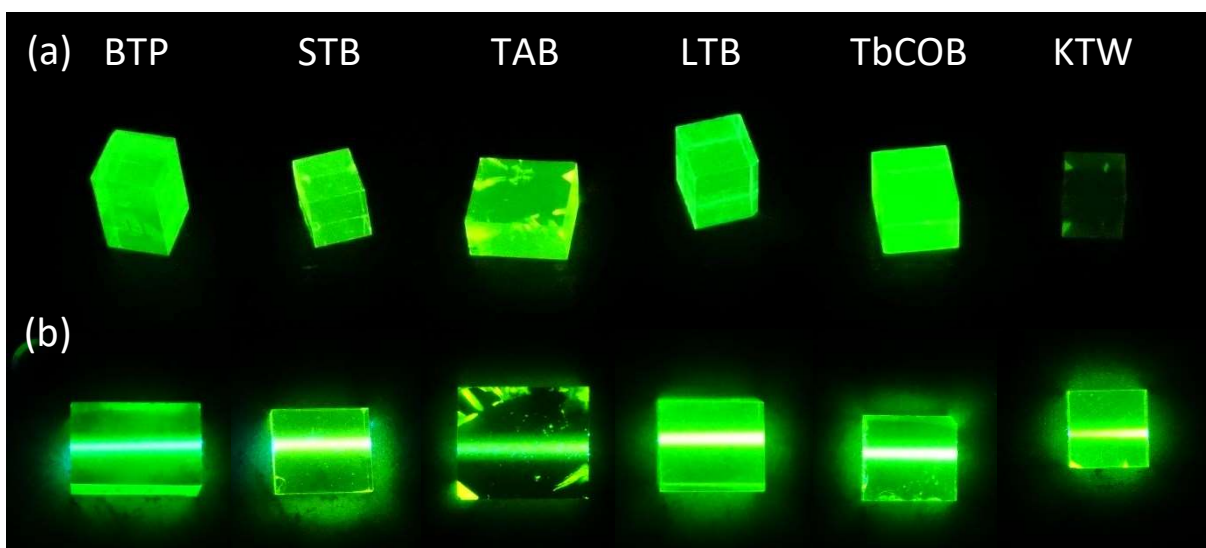
Figure 3.16 **Photographs showing the fluorescence of the terbium-based crystals: (a) excited by a 365-nm UV lamp (this photo was taken for all the crystals at the same time); (b) excited by a 486-nm laser diode.**

Fluorescence spectra of the Tb^{3+}-activated crystals were recorded under excitation at 378 nm. They can be converted to emission cross-sections, which quantifies the probability of optically induced transition events, as a function of wavelength using the Füchtbauer-Ladenburg equation described in detail in the Appendix A and the literature [32]:

$$\sigma_{em}(\lambda) = \frac{\lambda^5 I(\lambda)}{8\pi n^2 c \tau_{rad} \int \lambda I(\lambda) d\lambda} \tag{3.4}$$

where $I(\lambda)$ is the spectral irradiance and τ_{rad} is the radiative lifetime of the $^5D_4$ manifold. τ_{rad} of BTP, STB, LTB, and TbCOB were calculated from the Judd-Ofelt analysis in this work. Those of TAB and KTW were taken from the literature, which are, respectively, 2.07 ms and 0.5 ms [33,34]. Due to the lack of wavelength-dependent n values of TAB and KTW, those of their analogue compounds of $YAl_3(BO_3)_3$ and $KY(WO_4)_2$ were utilized [35,36].
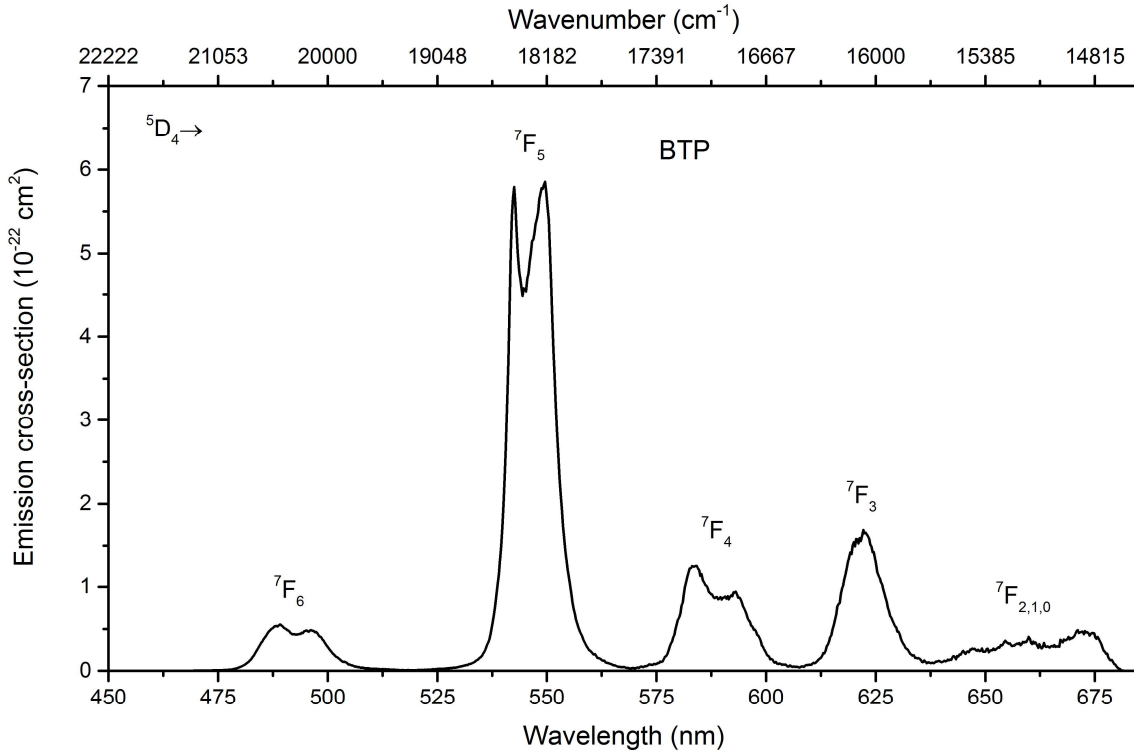
Figure 3.17   **Emission spectra of BTP.**
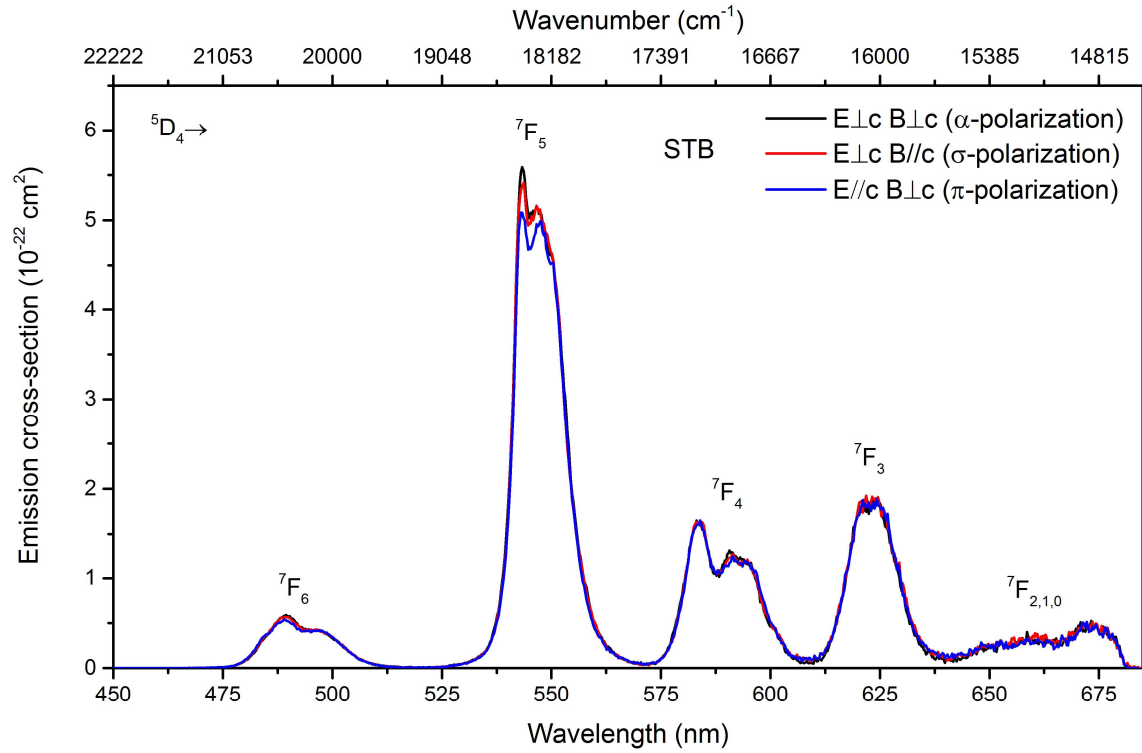
Figure 3.18   Polarized emission spectra of STB.
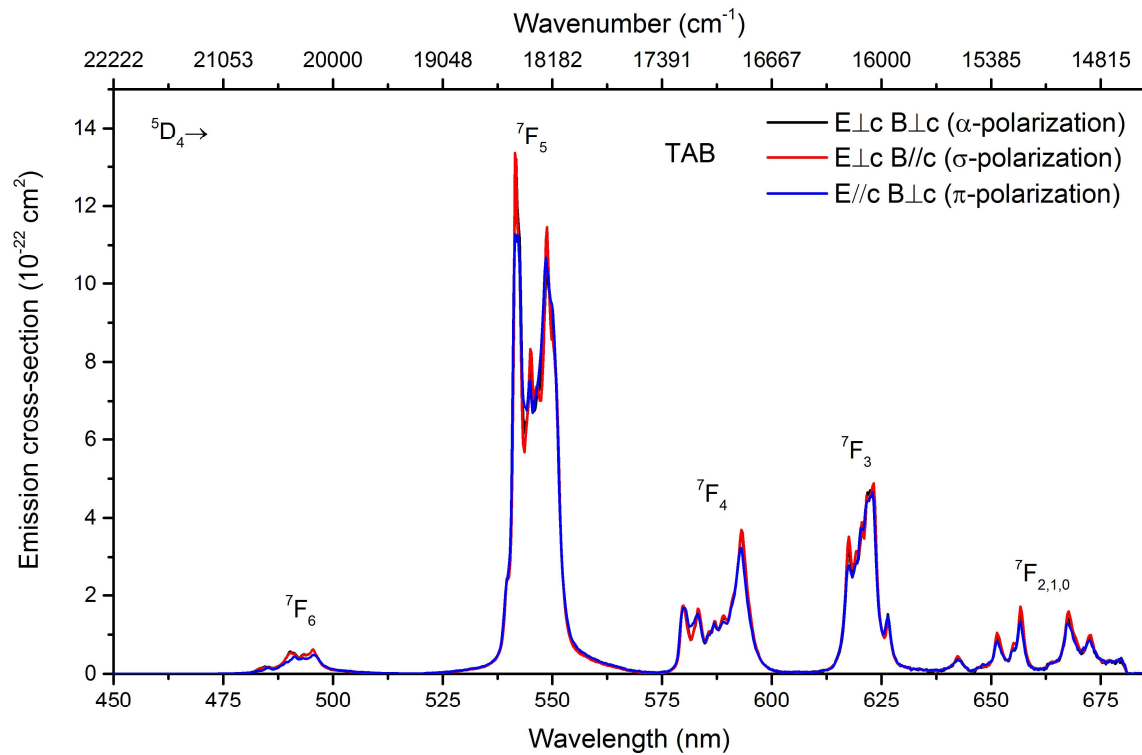
Figure 3.19   Polarized emission spectra of TAB.

(a)
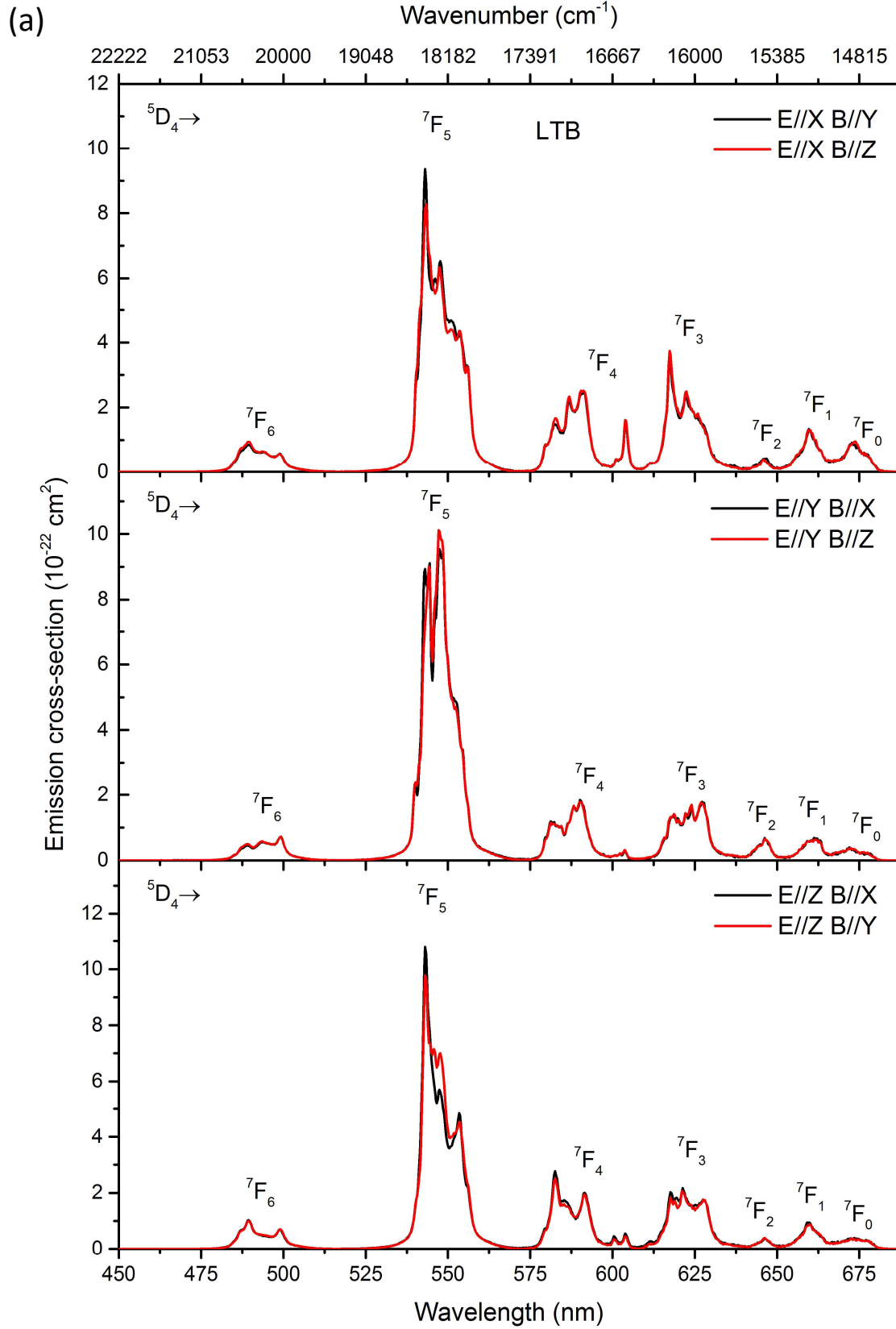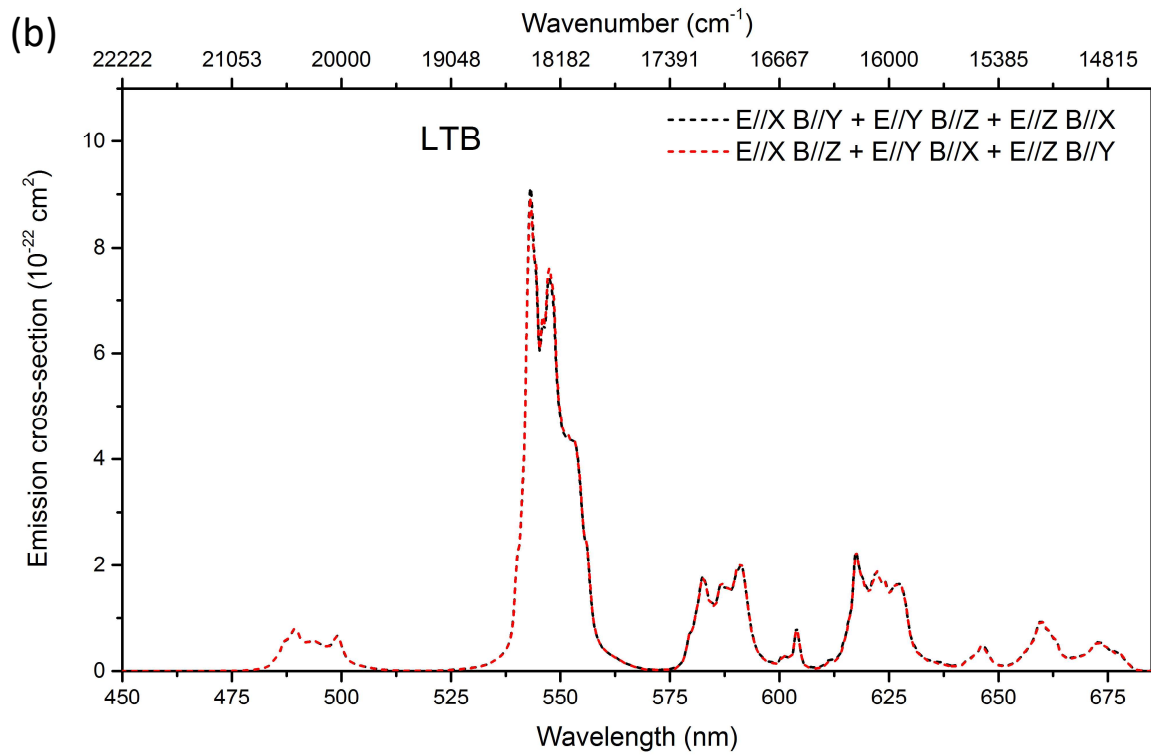
Figure 3.20 **(a) Polarized emission spectra of LTB; (b) "non-polarized" emission spectra.**

(a)
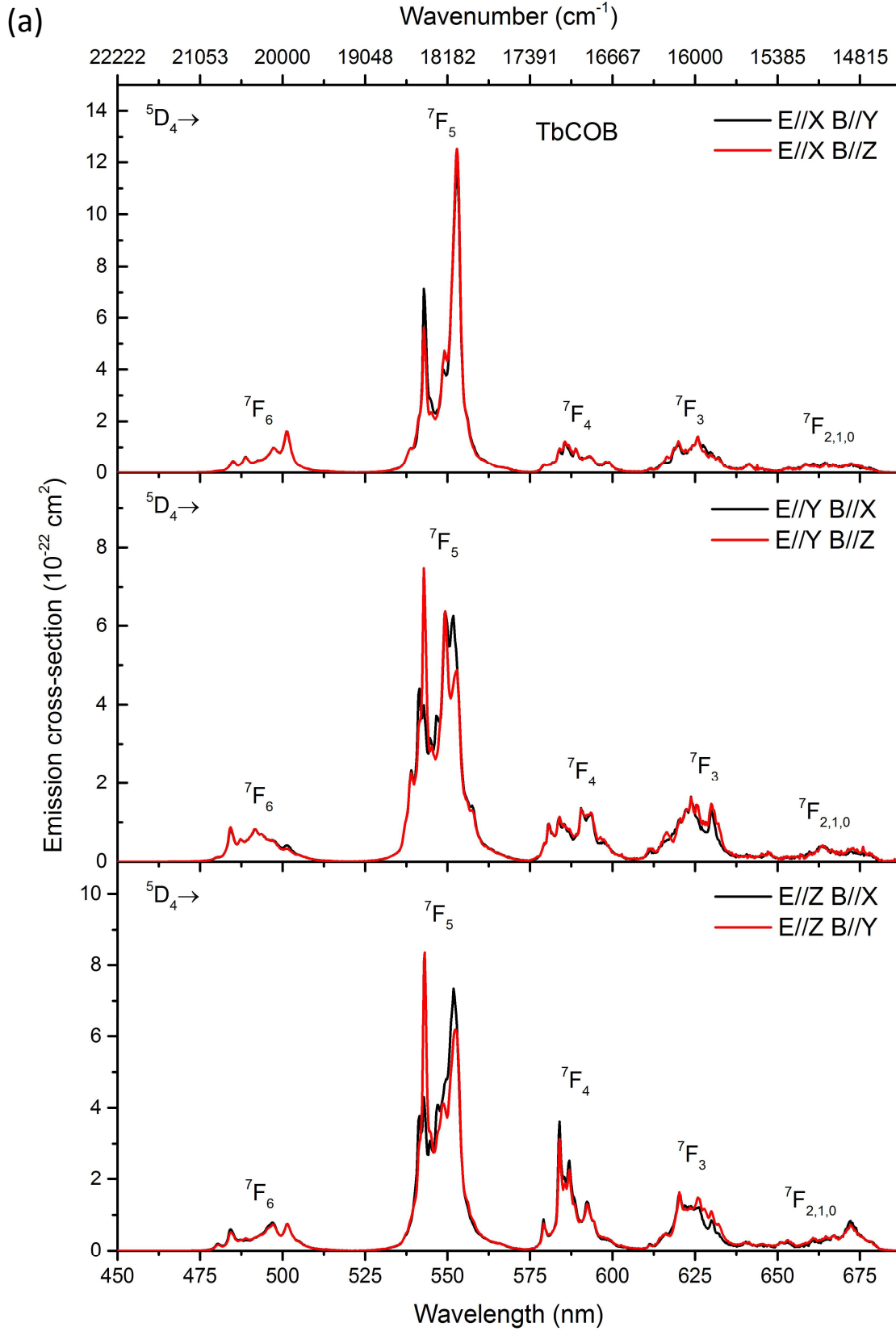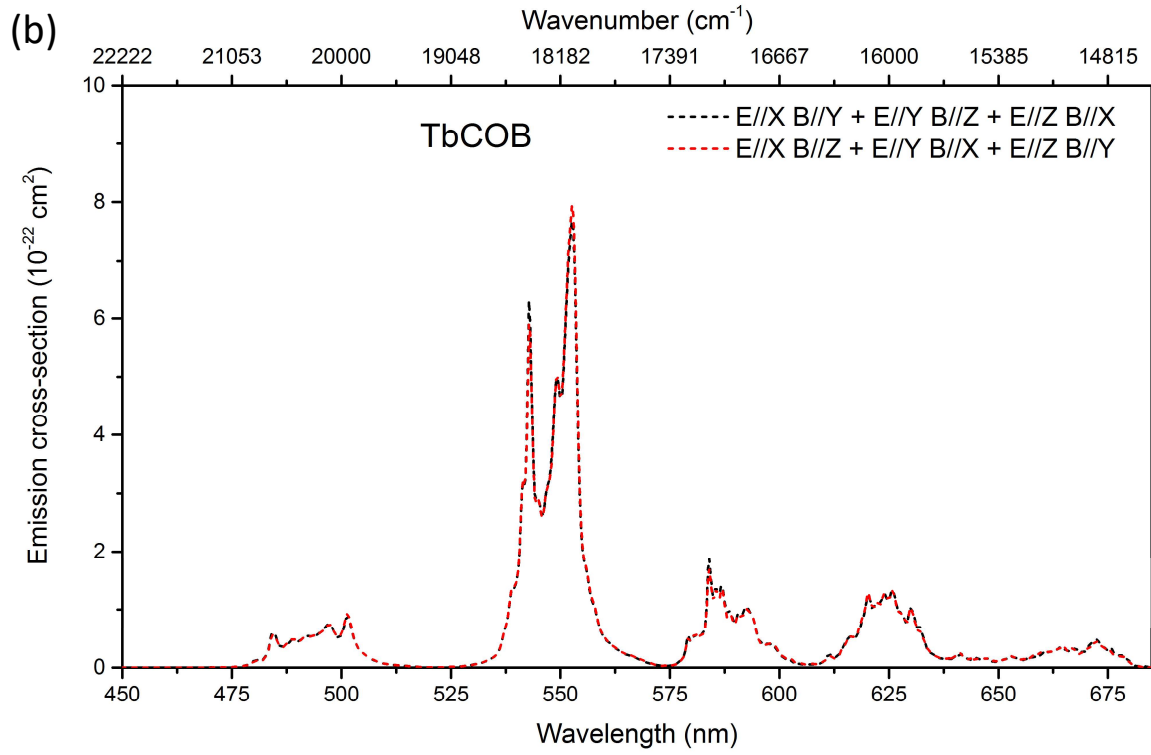
Figure 3.21 **(a) Polarized emission spectra of TbCOB; (b) "non-polarized" emission spectra.**

(a)
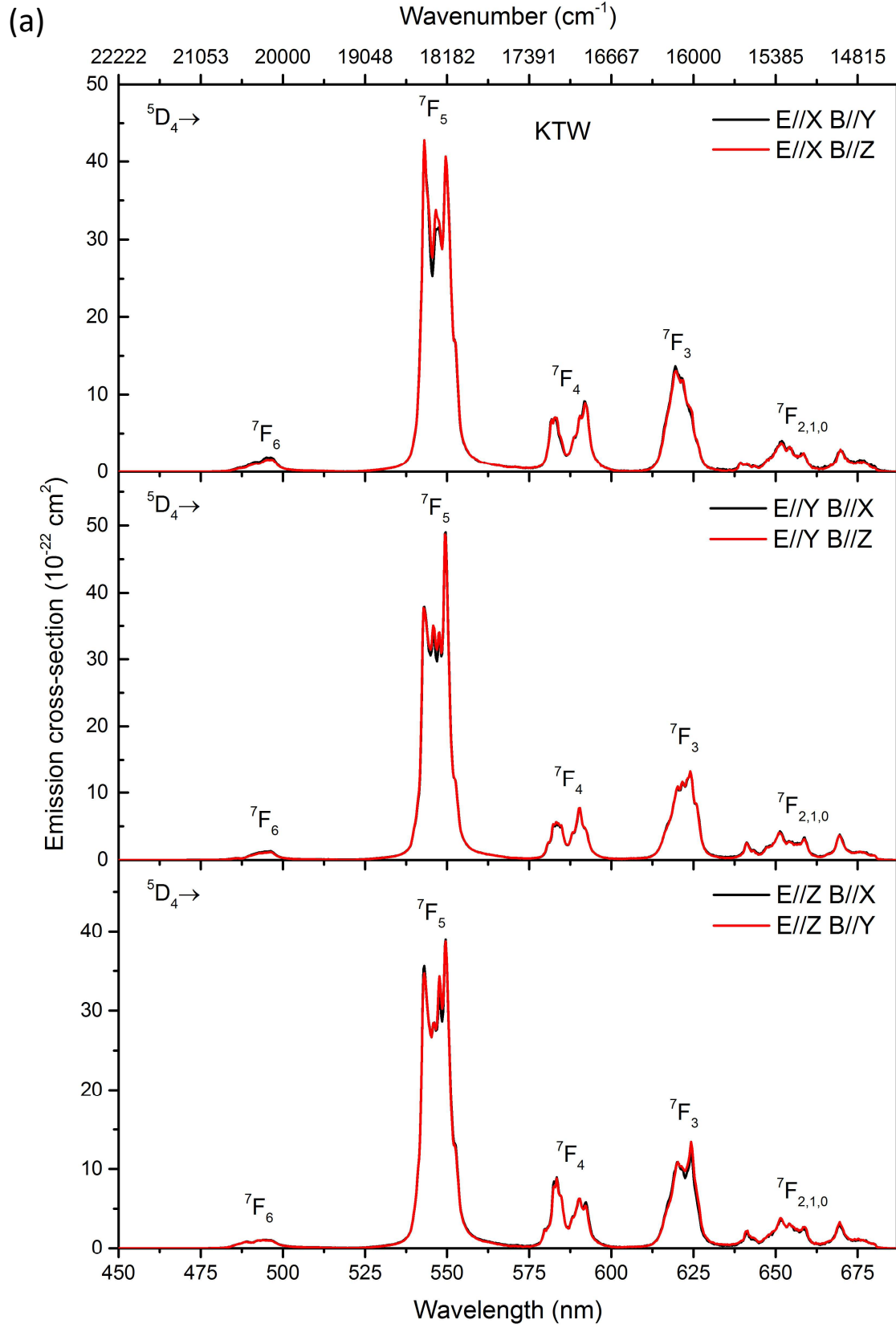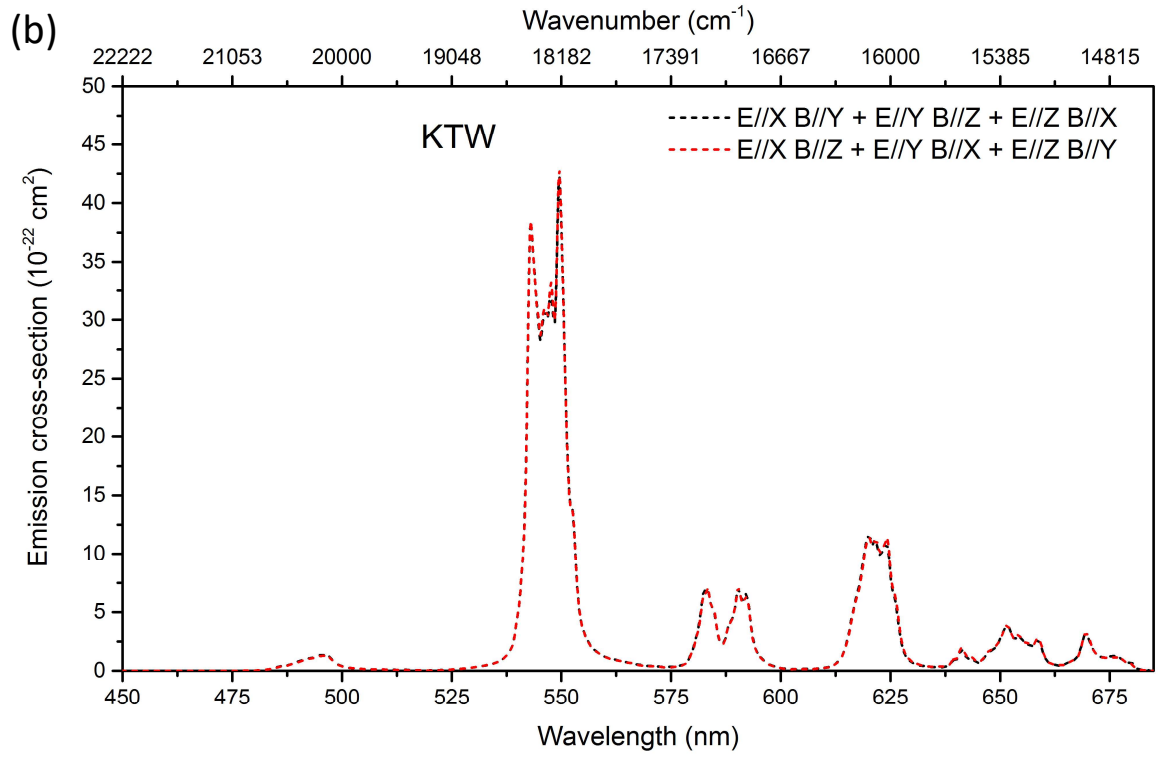
Figure 3.22 **(a) Polarized emission spectra of KTW; (b) "non-polarized" emission spectra.**

The above figures 3.17 to 3.22 illustrate the polarized emission spectra in the spectral range of 450 to 685 nm. Emission bands spreading over the visible spectral region are assigned to transitions from the $^5D_4$ manifold to ^7F_J ($J = 6, 5, 4, 3, 2, 1, 0$) multiplets. Radiative transitions from the $^5D_3$ energy level were not observed due to the efficient relaxation from $^5D_3$ to $^5D_4$ in these Tb^{3+}-concentrated systems. Spectral lineshape of BTP and STB are broad, resulting from their disordered structures. This is consistent with the observation from the absorption spectroscopy.

The spectral distribution of the emission bands can be characterized by the fluorescence branching ratio β, which defines the percentage of the emitted photon number of one of the transitions with respect to the total emitted photon number from their original excited state. β can be determined experimentally from the fluorescence spectrum by the following equation:

$$\beta_{exp} = \frac{\int_a^b \lambda I(\lambda) d\lambda}{\int \lambda I(\lambda) d\lambda} \tag{3.5}$$

where a and b are the starting and end wavelength of the transition spectral range. Furthermore, it can also be derived from the calculated transition probability in the framework of the Judd-Ofelt theory. The calculated and/or experimental branching ratios are listed in Table 3.14 to 3.20. The $^5D_4{\rightarrow}^7F_6$ and $^5D_4{\rightarrow}^7F_5$ transitions in these crystals give comparable experimental and calculated results. Nevertheless, transition probabilities to the $^7F_4$ and $^7F_3$ multiplets were underestimated while those to the $^7F_{2,1,0}$ multiplets were overestimated. In any cases, the highest branching ratio is observed for the $^5D_4{\rightarrow}^7F_5$ transition in the green spectral region, which varies from 50% to 70%.

Table 3.14 **Calculated oscillator strengths, radiative transition probabilities, branching ratios, and lifetime from the $^5D_4$ level of Tb^{3+} in BTP. Experimental branching ratios were presented as well for comparison.**

Transitions $^5D_4\rightarrow$	$\bar{\lambda}$ (nm)	f_{calc} ($\times 10^{-8}$)[a]	A (s^{-1})	β_{calc} (%)	β_{exp} (%)
$^7F_6$	489	5.90	47.6	16.8	11.7
$^7F_5$	543	22.5 (8.77)	146.3	51.8	61.3
$^7F_4$	589	2.69 (0.15)	14.8	5.3	12.2
$^7F_3$	624	3.46 (1.34)	17.0	6.0	10.0
$^7F_2$	650	2.89	13.0	4.6	
$^7F_1$	672	6.56	27.7	9.8	4.8
$^7F_0$	686	4.02	16.2	5.8	

$\tau_{rad} = 3.54\ ms$

[a] Judd-Ofelt parameters of $\Omega_2 = 2.53 \times 10^{-20} cm^2$, $\Omega_4 = 8.56 \times 10^{-20} cm^2$, and $\Omega_6 = 1.30 \times 10^{-20} cm^2$ were used. Values in bracket are nonzero MD oscillator strengths.

Table 3.15 **Calculated oscillator strengths, radiative transition probabilities, branching ratios, and lifetime from the $^5D_4$ level of Tb^{3+} in STB.**

Transitions $^5D_4\rightarrow$	$\bar{\lambda}$ (nm)	f_{calc} ($\times 10^{-8}$)[a]	A (s^{-1})	β_{calc}	β_{exp}[a]	β_{exp}^{α}	β_{exp}^{σ}	β_{exp}^{π}
$^7F_6$	486	6.42	54.8	16.7	11.8	11.7	11.8	11.8
$^7F_5$	537	24.4 (9.05)	169	52.3	56.3	57.1	56.2	55.7
$^7F_4$	577	3.05 (0.16)	18.3	5.66	15.6	15.5	15.5	15.9
$^7F_3$	612	3.91 (1.40)	20.8	6.43	12.3	11.6	12.2	12.3
$^7F_2$	641	3.03	14.7	4.54				
$^7F_1$	661	6.29	28.5	8.83	4.3	4.2	4.4	4.3
$^7F_0$	672	3.87	17.0	5.27				

$\tau_{rad} = 3.09\ ms$

[a] The experimental branching ratios are average of those obtained from all the polarized spectra.

Table 3.16 **Experimental branching ratios of the $^5D_4\rightarrow^7F_J$ transitions in TAB.**

Transitions $D_4\rightarrow$	β_{exp}	β_{exp}^{α}	β_{exp}^{σ}	β_{exp}^{π}
$^7F_6$	5.4	5.8	5.6	4.9
$^7F_5$	61.5	61.4	60.7	62.5
$^7F_4$	13.8	13.7	14.0	13.6
$^7F_3$	12.8	12.7	13.0	12.6
$^7F_2$				
$^7F_1$	6.5	6.4	6.8	6.3
$^7F_0$				

Table 3.17 Calculated oscillator strengths, radiative transition probabilities, branching ratios, and lifetime from the $^5D_4$ level of Tb^{3+} in LTB.

Transitions $^5D_4\rightarrow$	$\bar{\lambda}$ (nm)	f_{calc} (× 10^{-8})	A (s^{-1})	β_{calc}	β_{exp}	$\beta_{exp}^{E\|X\ B\|Y}$	$\beta_{exp}^{E\|X\ B\|Z}$	$\beta_{exp}^{E\|Y\ B\|X}$	$\beta_{exp}^{E\|Y\ B\|Z}$	$\beta_{exp}^{E\|Z\ B\|X}$	$\beta_{exp}^{E\|Z\ B\|Y}$
$^7F_6$	487	7.91	54.8	17.5	10.2	10.4	10.9	8.7	9.0	11.2	11.2
$^7F_5$	539	28.0 (8.51)	169	50.4	62.4	58.3	57.0	68.9	68.5	59.6	61.8
$^7F_4$	578	3.64 (0.15)	18.3	5.66	12.6	14.0	14.5	10.1	9.9	14.1	12.9
$^7F_3$	614	4.50 (1.31)	20.8	6.20	10.4	11.9	12.1	8.5	8.7	11.1	10.3
$^7F_2$	643	3.91	14.7	4.90							
$^7F_1$	663	8.18	28.5	9.62	4.4	5.5	5.5	3.8	3.9	4.0	3.8
$^7F_0$	674	5.05	17.0	5.74							

$\tau_{rad} = 2.93\ ms$

Table 3.18 Calculated oscillator strengths, radiative transition probabilities, branching ratios, and lifetime from the $^5D_4$ level of Tb^{3+} in TbCOB.

Transitions $^5D_4\rightarrow$	$\bar{\lambda}$ (nm)	f_{calc} (× 10^{-8})	A (s^{-1})	β_{calc}	β_{exp}	$\beta_{exp}^{E\|X\ B\|Y}$	$\beta_{exp}^{E\|X\ B\|Z}$	$\beta_{exp}^{E\|Y\ B\|X}$	$\beta_{exp}^{E\|Y\ B\|Z}$	$\beta_{exp}^{E\|Z\ B\|X}$	$\beta_{exp}^{E\|Z\ B\|Y}$
$^7F_6$	487	6.48	53.7	17.4	16.1	17.9	18.1	15.9	15.8	14.8	14.1
$^7F_5$	539	22.8 (8.91)	154	49.7	60.7	63.8	63.2	61.8	60.0	57.6	57.9
$^7F_4$	578	2.76 (0.15)	16.0	5.19	10.8	7.4	7.8	10.3	10.9	14.6	13.7
$^7F_3$	614	3.60 (1.38)	18.5	5.99	8.8	7.6	7.7	9.1	10.2	8.6	9.6
$^7F_2$	642	3.28	15.4	4.97							
$^7F_1$	663	7.39	32.5	10.5	3.6	3.4	3.3	2.9	3.2	4.4	4.7
$^7F_0$	673	4.55	19.4	6.26							

$\tau_{rad} = 3.23\ ms$

Table 3.19   Experimental branching ratios of the $^5D_4 \rightarrow {}^7F_J$ transitions in KTW.

Transitions $^5D_4 \rightarrow$	β_{exp}	$\beta_{exp}^{\mathbf{E\|X\ B\|Y}}$	$\beta_{exp}^{\mathbf{E\|X\ B\|Z}}$	$\beta_{exp}^{\mathbf{E\|Y\ B\|X}}$	$\beta_{exp}^{\mathbf{E\|Y\ B\|Z}}$	$\beta_{exp}^{\mathbf{E\|Z\ B\|X}}$	$\beta_{exp}^{\mathbf{E\|Z\ B\|Y}}$
$^7F_6$	4.4	5.3	4.6	4.0	3.5	4.5	4.2
$^7F_5$	68.3	67.7	68.9	69.0	69.8	67.3	67.1
$^7F_4$	9.9	10.4	10.5	8.5	8.7	10.9	10.4
$^7F_3$	11.8	11.3	11.1	12.2	12.1	11.7	12.3
$^7F_2$ $^7F_1$ $^7F_0$	5.7	5.3	4.9	6.3	5.9	5.6	6.0

The $^5D_4 \rightarrow {}^7F_{5,4,3}$ transitions obey the MD selection rules and are expected to show anisotropy in terms of the orientation of the magnetic field. According to the calculation performed by R. Zia and coworkers, the vacuum transition probabilities are 14.3, 0.058, and 1.76 s^{-1} for the terminal multiplets of $^7F_5$, $^7F_4$, and $^7F_3$ respectively. Furthermore, they also succeeded in measuring experimentally the proportion of the MD transition by energy-momentum spectroscopy using Tb:Y$_2$O$_3$, which is ca. 1/3 for the $^5D_4 \rightarrow {}^7F_5$ transition. This is in line with the Judd-Ofelt calculations of BTP, STB, LTB, and TbCOB. Comparison of the reported MD oscillator strengths to the calculated ED oscillator strengths from the Judd-Ofelt analysis shows a proportion around 1/3 as well.

It can be seen from the emission spectra with the same $\boldsymbol{E}$ vector while different $\boldsymbol{B}$ vector orientation that transitions without following the MD selection rules, viz. $^5D_4 \rightarrow {}^7F_{6,2,1,0}$, exhibit almost no difference. On the other hand, the intensity of transitions involved with MD interaction can noticeably depend on the magnetic field direction. This anisotropy is significant for the $^5D_4 \rightarrow {}^7F_5$ transition, especially in LTB and TbCOB, while not evident for the $^5D_4 \rightarrow {}^7F_4$ transition due to its negligible MD transition rate. The $^5D_4 \rightarrow {}^7F_5$ transition of TbCOB culminates at 549.3 nm with σ_{em} of 6.4 × 10^{-22} cm^2 in the $\boldsymbol{E} \parallel Y\ \boldsymbol{B} \parallel X$ polarized spectra while it peaks at at 542.8 nm with σ_{em} of 7.5 × 10^{-22} cm^2 in $\boldsymbol{E} \parallel Y\ \boldsymbol{B} \parallel Z$ polarization. Similarly, the $\boldsymbol{E} \parallel Z\ \boldsymbol{B} \parallel X$ and $\boldsymbol{E} \parallel Z\ \boldsymbol{B} \parallel Y$ polarized spectra give, respectively, σ_{em} of 7.3 × 10^{-22} cm^2 and 8.4 × 10^{-22} cm^2 at 551.8 nm and 543.1 nm.

The importance of concerning the MD anisotropy of the $^5D_4 \rightarrow {}^7F_5$ is self-evident, as the orientation of the gain material for laser operation at alternative wavelengths is analyzed from these spectroscopic properties. It can be deduced that the optimal orientation of TbCOB for laser operation at around 543 nm should be X-cut. One could not lead to this conclusion if both of the $\boldsymbol{E} \parallel Y\ \boldsymbol{B} \parallel Z$ and $\boldsymbol{E} \parallel Z\ \boldsymbol{B} \parallel Y$ polarized spectra were not measured. The polarized emission spectra of a biaxial crystal could be summed and averaged to derive two "non-polarized" spectra. The good overlap of the two sets of "non-polarized" spectra for LTB, TbCOB, and KTW reinforce the reliability of the spectroscopic measurements.

Besides its interesting MD anisotropy, the $^5D_4 \rightarrow {}^7F_5$ transition is highlighted because it gives the largest emission cross-section in all the compounds. This transition tends to give one principal and one secondary peak. The maximum σ_{em} are found to be 5.9×10^{-22} cm^2, 5.6×10^{-22} cm^2, 13×10^{-22} cm^2, 11×10^{-22} cm^2, 12×10^{-22} cm^2, and 49×10^{-22} cm^2 in BTP, STB, TAB, LTB, TbCOB, and KTW, respectively. The peak wavelength varies significantly with the host material. For example, it gives the largest cross-section at around 542 nm for TAB while the peak wavelength is 553 nm for TbCOB. The much shorter radiative lifetime of KTW (0.5 ms) than the other materials (2-3 ms) results in much larger transition cross-sections. These values are comparable to the other Tb^{3+}-doped oxide crystals, such as Tb:Na$_3$La$_9$O$_3$(BO$_3$)$_8$ (5.8×10^{-22} cm^2), Tb:YAlO$_3$ (11.1×10^{-22} cm^2), Tb:La$_2$CaB$_{10}$O$_{19}$ (14.4×10^{-22} cm^2), and Tb:KLu(WO$_4$)$_2$ (114×10^{-22} cm^2) [37–39,34]. The Tb^{3+}-doped fluoride crystals using which laser oscillation could be obtained give cross-sections ranging from 7.2×10^{-22} cm^2 to 19×10^{-22} cm^2. Thus, emission cross-sections of the studied materials should be large enough to lase in the green. Moreover, in spite of the relatively smaller peak σ_{em} of BTP and STB, their broaden lineshape lead to a small variation ($\sim$25%) of σ_{em} within the spectral range of 545±5 nm. This provides a possibility for output wavelength tuning in this region.

The $^5D_4 \rightarrow {}^7F_4$ transition is intriguing for laser emission as well. Despite its weaker transition cross-section than $^5D_4 \rightarrow {}^7F_5$ by a factor of 3 to 4, it can provide laser output wavelengths in the yellow and orange spectral region, which are difficult to achieve. In terms of the $^5D_4 \rightarrow {}^7F_4$ transition, the σ_{em} of TAB culminates at around 593 nm, which enters the orange spectral region, while TbCOB shows the largest σ_{em} at 584 nm, where yellow laser operation could be realized. The peak emission cross-section of the $^5D_4 \rightarrow {}^7F_5$ and $^5D_4 \rightarrow {}^7F_4$ transition in each polarization are tabulated in Table 3.20.

Table 3.20 Peak wavelength (in units of nm) and emission cross-section (in units of 10^{-22} cm^2) of the principal and secondary peak belonging to the $^5D_4\rightarrow^7F_5$ transition, and of the $^5D_4\rightarrow^7F_4$ transition.

Matrix	Polarization	$^5D_4\rightarrow^7F_5$				$^5D_4\rightarrow^7F_4$	
		λ_1	σ_{em}	λ_2	σ_{em}	λ	σ_{em}
BTP	Isotropic	542.5	5.8	549.6	5.9	584.2	1.3
STB	α	543.4	5.6	546.6	5.2	583.1	1.7
	σ	543.6	5.4	546.6	5.2	583.1	1.6
	π	543.4	5.1	547.7	5.0	583.9	1.6
TAB	α	541.7	13	548.8	10	593.1	3.7
	σ	541.5	13	548.8	11	593.1	3.5
	π	541.5	11	548.5	11	593.1	3.2
LTB	$E \parallel X\ B \parallel Y$	543.1	9.4	547.7	6.5	591.2	2.5
	$E \parallel X\ B \parallel Z$	543.4	8.3	547.4	6.3	591.2	2.5
	$E \parallel Y\ B \parallel X$	544.4	9.1	547.4	9.5	590.1	1.8
	$E \parallel Y\ B \parallel Z$	544.2	8.0	547.2	10	590.1	1.8
	$E \parallel Z\ B \parallel X$	543.1	11	547.4	5.7	586.2	2.8
	$E \parallel Z\ B \parallel Y$	543.1	9.8	547.7	7.0	586.2	2.5
TbCOB	$E \parallel X\ B \parallel Y$	542.8	7.1	552.8	12	585.6	1.2
	$E \parallel X\ B \parallel Z$	542.8	5.6	552.8	12	585.6	1.2
	$E \parallel Y\ B \parallel X$	541.5	4.4	549.3	6.4	590.4	1.4
	$E \parallel Y\ B \parallel Z$	542.8	7.5	549.3	6.4	590.4	1.4
	$E \parallel Z\ B \parallel X$	542.8	4.3	551.8	7.3	583.9	3.6
	$E \parallel Z\ B \parallel Y$	543.1	8.4	552.3	6.2	583.9	3.1
KTW	$E \parallel X\ B \parallel Y$	543.1	42	549.6	39	591.8	9.1
	$E \parallel X\ B \parallel Z$	543.1	43	549.6	41	591.8	8.5
	$E \parallel Y\ B \parallel X$	543.1	38	549.6	49	590.4	7.7
	$E \parallel Y\ B \parallel Z$	543.1	38	549.6	49	590.4	7.7
	$E \parallel Z\ B \parallel X$	543.1	36	549.6	39	583.4	8.9
	$E \parallel Z\ B \parallel Y$	543.1	35	549.6	39	583.4	8.8

Dy^{3+}-activated crystals

The visible spontaneous emission of Dy^{3+}-doped materials derives from the radiative decay of the ^{4}F$_{9/2}$ manifold, which separates with the next lower energy level by $\sim$7000 cm^{-1}. The excitation wavelength was set to be around 453 nm, which corresponds the energy of the ^{4}I$_{15/2}$ level. Emission transitions situated in the spectral region >900 nm exhibit very weak intensity and an estimated total branching ratio around 3%. They were omitted for the spectroscopic study. The resulting emission spectra were calibrated and converted to emission cross-sections with the Füchtbauer-Ladenburg equation described in the previous subsection. The radiative lifetime of the ^{4}F$_{9/2}$ state obtained by the Judd-Ofelt analysis in this work, and the reported wavelength-dependent refractive indices of the undoped materials [26–28] were used for the calculations of σ_{em}.

The polarized emission spectra of Dy:CYA, Dy:CAS, and Dy:YCOB are shown orderly in Figures 3.22, 3.23, and 3.24. The five main emission bands are attributed to transitions from the ^{4}F$_{9/2}$ excited state to the ^{6}H and ^{6}F terms. Since the emission bands are well separated, the branching ratio of each can be directly derived from the spectra. The fluorescence branching ratio can also be calculated from the Judd-Ofelt intensity parameters. The Judd-Ofelt calculation results for the emission transitions are given in Table 3.21 to 3.23. The β values derived from these two methods are in principle consistent. Nevertheless, a general trend is that the branching ratios of the ^{4}F$_{9/2}\rightarrow^6$F$_{11/2}$+^{6}H$_{9/2}$ fluorescence band are underestimated by the Judd-Ofelt calculation. Variation of the β_{exp} with host material is significant. For Dy:CYA, the cyan emission band originating from the ^{4}F$_{9/2}\rightarrow^6$H$_{15/2}$ transition yields higher β_{exp} than that of the ^{4}F$_{9/2}\rightarrow^6$F$_{11/2}$+^{6}H$_{9/2}$ deep-red transitions (17% vs. 12%), whereas it is the contrary for Dy:CAS (13% vs. 17%) and Dy:YCOB (10% vs. 22%). This characteristic results in the different colors of their fluorescence, which are shown in the insets of emission spectra. Meanwhile, the ^{4}F$_{9/2}\rightarrow^6$H$_{13/2}$ transition in the yellow spectral region always gives the highest branching ratio (more than 50%).
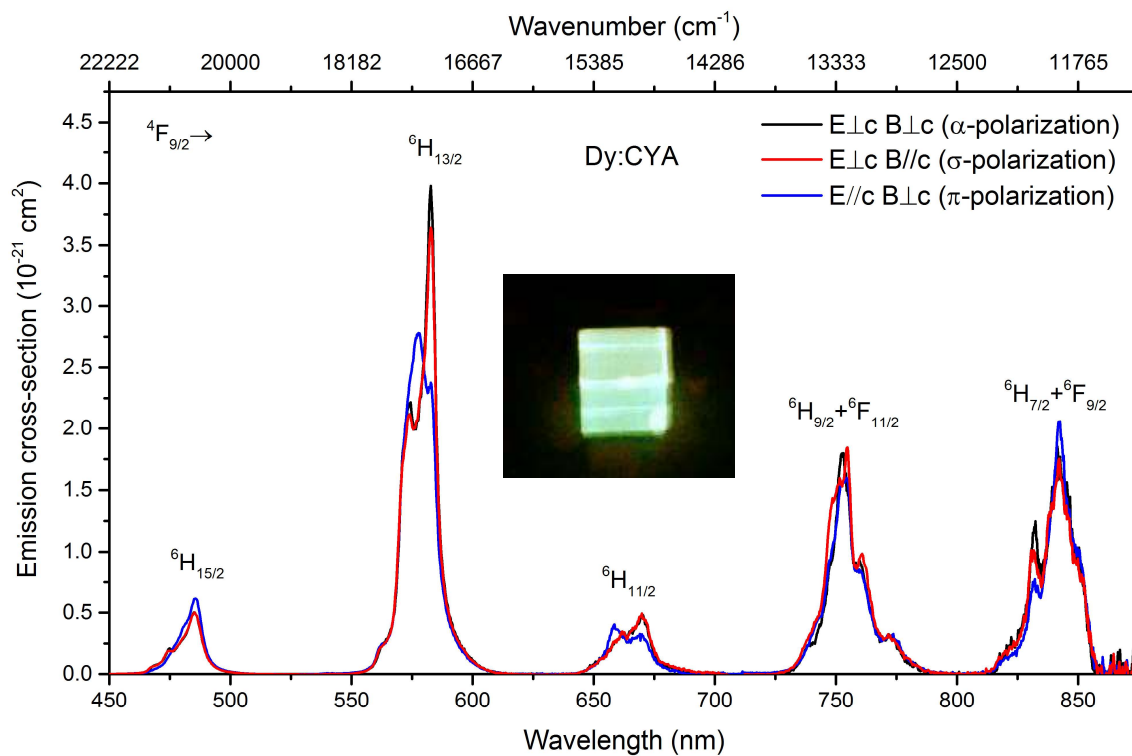
Figure 3.22   **Polarized emission spectra of Dy:CYA (the inset shows the fluorescence under 365 nm UV excitation).**
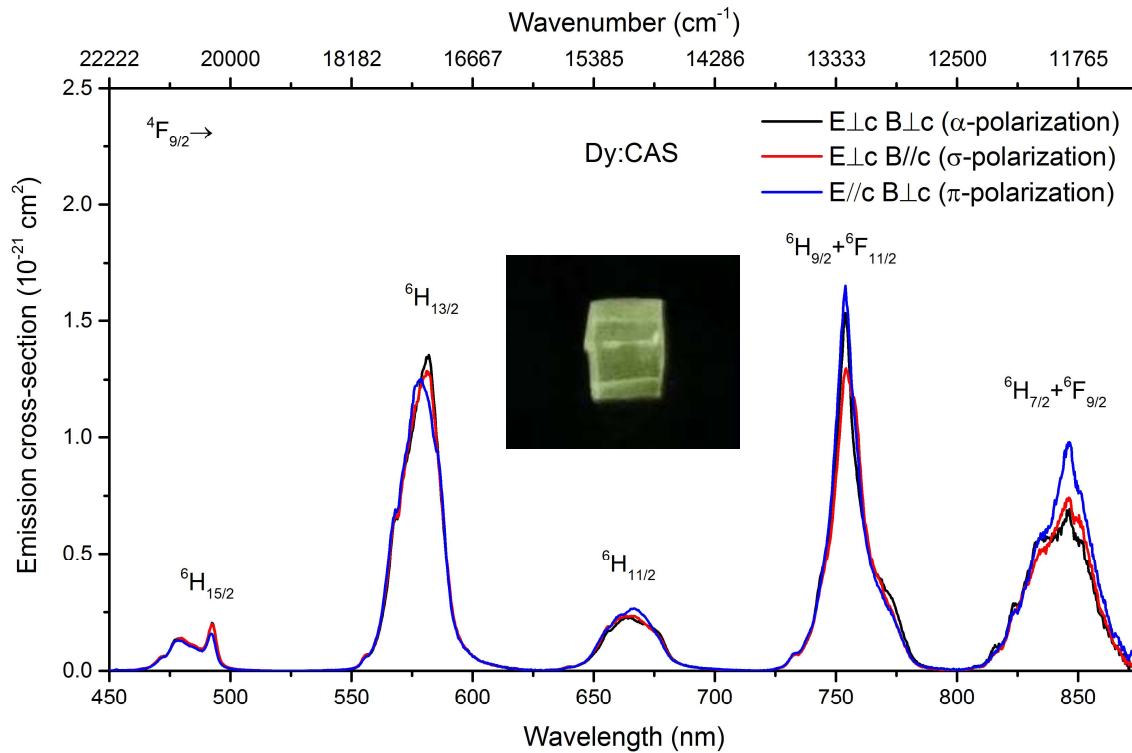
Figure 3.23   **Polarized emission spectra of Dy:CAS (the inset shows the fluorescence under 365 nm UV excitation).**
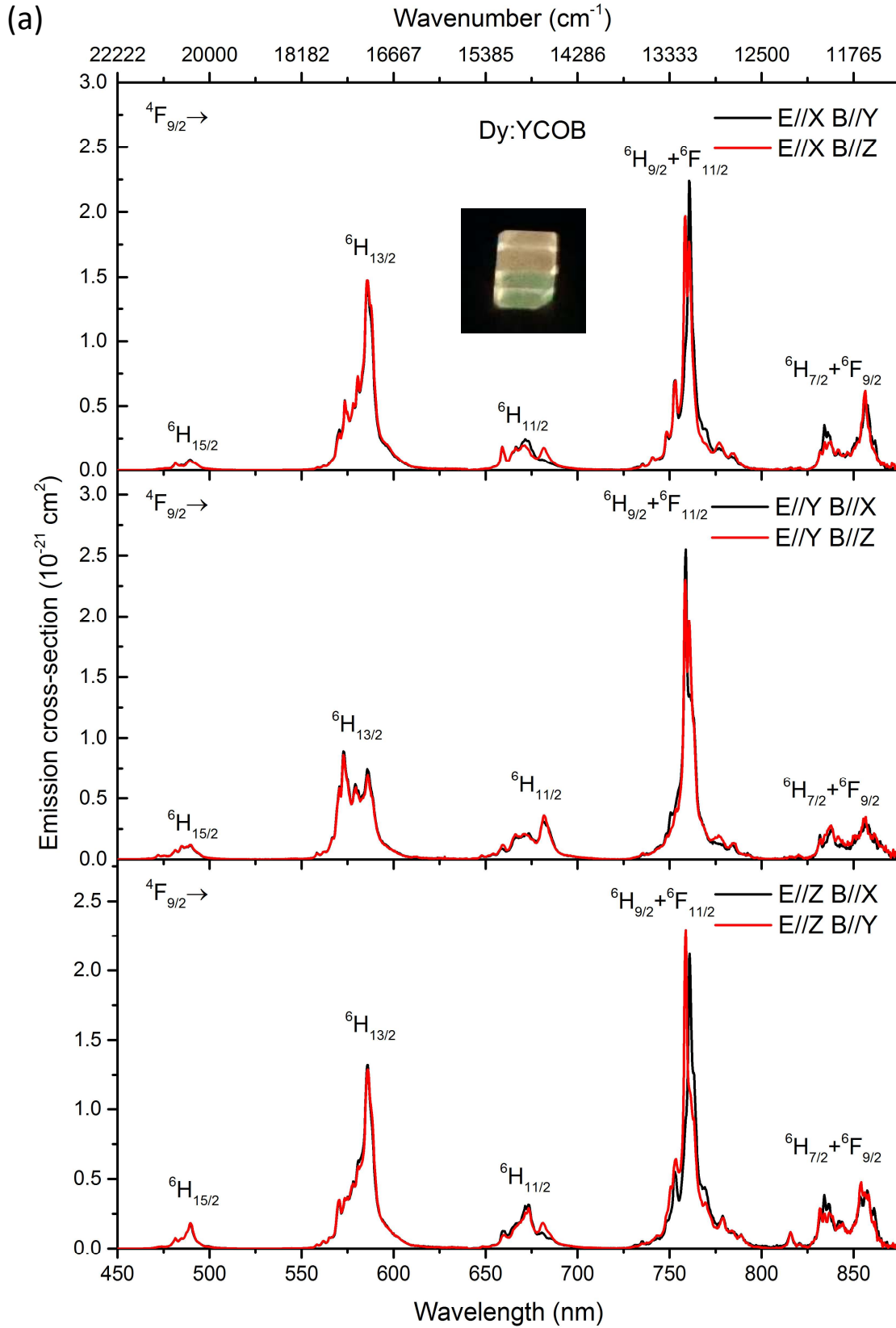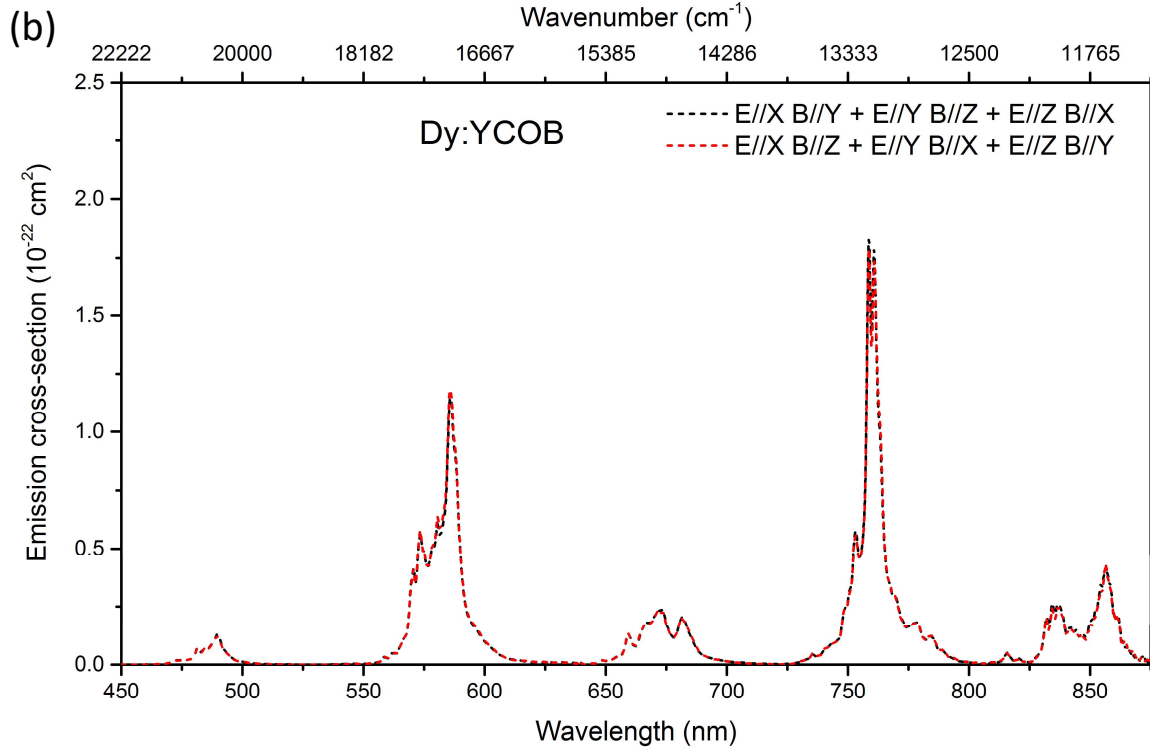
Figure 3.24 **(a) Polarized emission spectra of Dy:YCOB (the inset shows the fluorescence under 365 nm UV excitation); (b) "non-polarized" emission spectra.**

The Judd-Ofelt analysis shows that all the emission transitions ranging from 640 to 900 nm have non-zero MD oscillator strengths. For some transitions, the MD interaction is even predominant. Thus, the dependent behavior of fluorescence spectrum on the magnetic field of the emitted photon was observed indeed in these materials. For example, the intensity of the $^4F_{9/2} \rightarrow {}^6F_{11/2} + {}^6H_{9/2}$ transition of Dy:YCOB culminates, respectively, at 761 and 760 nm in the $E \parallel Z\, B \parallel X$ and $E \parallel Z\, B \parallel Y$ polarized spectrum.

Table 3.21   **Calculated oscillator strengths, radiative transition probabilities, branching ratios (given in percentage), and lifetime from the $^4F_{9/2}$ level of Dy:CYA.**

Transitions $^4F_{9/2}\rightarrow$	$\bar{\lambda}$ (nm)	f_{calc} (× 10⁻⁷)	A (s⁻¹)	β_{calc}	β_{exp}	β_{exp}^{α}	β_{exp}^{σ}	β_{exp}^{π}
$^6H_{15/2}$	472	2.71	303	14.7	16.8	15.9	16.0	18.4
$^6H_{13/2}$	566	15.5	1186	57.6	57.3	58.8	57.0	56.2
$^6H_{11/2}$	655	2.73 (0.36)	134	7.52	5.38	5.44	5.64	5.05
$^6F_{11/2}$	737	3.23 (1.80)	68.4	9.77	12.1	11.3	13.1	12.0
$^6H_{9/2}$	749	1.22 (0.11)	48.2					
$^6F_{9/2}$	820	1.89 (0.26)	58.9	7.02	8.33	8.49	8.19	8.31
$^6H_{7/2}$	841	2.25 (0.14)	71.8					
$^6H_{5/2}$	927	0.77	21.7	1.05				
$^6F_{7/2}$	979	1.36 (0.37)	24.9	1.66				
$^6F_{5/2}$	1138	0.74	13.8	0.67				
$^6F_{3/2}$	1248	~0	0.1	~0				
$^6F_{1/2}$	1341	0.04	0.5	0.02				

$\tau_{rad} = 485\ \mu s$

Table 3.22   **Calculated oscillator strengths, radiative transition probabilities, branching ratios, and lifetime from the $^4F_{9/2}$ level of Dy:CAS.**

Transitions $^4F_{9/2}\rightarrow$	$\bar{\lambda}$ (nm)	f_{calc} (× 10⁻⁷)	A (s⁻¹)	β_{calc}	β_{exp}	β_{exp}^{α}	β_{exp}^{σ}	β_{exp}^{π}
$^6H_{15/2}$	470	3.05	267	27.9	12.9	13.3	13.4	11.6
$^6H_{13/2}$	563	7.82	481	50.6	53.5	53.5	53.9	52.9
$^6H_{11/2}$	650	1.32 (0.32)	56.3	5.91	7.35	7.12	7.35	7.57
$^6H_{9/2}$	740	0.60 (0.09)	20.1	} 8.36	16.8	17.0	16.3	17.2
$^6F_{11/2}$	751	2.06 (1.54)	59.6					
$^6H_{7/2}$	830	1.03 (0.12)	27.6	} 5.03	9.39	9.13	8.24	10.8
$^6F_{9/2}$	835	0.81 (0.22)	20.4					
$^6H_{5/2}$	912	0.26	6.30	0.66				
$^6F_{7/2}$	999	0.58 (0.31)	11.4	1.20				
$^6F_{5/2}$	1164	0.20	3.05	0.32				
$^6F_{3/2}$	1281	~0	0.06	~0				
$^6F_{1/2}$	1377	0.01	0.09	0.01				

$\tau_{rad} = 1.05\ ms$

Table 3.23   Calculated oscillator strengths, radiative transition probabilities, branching ratios, and lifetime from the $^4F_{9/2}$ level of Dy:YCOB.

Transitions $^4F_{9/2}\rightarrow$	$\bar{\lambda}$ (nm)	f_{calc} ($\times 10^{-7}$)	A (s^{-1})	β_{calc}	β_{exp}	$\beta_{exp}^{\mathbf{E\|X\ B\|Y}}$	$\beta_{exp}^{\mathbf{E\|X\ B\|Z}}$	$\beta_{exp}^{\mathbf{E\|Y\ B\|X}}$	$\beta_{exp}^{\mathbf{E\|Y\ B\|Z}}$	$\beta_{exp}^{\mathbf{E\|Z\ B\|X}}$	$\beta_{exp}^{\mathbf{E\|Z\ B\|Y}}$
$^6H_{15/2}$	471	1.06	94.7	15.7	10.0	7.26	6.79	11.5	12.2	11.2	11.0
$^6H_{13/2}$	566	5.61	341	56.8	53.1	57.5	58.6	50.9	48.9	51.4	51.5
$^6H_{11/2}$	657	1.18 (0.32)	53.0	8.83	9.78	8.45	8.56	10.9	11.6	9.21	9.38
$^6F_{11/2}$	746	1.84 (1.58)	63.6	12.5	21.9	21.2	20.9	22.1	22.1	22.2	21.6
$^6H_{9/2}$	752	0.33 (0.09)	11.4								
$^6F_{9/2}$	829	0.44 (0.23)	12.3	3.94	5.55	5.61	5.14	4.55	5.28	6.01	6.47
$^6H_{7/2}$	847	0.43 (0.12)	11.4								
$^6H_{5/2}$	936	0.08	1.71	0.28							
$^6F_{7/2}$	996	0.44 (0.32)	8.47	1.41							
$^6F_{5/2}$	1164	0.23	3.23	0.54							
$^6F_{3/2}$	1280	~0	0.03	~0							
$^6F_{1/2}$	1379	~0	0.03	~0							

$\tau_{rad} = 1.66\ ms$

The $^4F_{9/2} \rightarrow {}^6H_{13/2}$ transition that can generate unique yellow laser emission is of great interest. The maximum cross-sections of this transition in each material are 4.0×10^{-21} cm^2 (Dy:CYA), 1.4×10^{-21} cm^2 (Dy:CAS), and 1.5×10^{-21} cm^2 (Dy:YCOB). These values are comparable to those of the reported gain materials, viz. 3.0×10^{-21} cm^2 (Dy:Y$_3$Al$_5$O$_{12}$), 1.7×10^{-21} cm^2 (Dy:LiLuF$_4$), and 6.4×10^{-21} cm^2 (Dy:ZnWO$_4$) [24,25,40]. The peak wavelength also varies with matrix and polarization. Versatile output wavelengths ranging from 573 to 583 nm might be realized by these Dy^{3+}-activated crystals.

Despite that the yellow emission band in Dy:YCOB yields the highest branching ratio, the largest emission cross-section is found around 760 nm in the deep red spectral region. It provides σ_{em} of 2.5×10^{-21} cm^2 in the $E \parallel Y$ $B \parallel X$ polarization, which is also the greatest value among these crystals in terms of this transition. Laser operation at this wavelength could also be viable. Spectroscopic data of the yellow $^4F_{9/2} \rightarrow {}^6H_{13/2}$ transition and the deep red $^4F_{9/2} \rightarrow {}^6F_{11/2} + {}^6H_{9/2}$ transitions are summarized in Table 3.24.

Table 3.24 **Peak wavelength (in units of nm) and emission cross-section (in units of 10^{-21} cm^2) of the $^4F_{9/2} \rightarrow {}^6H_{13/2}$ and $^4F_{9/2} \rightarrow {}^6F_{11/2} + {}^6H_{9/2}$ transitions.**

Matrix	Polarization	$^4F_{9/2} \rightarrow {}^6H_{13/2}$		$^4F_{9/2} \rightarrow {}^6F_{11/2} + {}^6H_{9/2}$	
		λ	σ_{em}	λ	σ_{em}
Dy:CYA	α	582.7	4.0	753.1	1.8
	σ	582.7	3.6	754.7	1.8
	π	577.6	2.8	754.4	1.6
Dy:CAS	α	581.9	1.4	753.9	1.5
	σ	581.7	1.3	754.1	1.3
	π	578.7	1.3	753.9	1.6
Dy:YCOB	$E \parallel X$ $B \parallel Y$	585.7	1.5	760.7	2.2
	$E \parallel X$ $B \parallel Z$	585.7	1.5	758.5	2.0
	$E \parallel Y$ $B \parallel X$	572.7	0.9	758.8	2.5
	$E \parallel Y$ $B \parallel Z$	572.7	0.9	758.3	2.3
	$E \parallel Z$ $B \parallel X$	586.0	1.3	760.9	2.1
	$E \parallel Z$ $B \parallel Y$	586.0	1.3	758.8	2.3

3.5 Fluorescence dynamics

The fluorescence dynamics of the upper laser level of an active medium can be characterized by the fluorescence intensity decay process from this level. A pulsed OPO laser (pulse duration ~7 ns) was used to excite the Tb^{3+}- and Dy^{3+}-activated crystals to the corresponding pump levels at room temperature. A gallium-phosphide-based photomultiplier (RCA 8850), which is sensitive to visible light, was employed to record the temporal evolution of the fluorescence intensity at a designated wavelength.

Tb^{3+}-activated crystals

Fluorescence decay curves of the Tb^{3+}-based crystals starting from the $^5D_4$ manifold were obtained via inband excitation at around 486 nm. Figure 3.25 illustrates the semi-logarithmic plot of the temporal fluorescence decay. The fluorescence intensity was monitored at the peak wavelength of the $^5D_4 \rightarrow {}^7F_5$ transition for each material. All the obtained curves can be well fitted into single-exponential functions. This indicates that all the terbium-based crystals are free from detrimental energy transfer processes from the $^5D_4$ level, which should result in non-exponential behaviors. The fluorescence lifetimes (τ_f) were derived from the linearly fitted curves and marked in Figure 3.25. Except for KTW with an evidently shorter value, others exhibit τ_f ranging from around 2~3 ms. The relatively long lifetimes does not only result from the absence of non-radiative processes, but also from the spin-forbidden nature of the $^5D_4 \rightarrow {}^7F_J$ transitions. The τ_f of KTW is in agreement with the reported value at 300 K of single crystalline KTW (270 µs) [22]. This relatively short lifetime is in line with the fact that KTW exhibits an evidently larger cross-section than the other materials with respect to the $^5D_4 \rightarrow {}^7F_5$ transition.

It is worth mentioning that the fluorescence decay curve of LTB was also obtained by monitoring at 604 nm, where additional emission lines appear (see also Figure 3.20). In the first place, they were suspected to be emission lines from the $^4G_{5/2} \rightarrow {}^6H_{7/2}$ transition of Sm^{3+}, a possible impurity in terbium oxide raw material, since it is not found in the other compounds and is almost separated from the main stream of the $^5D_4 \rightarrow {}^7F_4$ transition. Nevertheless, crystals of BTP, STB, LTB, and TbCOB were synthesized using the same batch of starting material and the Tb^{3+}-concentration of LTB is not significantly larger than the others. Moreover, these unique emission lines were observed in all the LTB crystals grown from three different runs, which excludes the possibility of introducing the impurity of Sm^{3+} by accident. The time-dependent fluorescence intensity monitored for this emission line shows a single-exponential decay behavior as well and gives τ_f of 2.62 ms, which is close to the τ_f of 2.65 ms monitored at 543 nm. Though we are not able to completely rule out the possibility of Sm^{3+}, it is reasonable to attribute the emission lines around 604 nm to the $^5D_4 \rightarrow {}^7F_4$ transition of Tb^{3+}.
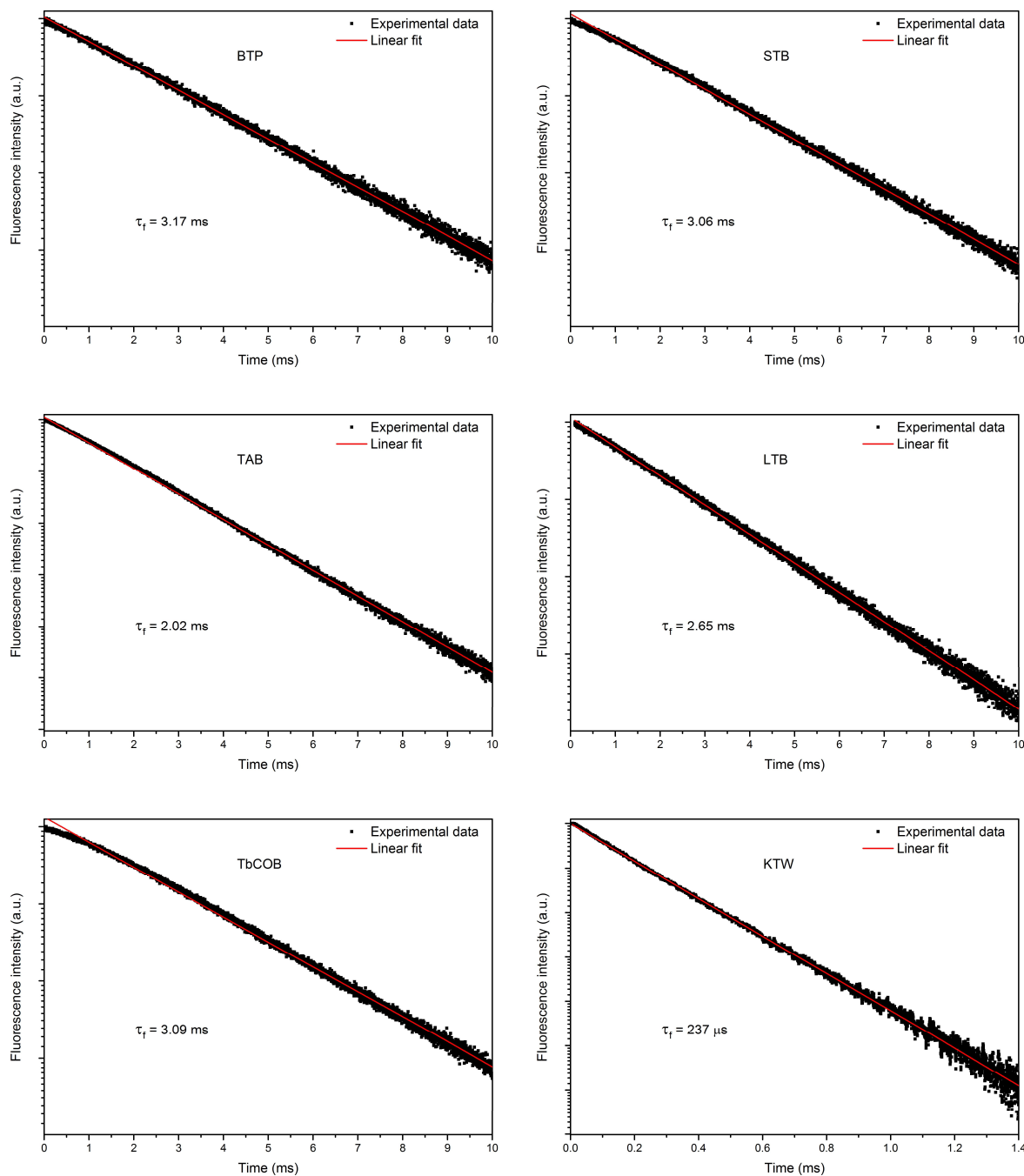
Figure 3.25   **Fluorescence decay profiles from the $^5D_4$ manifold of the Tb^{3+}-activated compounds.**

Comparison of the experimental fluorescence lifetime to the calculated radiative lifetime obtained via Judd-Ofelt analysis yields the quantum efficiency η ($\eta = \tau_f/\tau_{rad}$). As is listed in Table 3.25, most of the terbium-based crystals exhibit similar τ_f and τ_{rad} values and thus quantum efficiencies closed to unity. This, together with the single-exponential behavior, validates the primary assumption that high Tb^{3+}-concentration and large maximum phonon energy of the matrix would not undermine the $^5D_4$ excited-state lifetime. The measured fluorescence lifetimes of the fluoride host materials are even

longer, which are around 5 ms. This leads to a typically low power threshold for a laser oscillator on this level. For example, Tb:LiYF$_4$ can lase at 542 nm with only 8 mW of incident pump power [41].

Table 3.25   **Experimental and calculated lifetimes of Tb^{3+}-activated crystals.**

Matrix	Tb^{3+} concentration	τ_f (ms)	τ_{rad} (ms)	η
BTP	35×10^{20} cm^{-3}	3.17	3.54	90%
STB	48×10^{20} cm^{-3}	3.06	3.09	99%
TAB	55×10^{20} cm^{-3}	2.02	2.07[a]	98%
LTB	52×10^{20} cm^{-3}	2.65	2.93	90%
TbCOB	44×10^{20} cm^{-3}	3.09	3.23	96%
KTW	63×10^{20} cm^{-3}	0.237	0.50[b]	47%

[a] Reported in [33].

[b] Based on an analogue single crystal Tb:KLu(WO$_4$)$_2$ [34].

Dy^{3+}-activated crystals

Fluorescence intensity decay profiles of the Dy^{3+}-doped crystals were recorded under excitation around 453 nm, which corresponds to the terminal level of $^4I_{15/2}$. The decay processes take place from the $^4F_{9/2}$ state after rapid relaxation from the pump level. For comparison, polycrystalline samples with low doping levels were prepared and their decay curves were obtained through the same procedure. The decay curves plotted semi-logarithmically are shown in Figure 3.26. The as-grown single crystal samples with Dy^{3+} concentrations of 4.67×10^{20} cm^{-3} (3.7 at% Dy:CYA), 8.07×10^{20} cm^{-3} (12.1 at% Dy:CAS), and 3.86×10^{20} cm^{-3} (8.6 at% Dy:YCOB) exhibit non-exponential decay behaviors. On the other hand, the decay profiles of the polycrystalline samples with small doping concentrations are almost single exponential. It is known that cross-relaxation is the predominant non-radiative process from the $^4F_{9/2}$ level and multiphonon relaxation is negligible. It becomes efficient in a Dy^{3+}-concentrated systems due to a smaller statistic distance between two adjacent ions. The temporal fluorescence intensity is described by [42]:

$$I(t) = I(0) \sum_j \alpha_j e^{-tA_j} \tag{3.6}$$

where α_j and A_j are the fraction and transition rate of each decay process. Thus, the involvement of cross-relaxation leads to a non-exponential evolution of the fluorescence intensity. In this case, the mean lifetime τ_m can be employed to analyze the average time the population spend on the excited state:

$$\tau_m = \frac{\sum_j \alpha_j / A_j^2}{\sum_j \alpha_j / A_j} = \frac{\int_0^\infty t I(t) dt}{\int_0^\infty I(t) dt} \tag{3.7}$$

The mean fluorescence lifetimes of the $^4F_{9/2}$ manifolds were found to be 262 μs (Dy:CYA), 267 μs (Dy:CAS), and 354 μs (Dy:YCOB). The corresponding τ_f at low concentrations (∼0.5×10²⁰ cm⁻³) were linear-fitted to be, in the above sequence, 425 μs, 798 μs, and 1.24 ms. These values are slightly smaller than the radiative lifetimes obtained by the Judd-Ofelt analysis. By comparing τ_m with τ_{rad}, the quantum efficiency of the as-grown crystals are found to be 54%, 25%, and 21% (Table 3.26). One should notice that the quantum efficiency of Dy:YCOB is much smaller than that of Dy:CYA even though the Dy^{3+}-concentration of the latter is larger than the former. This indicates that the cross-relaxation rate, a host-dependent parameter related to the overlap of the initial and final states, is larger in Dy:YCOB than in Dy:CYA.

Besides the lifetime of $^4F_{9/2}$, that of $^6H_{13/2}$, the terminal level of the yellow $^4F_{9/2}\rightarrow^6H_{13/2}$ transition, is also of interest to study. It is reported that the long lifetime of this level hampers the laser performance of the $^4F_{9/2}\rightarrow^6H_{13/2}$ transition [43]. The population accumulation on the lower laser level results in reabsorption of the stimulated emission. The radiative lifetimes of the $^6H_{13/2}$ manifold were estimated to be 8 ms (Dy:CYA), 22 ms (Dy:CAS), and 46 ms (Dy:YCOB) via Judd-Ofelt calculations. Such long lifetime accentuates the importance of selecting a host material with suitable maximum phonon energy in order to promptly remove population from the lower laser level.

Table 3.26   **Experimental and calculated lifetimes of Dy^{3+}-activated crystals.**

Matrix	Dy^{3+} concentration	τ_f (ms)	τ_{rad} (ms)	η
Dy:CYA	4.67×10²⁰ cm⁻³	0.262	0.485	54%
Dy:CAS	8.07×10²⁰ cm⁻³	0.267	1.05	25%
Dy:YCOB	3.86×10²⁰ cm⁻³	0.354	1.66	21%
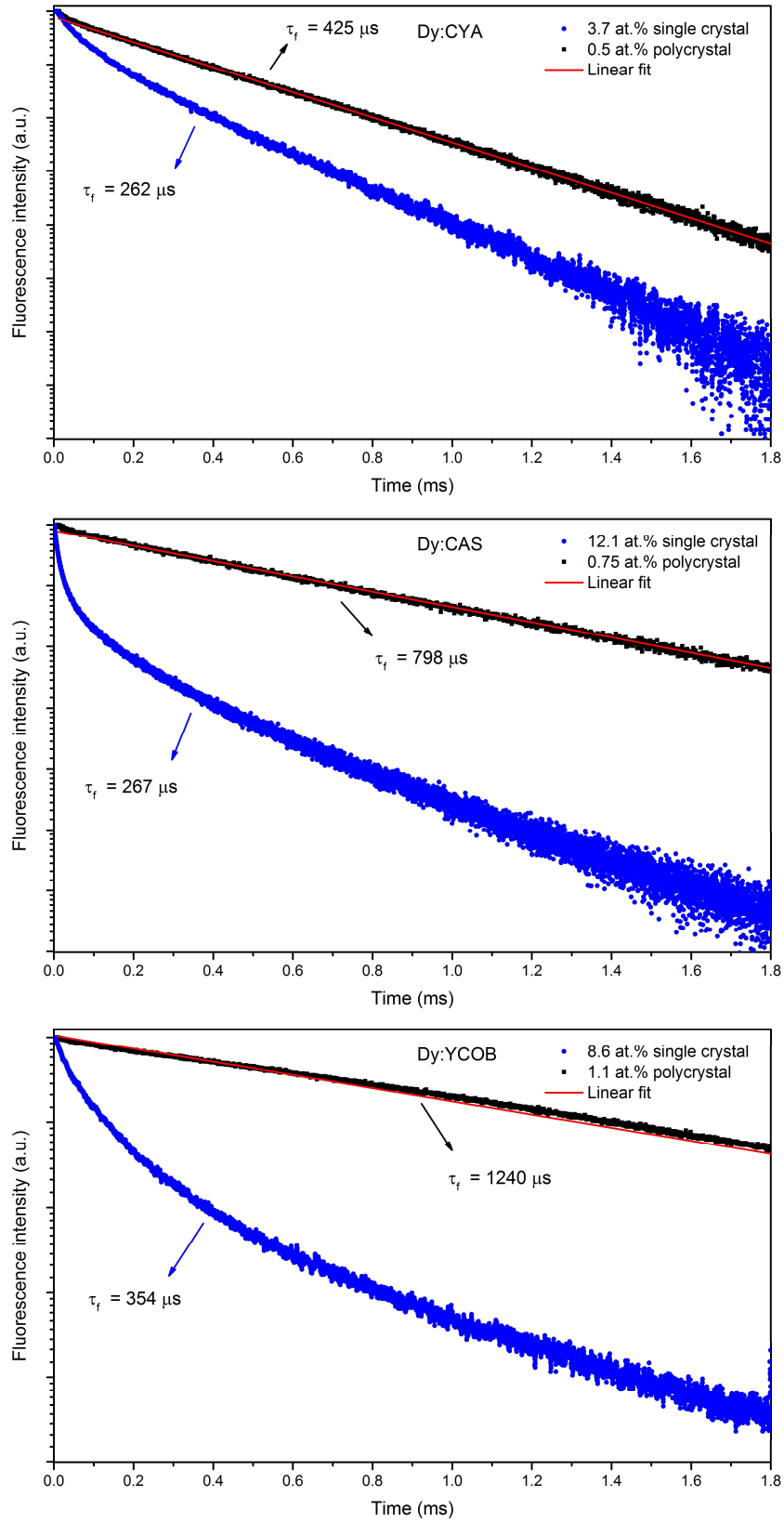
Figure 3.26 **Fluorescence decay profiles from the $^4F_{9/2}$ manifold of the Dy^{3+}-activated compounds.**

3.6 Excited-state absorption

Terbium-based gain media operated in the visible are prone to undergo ESA processes from the $^5D_4$ upper laser level to the energetically low-lying $4f^75d^1$ states and/or $4f^8$ manifolds located between 35000 and 45000 cm^{-1}. Population in the $^5D_4$ state can be excited to these levels by absorbing a photon in the visible spectral range provided by the pump and/or signal sources, the former and later are called pump ESA and signal ESA (in the case of optical resonator, "signal" refers to internal emission from the gain material), respectively.

ESA from the $^5D_4$ energy level have been well documented in various matrices. T. Yamashita et al. reported the non-linear behavior of gain by pumping a Tb^{3+}-doped fluoride fiber at 488 nm, pointing toward a pump ESA [44]. B. R. Reddy and coworkers were able to detect pump ESA at 488 nm and signal ESA in the near-IR using single-crystalline Tb:CaF$_2$ and Tb:YAlO$_3$ by observing spontaneous emissions from the $^5D_3$ manifold [45,46]. K. J. B. M. Nieuwesteeg et al. recorded ESA spectra for Tb:YAG, Tb:Y$_2$SiO$_5$, and Tb:LaOBr ceramics [47]. They were able to attribute the terminal level of the ESA transitions to the $4f^8$ and $4f^75d^1$ configurations.

It is worth mentioning that during the laser operation, signal ESA is much more critical than pump ESA. The former directly quenches the stimulated emission whereas the latter just ultimately reduces the pump efficiency. This can be reflected by the fact that Tb:LiYF$_4$ exhibits pump ESA at 486.2 nm while being able to lase with threshold power as low as 8 mW [41]. Thus, signal ESA is mainly concerned here.

ESA measurements were performed with the Tb^{3+}-based single crystals of BTP, STB, LTB, TbCOB, and KTW in a pump-probe approach. Significant scattering was observed when the laser beam was focused inside the TAB crystal, thus this measurement was not conducted on TAB. The setup of the experiment is schematically shown in Figure 3.27. A tunable pulsed OPO laser was employed as pump, which can provide maximum pulse energy around 70 mJ. A continuous-wave He-Ne laser emitting at 543.4 nm (Newport, 2 mW) was used as probe, which matches the wavelength of the $^5D_4{\rightarrow}^7F_5$ emission transition. The aligned beams were focused through the crystal sample and the photon intensity was detected by a CCD camera or a photomultiplier. It is worth noting that the beam size of the OPO laser was around five times larger than that of the He-Ne laser. That is to say, all the photons emitted from the He-Ne laser should undergo almost the same process in the medium, although only a tiny part of the photons could enter into the detectors through the slit.
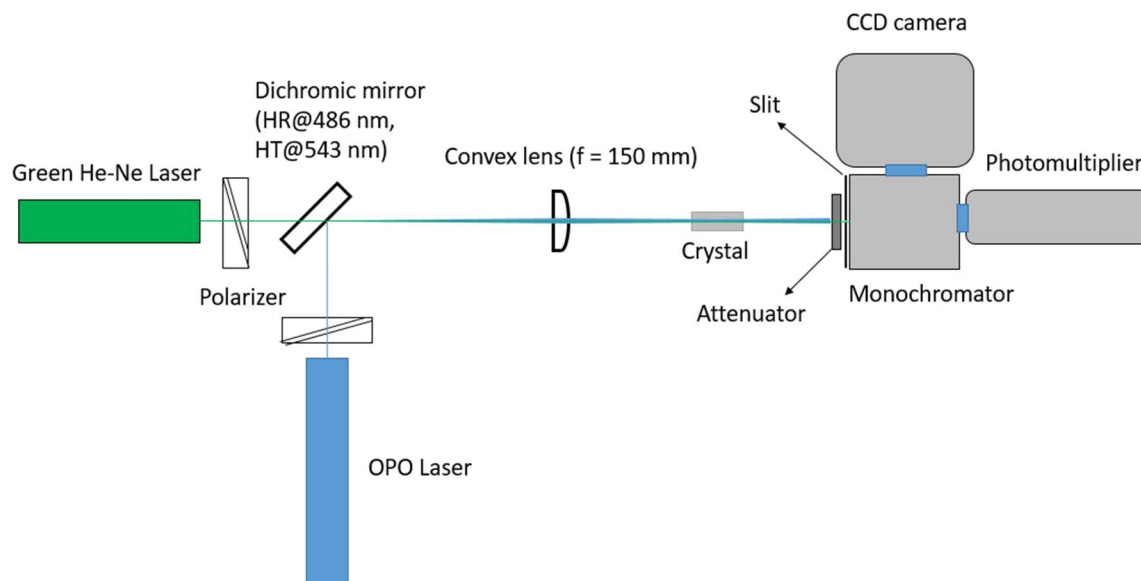
Figure 3.27   Experimental setup for the ESA measurement.

First, with the pump off, photon signal of the green laser after passing through the crystal was recorded by the CCD camera as reference. After turning on the pump, a substantial amount of ground-state population was excited to the $^5D_4$ energy level. The signal of the probe would be amplified by stimulated emission (SE) as well as spontaneous emission (SP) and weaken by ESA simultaneously. Nevertheless, the signal deriving from SP was neglected since it was measured to be more than 4 orders of magnitude weaker than that of the He-Ne laser. Thus, gain behavior can be studied by comparing the two spectra obtained before and after switching on the pump. Meanwhile, time evolution of the photon intensity at 543.4 nm after excitation could be detected by a gallium-phosphide-based photomultiplier as well. The spectra measured with the CCD camera (100 ns gate delay, 100 µs gate width, 300 accumulations) and time-evolution curves of the photon intensity at 543.4 nm (256 accumulations) are shown in Figure 2.44. Since the OPO pulse energy exhibited fluctuation of ~10%, the real-time value was monitored by an energy meter for each measurements.
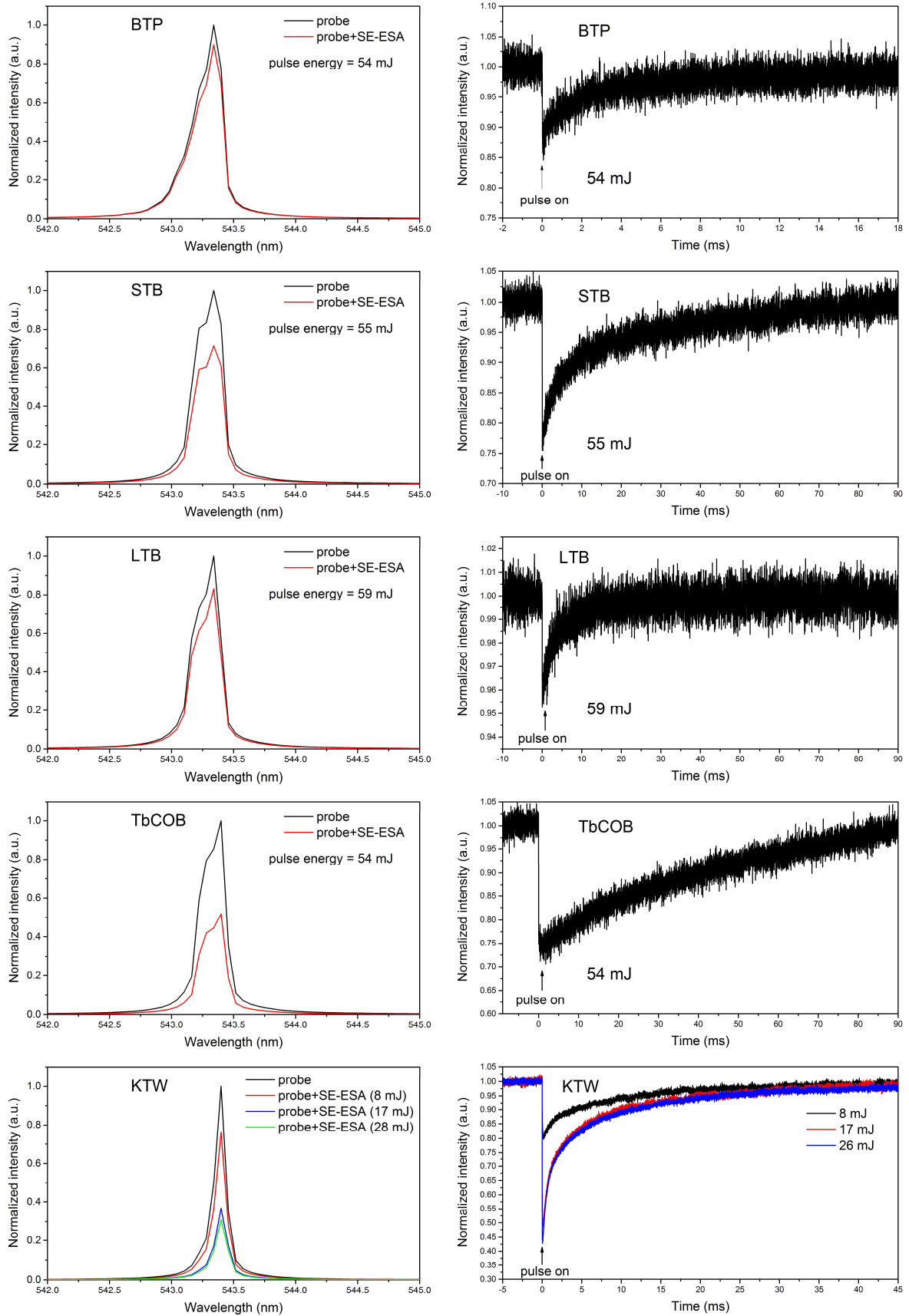
Figure 3.28 Left: emission spectra without (marked as "probe") and with the pump (marked as "probe+SE-ESA"); Right: time-evolution curves of the photon intensity monitored at 543.4 nm.

It can be seen from the spectra recorded by the CCD camera (Figure 3.28, left) that the probe signals exhibited noticeable reduction, after the crystals were excited to the $^5D_4$ state at their optimal absorption wavelength. The crystals were excited by laser pulses with similar energies ($\sim$55 mJ), except for KTW ($\leq$ 28 mJ). Power-dependent and saturation behavior (overlap of the spectra recorded with a 17 mJ pulse and a 28 mJ pulse) can be reliably observed with KTW. The peak intensity decreased by 10%, 29%, 17%, 48%, and 69% for BTP, STB, LTB, TbCOB, and KTW, respectively. This indicates that the ESA loss overwhelmed the SE gain in these crystals. The net optical gain coefficient g_{net} at 543.4 nm can be estimated by:

$$g_{net} = g_{int} - \alpha_{ESA} = \ln\left(\frac{I^{probe+SE-ESA}}{I^{probe}}\right)/l \tag{3.8}$$

where g_{int} and α_{ESA} are the internal gain coefficient and excited-state absorption coefficient. The g_{net} were found to be -0.1 cm^{-1}, -0.2 cm^{-1}, -0.1 cm^{-1}, -0.4 cm^{-1}, and -2.3 cm^{-1} for BTP, STB, LTB, TbCOB, and KTW, respectively. However, due to the fact that it was difficult to determine the integrated excited-state population density in the medium, we were not able to quantify the excite-state absorption cross-sections.

The temporal intensity curves recorded by the photomultiplier (Figure 3.28, right) are consistent with the above results based on the CCD camera. After the crystals were excited by the laser pulse, intensity of the signal beam obviously decreased. The decay curves reflect the time dependence of the $^5D_4$ population. All the ESA decay curves are non-exponential since the excited-state dynamics of $^5D_4$ is influenced by multiple processes, including the outflow by SE, SP, and ESA and inflow from the higher energy levels via relaxation.

Both experiments point out that KTW exhibits the largest ESA loss. This is expected owing to its intense GSA bands from 27500 cm^{-1} to 40000 cm^{-1}, which can be assigned to interconfigurational transitions and IVCT bands. A diagram showing the energetic positions of the $4f^8$ and $4f^75d^1$ configurations is presented in Figure 3.29. This graphic is depicted based on the absorption spectra recorded in this work and the reported VUV excitation spectra [15,17,18,22,48]. In the ESA measurements, electrons can be excited to an energetic position of $\sim$39000 cm^{-1} via step-wise absorption. The manifold of $^5K_9$ is expected at this energy level. Intraconfigurational ESA transitions to this level is possible, the oscillator strength of which in BTP was estimated to be 2.3$\times$10^{-7} via Judd-Ofelt calculations, which is close to that of its $^5D_4{\rightarrow}^7F_5$ emission transition. Meanwhile, interconfigurational ESA transitions to the $4f^75d^1$ configurations can also play a role as they are parity-allowed and have broader spectral linewidth. As discussed before, low-spin ^7D states of the selected terbium-based materials should have bary-center energies above the energetic position of 39000 cm^{-1}. However, the strong splitting of this state in STB and TbCOB leads to that the sum of the pump and probe energy drops in the broad ^7D band. With regard to BTP and LTB, this energetic position is mainly covered by the ^9D configuration. ESA transitions from the $^5D_4$ state to the ^7D and ^9D configurations are, respectively, singly and doubly spin-forbidden. The later should give smaller transition probability than the former. This might account for the excited-state dynamics in these materials that STB and TbCOB give larger negative gain than BTP and LTB. It

should be pointed out that the $^5D_4$ excited state can also be depopulated via energy-transfer upconversion in these Tb^{3+}-concentrated systems.
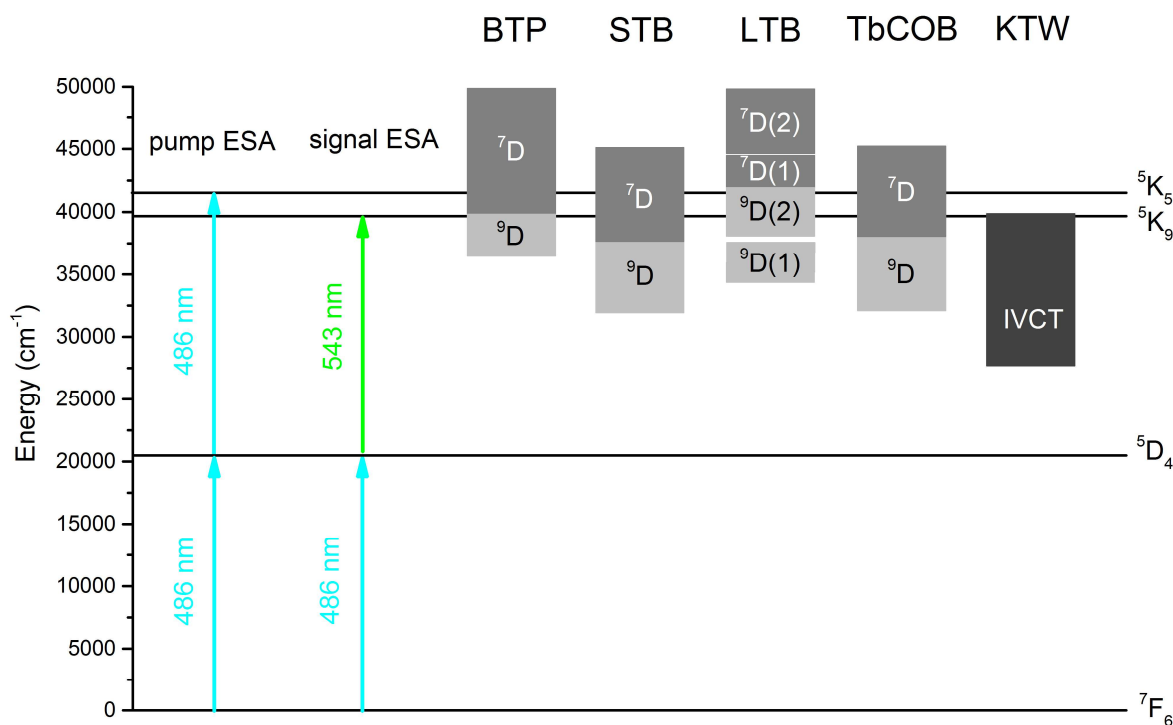
Figure 3.29   **ESA scheme and energetic positions of the $4f^8$ and $4f^7 5d^1$ configurations.**

In spite of these negative results, the optical gain properties characterized by this method is incomplete. We could only determine the gain behavior within a very narrow spectral range around 543.4 nm. The optical gain might be different at the other wavelengths within the $^5D_4 \rightarrow ^7F_5$ transition or even the yellow $^5D_4 \rightarrow ^7F_4$ transition at a lower (ca. 1300 cm^{-1}) energetic position.

3.7 Laser experiments

Based on the spectroscopic data obtained in this work, four-level systems can be constructed by pumping Tb^{3+}-activated media to the $^5D_4$ level around 485 nm or Dy^{3+}-activated media to the $^4I_{15/2}$ level around 450 nm. These two wavelengths could be achieved by commercial LDs. Frequency-doubled OPSLs can provide emissions in the spectral range of 480 to 488 nm as well. Laser experiments using the LD pumps were carried out in our laboratory in Chimie ParisTech. In addition to the materials fabricated in this work, high-quality crystals of $Tb:LiYF_4$, $Pr:YAlO_3$, and $Pr:LiYF_4$, whose laser properties have been reported, were available to examine the cavity setup. These crystals were kindly offered by R. Yasuhara from National Institute for Fusion Science, Japan. Collaboration with C. Kränkel from Leibniz-Institut für Kristallzüchtung provided us an opportunity to use the OPSL device. OPSL-pumped laser experiments were performed in Leibniz-Institut für Kristallzüchtung and operated by E. Castellano-Hernández.

3.7.1 Tb^{3+}-activated crystals under 486-nm LD pumping

A single-mode LD (Nichia) delivering emission around 486 nm with maximum output power of 200 mW was available for pumping the Tb^{3+}-activated crystals. A linear cavity was built up for the laser tests and is schematically shown in Figure 3.30. The pump beam was collimated with an aspheric lens and focused by a plano-convex lens with a focal length of 35 mm into the active medium. In this configuration, the beam size at the focusing point was measured to be around 40×50 μm with a COHERENT LaserCam HR beam view analyzer. The input mirror is planar and is anti-reflection coated ($T = 95\%$) at the pump wavelength and high-reflection coated ($T < 0.3\%$) from 542 to 670 nm. The output coupler has a radius of curvature of 300 mm and 99% reflection from 540 to 578 nm.
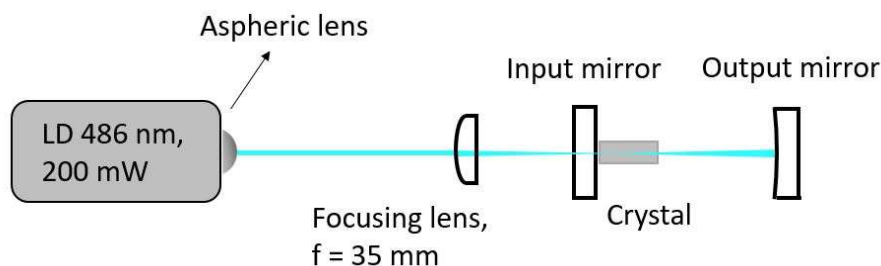
Figure 3.30   Schematic cavity setup for the 486-nm-LD-pumped laser experiments.

A c-cut 15% $Tb:LiYF_4$ crystal was used to examine this setup, which can produce laser emission under OPSL-pumping at a similar wavelength of 486.2 nm. The length of the gain crystal is 30 mm and in the best condition an absorbed power of ca. 75 mW could be achieved. Unfortunately, no laser action could be observed despite that the laser threshold of a 14% $Tb:LiYF_4$ crystal was reported to be merely 8 mW upon OPSL pumping [41]. The main difference with the reported setup is the pump source, which provides worse beam quality than the OPSL, and the radius of curvature of the output coupler (50 mm in the literature). Typically, the focal length of the focusing lens and the radius of curvature of

the output mirror should be similar to provide a good overlap of the pump beam and the oscillating laser beam. In this setup, the large radius of curvature of the output mirror (300 mm) makes the cavity similar to a plano-plano one. Further attempts of laser operation on the oxide-based crystals were not successful as well.

3.7.2 Tb³⁺-activated crystals under 486.2-nm OPSL pumping

OPSL-pumped laser experiments were conducted on the Tb^{3+}-activated oxide-based crystals elaborated in this work, viz. BTP (20 mm in length, arbitrary orientation), STB (20 mm in length, c-cut), LTB (11 mm in length, arbitrary orientation), and TbCOB (26.7 mm in length, b-cut). All the crystals were not anti-reflection coated. The frequency-doubled OPSL (COHERENT Genesis CX, 4W) produces almost collimated and linearly polarized output beams at 486.2 nm. The absorption efficiencies of the crystal samples at this wavelength were calculated to be, in the above sequence, 46%, 50%, 75%, and 32%. The pump system and laser cavity setup are shown in Figure 3.31. The half-wave plate and polarizing beam splitter were used to control the polarization and power of the incident beam. The beam waist diameter was calculated to be ~40 μm upon focusing with a plano-convex lens ($f = 100\ mm$). Both the input and output mirrors have a curvature of 100 mm and are high-reflection coated for the green emission. A Tb:LiLuF₄ crystal was first used to examine the alignment of the cavity and it was subsequently replaced by the oxide-based media. Despite that the fluoride crystal can lase with this setup, attempts to achieve laser operations of the most intense green emission for all these oxide-based crystals were not successful. In addition, thermally induced cracking of STB and LTB were observed at a high pumping power.
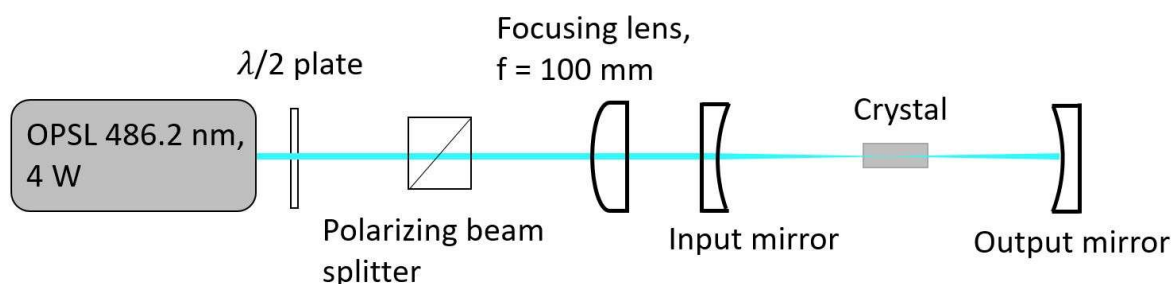
Figure 3.31   **Schematic cavity setup for the 486.2-nm-OPSL-pumped laser experiments.**

3.7.3 Dy³⁺-activated crystals under 442-nm LD pumping

The Dy^{3+}-activated crystals were pumped by a blue fiber-coupled LD (Shimadzu) to find laser actions. The LD pump has a fiber core diameter of 100 μm (0.22 NA) and emits around 442 nm with a maximum output power of 10 W. The output wavelength corresponds to the secondary peak of the $^{6}H_{15/2} \rightarrow {}^{4}I_{15/2}$ transition, which is a factor of 2~3 weaker than the main peak around 453 nm. A typical plano-concave cavity was setup (Figure 3.32). The focal length of both the collimating and the focusing lens is 75 mm. Spectroscopic study of the Dy^{3+}-doped crystals suggests two possible laser transitions with relatively

large cross-sections. One is yellow around 580 nm and another is deep red around 750 nm. Two input mirrors were available for lasing these two transitions. Both are anti-reflection coated at the pump wavelength and high-reflection coated at the corresponding output wavelength.
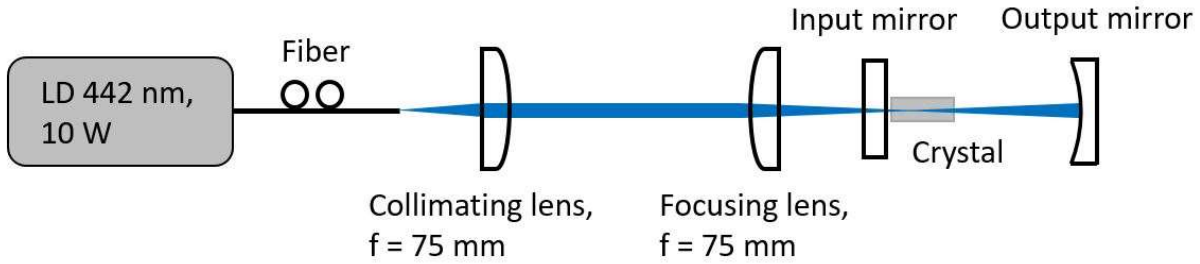
Figure 3.32   **Schematic cavity setup for the 442-nm-LD-pumped laser experiments.**

The first attempt was conducted for the emission around 750 nm. The output coupler used for lasing this transition has a radius of curvature of 75 mm and 97±1% reflection from 630 to 1120 nm. The pump and cavity configuration can be examined by the known gain material of $Pr:YAlO_3$ since its most intense emission around 747 nm is covered by the partial-reflection spectral range of this output coupler. A 6-mm-long c-cut $Pr:YAlO_3$ crystal with a nominal doping level of 0.5% was available for this test. It was able to lase at 747 nm and yielded a slope efficiency with respect to the absorbed power of 2% (Figure 3.33 (a)). The laser threshold was 1.2 W (absorbed pump power) and the absorption efficiency was ca. 45% at the maximum output power of the pump. The slope efficiency of this laser is much worse than that obtained by a single-mode LD, which is 45% with a 98%-reflection output coupler [49]. This is probably due to the worse beam quality of the fiber-coupled LD.

Further control experiment was conducted to verify the quality of the pump. Using this LD pump, we were able to lase a 0.5% $Pr:LiYF_4$ crystal resulting in slope efficiency of 25% at 640 nm with a 99%-reflection output mirror (Figure 3.33 (b)). This value is comparable to the reported fiber-coupled LD-pumped laser using $Pr:LiYF_4$ as gain medium in a similar condition, which is 23% [50].
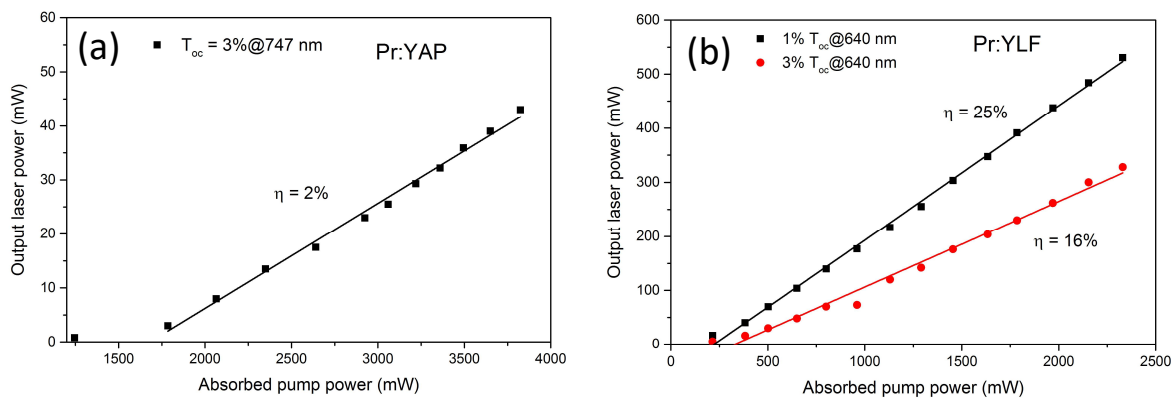
Figure 3.33   **Laser performances of (a) 0.5% $Pr:YAlO_3$ emitting at 747 nm, and (2) 0.5% $Pr:LiYF_4$**
emitting at 640 nm using the Shimadzu 442-nm fiber-coupled LD as pump source.

Keeping the resonator setup for the previous Pr:YAlO₃ laser experiment, the active medium was changed to Dy:CYA (a-cut, 10 mm) as well as Dy:YCOB (b-cut, 10 mm). The absorbed pump power at laser threshold of these two active media can be estimated using the equation $P_{thres}^{abs} = \frac{h\nu_p A l_{rt}}{\tau \sigma_{em}}$, where A is the beam diameter of the pump and l_{rt} is the round-trip losses. Assuming an ideal round-trip losses of 3%, the threshold pump power could be estimated to be 9 W and 6 W for Dy:CYA and Dy:YCOB, respectively. However, the maximum absorbed power of these two crystals were found to be only 3.6 W and 1.7 W, respectively. In the actual experiments, no laser behavior could be detected. To reduce the threshold pump power, the collimating lens was substituted to one with a longer focal length of 100 mm, which can result in a smaller beam size. Nevertheless, the laser performance based on Pr:LiYF₄ using this setup was not better than the original one.

Further efforts were made to lase the yellow emission transition of Dy:CYA. An output coupler giving 99.5% reflection at 574 nm was employed. The σ_{em} at this wavelength is ca. 2.2×10⁻²¹ cm² for both σ-polarization and π-polarization. The term $\tau\sigma_{em}$, which is proportional to the threshold pump power, in our case is a factor of 2 smaller than that of Dy:YAG, which can generate yellow laser emission with an incident pump power less than 1W [25]. However, no laser action can be observed in our configuration, probably owing to the larger beam diameter (100 μm vs. ~65 μm) and worse beam quality.

169

3.8 Conclusion of Chapter 3

In this chapter, the optical properties of six Tb^{3+}-activated compounds, viz. BTP, STB, TAB, LTB, TbCOB, and TbCOB, and three Dy^{3+}-activated compounds, viz. Dy:CYA, Dy:CAS, and Dy:YCOB, were studied. The orientations of the crystal samples were verified with optical conoscopy and X-ray diffraction and the optical indicatrix axes of the biaxial crystals of LTB, TbCOB, KTW, and Dy:YCOB were identified to allow accurate spectroscopic characterizations.

Tb^{3+}-activated crystals

Prisms of BTP, STB, and LTB were fabricated to measure the refractive index with minimum-deviation method. The refractive indices at 589.3 nm were found to be 1.694 for BTP, 1.746 (n_e) and 1.721 (n_o) for STB, and 1.591 (n_X), 1.647 (n_Y), and 1.651 (n_Z) for LTB. The wavelength-dependent experimental data of refractive index could be fitted into Sellmeier dispersion equations.

Polarization-dependent absorption and emission spectra were recorded in the UV-visible spectral region to study the optical transitions of Tb^{3+} in the matrices. The spectroscopic data were used to derive the transition cross-sections. Anisotropy of the MD transitions were observed, which is particularly pronounced for the relatively strong MD absorption transition of $^7F_6 \rightarrow ^5G_6$ and emission transition of $^5D_4 \rightarrow ^7F_5$. For example, with regard to the $^5D_4 \rightarrow ^7F_5$ transition, it gives σ_{em} of 4.0×10^{-22} cm^2 at 542.8 nm in the $\boldsymbol{E} \parallel Y \, \boldsymbol{B} \parallel X$ spectrum of TbCOB. In contrast, this value is 7.5×10^{-22} cm^2 at the same wavelength in the $\boldsymbol{E} \parallel Y \, \boldsymbol{B} \parallel Z$ spectrum, which has the same direction of the $\boldsymbol{E}$ vector.

The absorption bands terminated at the $4f^7 5d^1$ states were found in the spectral range of 260-280 nm in BTP, STB, LTB, and TbCOB. The center wavelengths of these bands are in good agreement with the values estimated by P. Dorenbos' method (calculate from the crystal-field depression). On the other hand, broad UV absorption bands were observed in TAB and KTW. The latter can be attributed to the IVCT band.

The maximum σ_{abs} of the $^7F_6 \rightarrow ^5D_4$ transition, which is suitable for semiconductor laser pumping, were found to be (in units of 10^{-22} cm^2) 0.96, 1.1, 9.5, 2.8, 5.4, and 14 for BTP, STB, TAB, LTB, TbCOB, and KTW, respectively. These values are comparable or even superior to those of the fluorides, which range from 1.5×10^{-22} cm^2 to 3×10^{-22} cm^2. The $^5D_4 \rightarrow ^7F_5$ emission transition in the green spectral region features the largest fluorescence branching ratio for all these materials, which varies from 56% to 68%. The maximum σ_{em} value of this transition were calculated by Füchtbauer-Ladenburg equation. They are (in units of 10^{-22} cm^2) 5.9, 5.6, 13.3, 11, 12, and 49 for BTP, STB, TAB, LTB, TbCOB, and KTW, respectively. Those of TAB, LTB, and TbCOB are comparable that of the most promising Tb^{3+}-activated gain material, $Tb:LiYF_4$, which is 19×10^{-22} cm^2. In addition, TAB and TbCOB can provide decent σ_{em} around 3.6×10^{-22} cm^2 at 593 nm and 584 nm, respectively. They can be used to produce the unique yellow or orange laser emissions.

The fluorescence decay curves were recorded to study the decay behavior of the $^5D_4$ manifold and calculate the fluorescence lifetime. The fluorescence decay profiles of these materials display a single-exponential behavior. This suggests minor energy transfer processes from the $^5D_4$ energy level in these Tb^{3+}-based media. By linear fits of the semi-logarithmic profiles, the fluorescence lifetimes were found to be 3.17 ms, 3.06 ms, 2.02 ms, 2.65 ms, 3.09 ms, and 0.237 ms for BTP, STB, TAB, LTB, TbCOB, and KTW, respectively.

Judd-Ofelt calculations were carried out using the experimental oscillator strengths obtained from the absorption spectra. The calculated oscillator strengths and fluorescence branching ratios were compared with the experimental values. They are overall in good agreement. The resulting radiative lifetimes are closed to the fluorescence lifetime data (except for KTW), indicating the absence of significant non-radiative processes that depopulate the $^5D_4$ upper state in these materials.

Excited-state absorption measurements were performed using a He-Ne laser emitting at 543 nm as probe, which matches the wavelength of the green $^5D_4 \rightarrow ^7F_5$ emission transition. The crystals were pumped with a pulsed OPO laser to the $^5D_4$ level and the variation of the intensity of the probe laser was monitored with a CCD camera as well as a photomultiplier. Results obtained from both detectors indicated ESA at the probe wavelength for BTP, STB, LTB, TbCOB, and KTW. The 2-cm-long KTW crystal exhibited a net gain coefficient of -2.3 cm^{-1} upon excitation of a 28 mJ pulse. This value is obviously greater than the other samples, which could be explained by the strong IVCT band at the ESA terminal level.

Laser experiments using a diode laser emitting at 486 nm with output capacity around 200 mW were essayed. However, this configuration was not able to generate laser oscillation even using a $Tb:LiYF_4$ crystal, whose laser operation has been demonstrated. In addition, the oxide-based crystals of BTP, STB, LTB, and TbCOB were tested using an OPSL which provides maximum 4W output emission at 486.2nm. Unfortunately, none of them showed any laser action despite the good pump and cavity conditions.

The spectroscopic data of the Tb^{3+}-activated crystals, including the maximum absorption and emission cross-sections (in units of 10^{-22} cm^2) and the corresponding peak wavelengths, branching ratio of the $^5D_4 \rightarrow ^7F_5$ transition, fluorescence lifetime from the $^5D_4$ level, and quantum efficiency, are summarized in Table 3.27. Those of $Tb:LiYF_4$ are given as reference.

Table 3.27   **Selected spectroscopic data of the Tb³⁺-activated crystals.**

Matrices	σ_{abs} ($^7F_6{\rightarrow}^5D_4$)	λ_{abs} (nm)	σ_{em} ($^5D_4{\rightarrow}^7F_5$)	λ_{em} (nm)	β_{exp} ($^5D_4{\rightarrow}^7F_5$)	τ_f ($^5D_4$)	η
BTP	0.96	484.6	5.9	549.6	61%	3.17 ms	90%
STB	1.1	483.6	5.6	543.4	56%	3.06 ms	99%
TAB	9.5	484.6	13	541.5	62%	2.02 ms	98%
LTB	2.8	486.2	11	547.2	62%	2.65 ms	90%
TbCOB	5.4	483.7	12	552.8	61%	3.09 ms	96%
KTW	14	487.0	49	549.6	68%	0.237 ms	47%
Tb:LiYF₄	3	488.7	19	543.9	-	5.0 ms[a]	-

[a] at a doping level of 16%.

Dy³⁺-activated crystals

Polarized absorption and emission spectra of the Dy³⁺-doped crystals of Dy:CYA, Dy:CAS, and Dy:YCOB were recorded. The broadening behaviors of spectral lineshape observed in Dy:CYA and Dy:CAS are related to the random distribution of Ca^{2+} and rare-earth ions over the same site. Anisotropy of the MD transitions, both absorption and emission, could be observed. The $^6H_{15/2}{\rightarrow}^4I_{15/2}$ transition around 450 nm was found to exhibit a relatively large contribution of the MD interaction, which is reflected by the MD anisotropy. For Dy:CYA and Dy:CAS, the ratios of peak σ_{abs} in the α-polarized spectra ($\boldsymbol{E} \perp c\ \boldsymbol{B} \perp c$) and the σ-polarized spectra ($\boldsymbol{E} \perp c\ \boldsymbol{B} \parallel c$) were found to be 57% and 30%, respectively. For Dy:YCOB, the σ_{abs} at 453.6 nm is $1.4{\times}10^{-21}$ cm² in the $\boldsymbol{E} \parallel Y\ \boldsymbol{B} \parallel X$ spectrum, while this value is $0.43{\times}10^{-21}$ cm² in the $\boldsymbol{E} \parallel Y\ \boldsymbol{B} \parallel Z$ spectrum. Besides, the $^6H_{15/2}{\rightarrow}^4I_{15/2}$ transition is highlighted because it is the most promising one for LD pumping. The maximum σ_{abs} are found to be $3.3{\times}10^{-21}$ cm², $1.3{\times}10^{-21}$ cm², and $1.8{\times}10^{-21}$ cm² in Dy:CYA, Dy:CAS, and Dy:YCOB, respectively. These values are comparable to those in the reported Dy³⁺-activated gain media.

The fluorescence branching ratios and emission cross-sections were calculated from the emission spectra. The $^4F_{9/2}{\rightarrow}^6H_{13/2}$ transition in the yellow spectral range provides the highest branching ratio, which is more than 50% in all the three compounds. The peak σ_{em} of this transition were found to be $4.0{\times}10^{-21}$ cm², $1.4{\times}10^{-21}$ cm², and $1.5{\times}10^{-21}$ cm² in Dy:CYA, Dy:CAS, and Dy:YCOB, respectively. The Dy:CYA crystal has even larger transition cross-section than the reported gain media of $Dy:Y_3Al_5O_{12}$ ($3.0{\times}10^{-21}$ cm²) and $Dy:LiLuF_4$ ($1.7{\times}10^{-21}$ cm²). It is considered to be a potential candidate for generating yellow laser emission. The Dy:YCOB crystal, on the other hand, gives an exceptionally high σ_{em} in the deep red spectral range, which is $2.5{\times}10^{-21}$ cm². This feature makes it interesting for laser operation around 760 nm using Dy:YCOB as gain medium.

The fluorescence dynamics of the upper laser level of $^4F_{9/2}$ were studied by recording the decay profiles from this level. The decay curves of the grown crystals are non-exponential, whereas those of the polycrystalline samples with low active-ion concentrations are single exponential. This is due to the cross-relaxation processes of Dy^{3+} in these crystals. Their mean fluorescence lifetime were calculated to be 262 µs (Dy:CYA), 267 µs (Dy:CAS), and 354 µs (Dy:YCOB).

The Judd-Ofelt analysis was performed to derive the theoretical oscillator strengths, branching ratios, and radiative lifetimes. The resulting oscillator strengths and branching ratios are comparable to the experimental values. The radiative lifetimes are slightly larger than the fluorescence lifetimes measured with the low-doping-level samples. The calculated radiative lifetimes result in quantum efficiencies of 54%, 25%, and 21% for Dy:CYA, Dy:CAS, and Dy:YCOB.

Laser experiments were performed using a fiber-coupled LD emitting at around 442 nm. The quality of this pump was examined by Pr^{3+}-activated gain media of Pr:YAP and Pr:YLF. The analysis of Pr^{3+}-laser performances suggested that the pump has worse beam quality than the single-mode LDs, but comparable to the other reported fiber-coupled LD. A linear plano-concave cavity was built up for lasing the yellow or deep red transitions. In practice, no laser output could be obtained.

The spectroscopic data of the Dy^{3+}-activated crystals, including the maximum absorption and emission cross-sections (in units of 10^{-22} cm^2) and the corresponding peak wavelengths, branching ratio of the $^4F_{9/2} \rightarrow {}^6H_{13/2}$ transition, fluorescence lifetime from the $^4F_{9/2}$ level, and quantum efficiency, are summarized in Table 3.28. Those of the reported Dy^{3+}-activated gain crystals are given as reference.

Table 3.28   Spectroscopic properties of the Dy^{3+}-activated crystals.

Matrices	σ_{abs} ($^6H_{15/2} \rightarrow {}^4I_{15/2}$)	λ_{abs} (nm)	σ_{em} ($^4F_{9/2} \rightarrow {}^6H_{13/2}$)	λ_{em} (nm)	β_{exp} ($^4F_{9/2} \rightarrow {}^6H_{13/2}$)	τ_f ($^4F_{9/2}$)	η
3.7 at% Dy: CaYAlO$_4$	3.3	452.2	4.0	582.7	58%	262 µs	54%
12 at% Dy: Ca$_2$Al$_2$SiO$_7$	1.3	452.0	1.4	581.9	51%	267 µs	25%
8.6 at% Dy: YCa$_4$O(BO$_3$)$_3$	1.8	453.6	1.5	585.7	53%	354 µs	21%
3 at% Dy: Y$_3$Al$_5$O$_{12}$	1.6	447	3.0	583	-	376 µs	-
5 at% Dy: ZnWO$_4$	-	-	6.4	575	-	158 µs	-
3.0 at% Dy: LiLuF$_4$	1.4	450	1.7	574	-	865 µs	-

References of Chapter 3

[1] CENTRED ACUTE BISECTRIX, https://brocku.ca/earthsciences/people/gfinn/optical/bxsign1.htm.

[2] Yuan Dongsheng, PhD dissertation: Equipment development and single crystal growth of micro-pulling-down, and the synthesis and investigations of functional crystal TbCOB, Shandong University, 2016.

[3] G. Aka, A. Kahn-Harari, F. Mougel, D. Vivien, F. Salin, P. Coquelin, P. Colin, D. Pelenc, J.P. Damelet, Linear- and nonlinear-optical properties of a new gadolinium calcium oxoborate crystal, $Ca_4GdO(BO_3)_3$, J. Opt. Soc. Am. B. 14 (1997) 2238. doi:10.1364/JOSAB.14.002238.

[4] X. Mateos, R. Solé, J. Gavaldà, M. Aguiló, J. Massons, F. Díaz, Crystal growth, optical and spectroscopic characterisation of monoclinic $KY(WO_4)_2$ co-doped with Er^{3+} and Yb^{3+}, Opt. Mater. 28 (2006) 423–431. doi:10.1016/j.optmat.2004.12.024.

[5] M.C. Pujol, M. Rico, C. Zaldo, R. Solé, V. Nikolov, X. Solans, M. Aguiló, F. Díaz, Crystalline structure and optical spectroscopy of Er^{3+}-doped $KGd(WO_4)_2$ single crystals, Appl. Phys. B. 68 (1999) 187–197. doi:10.1007/s003400050605.

[6] P. Loiko, A. Volokitina, X. Mateos, E. Dunina, A. Kornienko, E. Vilejshikova, M. Aguiló, F. Díaz, Spectroscopy of Tb^{3+} ions in monoclinic $KLu(WO_4)_2$ crystal application of an intermediate configuration interaction theory, Opt. Mater. 78 (2018) 495–501. doi:10.1016/j.optmat.2018.03.014.

[7] Q. Ye, B.H.T. Chai, Crystal growth of $YCa_4O(BO_3)_3$ and its orientation, J. Cryst. Growth. 197 (1999) 228–235. doi:10.1016/S0022-0248(98)00947-6.

[8] M. Burresi, D. van Oosten, T. Kampfrath, H. Schoenmaker, R. Heideman, A. Leinse, L. Kuipers, Probing the Magnetic Field of Light at Optical Frequencies, Science. 326 (2009) 550–553. doi:10.1126/science.1177096.

[9] T.H. Taminiau, S. Karaveli, N.F. van Hulst, R. Zia, Quantifying the magnetic nature of light emission, Nat. Commun. 3 (2012) 979. doi:10.1038/ncomms1984.

[10] C.M. Dodson, J.A. Kurvits, D. Li, M. Jiang, R. Zia, Magnetic dipole emission of $Dy^{3+}:Y_2O_3$ and $Tm^{3+}:Y_2O_3$ at near-infrared wavelengths, Opt. Mater. Express. 4 (2014) 2441. doi:10.1364/OME.4.002441.

[11] C.M. Dodson, R. Zia, Magnetic dipole and electric quadrupole transitions in the trivalent lanthanide series: Calculated emission rates and oscillator strengths, Phys. Rev. B. 86 (2012). doi:10.1103/PhysRevB.86.125102.

[12] M. Kasperczyk, S. Person, D. Ananias, L.D. Carlos, L. Novotny, Excitation of Magnetic Dipole Transitions at Optical Frequencies, Phys. Rev. Lett. 114 (2015). doi:10.1103/PhysRevLett.114.163903.

[13] W.T. Carnall, P.R. Fields, K. Rajnak, Electronic Energy Levels of the Trivalent Lanthanide Aquo Ions. III. Tb^{3+}, J. Chem. Phys. 49 (1968) 4447–4449. doi:10.1063/1.1669895.

[14] H. Jenssen, D. Castleberry, D. Gabbe, A. Linz, Stimulated emission at 5445 Å in Tb^{3+}:YLF, IEEE J. Quantum Electron. 9 (1973) 665–665. doi:10.1109/JQE.1973.1077559.

[15] D. Hou, H. Liang, M. Xie, X. Ding, J. Zhong, Q. Su, Y. Tao, Y. Huang, Z. Gao, Bright green-emitting, energy transfer and quantum cutting of $Ba_3Ln(PO_4)_3$: Tb^{3+} (Ln = La, Gd) under VUV-UV excitation, Opt. Express. 19 (2011) 11071. doi:10.1364/OE.19.011071.

[16] D.-Y. Wang, T.-M. Chen, B.-M. Cheng, Host Sensitization of Tb^{3+} Ions in Tribarium Lanthanide Borates $Ba_3Ln(BO_3)_3$ (Ln = Lu and Gd), Inorg. Chem. 51 (2012) 2961–2965. doi:10.1021/ic202241h.

[17] F. Zhang, Y. Wang, Y. Tao, Investigation of the luminescence properties of Tb^{3+}-doped $Li_6Y(BO_3)_3$ phosphors in VUV–VIS range, J. Lumin. 136 (2013) 51–56. doi:10.1016/j.jlumin.2012.11.021.

[18] L. Tian, Y.D. Park, S. Mho, I.-H. Yeo, P-76: Photoluminescence Characteristics of Eu^{3+} or Tb^{3+} Activated $Ca_4YO(BO_3)_3$, SID Symp. Dig. Tech. Pap. 36 (2005) 579. doi:10.1889/1.2036505.

[19] P. Dorenbos, The 5d level positions of the trivalent lanthanides in inorganic compounds, J. Lumin. 91 (2000) 155–176. doi:10.1016/S0022-2313(00)00229-5.

[20] A. Senthil Kumaran, S. Moorthy Babu, S. Ganesamoorthy, I. Bhaumik, A.K. Karnal, Crystal growth and characterization of KY(WO4)2 and KGd(WO4)2 for laser applications, J. Cryst. Growth. 292 (2006) 368–372. doi:10.1016/j.jcrysgro.2006.04.037.

[21] S. Mahlik, F. Diaz, P. Boutinaud, Luminescence quenching in $KYb(WO_4)_2$ -Tb^{3+} : An example of temperature-pressure equivalence, J. Lumin. 191 (2017) 18–21. doi:10.1016/j.jlumin.2017.02.007.

[22] S. Schwung, D. Rytz, B. Heying, U.C. Rodewald, O. Niehaus, D. Enseling, T. Jüstel, R. Pöttgen, The crystal structure and luminescence quenching of poly- and single-crystalline KYW2O8:Tb3+, J. Lumin. 166 (2015) 289–294. doi:10.1016/j.jlumin.2015.05.052.

[23] W.T. Carnall, P.R. Fields, K. Rajnak, Electronic Energy Levels in the Trivalent Lanthanide Aquo Ions. I. Pr^{3+}, Nd^{3+}, Pm^{3+}, Sm^{3+}, Dy^{3+}, Ho^{3+}, Er^{3+}, and Tm^{3+}, J. Chem. Phys. 49 (1968) 4424–4442. doi:10.1063/1.1669893.

[24] S.R. Bowman, S. O'Connor, N.J. Condon, Diode pumped yellow dysprosium lasers, Opt. Express. 20 (2012) 12906. doi:10.1364/OE.20.012906.

[25] G. Bolognesi, D. Parisi, D. Calonico, G.A. Costanzo, F. Levi, P.W. Metz, C. Kränkel, G. Huber, M. Tonelli, Yellow laser performance of Dy^{3+} in co-doped $Dy,Tb:LiLuF_4$, Opt. Lett. 39 (2014) 6628. doi:10.1364/OL.39.006628.

[26] A.A. Kaminskii, X. Xu, O. Lux, H. Rhee, H.J. Eichler, J. Zhang, D. Zhou, A. Shirakawa, K. Ueda, J. Xu, High-order stimulated Raman scattering in tetragonal $CaYAlO_4$ crystal-host for Ln^{3+}-lasant ions, Laser Phys. Lett. 9 (2012) 306–311. doi:10.1002/lapl.201110135.

[27] Z. Burshtein, Y. Shimony, I. Levy, A.M. Lejus, J.M. Benitez, F. Mougel, Refractive-index studies in $Ca_2Ga_2SiO_7$ and $SrLaGa_3O_7$ melilite-type compounds, J. Opt. Soc. Am. B. 13 (1996) 1941. doi:10.1364/JOSAB.13.001941.

[28] F. Mougel, G. Aka, F. Salin, D. Pelenc, B. Ferrand, A. Kahn-Harari, D. Vivien, Accurate Second Harmonic Generation phase matching angles prediction and evaluation of non linear coefficients of $Ca_4YO(BO_3)_3$ (YCOB) crystal, in: OSA, 2001: p. WB11. doi:10.1364/ASSL.1999.WB11.

[29] M.P. Hehlen, M.G. Brik, K.W. Krämer, 50th anniversary of the Judd–Ofelt theory: An experimentalist's view of the formalism and its application, J. Lumin. 136 (2013) 221–239. doi:10.1016/j.jlumin.2012.10.035.

[30] K.A. Gschneidner, L. Eyring, M.B. Maple, eds., Handbook on the physics and chemistry of rare earths. Vol. 25: ..., North-Holland Publ, Amsterdam, 1998.

[31] M. Hatanaka, S. Yabushita, Mechanisms of f–f hypersensitive transition intensities of lanthanide trihalide molecules: a spin–orbit configuration interaction study, Theor. Chem. Acc. 133 (2014). doi:10.1007/s00214-014-1517-2.

[32] B. Aull, H. Jenssen, Vibronic interactions in Nd:YAG resulting in nonreciprocity of absorption and stimulated emission cross sections, IEEE J. Quantum Electron. 18 (1982) 925–930. doi:10.1109/JQE.1982.1071611.

[33] S. Colak, W.K. Zwicker, Transition rates of Tb^{3+} in TbP_5O_{14}, $TbLiP_4O_{12}$, and $TbAl_3(BO_3)_4$: An evaluation for laser applications, J. Appl. Phys. 54 (1983) 2156–2166. doi:10.1063/1.332393.

[34] P. Loiko, A. Volokitina, X. Mateos, E. Dunina, A. Kornienko, E. Vilejshikova, M. Aguiló, F. Díaz, Spectroscopy of Tb^{3+} ions in monoclinic $KLu(WO_4)_2$ crystal application of an intermediate

configuration interaction theory, Opt. Mater. 78 (2018) 495–501. doi:10.1016/j.optmat.2018.03.014.

[35] A.A. Kaminskii, A.F. Konstantinova, V.P. Orekhova, A.V. Butashin, R.F. Klevtsova, A.A. Pavlyuk, Optical and nonlinear laser properties of the χ(3)-active monoclinic α-KY(WO$_4$)$_2$ crystals, Crystallogr. Rep. 46 (2001) 665–672. doi:10.1134/1.1387135.

[36] R. Martínez Vázquez, R. Osellame, M. Marangoni, R. Ramponi, E. Diéguez, Er^{3+} doped YAl$_3$(BO$_3$)$_4$ single crystals: determination of the refractive indices, Opt. Mater. 26 (2004) 231–233. doi:10.1016/j.optmat.2003.10.007.

[37] F. Shan, G. Zhang, X. Zhang, T. Xu, Y. Wu, Y. Fu, Y. Wu, Growth and spectroscopic properties of Tb^{3+}-doped Na$_3$La$_9$O$_3$(BO$_3$)$_8$ crystal, J. Cryst. Growth. 424 (2015) 1–4. doi:10.1016/j.jcrysgro.2015.04.040.

[38] B. Liu, J. Shi, Q. Wang, H. Tang, J. Liu, H. Zhao, D. Li, J. Liu, X. Xu, Z. Wang, J. Xu, Crystal growth, polarized spectroscopy and Judd-Ofelt analysis of Tb:YAlO$_3$, Spectrochim. Acta. A. Mol. Biomol. Spectrosc. 200 (2018) 58–62. doi:10.1016/j.saa.2018.04.006.

[39] F. Shan, Y. Fu, G. Zhang, T. Xu, X. Zhang, Y. Wu, Growth and spectroscopic properties of Tb^{3+} doped La$_2$CaB$_{10}$O$_{19}$ crystal, Opt. Mater. 49 (2015) 27–31. doi:10.1016/j.optmat.2015.08.020.

[40] F. Yang, C. Tu, H. Wang, Y. Wei, Z. You, G. Jia, J. Li, Z. Zhu, X. Lu, Y. Wang, Growth and spectroscopy of Dy^{3+} doped in ZnWO4 crystal, Opt. Mater. 29 (2007) 1861–1865. doi:10.1016/j.optmat.2006.10.014.

[41] P.W. Metz, D.-T. Marzahl, A. Majid, C. Kränkel, G. Huber, Efficient continuous wave laser operation of Tb^{3+}-doped fluoride crystals in the green and yellow spectral regions: Efficient continuous wave laser operation…, Laser Photonics Rev. 10 (2016) 335–344. doi:10.1002/lpor.201500274.

[42] A. Sillen, Y. Engelborghs, The Correct Use of "Average" Fluorescence Parameters, Photochem. Photobiol. 67 (1998) 475–486. doi:10.1111/j.1751-1097.1998.tb09082.x.

[43] Philip Werner Metz, PhD dissertation: Visible lasers in rare earth-doped fluoride crystals, Universit¨at Hamburg, 2014.

[44] T. Yamashita, Y. Ohishi, Amplification and Lasing Characteristics of Tb^{3+}-doped Fluoride Fiber in the 0.54 µm Band, Jpn. J. Appl. Phys. 46 (2007) L991–L993. doi:10.1143/JJAP.46.L991.

[45] Y.N. Forrester, R.S. Pandher, B.R. Reddy, S.K. Nash-Stevenson, Stepwise two-photon excitation studies in terbium-doped fluoride crystals, Opt. Mater. 19 (2002) 255–258. doi:10.1016/S0925-3467(01)00187-2.

[46] P. Kommidi, B.R. Reddy, Two-photon excitation studies in terbium doped yttrium aluminum oxide, J. Appl. Phys. 102 (2007) 076105. doi:10.1063/1.2786615.

[47] K.J.B.M. Nieuwesteeg, R. Raue, W. Busselt, On the saturation of Tb phosphors under cathode-ray excitation. I. Excited-state absorption in Tb-activated phosphor powders, J. Appl. Phys. 68 (1990) 6044–6057. doi:10.1063/1.346916.

[48] W. Zhao, S. Gao, S. An, B. Fan, S. Li, The luminescence properties of Sr$_3$Gd(BO$_3$)$_3$: Tb^{3+} phosphors under vacuum ultraviolet excitation, Chin. Sci. Bull. 57 (2012) 4513–4516. doi:10.1007/s11434-012-5418-2.

[49] M. Fibrich, H. Jelínková, J. Šulc, K. Nejezchleb, V. Škoda, Visible cw laser emission of GaN-diode pumped Pr:YAlO$_3$ crystal, Appl. Phys. B. 97 (2009) 363–367. doi:10.1007/s00340-009-3679-5.

[50] H. Tanaka, F. Kannari, Power scaling of continuous-wave visible Pr^{3+}:YLF laser end-pumped by high power blue laser diodes, in: OSA, 2017: p. ATu1A.3. doi:10.1364/ASSL.2017.ATu1A.3.

176

SUMMARY AND OUTLOOK

Summary

In the framework of this thesis, several Tb^{3+}- as well as Dy^{3+}-activated oxide-based crystals were fabricated and studied. These two active ions were chosen through a detailed state-of-the-art investigation of all the lanthanide ions in terms of the application prospect to visible lasers. The synthesis procedures for the selected materials were optimized to achieve single crystals with sufficient optical quality and size for the physical-property characterizations. Their potentials as visible laser gain media were investigated by characterizing the thermal and optical properties.

A preliminary investigation into the Tb^{3+} ion revealed that a couple of its characters may impede the laser operation in Tb^{3+}-activated oxide-based media, such as the propensity to excited-state absorption (ESA), the weak transition cross-sections, and the possibility of charge transfer upon excitation. These inconveniences can be to some extent circumvented by selecting a suitable host material, the criteria of which are described as follows: (1) a small crystal field strength, usually quantified by the crystal field depression $D(A)$, to enlarge the energy gap between the ground state and $4f^7 5d^1$ configuration, which is the probable terminal level of an ESA process; (2) the availability of high-concentration doping of Tb^{3+} to compensate the weak transition cross-sections; (3) the absence of ions with large electronegativity to avoid the charge transfer processes. Based on these considerations, the phosphate of $Ba_3Tb(PO_4)_3$ (BTP) as well as borates of $Sr_3Tb(BO_3)_3$ (STB), $Li_6Tb(BO_3)_3$ (LTB), and $TbCa_4O(BO_3)_3$ (TbCOB) were chosen. With regard to Dy^{3+}, the scope of suitable host material is larger, as it is not prone to suffer ESA or charge transfer processes. The oxide-based matrices of $CaYAlO_4$ (CYA), $YCa_4O(BO_3)_3$ (YCOB), and $Ca_2Al_2SiO_7$ (CAS) were selected for hosting Dy^{3+}, which have smaller $D(A)$ than YAG that can produce laser emission from Dy^{3+}.

The conventional Czochralski technique was applied to grow the selected Tb^{3+}-based and Dy^{3+}-doped crystals. The doping concentrations of Dy^{3+}, which impacts the cross-relaxation rate, were designated to be around 4.5×10^{20} cm^{-3} by referring to the reported Dy^{3+}-doped laser gain crystals. The polycrystalline starting materials were synthesized by solid-state reactions at high temperature. Their purities were examined by powder X-ray diffraction and were able to satisfy the subsequent crystal growths. A couple of problems occurred during the crystal fabrication processes. On one hand, formation of color centers were observed during the growth of STB and LTB in air atmosphere. The mechanism of the color centers were studied by absorption spectroscopy and electron paramagnetic resonance. By analyzing these data as well as the results reported in the literatures, the color centers could be attributed to oxidation of Tb^{3+} to Tb^{4+} in air. To circumvent this detrimental effect that influences the luminescence property of the material, further growths were carried out for STB and LTB in the reducing atmosphere containing 10% of H_2 and 90% of Ar. The resulting crystals are colorless. On the other hand, the as-grown crystals of LTB suffered cleavage or cracking. These drawbacks were

eliminated by employing a suitably oriented seed crystals and optimizing the growth conditions, including the crucible, growth parameters and control. Finally, single crystalline materials with good optical quality and without color centers were obtained. Besides, flux grown crystals of $TbAl_3(BO_3)_3$ (TAB) and $KTb(WO_4)_2$ (KTW) were also available for the following spectroscopic study.

The Dy^{3+} concentrations in different parts of the boule crystals were measured experimentally by electron probe micro-analysis. The segregation coefficients of Dy^{3+} in CYA and YCOB were found to be 1.06 and 0.86, respectively.

Thermal properties of the as-grown Tb^{3+}-based crystals were characterized. Their thermal conductivities and specific heat capacities were measured. LTB yields the largest thermal conductivity and specific heat capacity among these materials. The thermal expansion coefficients between 298 K and 1078 K were calculated from the temperature-dependent cell parameters, which were derived from the PXRD patterns recorded in this range. TbCOB was found to exhibit the least significant anisotropy in terms of thermal expansion coefficients.

All the crystals were oriented to the principal optical directions. For biaxial crystals of LTB, TbCOB, Dy:YCOB, and KTW, the relationship between the indicatrix and crystallographic axes were identified. The wavelength-dependent refractive indices of BTP, STB, and LTB were measured for the first time, using the standard method of minimum deviation. The resulting data can be fitted into Sellmeier dispersion equations.

The spectroscopic investigations mainly include absorption and emission spectra, fluorescence decay, and ESA. These data were used to calculate important parameters such as transition cross-sections, branching ratio, fluorescence lifetime, and experimental oscillator strength. The $^7F_6{\rightarrow}^5D_4$ transition around 485 nm of Tb^{3+} and the $^6H_{15/2}{\rightarrow}^4I_{15/2}$ transition around 450 nm of Dy^{3+} are particularly of interest since they match the output wavelengths of semiconductor pumps. These transitions have relatively small cross-sections ranging in orders of 10^{-22} to 10^{-21} cm^2 owing to the spin-forbidden nature. However, all the Tb^{3+}- as well as Dy^{3+}-activated crystals have comparable or even superior peak absorption cross-sections to the corresponding reported gain materials. With respect to the emission transitions, the green $^5D_4{\rightarrow}^7F_5$ transition of Tb^{3+} and the yellow $^4F_{9/2}{\rightarrow}^6H_{13/2}$ transition of Dy^{3+} feature large fluorescence branching ratios more than 50% in these matrices. Except for BTP and STB which have relatively weak transition cross-sections due to the significant spectral broadening, Tb^{3+}-activated crystals of LTB, TAB, and TbCOB as well as the Dy^{3+}-activated crystals exhibit comparable maximal emission cross-sections with the other gain materials. Besides, the TbCOB and TAB crystals are especially promising for lasing the yellow $^5D_4{\rightarrow}^7F_4$ transition, as they give relatively large σ_{em} at 593 nm and 584 nm, respectively. Furthermore, the Dy:YCOB crystal can provide an exceptionally high σ_{em} at 760 nm, which is interesting for laser operation in the deep red spectral range.

In addition, anisotropic behavior of the magnetic dipole absorption and emission transitions was universally observed in both Tb^{3+}- and Dy^{3+}-activated crystals. This phenomenon is due to the relatively large contribution from the magnetic dipole interaction for several transitions of Tb^{3+} or Dy^{3+}, which has been confirmed by theoretical calculations and experimental measurements. Routine polarized

spectral measurements that only take into account the anisotropy of electric dipole transitions result in inaccurate spectroscopic data. Moreover, the magnetic dipole transitions of $^5D_4{\rightarrow}^7F_5$ and $^6H_{15/2}{\rightarrow}^4I_{15/2}$ exhibit significant anisotropy. The former is used for green laser operation of Tb^{3+} and the latter is the most promising pump transition for Dy^{3+}-activated media. The inaccurate spectroscopic data of these two transitions may lead to a large uncertainty regarding the gain-crystal/cavity design.

The fluorescence decay curves were recorded to study the fluorescence dynamics of the upper laser levels. The decay curves of the Tb^{3+}-activated compounds from the $^5D_4$ level show a single exponential behavior, which indicates the absence of inter-ionic energy transfer processes. The fluorescence lifetimes were calculated to be as long as 2~3 ms. Thus, the Tb^{3+}-based materials are favorable for storing the pump energy. On the other hand, the decay profiles of the as-grown Dy^{3+}-doped single crystals are non-exponential, while those of the polycrystals with low doping concentrations are almost single exponential. This is due to the cross-relaxation processes from the $^4F_{9/2}$ manifold.

Judd-Ofelt analysis was performed to further study the $4f \rightarrow 4f$ intraconfigurational transitions. The electrostatic and spin-orbit interaction parameters, which vary with host material, were fitted to allow more accurate Judd-Ofelt calculations. The three Judd-Ofelt intensity parameters were calculated. The resulting oscillator strengths and branching ratios are overall in good agreement with the experimental data. The radiative lifetimes were used to derive the quantum efficiencies. Those of the Tb^{3+}-based compounds were found to be closed to unity (except that of KTW around 50%), which suggests negligible quenching processes such as multiphonon relaxation and cross-relaxation. Among the Dy^{3+}-doped crystals, Dy:CYA features the highest quantum efficiency of 54%.

Negative gain behavior at 543 nm was observed for the Tb^{3+}-based crystals of BTP, STB, LTB, TbCOB, and KTW. This indicates that the ESA processes overwhelm the stimulated emission at this wavelength. The ESA is especially significant for KTW, which is expected due to the strong inter-valence charge transfer band at the energetic position where ESA takes place.

Laser experiments were conducted with several LD or OPSL pumps. The Nichia LD (200 mW) emitting at 486 nm was not able to generate laser oscillation even using a 15%Tb:YLF crystal as gain medium. This is probably due to the low absorbed power (75 mW) and the lack of a suitable output coupler. Further attempts on the Tb^{3+}-based crystals of BTP, STB, LTB, and TbCOB were carried out by an OPSL with output power up to 4 W and excellent beam quality. Although laser operations of the fluorides could be realized by using this pump, none of the oxide-based crystals were able to produce green laser emission. This is somehow reflected by the negative results during the gain measurements at 543 nm. With regard to the Dy^{3+}-activated crystals, the main problems are the poor quality of the fiber-delivered LD pump (tested with Pr^{3+}-activated gain crystals) compared to the single-mode ones, and the mismatch of the pump output wavelength and the peak absorption wavelength of the media (442 nm vs. 453 nm).

Outlook

For the Tb^{3+}-based materials, their spectroscopic properties including the transition cross-sections and fluorescence lifetimes are overall comparable to the fluorides using which laser operations can be demonstrated. However, the negative gain and the unsuccessful laser operation in the green spectral region point toward predominant ESA processes over the stimulated emissions, even though the host materials were selected for their relatively small crystal-field depression, for example the $D(A)$ of BTP (17594 cm^{-1}) is comparable to that of KY$_3$F$_{10}$ (16084 cm^{-1}). This indicates that ESA from $^5D_4$ to higher $4f$ levels can make a contribution. More systematic wavelength-dependent gain measurements are essential at the moment to figure out the origin of the ESA processes in these Tb^{3+}-based crystals.

On the other hand, the criterion in terms of crystal-field depression should be even stricter. Oxide-based materials of TbMgB$_5$O$_{10}$ ($P2_1/c$, 12568 cm^{-1}), TbB$_3$O$_6$ ($C2/c$, 12526 cm^{-1}), LiTb(PO$_3$)$_4$ ($C2/c$, 13369 cm^{-1}), and TbPO$_4$ ($I4_1/amd$, 16007 cm^{-1}) with smaller $D(A)$ than KY$_3$F$_{10}$ (16084 cm^{-1}) might be hopeful to completely avoid ESA into the low-spin $5d$ states. Crystal growth of these materials or their isostructral compounds from the flux have been reported [1–4]. It would be an interesting subject to develop flux growth techniques to synthesize these crystals and study their spectroscopic properties, as this work mainly fabricates and characterizes terbium-based crystals grown from the melt.

Furthermore, lasing of the yellow $^5D_4{\rightarrow}^7F_4$ transition using these oxide crystals have not been attempted and is possible. Although its emission cross-section is smaller than the green $^5D_4{\rightarrow}^7F_5$ transition, the lower energy (~1300 cm^{-1}) might be able to circumvent the intense ESA transitions.

With regard to the Dy^{3+}-activated materials, the 3.7 at% Dy:CYA crystal is the most promising owing to its superior spectroscopic properties. The quantum efficiencies of the 12.1 at% Dy:CAS and 8.6 at% Dy:YCOB crystals are relatively low (<25%). Optimizations regarding the doping concentrations should be concerned. The experimental conditions must be improved as well to realize laser oscillations. A single-mode LD with better beam quality than the used fiber-coupled one is more favorable. Meanwhile, the output wavelength of the pump should match better with the main absorption peaks around 453 nm to increase the absorption efficiency.

References

[1] P. Becker, R. Fröhlich, Polymorphy of monoclinic terbium triborate, TbB$_3$O$_6$, Cryst. Res. Technol. 43 (2008) 1240–1246. doi:10.1002/crat.200800397.

[2] Y. Huang, F. Lou, S. Sun, F. Yuan, L. Zhang, Z. Lin, Z. You, Spectroscopy and laser performance of Yb^{3+}:GdMgB$_5$O$_{10}$ crystal, J. Lumin. 188 (2017) 7–11. doi:10.1016/j.jlumin.2017.03.070.

[3] B.M. Epelbaum, G. Schierning, A. Winnacker, Modification of the micro-pulling-down method for high-temperature solution growth of miniature bulk crystals, J. Cryst. Growth. 275 (2005) e867–e870. doi:10.1016/j.jcrysgro.2004.11.030.

[4] W. Böhm, H.G. Kahle, W. Wüchner, Spectroscopic Study of the Crystal Field Splittings in TbPO$_4$, Phys. Status Solidi B. 126 (1984) 381–392. doi:10.1002/pssb.2221260145.

APPENDIX A SUPPLEMENTARY THEORETICAL

BACKGROUND

This appendix chapter acts as an extension of the introduction to the theoretical principles of light-matter interaction. Beginning with a classical two-level system, the deduction of interaction between light and atomic systems leads to the concept of transition cross-sections, which are very important spectroscopic parameters in this study.

After the study of hydrogen atomic spectroscopy by N. Bohr based on a quantized model with great success, handling the light-matter interaction issue in quantum physical approaches has become a main stream. According to quantum field theory, light may be considered not only as an electro-magnetic wave but also as quantum mechanical photons which could be described by wavefunctions.

Atomic systems such as atoms, ions, and molecules exhibit discrete electronic energy states. The transition of electrons between two energy states is associated with either absorbing or emitting a photon, which carries an energy corresponding to the energetic gap $E_2 - E_1 = h\nu_{21}$. Assume that the population density on each levels is N_1 and N_2, when a monochromatic electromagnetic wave with frequency ν_{21} passes through this atomic system, the transition rate of electron from energy level **1** to **2** is given by:

$$\left(\frac{\partial N_1}{\partial t}\right)_{abs} = -B_{12}\rho N_1 v \tag{A.1}$$

where ρ is the radiation energy density and B_{12} is known as the Einstein B coefficient, which is a constant of proportionality. The product $B_{12}\rho$ is the absorption transition probability. After an electron has been excited to the energy level **2**, its population decays spontaneously to the lower energy level **1** at a rate of:

$$\left(\frac{\partial N_2}{\partial t}\right)_{sp} = -A_{21}N_2 \tag{A.2}$$

where A_{21} is the spontaneous emission transition probability and its reciprocal is known as the radiative lifetime. Spontaneous emission process undergoes individually in each atoms and thus the generated photons have random initial directions and phases. On the other hand, emission can also take place when the excited electron is stimulated by a photon $h\nu_{21}$. This process is called stimulated emission. In contrast to the spontaneous emission, the emitted photon has the same direction and phase as the initial photon. The rate equation of stimulated emission is expressed as:

$$\left(\frac{\partial N_2}{\partial t}\right)_{st} = -B_{21}\rho N_2 \tag{A.3}$$

The above deduction assumed a monochromatic wave with constant frequency ν_{21} and the energy gap has no spectral linewidth. To take into account their optical linewidth, the frequency distribution

of the incident photon energy density can be simply characterized by a frequency-dependent function $\rho(v)$. On the other hand, the atomic transition can be described by the lineshape function $g(v)$, which indicates the probability that the atom absorbs or emits a photon per unit frequency. It is normalized to unity over all the frequencies hence $\int g(v)dv = 1$. Given this definition, equation A.1 and A.3 could be rewritten in the forms

$$\left(\frac{\partial N_1}{\partial t}\right)_{abs} = -B_{12}N_1 \int \rho(v)g(v)\,dv \tag{A.4}$$

and

$$\left(\frac{\partial N_2}{\partial t}\right)_{st} = B_{21}N_2 \int \rho(v)g(v)\,dv \tag{A.5}$$

Further consider that the incident light for excitation has good monochromaticity, which is the case for spectroscopic measurements in this study, the lineshape function of the atomic transition can be treated as constant over this narrow spectral range. The above rate equations are simplified to be:

$$\left(\frac{\partial N_1}{\partial t}\right)_{abs} = -B_{12}N_1 g(v) \int \rho(v)\,dv = -B_{12}N_1 g(v)\rho \tag{A.6}$$

and

$$\left(\frac{\partial N_2}{\partial t}\right)_{st} = B_{21}N_2 g(v) \int \rho(v)\,dv = B_{21}N_2 g(v)\rho \tag{A.7}$$

In the abovementioned two-level system, the change rate of photon density in the medium derived from the stimulated processes approximately equals to

$$\frac{\partial N_p}{\partial t} = \left(\frac{\partial N_2}{\partial t}\right)_{st} - \left(\frac{\partial N_1}{\partial t}\right)_{abs} = B_{21}N_2 g_{em}(v)\rho - B_{12}N_1 g_{abs}(v)\rho \tag{A.8}$$

The spontaneously emitted photons are omitted since the fraction of these photons in the direction to the incident beam is negligible. The intensity of the incident light is amplified if $\frac{\partial N_p}{\partial t} > 0$. If this light amplification is small, spatial distribution of N_2, N_1, and ρ in an optical medium could be treated as constant. Hence the change rate of photon density in terms of path length of the incident beam in this medium is

$$\frac{\partial N_p}{\partial l} = \frac{\rho}{c/n}(B_{21}N_2 g_{em}(v) - B_{12}N_1 g_{abs}(v)) \tag{A.9}$$

where c is the light velocity in vacuum and n is the refractive index in the medium. Further associating equation A.9 to the Lambert-Beer law, the absorption coefficient $\alpha(v)$ could be correlated to the above equation in the form:

$$\alpha(v) = -\frac{1}{N_p}\frac{\partial N_p}{\partial l} = \frac{hv}{c/n}(B_{12}N_1 g_{abs}(v) - B_{21}N_2 g_{em}(v)) \tag{A.10}$$

Notice that the relationship between the photon density N_p (number of photon per unit volume) and the energy density ρ (photon energy per unit volume) is $\rho = h\nu \cdot N_p$. Deducing from the Boltzmann's thermodynamic equation, assuming that sublevels of **1** and **2** are populated equally, the relationship between the Einstein coefficients has been found to be $g_1 B_{12} = g_2 B_{21}$ and $A_{21} = \frac{8\pi h\nu^3}{(c/n)^3} B_{21}$, where g_1 and g_2 are the degeneracies of energy level **1** and **2**. Applying the former relational expression to equation A.10 and integrating over all the frequencies in the transition spectral range yields:

$$\int \alpha(\nu)d\nu = \int \frac{B_{21}h\nu}{c/n}\left(\frac{g_2}{g_1}N_1 g_{abs}(\nu) - N_2 g_{em}(\nu)\right)d\nu \qquad (A.11)$$

Recall the assumption made for equation A.6 and A.7 that the incident light is quasi-monochromatic and thus the frequencies in this narrow spectral range can be averaged to ν_0, where the spectral line center at. Moreover, the lineshape functions $g_{abs}(\nu)$ and $g_{em}(\nu)$ are only frequency-dependent and normalized over the spectral range of the transition. Finally, we are able to obtain the Füchtbauer–Ladenburg equation, which relates the integrated absorption coefficient, a measurable physical quantity, to the Einstein coefficients and the energy-level populations:

$$\int \alpha(\nu)d\nu = \frac{B_{21}h\nu_0}{c/n}\left(\frac{g_2}{g_1}N_1 - N_2\right) \qquad (A.12)$$

According to the Einstein relationship mentioned above, B_{21} could be substituted by A_{21}, which is easier to be achieved. The equation A.10 becomes:

$$\alpha(\nu) = \frac{A_{21}c^2}{8\pi\nu_0{}^2 n^2}\left(\frac{g_2}{g_1}N_1 g_{abs}(\nu) - N_2 g_{em}(\nu)\right) = \sigma_{12}N_1 - \sigma_{21}N_2 \qquad (A.13)$$

where σ_{12} and σ_{21} are the absorption and emission cross-section, respectively. The stimulated emission cross-section is thus written as:

$$\sigma_{21}(\nu) = \frac{A_{21}c^2}{8\pi\nu_0{}^2 n^2} g_{em}(\nu) \qquad (A.14)$$

In the occasion of a laser operation where the initial photon that triggers stimulated emission comes from spontaneous emission, ν_0 in the above equation can be simply replaced by ν. Further extend the two-level system described above to a more realistic situation where multiple excitation states decay simultaneously from an upper level j to several multiplets i. Under steady-state low level excitation, where $\left(\frac{\partial N_j}{\partial t}\right)_{sp}$ is constant and stimulated emission is negligible, the spontaneous emission intensity of the $j \rightarrow i$ transition in a spectral range of $d\nu$ is expressed as:

$$I_{ji}(\nu)d\nu = A_{ji}N_j h\nu g_{em}(\nu)d\nu \qquad (A.15)$$

where $I(\nu)$ is light intensity in dimension of photon power per unit frequency. The integral $\int \sum_i \frac{I_{ji}(\nu)}{h\nu} d\nu$ stands for the total number of emitting photon per unit time. Assume that nonradiative

decay is negligible, it is equal to $\sum_i A_{ji} N_j$. By introducing this relationship to equation A.15 and integrating over all frequencies, the lineshape function is described as:

$$g_{em}(v) = \frac{I(v)/hv}{\int \frac{I(v)}{hv} dv} \tag{A.16}$$

Summing all the $j \rightarrow i$ transitions and expanding the lineshape function, equation A.15 becomes:

$$\sigma_{em}(v) = \frac{c^2 v^{-3} I(v)}{8\pi n^2 \tau_{rad} \int \frac{I(v)}{v} dv} \tag{A.17}$$

In this study, the emission spectral measurements are based on a grating monochromator, which measures spectral intensity as a function of wavelength. By introducing the relationship of $I(v)dv = -I(\lambda)d\lambda$, the effective stimulated emission cross-section σ_{em} can be deduced to be:

$$\sigma_{em}(\lambda) = \frac{\lambda^5 I(\lambda)}{8\pi n^2 c \tau_{rad} \int \lambda I(\lambda) d\lambda} \tag{A.18}$$

This equation gives $\sigma_{em}(\lambda)$ as a consecutive function of wavelength and makes it possible to measure σ_{em} from spontaneous emission instead of stimulated emission which is much more difficult to be observed. The $I(\lambda)$ values, which stand for spectral irradiance in dimension of photon power per unit wavelength, can be obtained from a calibrated fluorescence spectrum and τ_{rad} is usually calculated from Judd-Ofelt analysis.

APPENDIX B EXPERIMENTAL PROCEDURES

B.1 Synthesis of polycrystalline materials

All the polycrystalline raw materials in this work were synthesized via conventional solid-state reactions. The weight of raw materials to be prepared are determined by assuming that the molten polycrystals would fill 70-80% of the crucible. The reactants were weighed and ball-milled for 3×20 minutes (200 rpm). A Fritsch PULVERISETTE planetary mill equipped with agate bowls and balls was employed for the ball milling. The ground mixtures were then transferred to a ceramic mortar and further mixed up with a pestle. The powders were isostatically compressed into a cylinder. The cylinder was placed on platinum foils and sintered in a resistance furnace. The heating rates were set to be 1-5°C/h, depending on the material, and the cooling rate was a uniform value of 5°C/h.

Phase purity of the as-sintered polycrystals was verified with Powder X-ray diffraction by a Panalytical X'Pert Pro diffractometer. Diffraction patterns were collected with Cu Kα1 radiation (45 kV and 40 mA). The assignment of phase as well as the quantification analysis were performed using the High Score software.

It is worth noting that the preparation methodology of the polycrystalline raw materials for the Czochralski growth were optimized in advance by using pressed tablets in small quantity (~5 g). The program that gives the XRD pattern with least impure phases was adopted.

B.2 Crystal growth and supplementary crystallographic data

This part mainly describes the general setup for the furnace and procedure for the Czochralski growth in this study. The growth parameters, which vary with material, will be given in each subsection.

Two different Czochralski furnaces were used in this study. One is home-made (denoted furnace 1) and another is a JGD series furnace manufactured by Sichuan Institute of Piezoelectric and Acoustooptic Technology (denoted furnace 2). The former enables crystal growth in running atmosphere while the latter in sealed atmosphere. The power regulation is realized by a fuzzy control system for furnace 1 and by a PID controller for furnace 2. A graphical representation of a typical setup using furnaces 2 is give in Figure B.1. The setup for furnace 1 is similar, except that the external wall is replaced by a silica tube filled with alumina fiber.

A crucible charged with polycrystalline raw materials was placed at the center of the inductive coil. The crucible was surrounded by zirconia grains and its vertical position could be adjusted. The top of the crucible was usually placed 1 cm below the topmost coil. Several kinds of alumina or zirconia refractories were installed as thermal insulator. These refractories could also be removed or added to optimize the temperature field for the crystal growth.
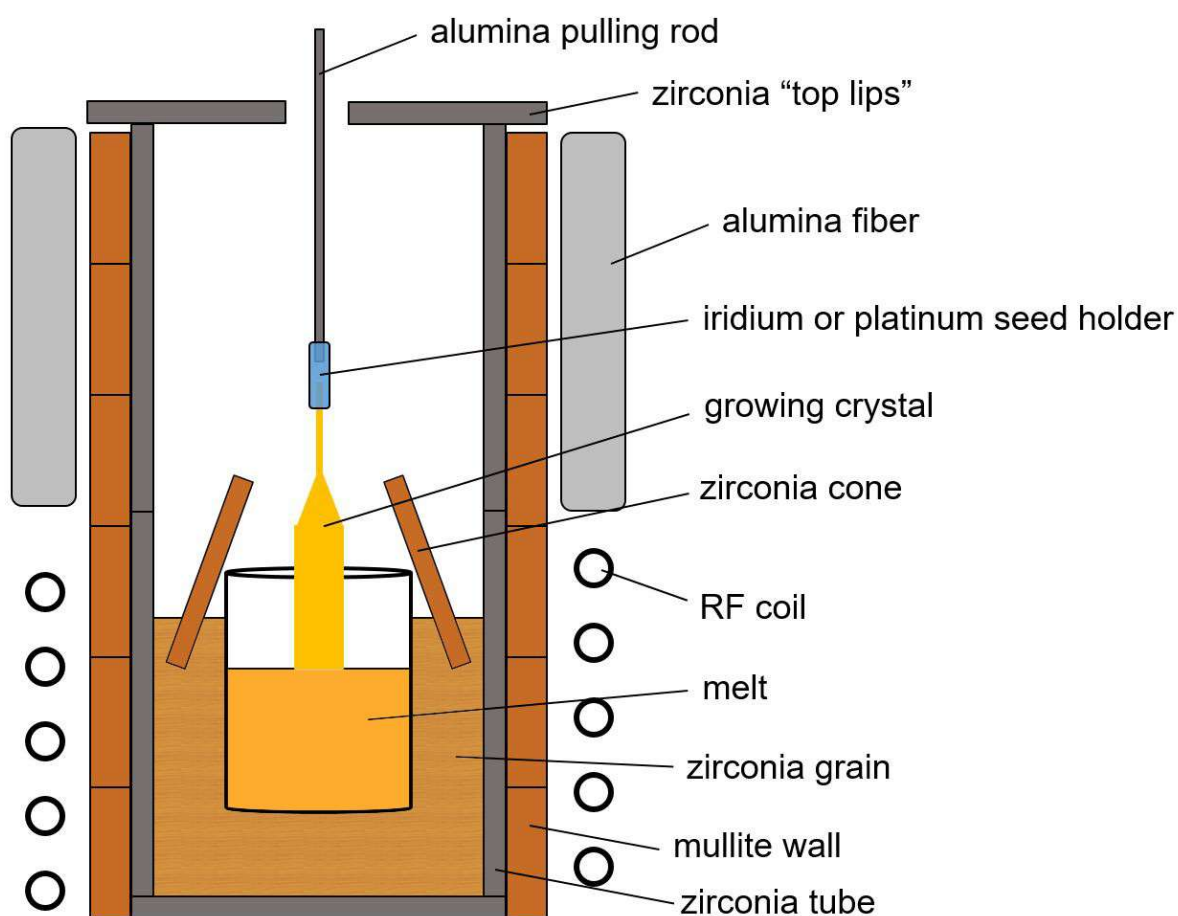
Figure B.1   **Schematic setup for a typical Czochralski growth using furnace 2.**

186

Furnace 2 has a sealed chamber which enables different protection atmosphere. Air was pumped out of the chamber until the pressure reached ~5 Pa to ensure the air tightness, followed by the inlet of the designated atmosphere. A sensor was equipped inside the chamber to monitor the real-time pressure during the growth process. Protection gas could be supplemented automatically if necessary.

After the atmosphere was applied, the crucible was inductively heated to melt the raw materials. The elevation of power, which was conducted linearly by a preset program, was set to be as slow as possible (usually ~14 h) to avoid the thermal shock to the crucible and refractories. In most cases, further more raw materials were needed to fill the crucible after melting the first batch. For furnace 1, raw materials could be supplemented directly from the top of the furnace chamber, while for furnace 2, they could only be refilled after cooling down the crucible. This process was repeated for 2 to 3 times until the total amount of the raw material could fill 70 to 80% of the volume of the crucible after melted.

For a growth using the Pt/Ir wire as a growth starter, the power was carefully increased until the raw materials were almost completely melted. At this moment, a small polycrystalline crust should be floating at the center of the crucible and the wire was introduced to it, which then acted as a seed. For a growth with a crystal seed, the seed was slowly descended toward the melt after the raw materials were just completely melted. In both cases, the descent stopped as soon as the wire/seed contacted the crust/melt.

After the contact, the position of the wire/seed was kept unchanged and the rotation was turned on with the designated speed during the growth. The power of the RF generator was adjusted manually until the equilibrium of the crystallization, where the reading on the electronic scale no more changes. The crystal was then pulled up and the growth parameters as well as the power regulation were controlled by a preset program. Nevertheless, these parameters could be modified during the growth if needed.

At the end of growth, the crystal was removed from the melt with a pulling rate of 8-12 mm/h. After separation from the melt, the crystal was continued to elevate to a position around 5 mm above the melt. Typically, the crystal was slowly cooled down to room temperature in 36-48 h to avoid cracking.

B.2.1 Ba$_3$Tb(PO$_4$)$_3$

According to the single crystal refinement in the literature [1], the atomic coordinates of BTP are listed in Table B.1.

The Czochralski growth of BTP was carried out using furnace 2. The growth parameters are presented in Table B.2, where Φ1 and Φ2 stand for the designated diameter of the crystal at the beginning and the end of the part, respectively, and PID are the parameters for the power regulation (same below). Evolutions of the actual weight, growth speed, and power are schematically presented in Figure B.2.

Table B.1   Atomic coordinates of BTP (space group: $I\bar{4}3d$).

Atom	Wyckoff	occupancy	x	y	z
Ba	16c	0.75	0.9402	0.4402	0.0598
Tb	16c	0.25	0.9230	0.4230	0.770
P	12a	1	1	0.75	0.125
O(1)	48e	0.75	1.0990	0.6799	0.0445
O(2)	48e	0.25	1.1140	0.7770	0.0490

Table B.2   Designated growth parameters of BTP.

Part	Φ1 (mm)	Φ2 (mm)	Length (mm)	Pulling speed (mm/h)	Rotation (rpm)	P	I	D
neck	7	7	40	1.5	12	0.01	100	30
shoulder	7	25	30	1.5	12	0.01	100	30
body	25	25	50	1.5	12	0.01	100	30
bottom	25	1	20	1.5	12	0.01	100	30
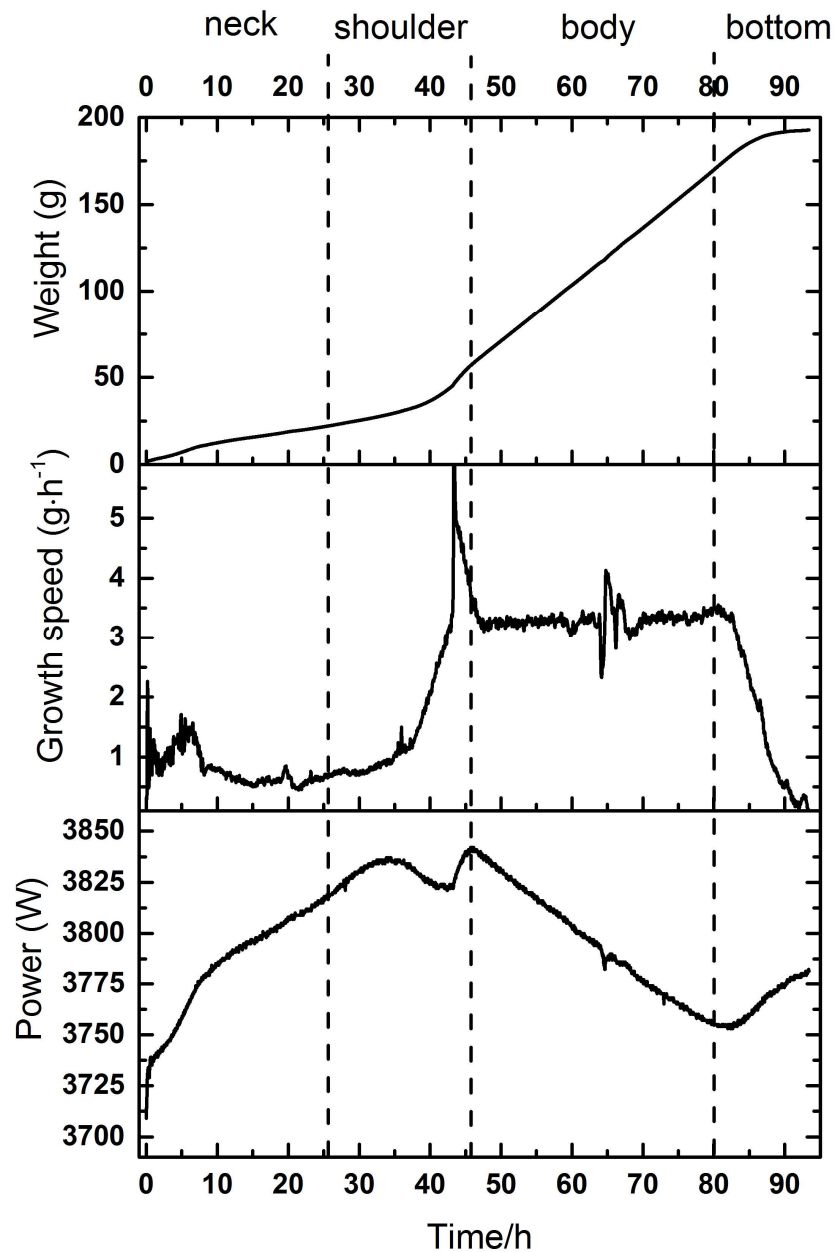
Figure B.2 **Evolution of weight of crystal, growth speed, and power during the growth of BTP.**

PXRD pattern of the as-grown crystal sample of BTP is shown in Figure B.3. No secondary phase could be detected. A theoretical line profile was refined using the software FullProf Suite [2] to match the measured diffraction profile. Profile matching refinement yields a cubic cell parameter of 10.466 Å, which is consistent with the value of 10.4484 Å based on single-crystal XRD refinement [1].
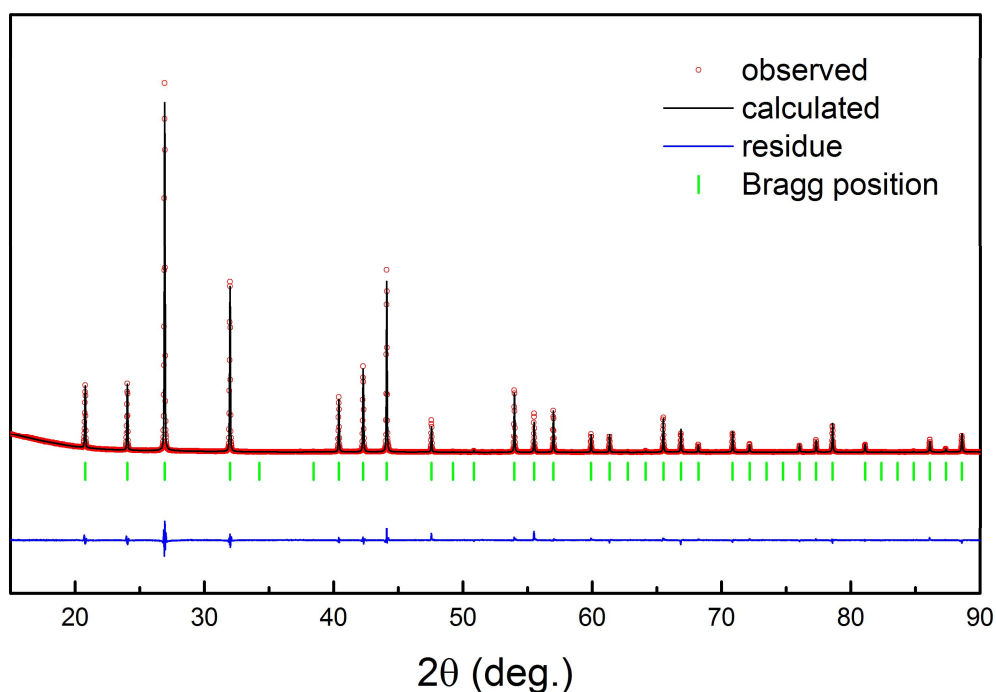
Figure B.3 **Experimental and refined PXRD pattern of BTP crystal sample.**

B.2.2 Sr₃Tb(BO₃)₃

The atomic coordinates of STB based on a PXRD refinement [3] (ICCD code:04-009-3070) are listed in Table B.3.

Table B.3 **Atomic coordinates of STB (space group: $R\overline{3}$).**

Atom	Wyckoff	x	y	z
Sr	18f	0.0966	0.2934	0.1419
Tb(1)	3a	0	0	0
Tb(2)	3b	0	0	0.5
B	18f	0.1927	0.1366	0.2661
O(1)	18f	0.1554	0.0350	0.3600
O(2)	18f	0.1644	0.1122	0.1191
O(3)	18f	0.4030	0.0743	0.0198

The Czochralski growth of STB1 and STB2 were carried out using furnace 1 and 2 respectively. The growth parameters are presented in Table B.4 and B.5. Curves of the monitored data during the growth of STB2 are illustrated in Figure B.4. The oscillating growth rate at the bottom part is somehow related to its irregular shape.

Table B.4   Designated growth parameters of STB1

Step	Φ1 (mm)	Φ2 (mm)	Length (mm)	Pulling speed (mm/h)	Rotation (rpm)
neck	6	6	25	0.7	10
shoulder	6	22	22	0.7	10
body	22	22	37	0.7	10
bottom	22	0	11	0.7	10

Table B.5   Designated growth parameters of STB2[a]

Step	Φ1 (mm)	Φ2 (mm)	Length (mm)	Pulling speed (mm/h)	Rotation (rpm)	P	I	D
neck	7	7	10	1	10	0.1	100	50
shoulder	7	25	25	1→0.6[b]	10	0.1	100	50
body	25	25	35	0.6	10	0.1	100	50
bottom	25	1	20	0.6→1	10	0.1	100	50

[a] Several trials of the growth have been performed. A large fluctuation of the electronic scale was recorded at around 6:00 a.m. for each failed growth. The problem was solved by turning off the heating system in the Czochralski furnace room.

[b] The pulling speed was changed gradually by the program within this part (same below).
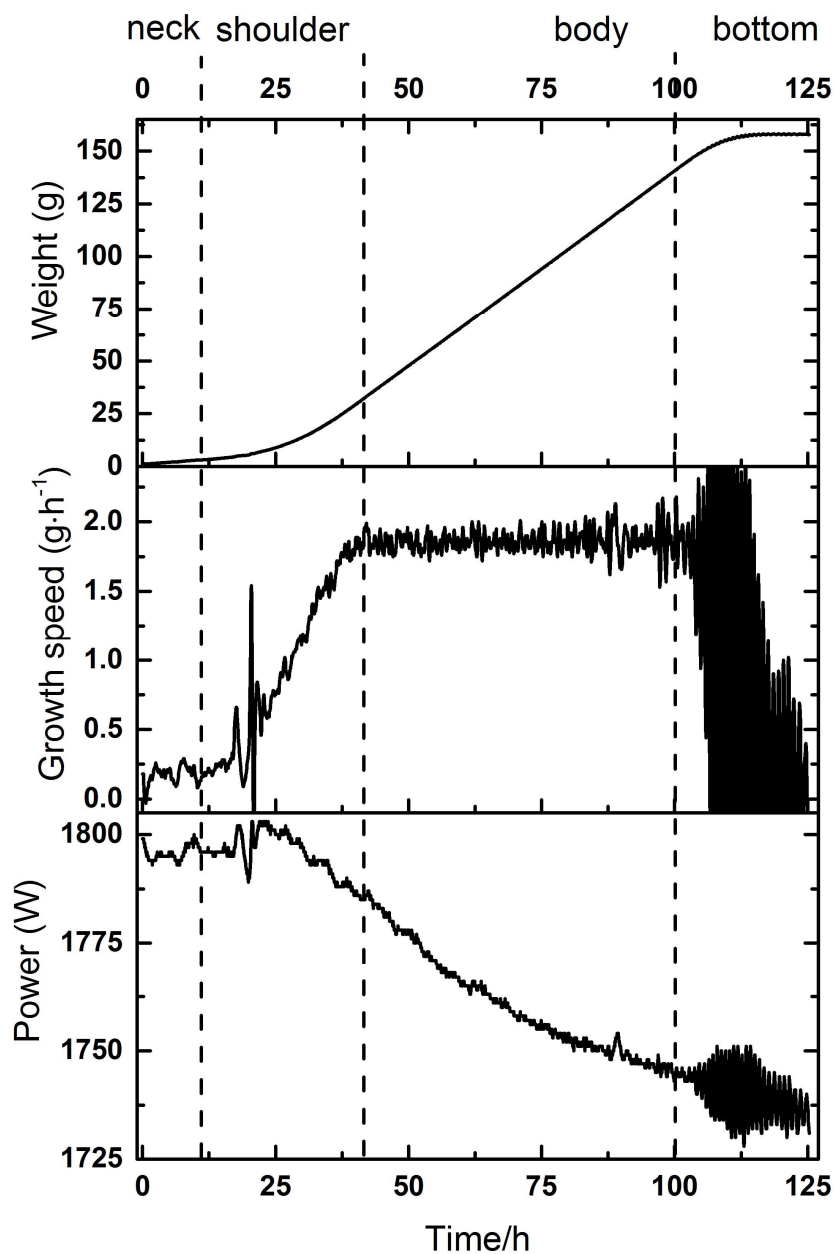
Figure B.4   Evolution of weight of crystal, growth speed, and power during the growth of STB2.

PXRD pattern of STB is shown in Figure B.5. No difference could be detected between the patterns of STB before and after annealing in reducing atmosphere. Profile matching refinement gives cell parameters of $a = b = 12.520$ Å, $c = 9.258$ Å, which are comparable to the data obtained by single-crystal XRD.
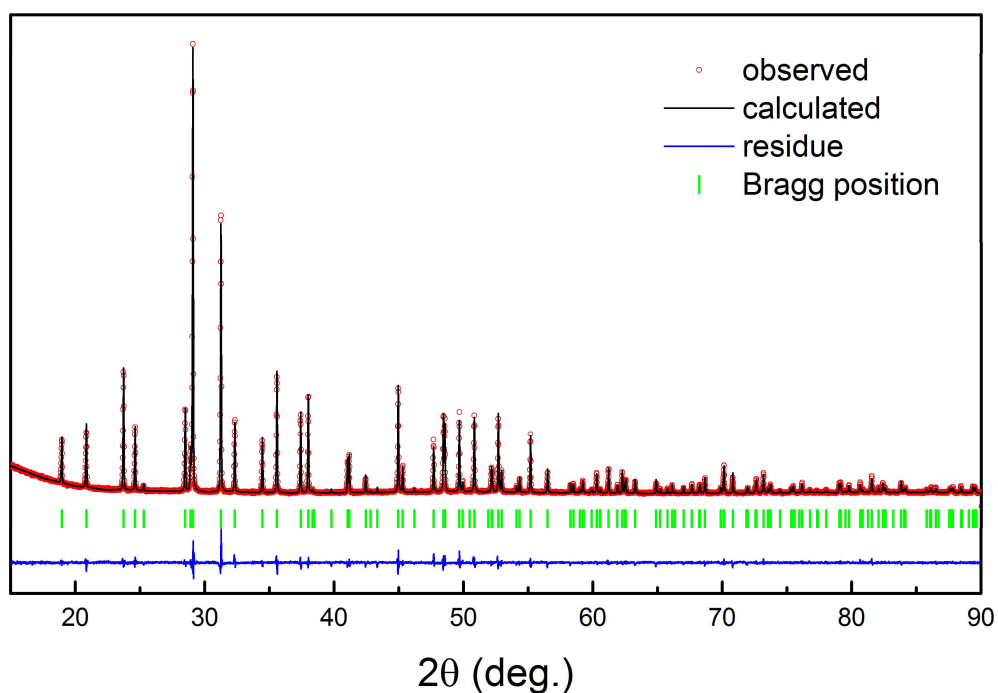
Figure B.5   **Experimental and refined PXRD pattern of STB crystal sample.**

B.2.3 TbAl₃(BO₃)₄

The atomic coordinates of TAB based on the refinement (reference ICCD code: 00-0008-7538) are listed in Table B.6.

Table B.6   **Atomic coordinates of TAB.**

Atom	Wyckoff	x	y	z
Tb	3b	0	0	0.5
Al	9e	0.4557	0	0.5
B(1)	9d	0.5465	0	0
B(2)	3a	0	0	0
O(1)	18f	0.20977	0.19783	0.31723
O(2)	9d	0.1337	0	0
O(3)	9d	0.41050	0	0

B.2.4 Li₆Tb(BO₃)₃

Crystal growth of LTB1 was performed using furnace 1, while for LTB2 and LTB3, furnace 2 was employed. The setups of the furnace chamber regarding these three growth were almost the same.

The zirconia grains surrounding the crucible and the cone were taken off. The set growth parameters are presented in Table B.7-2.9. The growth curves of LTB2 and LTB3 are shown in Figure B.6 and B.7, respectively.

Table B.7   Designated growth parameters of LTB1

Step	Φ1 (mm)	Φ2 (mm)	Length (mm)	Pulling speed (mm/h)	Rotation (rpm)
neck	6	6	25	0.5	5
shoulder	6	22	16	0.5	5
body	22	22	45	0.5	5
bottom	22	0	11	0.5	5

Table B.8   Designated growth parameters of LTB2

Step	Φ1 (mm)	Φ2 (mm)	Length (mm)	Pulling speed (mm/h)	Rotation (rpm)	P	I	D
neck	9	9	15	1	5	0.05-0.15[a]	120	90
shoulder	9	25	30	1→0.5[a]	5	0.15	120	90
body	25	25	50	0.5	5	0.05-0.15	120	90
bottom	25	1	20	0.5	5	0.15	120	90

[a] Modifications regarding the feedback parameters were attempted to stabilize the growth.

Table B.9   Designated growth parameters of LTB3

Step	Φ1 (mm)	Φ2 (mm)	Length (mm)	Pulling speed (mm/h)	Rotation (rpm)	P	I	D
neck	7	7	25	0.6	6	0.05	120	90
shoulder	7	25	30	0.6→0.4	6	0.05	120	90
body	25	25	30	0.4	6	0.04-0.05	120	90
bottom	25	1	20	0.4→0.6	6	0.05	120	90
tail	1	1	45	0.6	6	0.05	120	90
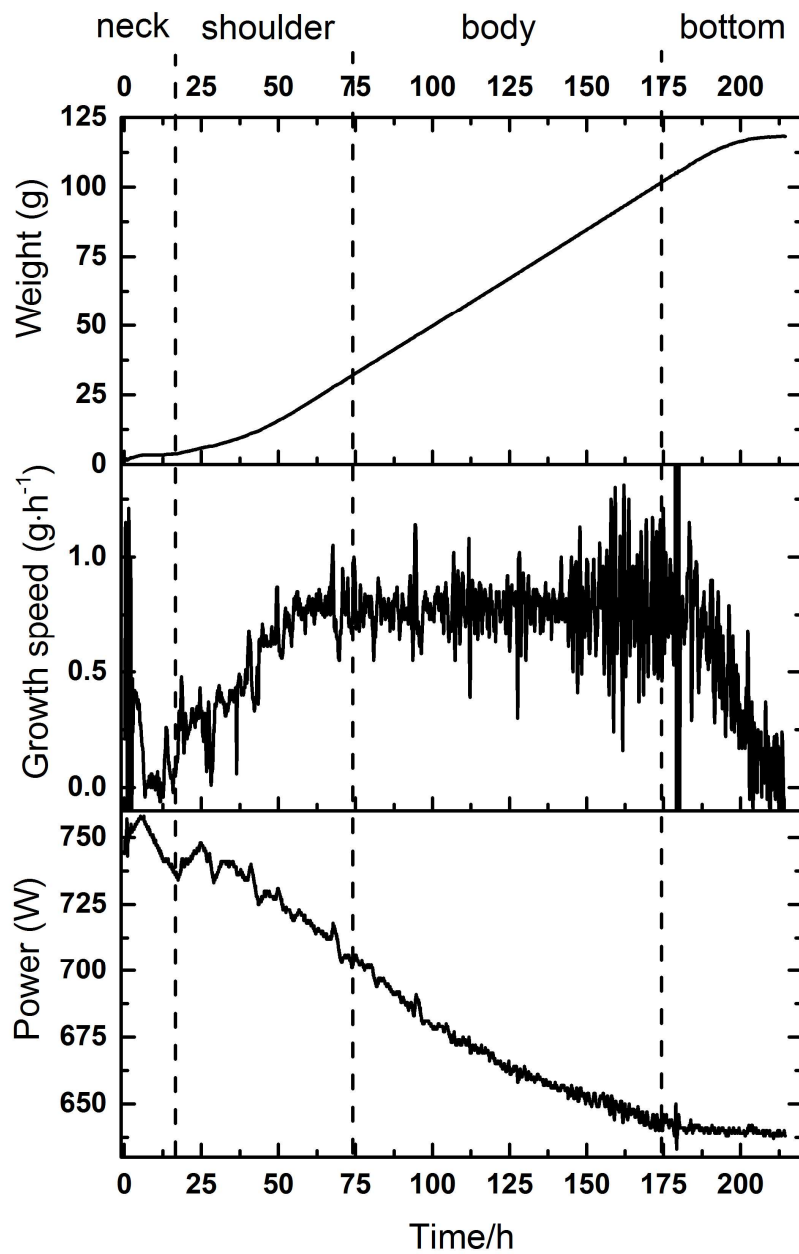
Figure B.6   Evolution of weight of crystal, growth speed, and power during the growth of LTB2.
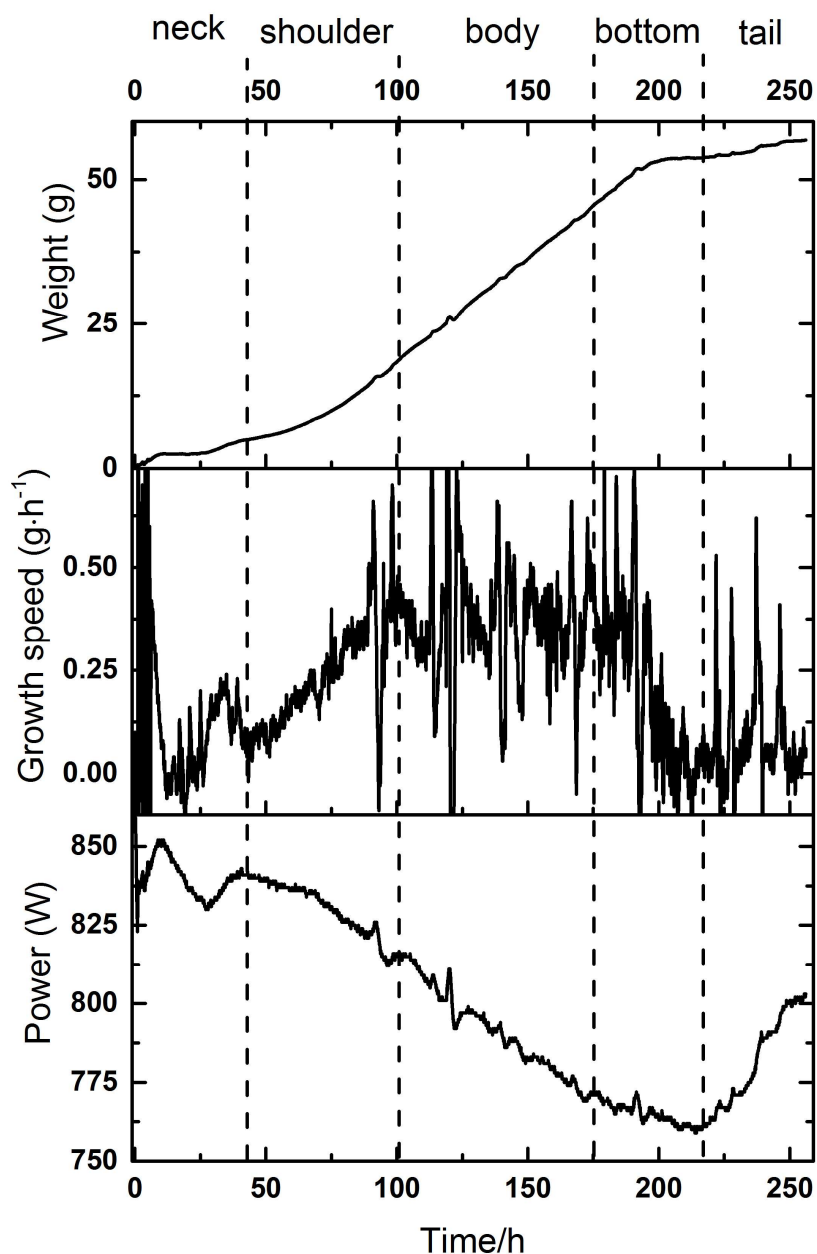
Figure B.7   **Evolution of weight of crystal, growth speed, and power during the growth of LTB3.**

Single crystal X-ray diffraction data for LTB were collected on an Oxford Diffraction Xcalibur-S diffractometer equipped with a Sapphire 3 CCD detector with Mo Kα radiation (λ = 0.71073 Å, graphite monochromator) at room temperature. The size of the single crystal sample is 0.12 × 0.49 × 0.86 mm, which was obtained from LTB2. The structure was resolved by Patterson method and the refinement was carried out with SHELX-2017 by full-matrix least-squares minimization and difference Fourier methods. All atoms were refined with anisotropic displacement parameters. The atomic coordinates and anisotropic displacement parameters are given in Table B.10.

Table B.10 Atomic coordinates and displacement parameters (in units of $10^3 \, \text{Å}^3$) of LTB (space group: $P/2_1c$).

Atom	x	y	z	U_{11}	U_{22}	U_{33}	U_{23}	U_{13}	U_{12}
Tb(1)	0.4198	0.8102	0.8464	6.23	5.67	7.31	-0.12	2.09	-0.08
O(1)	0.3509	0.8159	1.1653	14	8.1	7.4	-0.6	2.5	-2
O(2)	0.7614	0.7987	0.9456	9	7.4	13.6	0	1.5	0
O(3)	0.2227	0.9319	0.7694	7.4	8.6	13.9	-1.6	2.1	-0.9
O(4)	0.0765	0.8031	0.7249	10	6.6	15.7	-0.5	1.8	0.5
O(5)	0.6221	0.9267	0.9577	8	8.1	21.9	-4	2.8	1.4
O(6)	0.4935	0.8258	0.5265	13.5	10.9	7.1	0.9	3.4	-0.2
O(7)	-0.1069	0.9222	0.5765	8.5	13.4	14.3	1.3	2.6	1.3
O(8)	0.9640	0.9119	1.0884	7.8	14	14.2	-4.4	3	-2.7
O(9)	0.4148	0.9469	0.3253	15.1	6.7	11.5	-0.4	4	-0.3
B(1)	0.4170	0.8652	0.3384	6	7.4	12.5	0.3	4.4	-0.6
B(2)	0.7865	0.8801	1.0013	9	6.7	7.2	3	2.3	-0.1
B(3)	0.0590	0.8858	0.6874	7.1	10.7	10.6	-2.1	3.8	-1.2
Li(1)	0.0594	0.7054	0.5475	14	12	25	-4	2	3
Li(2)	-0.3602	0.9492	0.5852	17	17	23	-5	2	6
Li(3)	0.7849	0.7052	1.1333	11	16	24	5	4	0
Li(4)	0.5721	0.9964	0.1774	12	11	22	0	6	-2
Li(5)	1.1935	0.9635	1.0573	17	29	22	-5	9	-8
Li(6)	0.9538	0.9699	1.3290	25	13	15	-1	5	-3

PXRD was performed as well on the ground powder sample from the as-grown LTB1 crystal. The diffraction pattern indicates no secondary phase, as is illustrated in Figure B.8. Profile matching refinement using Fullprof Suite gives cell parameters of $a = 7.210 \, \text{Å}, b = 16.476 \, \text{Å}, c = 6.672 \, \text{Å}, \beta = 105.36°$. They are in good agreement with the values obtained by single crystal refinement ($a = 7.2030(2) \, \text{Å}, b = 16.4723(3) \, \text{Å}, c = 6.6678(2) \, \text{Å}, \beta = 105.326°$).
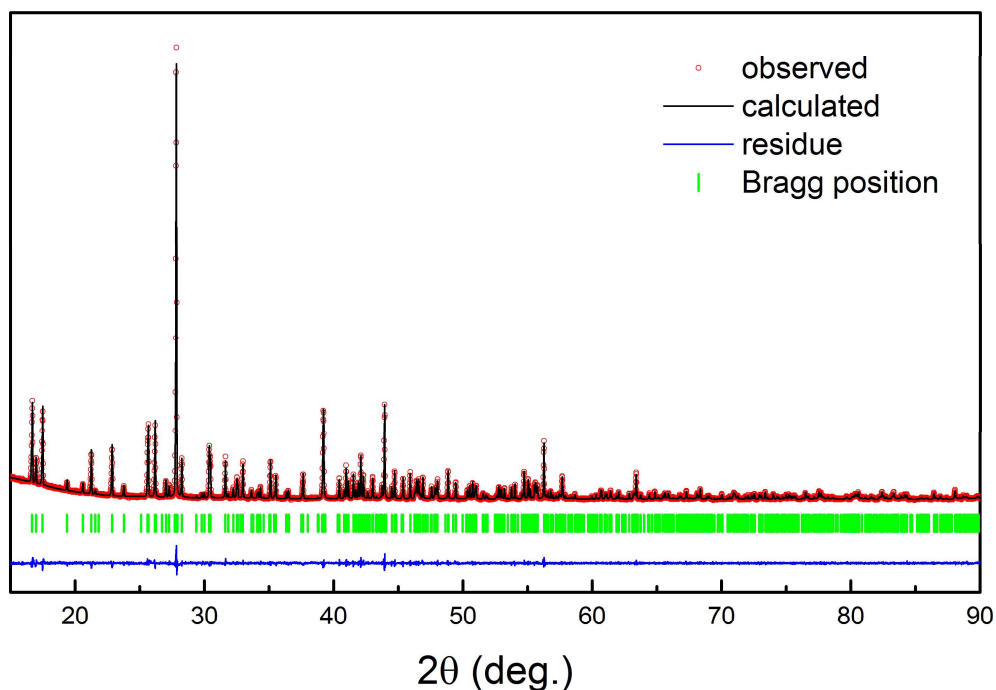
Figure B.8   **Experimental and refined PXRD pattern of LTB crystal sample.**

B.2.5 Ca₄TbO(BO₃)₃

Crystallographic positions of atoms in TbCOB are presented in Table B.11 [4]. Designated parameters for the crystal growth of TbCOB is given in Table B.12. Curves of the monitored data during the growth are illustrated in Figure B.9.

Table B.11   **Atomic coordinates of TbCOB (space group: Cm).**

Atom	Wyckoff	Occupancy	x	y	z
Tb(1)/Ca(1)	2a	0.96(2)/0.04(2)	0.00003	0	0.0041
Tb(2)/Ca(2)	4b	0.043(7)/0.957(7)	0.1400	0.38742	0.3192
Ca(3)	4b	1.0	0.2589	0.18157	0.6424
B(1)	2a	1.0	0	0.684	0.008
B(2)	4b	1.0	0.1945	0.065	0.011
O(1)	2a	1.0	0	0.409	0.009
O(2)	4b	1.0	0.4579	-0.0736	0.735
O(3)	2a	1.0	0.192	0	0.594
O(4)	4b	1.0	0.0818	0.1426	0.064
O(5)	4b	1.0	0.9665	0.2688	0.263
O(6)	4b	1.0	0.7876	0.1718	-0.130

Table B.12   Designated growth parameters of TbCOB

Step	Φ1 (mm)	Φ2 (mm)	Length (mm)	Pulling speed (mm/h)	Rotation (rpm)	P	I	D
neck	7	7	30	1	20	0.05	120	90
shoulder	7	25	30	1	20	0.05	120	90
body	25	25	50	1	20	0.03-0.05	120	90
bottom	25	1	20	1	20	0.03	120	90

PXRD pattern of the as-grown TbCOB, as is shown in Figure B.10, indicates no secondary phase. Profile matching refinement yields cell parameters of $a = 8.083\ \text{Å}, b = 16.024\ \text{Å}, c = 3.551\ \text{Å}, \beta = 101.241°$. They are in good agreement with the values obtained by single crystal refinement [4].
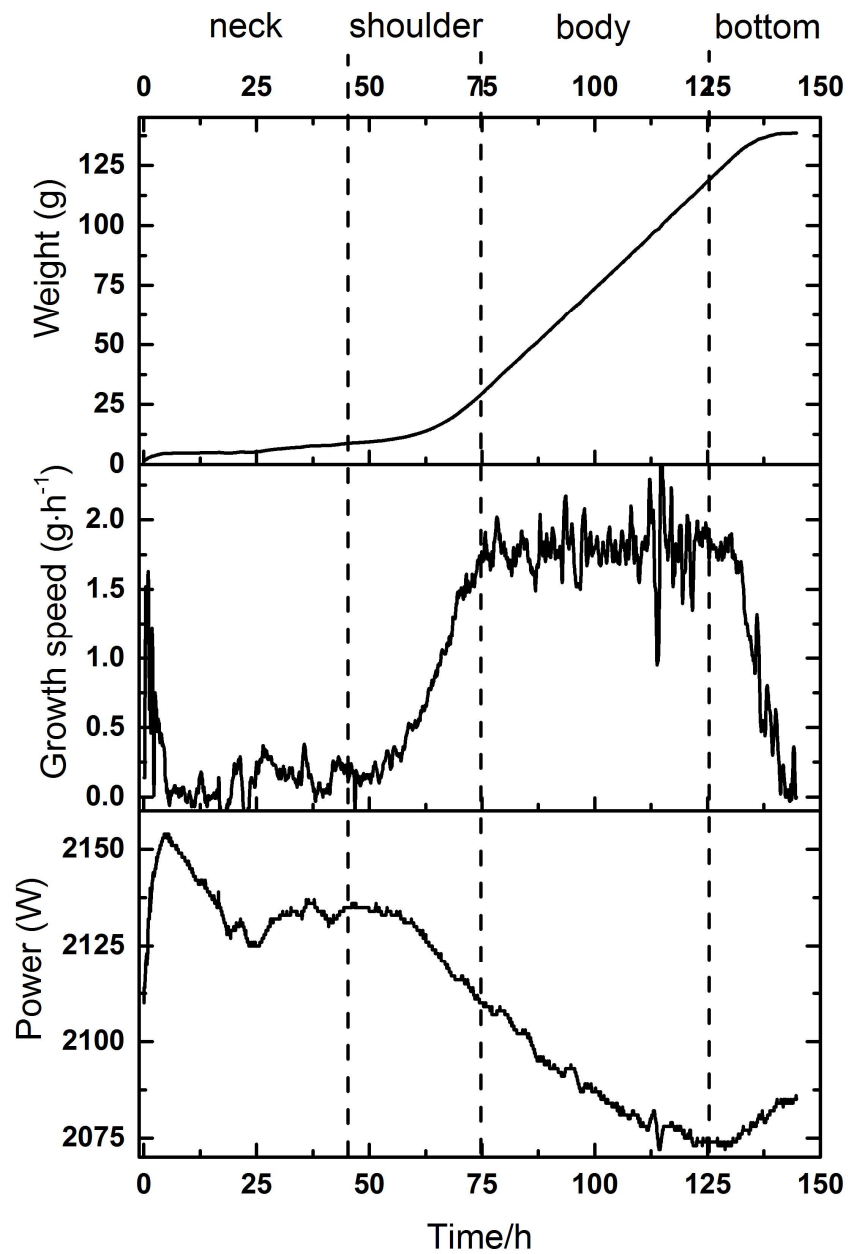
Figure B.9   Evolution of weight of crystal, growth speed, and power during the growth of TbCOB.
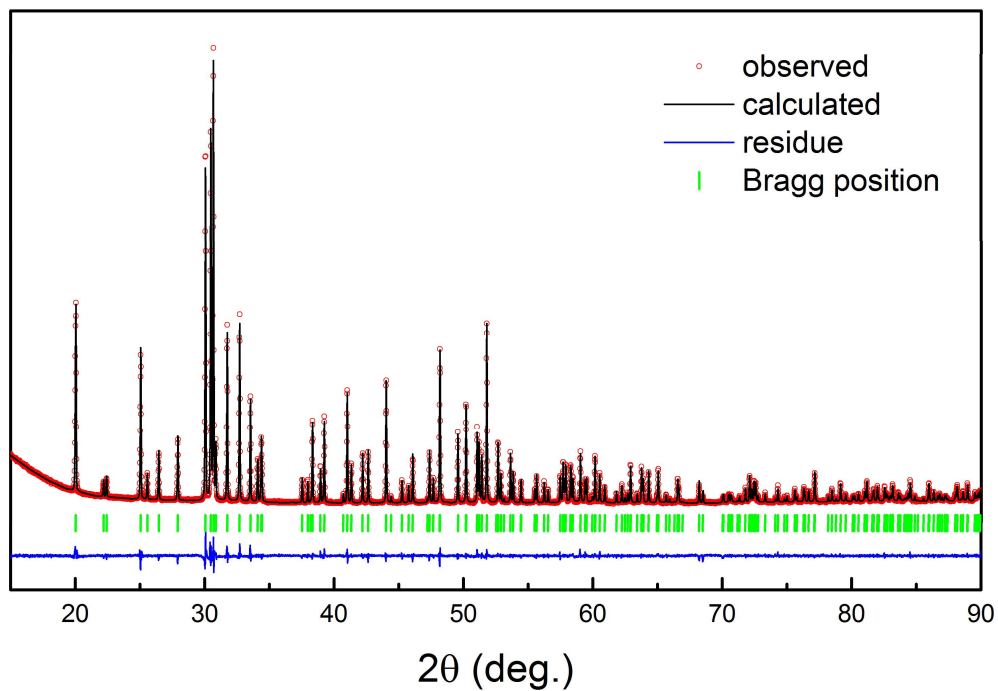
Figure B.10   Experimental and refined PXRD pattern of TbCOB crystal sample.

B.2.6 KTb(WO₄)₂

The atomic coordinates of TbCOB based on the refinement [5] are listed in Table B.13.

Table B.13   Atomic coordinates of KTW.

Atom	Wyckoff	x	y	z
K	4e	0	0.70006	3/4
Tb	4e	0	0.27161	3/4
W	8f	0.19551	0.00004	0.23581
O(1)	8f	0.1267	0.5787	0.1887
O(2)	8f	0.0239	0.1078	0.9714
O(3)	8f	0.2265	0.3419	0.1277
O(4)	8f	0.1894	0.9250	0.9410

B.2.7 Dy:CaYAlO₄

Crystallographic as well as selective physical properties of CYA are presented in Table B.14. An iridium crucible with a height of 50 mm and a diameter of 50 mm was used. Designated parameters for the crystal growth of Dy:CYA is given in Table B.14. Curves of the monitored data during the growth are

illustrated in Figure B.11. The significant oscillation of the growth rate could be caused by the evaporation of Al_2O_3 from the crystal or improper power regulation.

Table B.14   Designated growth parameters of Dy:CYA.

Step	Φ1 (mm)	Φ2 (mm)	Length (mm)	Pulling speed (mm/h)	Rotation (rpm)	P	I	D
neck	6	6	35	1	15	0.12	120	90
shoulder	6	25	25	1→0.7	15	0.1	120	90
body	25	25	45	0.7	15	0.1	120	90
bottom	25	1	20	0.7→1	15	0.1	120	90

In spite of the evaporation phenomenon during the growth, no secondary phase formation could be detected in the PXRD pattern of the as-grown crystal sample (Figure B.12). The cell parameters were found to be $a = 3.645$ Å and $c = 11.875$ Å via profile matching refinement. These values are very close to those of the pure CYA. This is due to the proximity of the ionic radius of Dy^{3+} and Y^{3+}, and the relatively low doping level in terms of the Ca/Y site (~1.8 %).

Figure B.11 Evolution of weight of crystal, growth speed, and power during the growth of Dy:CYA.

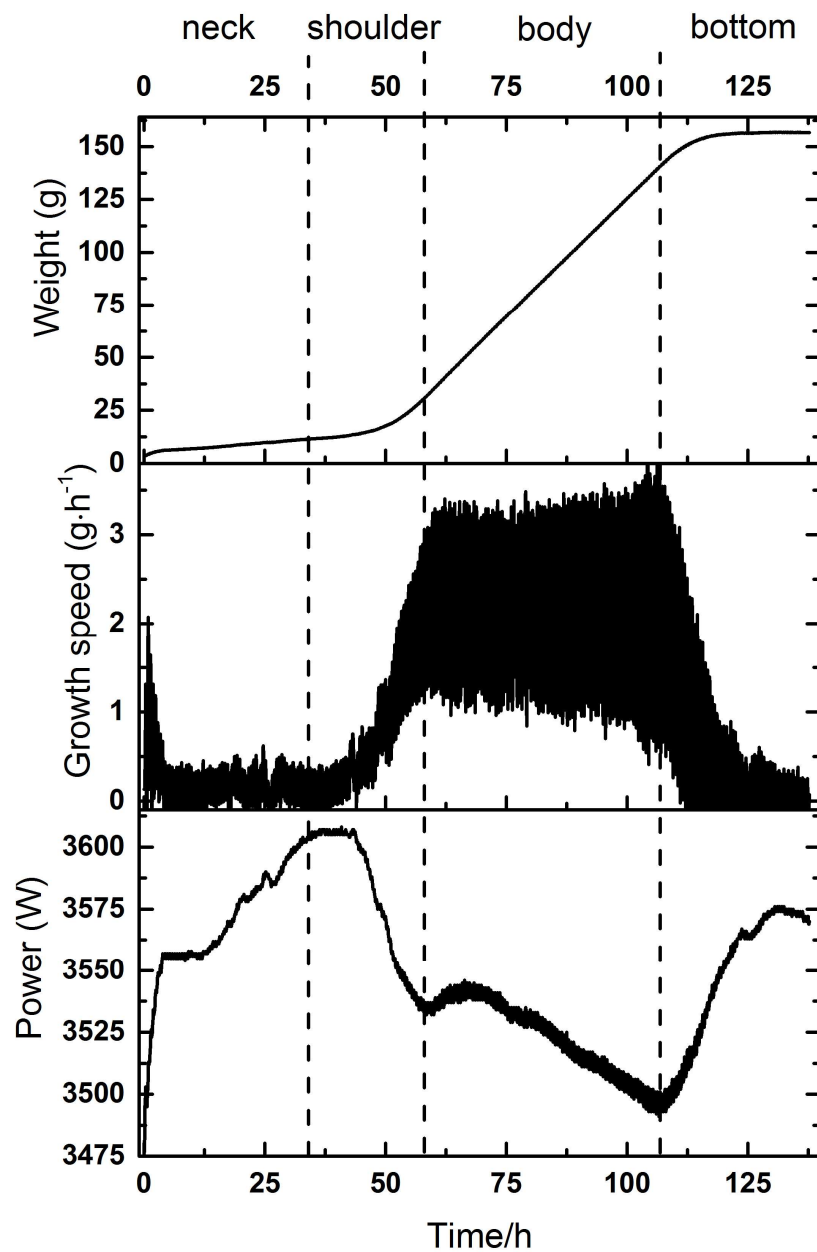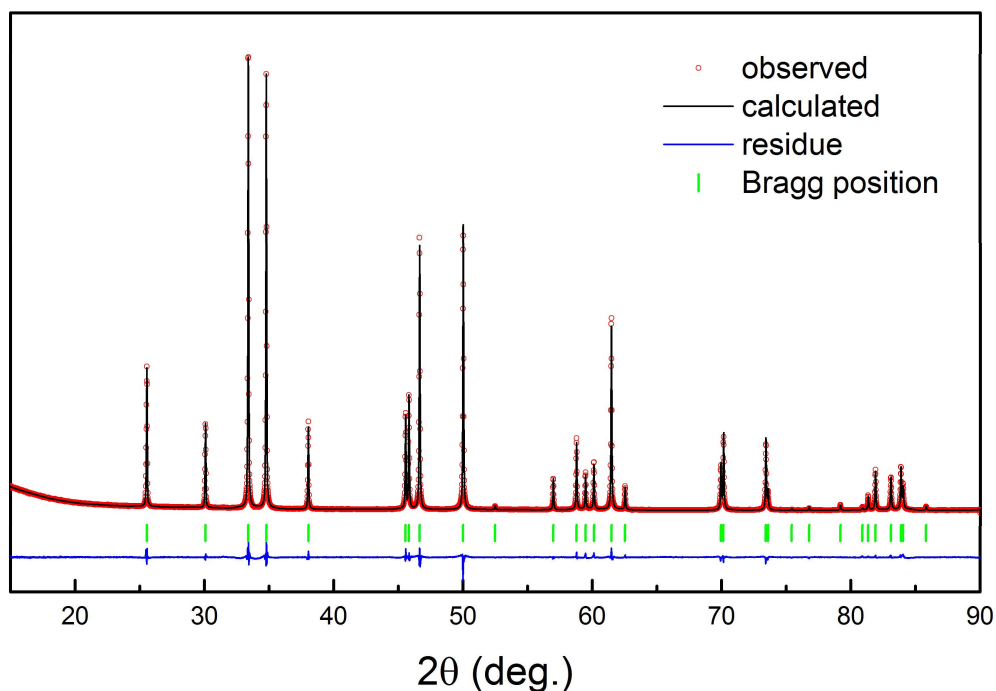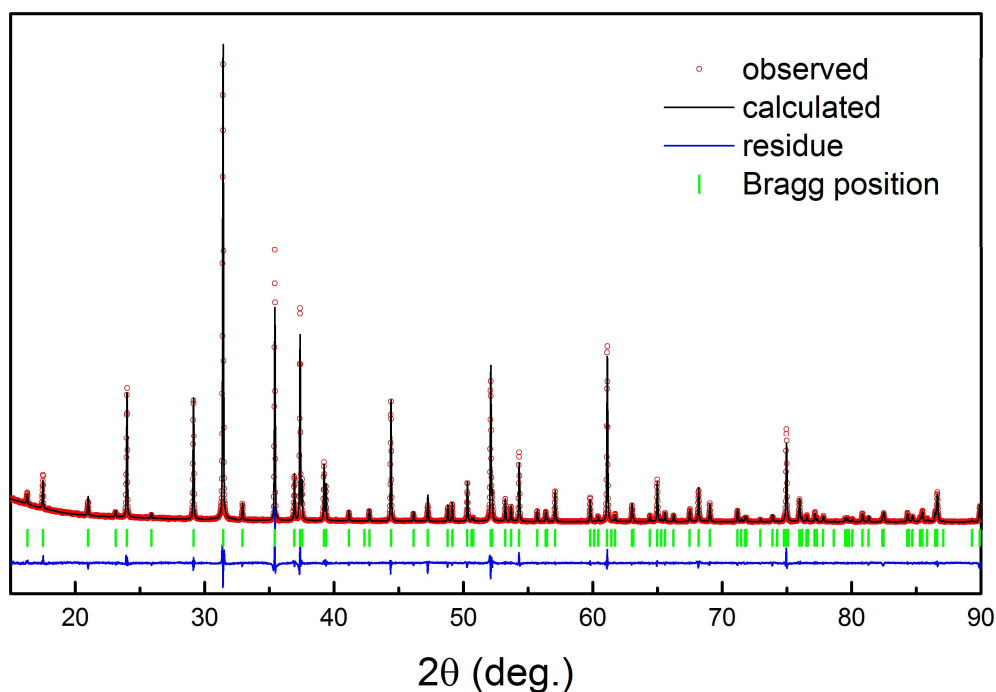**Figure B.12   Experimental and refined PXRD pattern of Dy:CYA crystal sample.**

B.2.8 Dy:CAS

The atomic coordinates of CAS are presented in Table B.15.

Table B.15   Atomic coordinates of CAS [6] (space group: $P\overline{4}2_1m$).

Atom	Wyckoff	Occupancy	x	y	z
Ca	4e	1	0.3389	0.1611	0.5104
Si	4e	0.5	0.1434	0.3566	0.9540
Al(2)	4e	0.5	0.1434	0.3566	0.9540
Al(1)	2a	1	0	0	0
O(1)	2c	1	0.5	0	0.1765
O(2)	4e	1	0.1427	0.3573	0.2835
O(3)	8f	1	0.0876	0.1678	0.8078

PXRD pattern of Dy:CAS (Figure B.13) does not exhibit any secondary phases, in spite of the significant optical inhomogeneity and inclusions inside the crystals. The refined cell parameters were found to be $a = 7.691$ and $c = 5.065$, which do not deviate too much from pure CAS. This can be accounted for by the fact that the cell parameters are simultaneously affected by doping smaller Dy^{3+} ions (r = 91.2 pm) in larger Ca^{2+} (r = 100 pm) sites and doping larger Al^{3+} ions (r = 53.5 pm) in smaller Si^{4+} (r = 40 pm) sites.

Figure B.13   Experimental and refined PXRD pattern of Dy:CAS crystal sample.

B.2.9 Dy:YCOB

The designated parameters for the crystal growth of Dy:YCOB is given in Table B.16. Curves of the monitored data during the growth are illustrated in Figure B.15.

Table B.16   Designated growth parameters of Dy:YCOB.

Step	Φ1 (mm)	Φ2 (mm)	Length (mm)	Pulling speed (mm/h)	Rotation (rpm)	P	I	D
neck	7	7	30	1	15	0.08-0.15	120	90
shoulder	7	22	30	1	15	0.08-0.1	120	90
body	22	22	50	1	15	0.08	120	90
bottom	22	1	20	1	15	0.08	120	90

Profile matching refinement of the ground crystal sample of Dy:YCOB (PXRD patterns are shown in Figure B.14) gives cell parameters: $a = 8.076, b = 16.018, c = 3.531, \beta = 101.172$. The unit cell volume is 448.08 Å^3, which is larger than that of YCOB owing to the slightly larger ionic radius of Dy^{3+} than Y^{3+}.
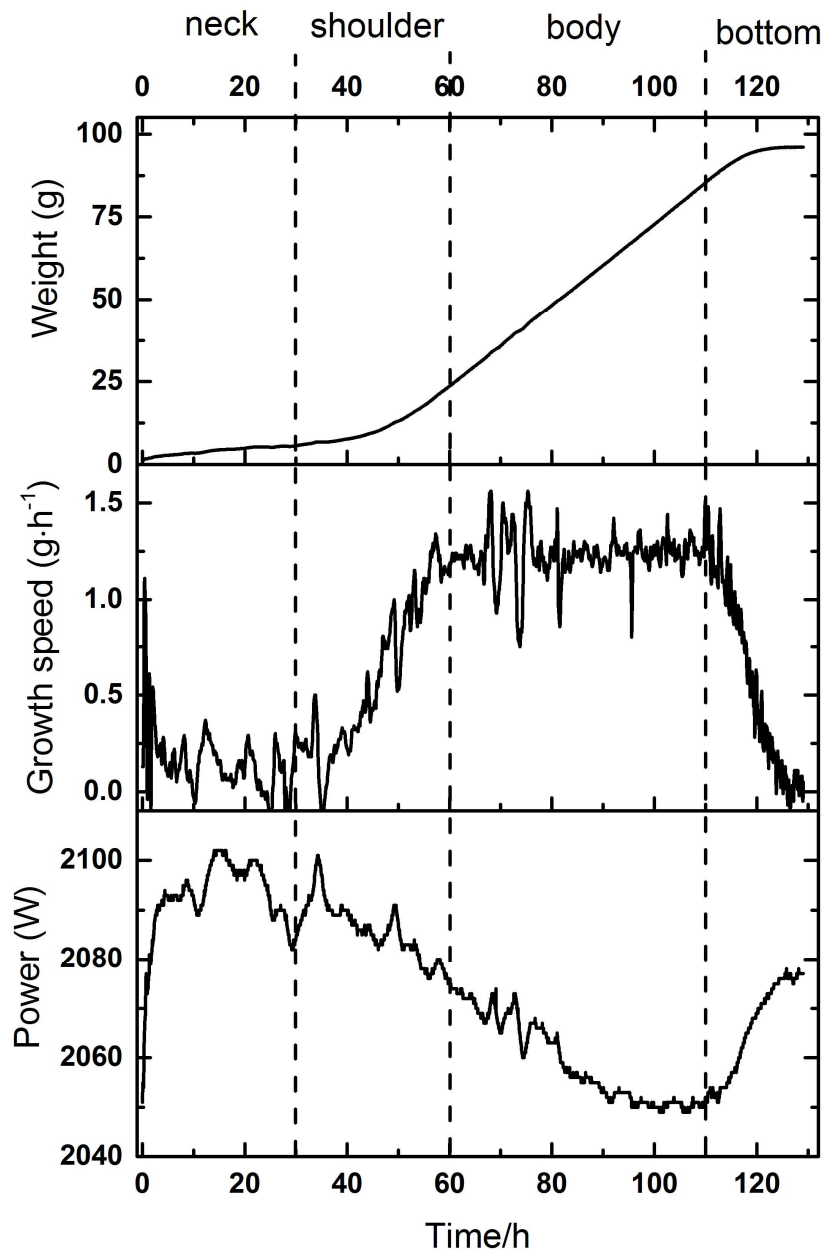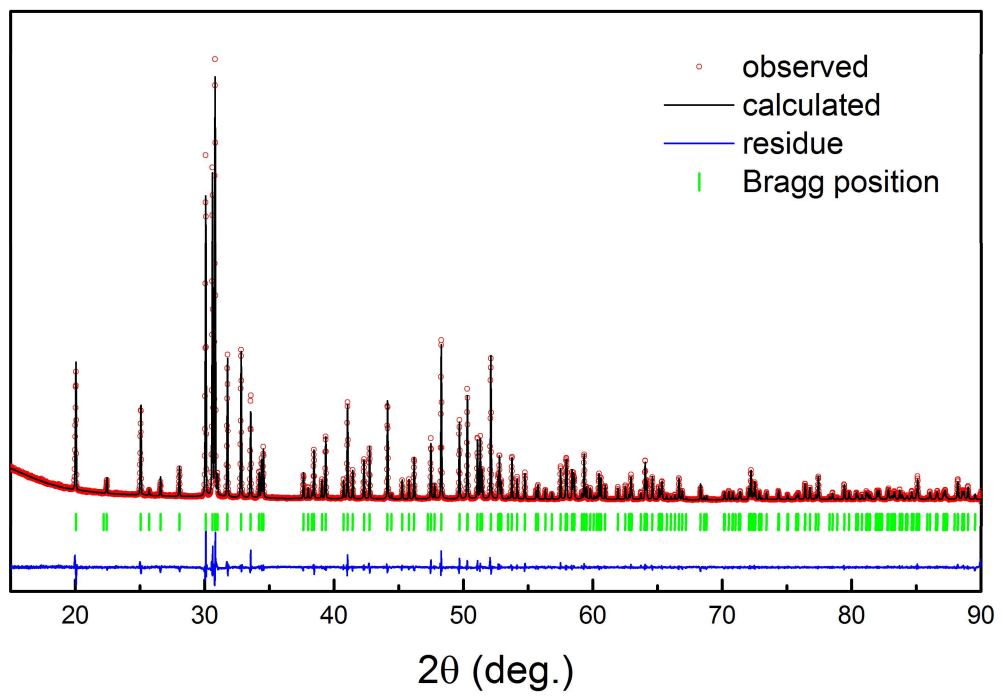
Figure B.14   Evolution of weight of crystal, growth speed, and power during the growth of Dy:YCOB.

Figure B.15 **Experimental and refined PXRD pattern of Dy:YCOB crystal sample.**

B.3 Physical property characterization

B.3.1 Optical microscopy

Optical microscopic photographs were obtained by a KEYENCE VHX-5000 microscope. An objective with a maximum capacity of 200× was used. The light passed through a polarizer, the crystal, an analyzer, and into the objective, orderly. The polarizer and analyzer were crossed with each other so that optical inhomogeneity could be easily detected in the medium.

B.3.2 Electron probe micro-analysis

Electron probe micro-analysis was performed on a CAMECA SX100 micro-analyzer with 4 wavelength-dispersive spectrometers. Crystals from different parts of the boule and the residue inside the crucible after the crystal growth were used for the analysis. A series of measurements was performed at ten random positions of each samples and the resulting data were averaged.

B.3.3 Electron paramagnetic resonance

The EPR measurements were carried out at room temperature using a Bruker ELEXSYS E500 spectrometer operating at X-band (~9.4 GHz) with 10 kHz field modulation. The magnetic field was swept from 50 to 5000 G. Before measuring the specimen, a blank was recorded to eliminate the possibility of interference by the background resonance of the cavity and/or sample tube. The spectra were recorded with Bruker 4122SHQE/0111 resonator.

B.3.4 Thermal conductivity and effusivity

Thermal conductivity as well as effusivity of the bulk crystal samples were measured at room temperature by a TCi thermal conductivity analyzer based on modified transient plane source. Water was used as contact reagent. The measurements were repeated for 10 times and the resulting data were averaged. Some significantly deviated data were excluded, which were usually observed during the first run.

B.3.5 Thermal expansion

Temperature-dependent PXRD measurements were carried out with an Anton Paar HTK 1200 N furnace directly mounted in the diffractometer. The temperature was increased to the designated value at a rate of 15°C/min. Before each measurement, the diffractometer was standby for 2 minutes in order to reach thermal equilibrium. The obtained PXRD patterns were refined by the Fullprof Suite to derive the cell parameters.

B.3.6 Laue X-ray diffraction

An ENRAF NONIUS DIFFRACTIS 601 was used as the X-ray (Cu Kα1 radiation) source for Laue diffraction. The typical working voltage and current of the X-ray tube were 45 kV and 35 mA. A PHOTONIC SCIENCE 2000 CCD camera with a resolution of 254×166 pixels was used to detect the X-ray photon signal. A precisely oriented silicon wafer mounted on the sample holder was used as a reference and the crystal sample was optically aligned to the silicon wafer to obtain accurate diffraction patterns. The exposure lasted for 450 seconds. The obtained diffraction patterns were dealt with ORIENTEXPRESS software to find the crystallographic orientations. Figure B.16 illustrates the diffraction patterns of LTB and TbCOB oriented to the b-axis.
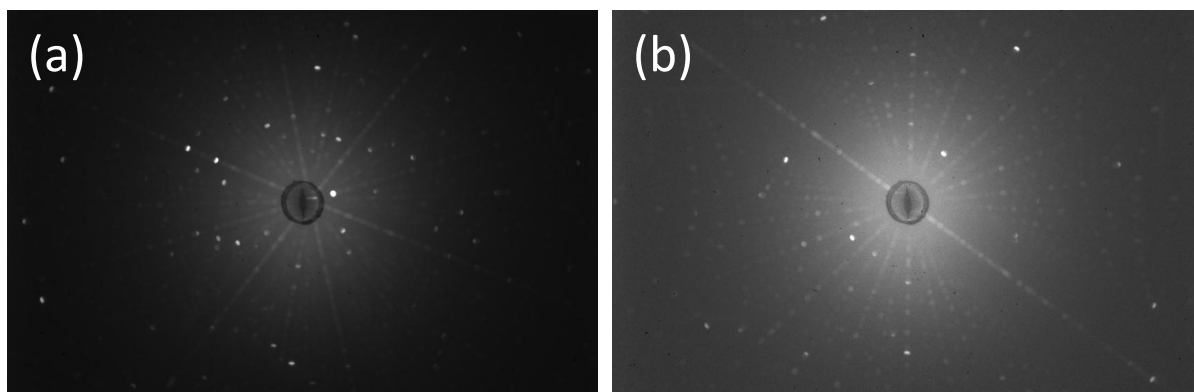

Figure B.16   **Laue diffraction patterns of b-oriented (a) LTB and (b) TbCOB.**

B.3.7 Ground-state absorption

Ground-state absorption spectra were recorded with Varian CARY 5000 or CARY 6000i spectrophotometers at room temperature. The former allows for measurements in a spectral range from 175 to 3300 nm (detectors: scintillating from 175nm-800nm; PbS from 800nm-3300nm) while the latter limits to 1800 nm (detector: InGaAs from 175nm-1800nm). The double beam mode was used for all the measurements with an empty sample holder as reference and the background was calibrated automatically by the photometers.

Except for the optically isotropic BTP, all the crystals were measured with a polarizer placed between the lamp source and sample to obtain polarized spectra. For the measurements in the spectral region less than 1800 nm, a calcite-based polarizer was employed. A TiO_2-based polarizer which shows a wider transparent range was utilized for wavelength larger than 1800 nm. To avoid the different response of the photometer to different polarized light, direction of the crystal sample was adjusted to obtain different polarized spectra instead of turning the polarizer. Optical loss of the polarizers was taken into account for the background calibration as well.

The aperture of the sample holder was 5 mm providing good signal-to-noise ratio. The thickness of the samples was typically around 5 mm. To record the intense $4f \rightarrow 5d$ transitions in the terbium-based crystals, samples with thickness less than 1 mm were prepared in order to avoid saturation. The slit

width of monochromator and data interval of each measurement were properly configured to ensure that the obtained spectra were fully resolved.

For a typical measurement, a spectrum with absorbance as a function of wavelength was obtained. After calibrating the spectrum for reflection of the crystal, the absorbance values can be converted to absorption coefficients according to Lambert-Beer law:

$$\alpha(\lambda) = \frac{Abs(\lambda)}{l \cdot log_{10}e}$$

where l is the thickness of the crystal sample. The optical density of light for absorption spectroscopic measurement is so small that the excited-state population in the crystal is negligible. The equation A1.13 described in Appendix A thus becomes:

$$\alpha(v) = \sigma_{abs}N$$

where N is the density of active ion in the crystal. For terbium-based crystals, which have stoichiometric chemical formula, the nominal concentrations of Tb^{3+} were used. The concentrations of Dy^{3+} in dysprosium-doped crystals were derived from EPMA analysis.

B.3.8 Judd-Ofelt analysis

Judd-Ofelt analysis in this work was performed with the RELIC software developed by M. P. Hehlen and coworkers [7], including, chronologically, the fitting of electrostatic intensity parameters and spin-orbit coupling parameter, the calculation of reduced matrix elements, the fitting of Judd-Ofelt intensity parameters, and the calculation of transition oscillator strengths and probabilities. The electrostatic interaction parameters $F_{(2)}$, $F_{(4)}$, $F_{(6)}$, and spin-orbit coupling parameter ζ are directly related to the corresponding $\hat{H}$-matrices in the forms below:

$$\langle 4f^N SL||\hat{H}_e||4f^N S'L'\rangle = \sum_{k=0}^{3} e_k E^{(k)}$$

in which

$$E^{(0)} = F_{(0)} - 10F_{(2)} - 33F_{(4)} - 286F_{(6)}$$

$$E^{(1)} = (70F_{(2)} - 231F_{(4)} - 2002F_{(6)})/9$$

$$E^{(2)} = (F_{(2)} - 3F_{(4)} - 7F_{(6)})/9$$

$$E^{(3)} = (5F_{(2)} + 6F_{(4)} - 91F_{(6)})/3$$

and

$$\langle 4f^N SLJ||\hat{H}_{so}||4f^N S'L'J'\rangle = \zeta(-1)^{J+L+S'}\sqrt{l(l+1)(2l+1)}$$

$$\times \begin{Bmatrix} S & S' & 1 \\ L' & L & J \end{Bmatrix} \langle l^N SL||V^{(11)}||l^N S'L'\rangle$$

The $F_{(0)}$ parameter simply produces a uniform shift of the energies of all the states of the configuration and thus is not necessary to be calculated. These four parameters are host-dependent and can be obtained by fitting the default values given in the manual of the software to a couple of experimental $^{2S+1}L_J$ multiplet energies. The barycenter energies can be precisely calculated from determining the energy and degeneracy of the stack levels generated by crystal-field splitting. Considering the complexity of this method, it is usually more realistic to obtain these values from ground-state absorption spectroscopy by assuming that the ground state is equally populated at room temperature and that all stack-level transitions contribute to the observed absorption spectrum. As a result, the barycenter energy E_B of a ground-state absorption transition is approximately equal to the energy where the integrated absorption cross-sections, which are proportional to the amount of populated electrons, of the low-energy side ($E < E_B$) and of the high-energy side ($E > E_B$) are equal (Figure B.17). For Tb^{3+}-based materials, relatively strong GSA transitions to the manifolds of $^5D_4$, $^5G_6$, $^5L_{10}$, $^5G_5$, $^5L_9$, $^5L_8$, and $^5L_7$ were used for the fitting of the electrostatic and spin-orbit interaction parameters. For Dy^{3+}-based materials, GSA transitions to $^6H_{13/2}$, $^6H_{11/2}$, $^6F_{5/2}$, $^6F_{3/2}$, $^4F_{9/2}$, $^4I_{15/2}$, and $^4G_{11/2}$ were used.
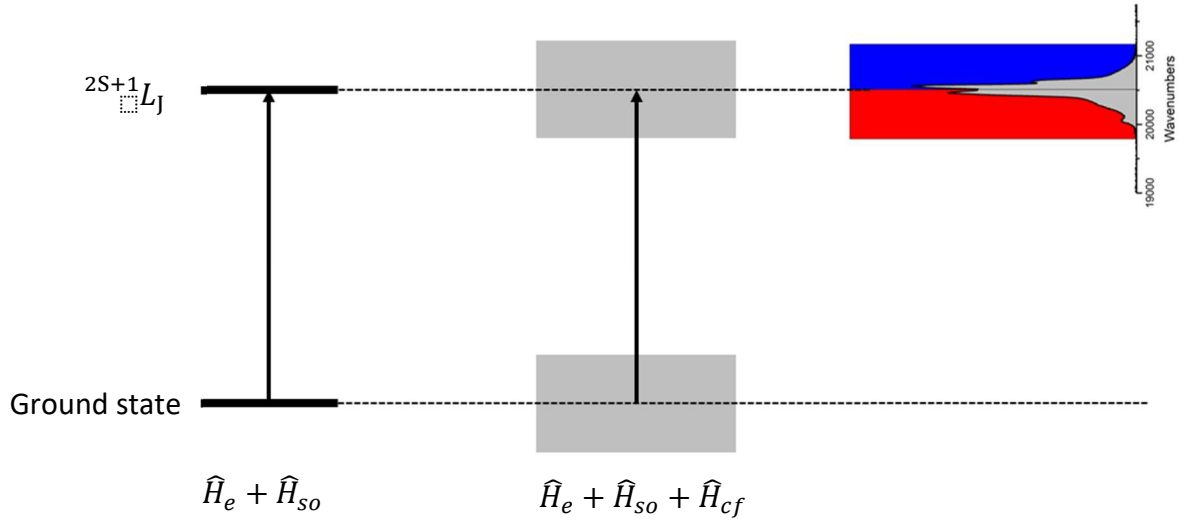
Figure B.17   **Determination of the barycenter energy of an energy level from ground-state absorption spectrum. The integral area of the red part is equal to the blue part.**

With the electrostatic and spin-orbit interaction parameters, the reduced matrix elements for the electric and magnetic dipole transitions can be calculated accordingly. It should be pointed out that the model for calculating the magnetic dipole elements $\langle l^N SLJ||\mathbf{L} + g\mathbf{S}||l^N S'L'J'\rangle$ employed in the RELIC software is rather rough. It is only related to the S, L, and J quantum numbers:

$$\langle l^N SLJ||\mathbf{L} + g\mathbf{S}||l^N S'L'J'\rangle = g\sqrt{J(J+1)(2J+1)}$$

for $J' = J$ and

$$\langle l^N SLJ||\mathbf{L} + g\mathbf{S}||l^N S'L'J'\rangle = (g-1)\sqrt{\frac{(S+L+J+1)(J+L-S)(J+S-L)(S+L-J+1)}{4J}}$$

for $J' = 1 \pm J$. The calculated oscillator strengths derived from the magnetic dipole transitions using this method matched poorly with the observed data, especially in the case of $J' = J$. More recently, C. M. Dodson and R. Zia managed to calculate the magnetic dipole oscillator strengths for all the trivalent lanthanide ions in a much more sophisticated approach in which a multi-parameter free ion Hamiltonian was used [8]. The vacuum MD oscillator strengths reported by C. M. Dodson and R. Zia are tabulated in Table B.17 and Table B.18. The calculated values are in good agreement with the experimental data, for example, the $^5D_4 \rightarrow {}^7F_J$ ($J = 3, 4, 5$) emission transitions of Tb^{3+} [9–11]. Further considering that the reduced matrix elements of the $\boldsymbol{L} + g\boldsymbol{S}$ tensor operator do not vary a lot with the coordination environment, the reported values in the literatures were used for Judd-Ofelt calculations for all the terbium and dysprosium-based compounds in this thesis. The obtained and used reduced matrix elements are tabulated in Table B.19.

Table B.17 **Reported energy level, matrix elements (in aqueous solution) of** $\left|\langle l^N SL \, ||U^{(\lambda)}|| l^N S'L'J'\rangle\right|^2$ **, and non-zero MD oscillator strengths of the ground-state absorption transitions of Tb^{3+} [8,12].**

Transitions $^7F_6 \rightarrow$	Energy (cm^{-1})	λ(nm)	$U^{(2)a}$	$U^{(4)}$	$U^{(6)}$	f_{MD}^{vacuum}
				$\times 10^4$		
$^5D_4$	20545	487	10	8	13	
$^5D_3$	26336	380	0	2	14	
$^5G_6$	26425	378	17	45	118	5.0×10^{-8}
$^5L_{10}$	27146	368	0	4	592	
$^5G_5$	27795	360	12	18	135	3.8×10^{-9}
$^5D_2$	28150	355	0	~ 0	8	
$^5G_4$	28319	353	1	3	91	
$^5L_9$	28503	351	0	21	446	
$^5G_3$	29007	345	0	1	31	
$^5L_8$	29202	342	~ 0	1	235	
$^5L_7$	29406	340	5	1	119	4.8×10^{-11}
$^5L_6$	29550	338	1	1	3	1.4×10^{-9}
$^5G_2$	29577	338	0	~ 0	5	
$^5D_1$	30658	326	0	0	3	
$^5D_0$	31228	320	0	0	1	
$^5H_7$	31557	317	60	19	131	4.8×10^{-10}
$^5H_6$	33027	303	27	~ 0	126	3.7×10^{-10}
$^5H_5$	33879	295	4	2	37	

^{a} $U^{(\lambda)} = \left|\langle l^N SLJ || \boldsymbol{U}^{(\lambda)} || l^N S'L'J'\rangle\right|^2$

Table B.18 **Reported energy level, matrix elements (in aqueous solution) of**

$\left|\langle l^N SLJ \| U^{(\lambda)} \| l^N S'L'J' \rangle\right|^2$ **, and non-zero MD oscillator strengths of ground-state absorption transitions of Dy^{3+} [8,13].**

Transitions $^6H_{15/2}\rightarrow$	Energy (cm^{-1})	λ(nm)	$U^{(2)}$	$U^{(4)}$	$U^{(6)}$	f_{MD}^{vacuum}
				$\times 10^4$		
$^6H_{13/2}$	3506	2852	2460	4140	6820	2.2×10^{-7}
$^6H_{11/2}$	5833	1714	920	370	6410	
$^6H_{9/2}$	7692	1300	0	176	1980	
$^6F_{11/2}$	7730	1294	9390	8290	2050	
$^6F_{9/2}$	9087	1100	0	5740	7210	
$^6H_{7/2}$	9115	1097	0	7	392	
$^6H_{5/2}$	10169	983	0	0	26	
$^6F_{7/2}$	11025	907	0	1360	7150	
$^6F_{5/2}$	12432	804	0	0	3450	
$^6F_{3/2}$	13212	757	0	0	610	
$^4F_{9/2}$	21144	473	0	47	295	
$^4I_{15/2}$	22293	449	73	3	654	5.5×10^{-8}
$^4G_{11/2}$	23321	429	4	145	3	
$^4F+^4I+^4K+^4M$	25750-26400	388-379	150^a	931	2268	6.1×10^{-9}
$^4D+^4F+^4G+^4I+^4K+^4M$ $+^4P$	27200-30200	368-331	28	5410	2630	2.4×10^{-9}
$^4F+^4G+^4K+^4L+^4M+^4P$	30800-32000	325-312	64	270	1260	

^{a} sum of the squared matrix elements of all the included transitions

Table B.19 Calculated reduced matrix elements which were used for Judd-Ofelt analysis of the terbium- and dysprosium-based compounds in this thesis. The $\langle l^N SLJ||L+gS||l^N S'L'J'\rangle$ terms were collected from the literatures [8,9].

SLJ	S'L'J'	$|\langle l^N SLJ||U^{(2)}||l^N S'L'J'\rangle|$				$|\langle l^N SLJ||U^{(4)}||l^N S'L'J'\rangle|$				$|\langle l^N SLJ||U^{(6)}||l^N S'L'J'\rangle|$				$L+gS$ [a]
		BTP	STB	LTB	TbCOB	BTP	STB	LTB	TbCOB	BTP	STB	LTB	TbCOB	
$^7F_6$	$^5D(3)_2$	0	0	0	0	0.0119	0.0141	0.0140	0.0142	0.0402	0.0365	0.0365	0.0365	
	$^5D(3)_3$	0	0	0	0	0.0295	0.0316	0.0315	0.0317	0.0424	0.0411	0.0411	0.0412	
	$^5D(3)_4$	0.0298	0.0275	0.0275	0.0274	0.0364	0.0399	0.0399	0.0401	0.0360	0.0364	0.0365	0.0365	
	$^5G(2)_4$	0.0104	0.0104	0.0104	0.0104	0.0126	0.0131	0.0132	0.0131	0.0976	0.0971	0.0973	0.0971	
	$^5G(3)_5$	0.0321	0.0331	0.0333	0.0332	0.0296	0.0297	0.0300	0.0298	0.1246	0.1231	0.1233	0.1232	0.204
	$^5G(3)_6$	0.0407	0.0444	0.0447	0.0445	0.0515	0.0495	0.0499	0.0496	0.1253	0.1220	0.1220	0.1220	0.782
	$^5L_7$	0.0394	0.0336	0.0325	0.0336	0.0180	0.0137	0.0130	0.0137	0.1171	0.1076	0.1067	0.1076	0.0229
	$^5L_8$	0.0032	0.0029	0.0030	0.0029	0.0142	0.0143	0.0143	0.0143	0.1343	0.1296	0.1301	0.1297	
	$^5L_9$	0	0	0	0	0.0439	0.0419	0.0420	0.0419	0.1953	0.1915	0.1922	0.1917	
	$^5L_{10}$	0	0	0	0	0.0247	0.0259	0.0258	0.0259	0.2217	0.2194	0.2202	0.2196	
$^5D(3)_4$	$^7F_0$	0	0	0	0	0.0415	0.0432	0.0433	0.0433	0	0	0	0	
	$^7F_1$	0	0	0	0	0.0525	0.0546	0.0547	0.0547	0	0	0	0	
	$^7F_2$	0.0349	0.0369	0.0370	0.0370	0.0283	0.0295	0.0294	0.0295	0.0100	0.0103	0.0104	0.0104	
	$^7F_3$	0.0485	0.0497	0.0498	0.0498	0.0072	0.0077	0.0080	0.0077	0.0227	0.0234	0.0235	0.0234	0.332
	$^7F_4$	0.0131	0.0136	0.0136	0.0136	0.0263	0.0280	0.0285	0.0281	0.0352	0.0362	0.0363	0.0363	0.108
	$^7F_5$	0.1146	0.1157	0.1160	0.1159	0.0204	0.0202	0.0205	0.0202	0.0460	0.0466	0.0467	0.0467	0.790
	$^7F_6$	0.0298	0.0275	0.0275	0.0274	0.0364	0.0399	0.0399	0.0401	0.0360	0.0364	0.0365	0.0365	

[a] $L+gS = |\langle l^N SLJ||L+gS||l^N S'L'J'\rangle|$

214

SLJ	$S'L'J'$	$\|\langle l^N SLJ\|\|U^{(2)}\|\|l^N S'L'J'\rangle\|$			$\|\langle l^N SLJ\|\|U^{(4)}\|\|l^N S'L'J'\rangle\|$			$\|\langle l^N SLJ\|\|U^{(6)}\|\|l^N S'L'J'\rangle\|$			$L+gS$
		Dy:CYA	Dy:CAS	Dy:YCOB	Dy:CYA	Dy:CAS	Dy:YCOB	Dy:CYA	Dy:CAS	Dy:YCOB	
$^6H_{15/2}$	$^6F_{3/2}$	0	0	0	0	0	0	0.2469	0.2471	0.2469	
	$^6F_{5/2}$	0	0	0	0	0	0	0.5880	0.5873	0.5880	
	$^6F_{7/2}$	0	0	0	0.3672	0.3653	0.3660	0.8473	0.8460	0.8475	
	$^6F_{9/2}$	0	0	0	0.7529	0.7534	0.7497	0.8586	0.8551	0.8619	
	$^6F_{11/2}$	0.9673	0.9796	0.9730	0.9114	0.9041	0.9086	0.4467	0.4816	0.4619	
	$^6H_{5/2}$	0	0	0	0	0	0	0.0482	0.0492	0.0471	
	$^6H_{7/2}$	0	0	0	0.0312	0.0304	0.0332	0.1866	0.1887	0.1819	
	$^6H_{9/2}$	0	0	0	0.1539	0.1472	0.1630	0.4225	0.4287	0.4119	
	$^6H_{11/2}$	0.3091	0.2666	0.2903	0.1872	0.2250	0.2042	0.8022	0.7824	0.7936	
	$^6H_{13/2}$	0.4956	0.4956	0.4956	0.6435	0.6436	0.6437	0.8242	0.8254	0.8244	5.06
	$^4F(3)_{9/2}$	0	0	0	0.0726	0.0783	0.0830	0.1792	0.1837	0.1880	
	$^4G(4)_{11/2}$	0.0037	0.0044	0.0006	0.1079	0.1037	0.1007	0.0395	0.0416	0.0460	
	$^4I(3)_{15/2}$	0.0852	0.0858	0.0867	0.0193	0.0185	0.0188	0.2728	0.2656	0.2715	1.03
$^5D(3)_4$	$^6F_{1/2}$	0	0	0	0.0160	0.0153	0.0154	0	0	0	
	$^6F_{3/2}$	0	0	0	0.0061	0.0038	0.0061	0.0152	0.0137	0.0151	
	$^6F_{5/2}$	0.0791	0.0767	0.0784	0.0330	0.0304	0.0324	0.0195	0.0196	0.0190	
	$^6F_{7/2}$	0.0155	0.0197	0.0189	0.0685	0.0687	0.0720	0.0522	0.0479	0.0488	0.684
	$^6F_{9/2}$	0.0314	0.0313	0.0344	0.0788	0.0850	0.0876	0.0313	0.0332	0.0361	0.524
	$^6F_{11/2}$	0.0513	0.0431	0.0444	0.0649	0.0665	0.0696	0.0594	0.0524	0.0589	1.31
	$^6H_{5/2}$	0.0016	0.0021	0.0019	0.0598	0.0598	0.0610	0.0352	0.0399	0.0394	
	$^6H_{7/2}$	0.0302	0.0288	0.0304	0.0908	0.0921	0.0935	0.0840	0.0880	0.0897	0.387
	$^6H_{9/2}$	0.0491	0.0446	0.0470	0.0535	0.0586	0.0578	0.0573	0.0603	0.0606	0.321
	$^6H_{11/2}$	0.1006	0.1057	0.1083	0.0501	0.0542	0.0577	0.0552	0.0582	0.0578	0.553
	$^6H_{13/2}$	0.2253	0.2293	0.2338	0.1262	0.1252	0.1274	0.2416	0.2408	0.2490	
	$^6H_{15/2}$	0	0	0	0.0726	0.0783	0.0830	0.1792	0.1837	0.1880	

215

After obtaining the reduced matrix elements $\langle l^N SLJ||\boldsymbol{U}^{(\lambda)}||l^N S'L'J'\rangle$ $(\lambda = 2,4,6)$ and $\langle l^N SLJ||\boldsymbol{L} + g\boldsymbol{S}||l^N S'L'J'\rangle$, the Judd-Ofelt intensity parameters can be fitted from the experimental oscillator strengths. In a practical case, the overlap of transitions makes it difficult to assign the oscillator strength of an absorption band to each comprised transitions. The total oscillator strength of a number of i overlapped transitions is the sum of the electric and magnetic dipole counterparts:

$$f = \frac{8\pi^2 m_e}{3h(2J+1)} \sum_i \nu_i \frac{\chi^{abs}_{ED,i}}{n_i} \sum_{\lambda=2,4,6} \Omega_\lambda \left| \langle l^N SLJ||\boldsymbol{U}^{(\lambda)}||l^N S'L'J'\rangle \right|^2_i$$
$$+ \frac{h\nu}{6m_e c^2 (2J+1)} \sum_i n_i |\langle l^N SLJ||\boldsymbol{L} + g\boldsymbol{S}||l^N S'L'J'\rangle|^2_i$$

Since the energy and refractive index of each transitions within this absorption band do not vary significantly, they can be replaced by the averaged values. The above equation becomes:

$$f = \frac{8\pi^2 m_e}{3h} \frac{\nu}{(2J+1)} \frac{\chi^{abs}_{ED}}{n} \sum_{\lambda=2,4,6} \Omega_\lambda \left| \langle l^N SLJ||\boldsymbol{U}^{(\lambda)}||l^N S'L'J'\rangle \right|^2_{tot}$$
$$+ \frac{h\nu}{6m_e c^2} \frac{n}{(2J+1)} |\langle l^N SLJ||\boldsymbol{L} + g\boldsymbol{S}||l^N S'L'J'\rangle|^2_{tot}$$

where

$$\left| \langle l^N SLJ||\boldsymbol{U}^{(\lambda)}||l^N S'L'J'\rangle \right|^2_{tot} = \sum_i \left| \langle l^N SLJ||\boldsymbol{U}^{(\lambda)}||l^N S'L'J'\rangle \right|^2_i$$

$$|\langle l^N SLJ||\boldsymbol{L} + g\boldsymbol{S}||l^N S'L'J'\rangle|^2_{tot} = \sum_i |\langle l^N SLJ||\boldsymbol{L} + g\boldsymbol{S}||l^N S'L'J'\rangle|^2_i$$

Using the RELIC software, least-square fitting of the overlapped transitions can be realized by adding these "total" reduced matrix elements to its database (*.arc file).

It is also worth mentioning the input of the refractive index for Judd-Ofelt analysis. Since "non-polarized" oscillator strengths are used for calculation, a "non-polarized" refractive index dispersion equation is required. Typically, the measured refractive indices along principal optical directions are averaged by the equation $n_{avg} = (2n_0 + n_e)/3$ for uniaxial and $n_{avg} = (n_X + n_Y + n_Z)/3$ for biaxial crystals. One may notice that this n_{avg} does not exactly lead to the local-field correction $\frac{\chi^{abs}_{ED}}{n}$ for ED transitions ($\chi^{abs}_{ED} = (n^2+2)^2/9$), which should equal to $(2\frac{\chi^{abs}_o}{n_0} + \frac{\chi^{abs}_e}{n_e})/3$ for uniaxial and $(\frac{\chi^{abs}_X}{n_X} + \frac{\chi^{abs}_Y}{n_Y} + \frac{\chi^{abs}_Z}{n_Z})/3$ for biaxial crystals. Nevertheless, it has been deduced that for STB, the relative error regarding the local-field correction generated by this approximation is in the order of 10^{-5}, which is totally acceptable.

B.3.9 Emission spectroscopy and fluorescence decay

A tunable Ekspla NT342B optical parametric oscillator (OPO) laser based on Nd:YAG operated in pulse mode was adopted as the excitation source to obtain the emission spectra and the fluorescence decay profiles. The laser pulse has a duration of ca. 7 ns with an energy in the order of 10 mJ. The OPO laser worked in a repetition rate of 10 Hz. The intensity of the laser beam was adjusted by an external polarizer.

The polarized emission spectra were detected by a CCD camera (Princeton Instruments, 1024×268 pixels) equipped with a monochromator (Acton Research, 300 grooves/mm, 500-nm blaze). A spectral resolution of 0.276 nm could be obtained in this setup. The gate width and gate delay were fixed to be 100 µs for each measurements. Two gate times were averaged for each exposure to improve the spectral stability. To avoid the different response of the CCD camera to different polarizations, position of the crystal sample was adjusted to derive the corresponding polarized spectra instead of turning the polarizer. The laser beam was aligned to the slit so that only the fluorescence in the light route could be detected. Perpendicularity of the crystal as well as the polarizer to the laser beam was examined optically. Measurements of the fluorescence spectra were accumulated for >100 times to increase the signal-to-noise ratio. The resulting fluorescence signals were calibrated to relative spectral irradiance (power per unit area per unit wavelength) for the response of the apparatus.

Time evolution of the fluorescence intensity was monitored using an RCA 8850 photomultiplier. The photomultiplier is based on gallium phosphide semiconductor and the response time is ca. 3.3×10^{-8} s. The fluorescence decay data were accumulated and averaged for 256 runs. Setup for the fluorescence spectrum and decay measurements is illustrated in Figure B.18.
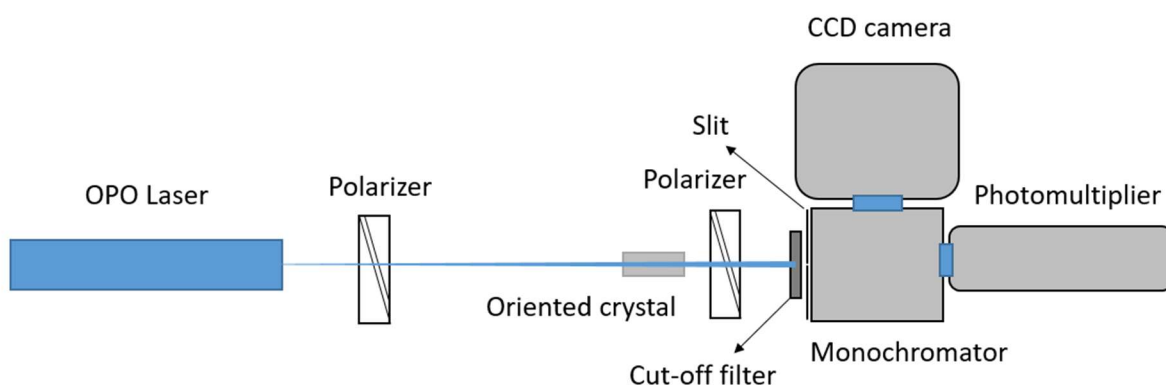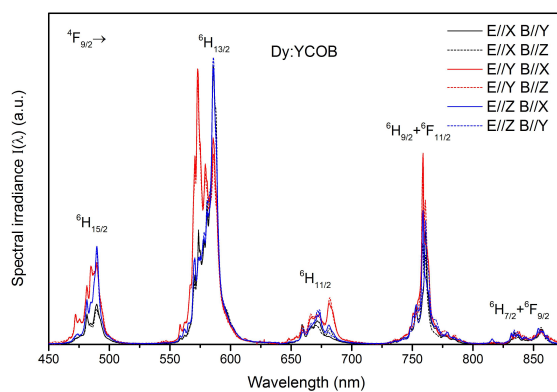

Figure B.18   Experimental setup for the fluorescence spectroscopic measurements.

The calibrated fluorescence spectra in units of spectral irradiance (power per unit area per unit wavelength) are shown in Figure B.19.

217
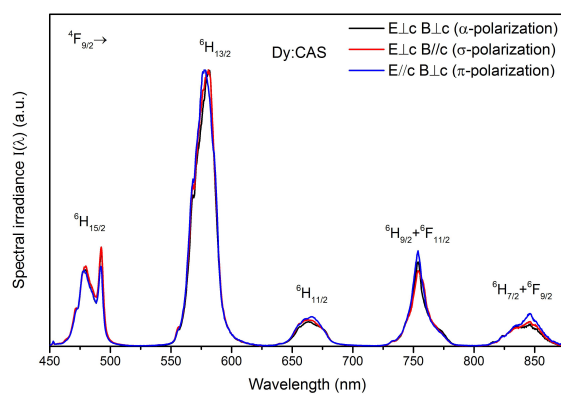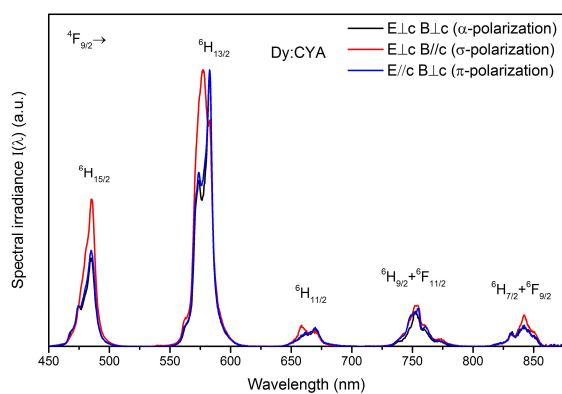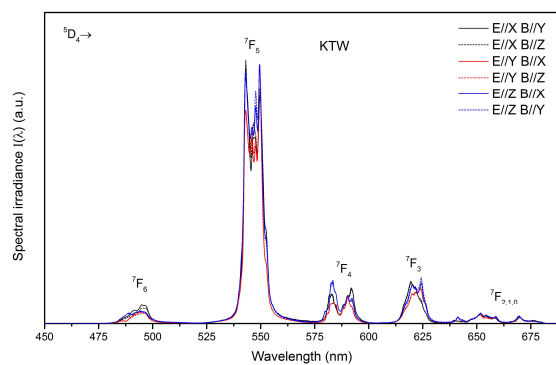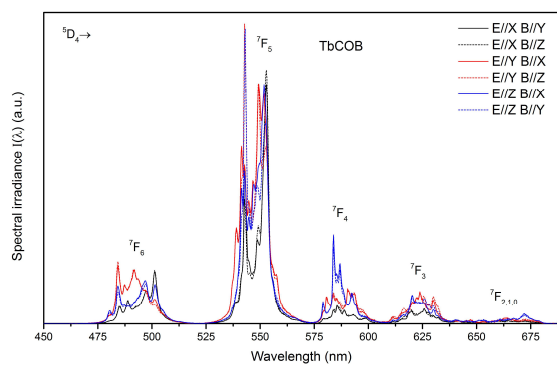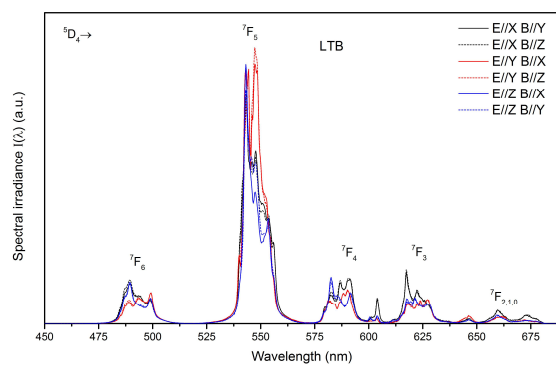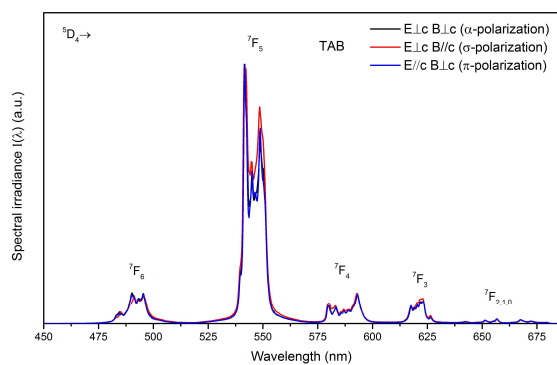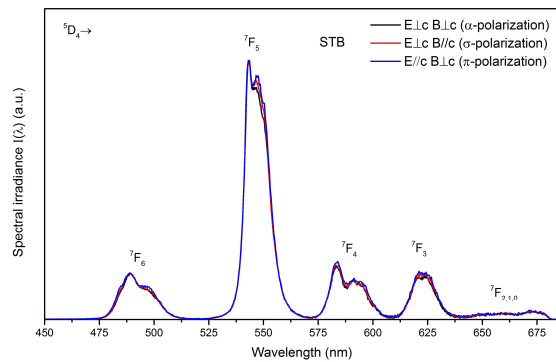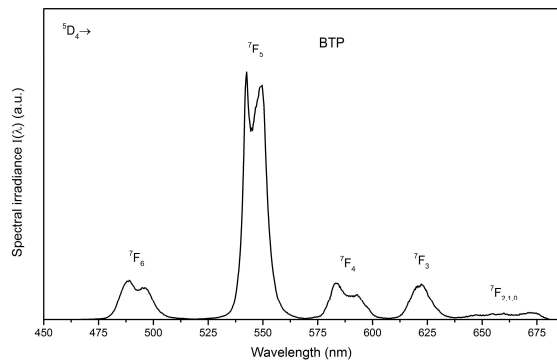
(continued from previous page)

Figure B.19   Calibrated fluorescence spectra in arbitrary units of spectral irradiance.

The fluorescence decay curve monitored at 604 nm for LTB, a susceptible parasitic emission band, is illustrated in Figure B.20. The weak intensity of this emission line results in a small signal-to-noise ratio. The fluorescence lifetime is linear-fitted to be 2.62 ms.
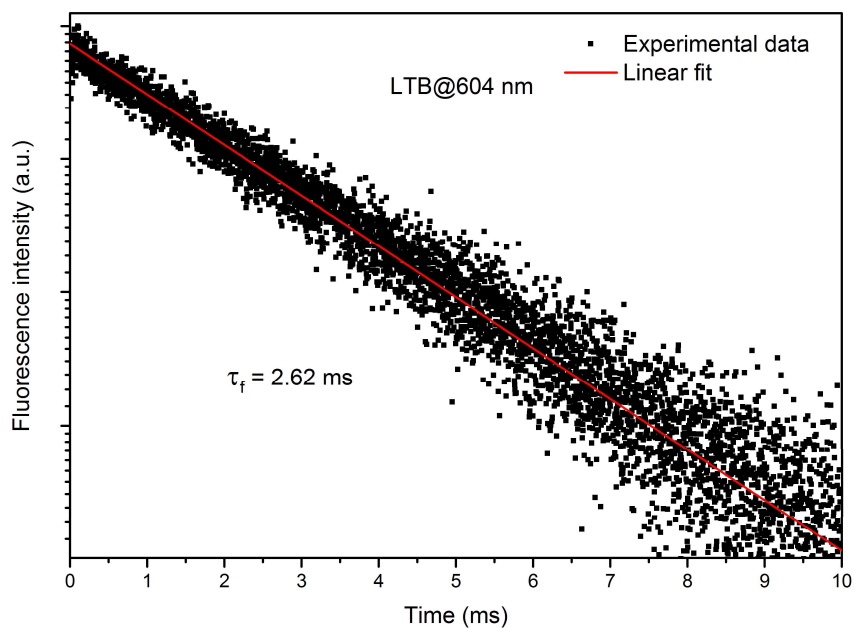
Figure B.20   Fluorescence decay curve of LTB monitored at 604 nm.

References of Appendix B

[1] X. Chen, Z. Gong, Q. Wan, S. Wu, F. Guo, N. Zhuang, J. Chen, $Ba_3Tb(PO_4)_3$: Crystal growth, structure, magnetic and magneto-optical properties, Opt. Mater. 44 (2015) 48–53. doi:10.1016/j.optmat.2015.02.029.

[2] J. Rodríguez-Carvajal, Recent advances in magnetic structure determination by neutron powder diffraction, Phys. B Condens. Matter. 192 (1993) 55–69. doi:10.1016/0921-4526(93)90108-I.

[3] K.I. Schaffers, P.D. Thompson, T. Alekel, J.R. Cox, D.A. Keszler, STACK Crystal Chemistry, Chem. Mater. 6 (1994) 2014–2022. doi:10.1021/cm00047a022.

[4] Yuan Dongsheng, Equipment development and single crystal growth of micro-pulling-down, and the synthesis and investigations of functional crystal TbCOB, Shandong University, 2016.

[5] S. Schwung, D. Rytz, B. Heying, U.C. Rodewald, O. Niehaus, D. Enseling, T. Jüstel, R. Pöttgen, The crystal structure and luminescence quenching of poly- and single-crystalline $KYW_2O_8:Tb^{3+}$, J. Lumin. 166 (2015) 289–294. doi:10.1016/j.jlumin.2015.05.052.

[6] I. Swainson, M. Dove, W. Schmahl, A. Putnis, Neutron powder diffraction study of the Akermanite-gehlenite solid solution series, Phys. Chem. Miner. 19 (1992). doi:10.1007/BF00202107.

[7] M.P. Hehlen, M.G. Brik, K.W. Krämer, 50th anniversary of the Judd–Ofelt theory: An experimentalist's view of the formalism and its application, J. Lumin. 136 (2013) 221–239. doi:10.1016/j.jlumin.2012.10.035.

[8] C.M. Dodson, R. Zia, Magnetic dipole and electric quadrupole transitions in the trivalent lanthanide series: Calculated emission rates and oscillator strengths, Phys. Rev. B. 86 (2012). doi:10.1103/PhysRevB.86.125102.

[9] T. Hoshina, Radiative Transition Probabilities in Tb^{3+} and Fluorescence Colors Producible by Tb^{3+}-Activated Phosphors, Jpn. J. Appl. Phys. 6 (1967) 1203–1211. doi:10.1143/JJAP.6.1203.

[10] W.T. Carnall, P.R. Fields, K. Rajnak, Spectral Intensities of the Trivalent Lanthanides and Actinides in Solution. II. Pm^{3+}, Sm^{3+}, Eu^{3+}, Gd^{3+}, Tb^{3+}, Dy^{3+}, and Ho^{3+}, J. Chem. Phys. 49 (1968) 4412–4423. doi:10.1063/1.1669892.

[11] M.J. Weber, T.E. Varitimos, B.H. Matsinger, Optical Intensities of Rare-Earth Ions in Yttrium Orthoaluminate, Phys. Rev. B. 8 (1973) 47–53. doi:10.1103/PhysRevB.8.47.

[12] W.T. Carnall, P.R. Fields, K. Rajnak, Electronic Energy Levels of the Trivalent Lanthanide Aquo Ions. III. Tb^{3+}, J. Chem. Phys. 49 (1968) 4447–4449. doi:10.1063/1.1669895.

[13] W.T. Carnall, P.R. Fields, K. Rajnak, Electronic Energy Levels in the Trivalent Lanthanide Aquo Ions. I. Pr^{3+}, Nd^{3+}, Pm^{3+}, Sm^{3+}, Dy^{3+}, Ho^{3+}, Er^{3+}, and Tm^{3+}, J. Chem. Phys. 49 (1968) 4424–4442. doi:10.1063/1.1669893.

Résumé

Les lasers visibles sont nécessaire et utilisés dans large domaine d'applications. À ce jour, l'obtention de sources lasers visibles de haute qualité repose sur un processus de conversion de fréquence des lasers à base de Nd^{3+} ou Yb^{3+} émettant dans l'infrarouge. Une nouvelle classe de lasers activés par des ions Lanthanides émiettant directement dans la région spectrale visible a été développée récemment. Ces lasers ne présentent pas l'inconvénient des lasers visibles traditionnels, tels que la perte d'énergie inévitable pendant le processus de conversion de fréquence, ce qui ouvre des perspectives de recherche prometteuses.

Un défi de ce sujet reste la génération d'émission laser efficace en utilisant des matériaux à base d'oxyde activés par des ions Tb^{3+} ou Dy^{3+}. Ces travaux de thèse se concentrent sur la fabrication et l'étude des propriétés physiques d'une sélection de monocristaux à base d'oxyde activés par des ions Tb^{3+} ou Dy^{3+}: $Ba_3Tb(PO_4)_3$, $Sr_3Tb(BO_3)_3$, $TbAl_3(BO_3)_3$, $Li_6Tb(BO_3)_3$, $TbCa_4O(BO_3)_3$, $KTb(WO_4)_2$, $Dy:CaYAlO_4$, $Dy:YCa_4O(BO_3)_3$, and $Dy:Ca_2Al_2SiO_7$ La technique classique de croissance cristalline dite Czochralski a été utilisée pour la préparation de monocristaux et les conditions de croissance ont été optimisées. Des monocristaux de bonne qualité optique de ces composés ont été obtenus. Les propriétés thermiques en particulier celles des cristaux à base de Tb^{3+} ont été étudiées. La majeure partie des travaux a concerné la caractérisation de leurs propriétés optiques, y compris les indices de réfraction, les spectres d'absorption et d'émission, les paramètres de Judd-Ofelt, la dynamique de fluorescence et l'absorption de l'état excité. Les sections efficaces de transitions et les durées de vie de l'état excité des cristaux d'oxyde activés par Tb^{3+} se sont avérées être comparables à celles des cristaux de fluorure. Le cristal $Dy:CaYAlO_4$ a des propriétés spectroscopiques pour une émission laser dans le jaune comparativement aux résultats publiés pour le cristal Dy:YAG. Des tests lasers ont été envisagés en utilisant des sources de pompage laser à base de semi-conducteurs émettant dans le bleu.

Mots Clés

Terbium, dysprosium, croissance monocristalline, spectroscopie optique, laser visible

Abstract

Visible lasers are useful in a variety range of fields. To date, high-quality visible lasers rely on the frequency conversion of Nd^{3+}- or Yb^{3+}-based infrared-emitting lasers. A new class of Ln^{3+}-activated lasers operating directly with emission transitions in the visible spectral region has been developed recently, which do not feature the inconvenience of the traditional visible lasers, such as the inevitable energy loss during the frequency conversion process, and have promising research prospects.

The current challenge is to generate efficient laser emissions using Tb^{3+}- or Dy^{3+}-activated oxide-based gain materials. This PhD thesis concentrates on the fabrication and physical-property study of several selected Tb^{3+}- or Dy^{3+}-activated oxide-based single crystals: $Ba_3Tb(PO_4)_3$, $Sr_3Tb(BO_3)_3$, $TbAl_3(BO_3)_3$, $Li_6Tb(BO_3)_3$, $TbCa_4O(BO_3)_3$, $KTb(WO_4)_2$, $Dy:CaYAlO_4$, $Dy:YCa_4O(BO_3)_3$, and $Dy:Ca_2Al_2SiO_7$. The conventional Czochralski technique was employed for the single-crystal preparation and the growth conditions were optimized. Single crystals of these compounds with good optical quality were obtained. Thermal properties of the Tb^{3+}-based crystals were studied. The main effort was devoted to the characterization of their optical properties, including the refractive index, absorption and emission spectra, Judd-Ofelt parameters, fluorescence dynamic, and excited-state absorption. The transition cross-sections and upper-state lifetimes of the Tb^{3+}-activated oxide crystals were found to be comparable to those of the fluorides. The $Dy:CaYAlO_4$ crystal has comparable spectroscopic properties for yellow laser operation to the reported results of the Dy:YAG gain medium as well. Laser experiments were essayed using pump sources of blue-emitting semiconductor lasers.

Keywords

Terbium, dysprosium, single crystal growth, optical spectroscopy, visible laser